III-V Microdisk Lasers on Silicon-on-Insulator: Fabrication Optimizations and Novel Applications

III-V-microschijflasers op silicium-op-isolator: fabricageoptimaliseringen en nieuwe toepassingen

Pauline Mechet

Promotoren: prof. dr. ir. G. Morthier, prof. dr. ir. G. Roelkens
Proefschrift ingediend tot het behalen van de graad van
Doctor in de Ingenieurswetenschappen: Fotonica

Vakgroep Informatietechnologie
Voorzitter: prof. dr. ir. D. De Zutter
Faculteit Ingenieurswetenschappen en Architectuur
Academiejaar 2013 - 2014

UNIVERSITEIT GENT

ISBN 978-90-8578-671-9
NUR 959
Wettelijk depot: D/2014/10.500/17

Promotoren:

Prof. dr. ir. G. Morthier	Universiteit Gent, INTEC
Prof. dr. ir. G. Roelkens	Universiteit Gent, INTEC

Examencommissie:

Prof. dr. ir. R. Van de Walle (voorzitter)	Universiteit Gent, ELIS
Prof. dr. ir. G. Morthier (promotor)	Universiteit Gent, INTEC
Prof. dr. ir. J. Danckaert	Vrije Universiteit Brussel, APHY
Dr. F. Raineri	Université Paris 7, CNRS-LPN
Dr. ir. H. Ambrosius	Technische Universiteit Eindhoven
Prof. dr. ir. J. Beeckman (secretaris)	Universiteit Gent, ELIS
Prof. dr. ir. D. Van Thourhout	Universiteit Gent, INTEC
Prof. dr. ir. G. Roelkens (promotor)	Universiteit Gent, INTEC

Universiteit Gent
Faculteit Ingenieurswetenschappen en Architectuur

Vakgroep Informatietechnologie (INTEC)
Sint-Pietersnieuwstraat 41
9000 Gent
België

Tel.: +32-9-264.33.16
Fax: +32-9-264.35.93
http://www.intec.ugent.be

Table of Contents

List of Figures

List of Tables

List of Acronyms

A

AC	Alternating Current
AF	Buffered hydrofluoric acid
AOFF	All-Optical Flip-Flop
AOSP	All-Optical Signal Processing
AR	Anti-Reflection
ASE	Amplified Spontaneous Emission
ATT	Attenuator
AWG	Arrayed Waveguide Grating

B

BER	Bit Error Rate
BERT	Bit Error Rate Tester
BOX	Buried OXide

C

CMOS	Complementary Metal Oxide Semiconductor
CMP	Chemical Mechanical Polishing
CW	ClockWise
CCW	Counter-ClockWise

D

DBR	Distributed Bragg Reflector
DFB	Distributed FeedBack
DUV	Deep Ultra Violet
DVS-BCB	Divinylsiloxane-Benzocyclobutene

E

EBL	Electron-Beam Lithography
EDFA	Erbium-Doped Fiber Amplifier

F

FDL	Fiber Delay Line
FDTD	Finite Difference Time Domain
FEC	Forward Error Correction
FIB	Focused Ion Beam
FP	Fabry-Perot
FSR	Free Spectral Range
FTTH	Fiber-To-The-Home
FWHM	Full Width at Half Maximum

G

Gbps	Giga bits per second
GSG	Ground Signal Ground

H

HF	HydroFluoric acid
HSPD	High Speed PhotoDiode

I

IC	Integrated Circuit
ICP	Inductively Coupled Plasma
IPA	Isopropyl alcohol, Isopropanol

K

KOH	Potassium hydroxide

L

LD	Laser Diode
LED	Light Emitting Diode
LN	Lithium Niobate
LPCVD	Low-Pressure Chemical Vapour Deposition

M

MMI	Multi-Mode Interferometer
MOSFET	Metal-Oxide-Semiconductor Field-Effect Transistor
MOVPE	MetalOrganic Vapour Phase Epitaxy
MQW	Multiple Quantum Well
MZI	Mach-Zehnder Interferometer

N

NRZ	Non-Return-to-Zero

O

OBPF	Optical Band-Pass Filter

ODL	Optical Delay-Line
OEO	Optical-Electrical-Optical
OSNR	Optical Signal-to-Noise Ratio

P

PCW	Polarization Controlling Wheels
PhC	Photonic Crystal
PIC	Photonic Integrated Circuit
PECVD	Plasma-Enhanced Chemical Vapour Deposition
PPG	Pulse Pattern Generator
PRBS	Pseudo-Random Bit Sequences

Q

Q-factor	Quality-Factor

R

RF	Radio Frequency
RI	Refractive Index
RIE	Reactie Ion Etching
RZ	Return-to-Zero

S

SA	Saturable Absorber
SCCM	Standard Cubic Centimeters per Minute
SEM	Scanning Electron Microscope
SLED	Superluminescent LED
SMF	Single Mode Fibre
SNR	Signal-to-Noise Ratio
SOA	Semiconductor Optical Amplifier
SOI	Silicon-On-Insulator
SP	Signal processing

SRFF	Set-Reset Flip-Flop

T

TE	Transverse Electric
TL	Tunable Laser
TLM	Transmission Line Model
TM	Transverse Magnetic

U

UV	Ultraviolet

V

VCSEL	Vertical-Cavity Surface-Emitting Laser
VOA	Variable Optical Attenuator

W

WDM	Wavelength-Division Multiplexing
WZ	Wurtzite

Z

ZB	ZincBlend

Nederlandse Samenvatting

Terugkijkend op de twintigste eeuw, kan de invloed van de microelektronica op onze maatschappij moeilijk overschat worden. Mede als gevolg daarvan groeide ook de telecommunicatie enorm op het einde van de vorige eeuw en dit had een revolutionaire impact op elk aspect van ons leven. Afstand is niet langer een obstakel voor communicatie. Het weidverbreidde gebruik van radio, televisie, smartphones en het toenemend aantal computernetwerken hebben het leven van alledag drastisch veranderd en dit zal ook in de toekomst het geval zijn aangezien nieuwe internet-gebaseerde toepassingen nog volop worden ontwikkeld. Nooit in de geschiedenis was het zo gemakkelijk om te communiceren en was informatie zo toegankelijk.

De volgende wetenschappelijke omwenteling na deze van de microelektronica komt al om de hoek kijken. In de komende decades kan de nanofotonica voor een vergelijkbare impact op ons leven zorgen. Men kan zich inderdaad afvragen of elektronen nog steeds de hoop op verwerking van enorme hoeveelheden informatie zullen kunnen belichamen. Fotonen zouden een valabel alternatief kunnen vormen voor verschillende toepassingen. In tegenstelling tot elektronen kennen ze geen intrinsieke verliezen in Photonic Integrated Circuits en veroorzaken dus geen opwarming. Deze eigenschap maakt hen zeer relevant voor het transport van informatie. Er mag echter niet over het hoofd gezien worden dat deze hoge snelheid het ook moeilijk maakt om fotonen vast te houden over een langere tijdsduur en bv. een optisch geheugenelement te maken. Een dergelijk optisch geheugenelement, dat de functionaliteit van een elektronische transistor bezit, blijft een van de meest tot de verbeelding sprekende uitdagingen bij het ontwikkelen van fotonica tot een volwassen technologie.

De uitvinding van de laser en de glasvezel in de zestiger jaren waren de start van heel wat onderzoek op optische communicatiesystemen. In dergelijke systemen draagt het gemoduleerde licht van een laserbron informatie met hoge bitrate over grote afstanden via dunne optische vezels. Het onderliggende mechanisme van lichtpropagatie in een glasvezel is totale interne reflectie: wanneer licht komende uit een dicht medium een interface bereikt onder een

voldoende scherpe hoek wordt het licht compleet en zonder verlies gereflecteerd. Het glas dat gebruikt wordt voor de fabricatie van optische vezels is silica (SiO_2) en dat heeft, indien voldoende zuiver, heel lage verliezen (0.1-0.2 dB/km) rond de telecommunicatiegolflengtes van 1.3 en 1.55μm. Tegenwoordig worden optische vezels gebruikt voor het transport van enorme hoeveelheden informatie met bitrates tot 640Gb/s, bitrates die de maximale snelheden van conventionele elektronica ruimschoots overschrijden. De discrepantie tussen de beschikbare hoge optische bandbreedte en de beperkte snelheid van signalen die door elektronische circuiten kunnen behandeld worden wordt beschouwd als een hinderlijke flessenhals in optische-netwerkknooppunten.

Teneinde optische signalen te kunnen behandelen in netwerkknooppunten worden deze eerst omgezet in elektronische signalen met behulp van een fotodiode. Na de elektronische verwerking worden de signalen dan opnieuw naar het optische domein geconverteerd, waarna ze opnieuw door een glasvezel gestuurd worden tot aan het volgende netwerkknooppunt. Dergelijke opto-elektronische en electro-optische conversies zijn niet alleen tijdsrovend en vermogenintensief, maar de elektronica om signalen bij hoge bitrates te verwerken is ook enorm duur. Er is daarom een grote behoefte aan componenten die de signaalverwerking deels of volledig in het optische domein kunnen doen. Dit leidde enkele jaren terug ook tot de notie van optische of transparante netwerken, netwerken waarin niet alleen het signaaltransport optisch gebeurt, maar ook de signaalverwerking in de knooppunten. We zien verder dat optische communicatie niet beperkt blijft tot lange-afstandsnetwerken, maar ook op kleinere schaal in intra-chip of on-chip interconnectienetwerken doordringt. De hoge datasnelheden in de huidige computers vereisen interconnecties die veel hogere informatiedichtheden toelaten en die uitsluitend door optische links kunnen verzekerd worden. Fotonica of optica kan ook het energieverbruik reduceren aangezien dan enkel de fotodetector aan ontvangstzijde moet opgeladen worden en niet langer ook de elektrische verbindingen. De eerste commerciÃńle producten gebaseerd op optische interconnecties zijn recent geintroduceerd voor toepassingen in datacentra en computer clusters. De technologie voor optische interconnecties op chips staat nog in de kinderschoenen, maar de performantie van deze interconnecties is mogelijks veel beter dan deze van hun elektronische tegenhanger en zou toelaten aan de hoge toekomstige vereisten te voldoen. De evolutie van optische interconnecties doet het idee rijzen van een transparante computer waarin alle bewerkingen uitsluitend in het optische domein verwezenlijkt worden.

De voorbije 20 jaar is heel intensief gewerkt op het ontwikkelen van micoschaal lasers. Alhoewel het uitgangsvermogen van zulke lasers eerder laag is,

kunnen ze wel met hoge dichtheid geïntegreerd worden op chips en verwacht men algemeen dat ze ook een heel snelle dynamica vertonen omwille van de kleine propagatietijden in de laserkaviteit. Microschijf lasers hebben een cirulaire kaviteitsstructuur en werden voor het eerst rond 1992 voorgesteld. De hoge-kwaliteitsresonanties in zo′n laser zijn gebaseerd op "whispering gallery" modes, dit zijn modes die langs de randen van de microschijf propageren en bestaan uit een mode in wijzerzin en een mode in tegenwijzerzin. Wanneer de koppeling tussen de twee modi (in wijzer- en tegenwijzerzin) voldoende klein is, kan winstonderdrukking er voor zorgen dat één mode dominant is en de andere onderdrukt. Dit directioneel gedrag van de laser kan gebruikt worden om een optisch flip-flop te bekomen. Injectie van een optische puls faciliteert namelijk lasering in de richting van de puls. En injectie van een puls in de tegenovergestelde richting doet de laser werken in de andere directionele mode. Dit bistabiel gedrag is heel bruikbaar voor set-reset flip-flop werking.

Logische systemen bestaan typisch uit verschillende blokken (bv. combinatorische logica, bestaande uit poorten en sequentiele logica bestaande uit bv. flip-flops), die elk een bepaalde logische bewerking met beperkte functionaliteit uitvoeren. Complexe functies kunnen dus enkel ontstaan indien de poorten en flip-flops onderling verbonden zijn en indien hun functionaliteit gecombineerd wordt in subsystemen. Teneinde meerdere logische blokken te kunnen concateneren moeten die blokken, of ze nu optisch of elektronisch zijn, aan een aantal voorwaarden voldoen. In een commentaarstuk gepubliceerd in Nature Photonics heeft D. A. B. Miller van Stanford University deze voorwaarden in detail omschreven voor optische systemen en criteria opgelijst die moeten vervuld worden om optische logica competitief te maken. Deze criteria hebben betrekking op cascadeerbaarheid, fan-out, signaalregeneratie en isolatie. Cascadeerbaarheid definieert het aantal identieke poorten of logische blokken die zonder verlies aan signaalintegriteit kunnen geconcateneerd worden. De uitgang van een poort moet de correcte vorm (bv. amplitude) hebben om als ingang van de volgende poort te kunnen dienen. Indien bv. het signaal na de tweede poort teveel gedegradeerd is, is de cascadeerbaarheid beperkt tot 2 poorten. Er kan hierbij vermeld worden dat in CMOS logische poorten het signaal geregenereerd wordt en zo cascadeerbaarheid gegarandeerd wordt. In het optische geval dienen uitgangs- en ingangsgolflengte, pulsvorm en bundelvorm compatibel te zijn. Fan-out is het aantal identieke poorten die door het uitgangssignaal van een poort kunnen aangestuurd worden. Wanneer de uitgang van de eerste poort in meerdere aansturingssignalen verdeeld wordt, daalt ook de kwaliteit van het signaal. In digitale elektronica is de fan-out typisch tot twee of vier beperkt omdat de spanningen kleiner worden met grotere fan-out. De kwaliteit van het logische signaal moet derhalve regelmatig hersteld

worden zodat degradaties van de signaalkwaliteit niet doorheen het systeem propageren. Bij signaalregeneratie wordt het signaal herversterkt en in vorm hersteld en soms ook gehersynchroniseerd met de klok. In CMOS vervullen invertorketens deze functie. Bij optische signalen moet de bundelkwaliteit en/of de pulskwaliteit eventueel hersteld worden, evenals de signaalniveaus. Tenslotte moet het systeem zo ontworpen worden dat gereflecteerde signalen geïsoleerd worden. In microelektronica kan dit eenvoudigweg bereikt worden door het invoegen van een isolerende laag tussen de ingang en de uitgang van logische blokken. Transistors zorgen voor deze isolatie, maar het golfkarakter van licht laat dergelijke isolatie veel minder gemakkelijk toe. Idealiter willen we een component met gescheiden ingangs- en uitgangsbundels. In het geval van onvoldoende ingangs-uitgangsisolatie wordt een deel van het uitgangssignaal teruggevoed naar de ingang en overlapt daar met het ingangssignaal. Dit kan leiden tot corrupte signalen aan de uitgang of zelfs oscillerend gedrag. Dit laatste effect treedt bv. op bij het koppelen van twee microschijflasers naar dezelfde busgolfgeleider. In een dergelijke configuratie zou een isolator tussen de twee componenten dienen geplaatst te worden teneinde propagatie in slechts één richting toe te laten. Inderdaad, in optische flip-flops bv. zorgt elke reflectie terug naar de microschijf voor extra koppeling tussen de mode in wijzerzin en deze in tegenwijzerzin, iets wat de bistabiele werking in gevaar kan brengen. Ook kan de uitgang van een microschijflaser een andere microschijflaser injectievergrendelen.

Dit doctoraat werd uitgevoerd in het kader van het Europese FP7-project HISTORIC. HISTORIC staat voor Heterogeneous InP on Silicon Technology for Optical Routing and LogIC, en was een samenwerking tussen vier partners, zijnde de Technische Universiteit Eindhoven (TU/e) in Nederland, het Laboratoire de Photonique et Nanostructures (LPN, CNRS) in Frankrijk, IBM Zurich in Zwitzerland en imec-Universiteit Gent. Het project startte in 2008 en duurde drie en een half jaar. Het had als doel om fotonisch geïntegreerde circuits bestaande uit een relatief groot aantal actieve en passieve fotonische elementen en voor gebruik in bv. optisch pakketschakelen te ontwerpen, te ontwikkelen en te testen. De bouwblokken voor de digitale fotonische circuiten zijn ultra-compacte poorten gebaseerd op microschijflasers en fotonische-kristallasers, lasers welke gefabriceerd worden gebruik makend van heterogene integratie van InP membranen op SOI (silicium op isolator) passieve optische circuiten. Diverse benaderingen voor de ultra-compacte lasers werden onderzocht, waarbij telkens gebruik werd gemaakt van zowel de hoge-precisie groei- en procestechnieken die beschikbaar zijn binnen het InP-platform als de extreme nauwkeurigheid van state-of-the-art CMOS procestechnologie.

Ontwikkeling en optimalisatie van de microschijflaserfabricatie: Diverse processtappen in de fabricatie van microschijflasers werden ontwikkeld of geoptimaliseerd. In parallel met het werk gericht op een meer betrouwbare standaard fabricatieprocedure, steunend op contactlithografie, werd ook een proces gebaseerd op elektronenbundellithografie ontwikkeld en geoptimiseerd. Hiertoe werden optisch gepompte heterogeen geïntegreerde microschijflasers, gedefinieerd met behulp van elektronenbundellithografie, bestudeerd. Detectie van de e-bundel alignatiemerkers liet toe om de microschijflasers heel nauwkeurig met betrekking tot de siliciumgolfgeleiders te aligneren. De standaardafwijking in de lasergolflengtes is, dankzij de technologieoptimalisatie, kleiner dan 500pm over een chip. De afwijking in microschijfdiameter is niet groter dan enkele nanometers. Een belangrijke ontwerpparameter is verder ook de koppeling tussen de microschijf en de toegangsgolfgeleider. Dankzij de elektronenbundellithografie is de afwijking op de relatieve positive van de microschijf t.o.v. de toegangsgolfgeleider beperkt tot enkele tientallen nanometer t.o.v. de ontwerpwaarde. De procesoptimalisatie beschreven in het doctoraat maakt tenslotte ook de fabricatie van complexe fotonisch geïntegreerde circuits voor optische signaalverwerking mogelijk. Identieke poorten of logische blokken die meerdere gecascadeerde microschijflasers op dezelfde chip vereisen kunnen door de procesoptimisatie zonder verlies aan signaalintegriteit met elkaar verbonden worden. Een laatste optimalisatie die onderzocht werd is het vervangen van de tunneljuncties door een p-i-n epitaxiaalstructuur. 2D-FDTD en elektrische injectie simulaties toonden aan dat een p-i-n structuur een relevant alternatief is voor de moeilijk te groeien structuur met tunneljuncties.

Unidirectionaliteit in microschijf lasers: De optimalisatie van microschijflasers werd uitgebreid met een studie van de gevoeligheid voor externe reflecties. Een grondige theoretische en numerieke studie werd uitgevoerd van het unidirectioneel gedrag van microschijflasers gekoppeld aan een busgolfgeleider, die aan één kant eindigt met een relatief sterke reflector. Bij relatief lage uitgangsvermogens wordt de verhouding tussen vermogens in wijzer- en tegenwijzerzin gegeven door de verhouding van de koppelingsconstanten die de koppeling tussen in wijzer- en tegenwijzerzin propagerende modi bepalen. Bij hogere vermogens wordt die vermogenverhouding echter sterk afhankelijk van de winstonderdrukking en kan ze veel groter worden dan de verhouding van de koppelingsconstanten. De gevoeligheid voor externe reflecties van deze lasers werd terzelfdertijd onderzocht. Uit de studie kan besluit worden dat microschijf lasers (en ring lasers) in het algemeen gevoeliger zijn voor externe reflecties dan traditionele Fabry-Perot, DFB en DBR laser diodes. Enkel bij hoge vermogens, waar de reflectiegevoeligheid sterk beinvloedt wordt door winstonderdrukking, kan zij beter zijn dan bij traditionele randemitterende lasers. Stabiele unidi-

rectionele werking werd ook experimenteel onderzocht en gedemonstreerd bij heterogeen geïntegreerde microschijflasers, waarbij de busgolfgeleider aan één kant voorzien was van een passief, sterk reflecterend Bragg rooster. Een dergelijk passieve reflector leidt niet tot bijkomende verliezen of bijkomend vermogenverbruik voor het systeem, maar laat wel toe om het geheugeneffect bij microschijflasers te vermijden. Dit kan bovendien ook gebruikt worden om imperfecties, zoals zijwandruwheid, die de unidirectionele werking bemoeilijken tegen te werken. Meerdere lasers van eenzelfde circuit kunnen dan in dezelfde richting laseren, met een hogere efficiëntie en zonder dat de laserwerking van richting verandert tengevolge temperatuurs- of stroomvariaties. Dit maakt microschijflasers aantrekkelijker voor bv. optische interconnecties.

Optische signaalverwerkingstoepassingen van III-V microschijflasers op SOI: Een basisvereiste voor optische logische poorten is restauratie van het logische niveau. De kwaliteit van het logische signaal moet worden gerestaureerd zodat de signaaldegradaties niet doorheen het systeem propageren. Met andere woorden, het signaal moet opgekuist worden na een bepaald aantal poorten. Voor optische signalen is het noodzakelijk om daarbij zowel de bundelkwaliteit, de pulsvorm en het signaalniveau te restaureren. In het doctoraat wordt een optische signaalregenerator voor 10Gb/s NRZ signalen gedemonstreerd die met heel lage ingangsvermogens werkt en gebaseerd is op een heterogeen geïntegreerde, elektrisch gepompte microschijflaser met 10μm diameter, volledig gefabriceerd in een CMOS pilootlijn. Het schema resulteert in een verbetering van de BER (Bit Error Rate) en werkt met sub-mW ingangsvermogens. De laser werkt in continu regime, is monomodaal bij kamertemperatuur en verbruikt 6mW elektrisch vermogen. Simulaties wijzen op mogelijke maximum snelheden van 20Gb/s.

De basisvereisten voor optische logische poorten zoals opgelijst door D. A. B. Miller kunnen nu geëvalueerd worden. Cascadeerbaarheid werd nog niet gedemonstreerd, maar de fabricatie met behulp van elektronenbundellithografie toonde aan dat de diameters van nominaal identieke microschijven slechts met een paar nanometers variëren. De procesverbeteringen zetten ook de deur open voor hogere uitgangsvermogens in de busgolfgeleiders, wat tot een verbetering van de fan-out kan leiden. 2R regeneratie werd experimenteel gedemonstreerd, maar ook onderzocht d.m.v. simulaties. Tenslotte werd ook de gevoeligheid van microschijflasers voor externe feedback en reflecties gekarakteriseerd.

English summary

Looking back on the twentieth century, the influence of microelectronics on our society can hardly be overestimated. Telecommunications have grown so much in the twentieth century that they revolutionized every aspect of our lives. Distance is no longer an obstable to communicating. The wide-spread use of the radio, the television, of smart phones, and the growth of computer networks have drastically changed our everyday lives and will continue to do so as new internet-based services keep on being implemented. Never in history has it been so easy to communicate and to have access to information so close at hand.

The next scientific revolution after microelectronics could be emerging already. Nanophotonics could have a similar impact on our lives in the next coming decades. Indeed, we can wonder if electrons will still then embody the same hope for processing huge amounts of information. Light, and more precisely photons, could become a valuable alternative for many applications. Light beams have practically unlimited information capacity (very broad bandwidth), very low transmission losses and do not dissipate heat. These qualities make them relevant for the transport of information. However, it must not be overlooked that the speed of photons makes them very difficult to trap over a long period of time in order to construct an optical memory element for instance. Such an optical memory element that could replace the functionality of an electronic transistor remains one of the most thrilling challenges in the establishment of photonics as a mature technology.

The invention of the laser and of the optical fiber in the 1960′s initiated the research towards optical communication systems. In such systems, the modulated light from a laser source carries information over very long distances and at extremely high bit rates thanks to the use of thin optical fibers made of glass. The underlying physical principle of an optical fiber can be understood from total internal reflection: when light that is travelling in a dense medium hits a boundary at a steep angle, the light will be completely reflected without loss. The glass used for the fabrication of optical fibers is called silica (SiO_2) and has

very low losses (0.1-0.2dB/km) around the telecommunication wavelengths of 1.3μm and 1.55μm. Nowadays, optical fibers allow us to transport enormous amounts of information with bitrates up to 640Gb/s that largely exceed the speed that conventional electronics can process (typically 40Gb/s). The mismatch between the available high optical bandwidth and the limited speed of the signals transported by electronic circuits is considered as a major bottleneck in optical network nodes.

In order to process light signals in such a network node, they are first converted to electrical signals by a photodiode. After the electronic processing is done, they are converted again to the optical domain and sent through an optical fiber to the next network node. These opto-electronic and electro-optic conversions are not only power and time consuming, but also the electronics needed to process these signals at such high bitrates is very expensive. There is a clear need for devices that can do the processing partly or completely within the optical domain, leading to the notion of "all-optical networks" or "transparent networks" where not only the transport of signals is done optically, but also their processing. We see that optical telecommunication is not only progressing in long-distance optical networks, but also on a much smaller scale in intra-chip or on-chip interconnects. The high data rates in current information processing machines require connections that can contain much higher densities of information which can only be provided by optical links. Optics can also reduce the energy consumption as there is no need to charge the lines to the signal voltage: we only need to provide enough energy to charge a photodetector at the receiving end. The first commercial products, based on optical interconnects for application in large data-centers and computer clusters, have recently been introduced. Optical interconnects on a chip-scale level are still in their infancy, but their performance can surpass that of electronic interconnects and could allow for future demands to be met. The evolution of optical interconnects raises the idea to implement a transparent computer where all the processing and logic are implemented solely within the optical domain.

A lot of research has been done on the development of microscale lasers over the past 20 years. Though the optical output power of such ultra-small lasers is very low, they can be densely integrated on a chip and are in general expected to have very fast dynamics due to the small cavity roundtrip time. Microdisk lasers have a circular cavity structure and were proposed for the first time in 1992. The high-quality resonances in such a laser are based on whispering gallerymodes. These are modes confined very close to the edges of the microdisk. The whispering gallery mode in a microdisk consists of a clockwise (CW) and counterclockwise (CCW) propagating mode. When the coupling be-

tween the two modes is small, a cross-gain saturation will cause one of the two modes to dominate. This directional behaviour of the laser can be used for flip-flop operation. Indeed, injecting a pulse into the microdisk will facilitate lasing in the direction of that pulse. When we inject a pulse in the opposite direction, the laser will start to operate in the other directional mode. This bistable behaviour is therefore usefull for set-reset flip-flop operation.

Logic systems typically consist of several building blocks (e.g. combinational logic, i.e. gates and sequential logic, i.e. flip-flops), each performing certain logic operations with a limited set of functionality. Complex functions can hence only arise if the gates can be connected and their functionality combined to larger subsystems. To concatenate several identical logic blocks, independent of whether their working principle is electronic or optical, they must fulfil certain requirements. In his commentary letter published in Nature Photonics, D. A. B. Miller from Stanford University extensively investigated the device requirements specifically for all-optical systems and lists criteria that need to be fulfilled by photonics to be competitive for optical logic. The prerequisites for building logic systems are cascadability, fan-out, signal refreshing and isolation, which are closely related. Cascadability defines the number of identical gates or logic blocks that can be concatenated without losing signal integrity. The output of one stage must be in the correct form to drive the input of the next stage. For instance, if after the second stage, the signal has degraded so much that the following stage cannot process the information, the cascadability is then limited to two gates. It is worth mentioning that in CMOS logic gates, each stage refreshes the signal and assures cascadability. In optics, the output and input wavelengths, beam shapes and pulse shapes should be compatible. Fan-out defines the number of identical gates which can be driven with the output of one stage. As the output of the first stage is split into the amount of driven stages, the signal quality also degrades. In electronics, the fan-out is limited to 2-4 due to the ever-more reduced operation voltages. The quality of the logic signal must be restored so that degradations in signal quality do not propagate through the system. Signal refreshing means that the signal is re-amplified, re-shaped and if necessary also re-timed. In CMOS, inverter chains fulfil this functionality. In optics, we must consider restoring beam quality and/or pulse quality as well as signal-level ranges. Finally, designing a system that isolates reflected signals is a real challenge. In microelectronics, this can be simply achieved by adding an isolating layer between the input and the output of logic blocks (for instance, a gate dielectric). Transistors provide this isolation, but the microscopic physics of nonlinear optical processes and stimulated emission typically does not. Ideally, we want a device with separate input and output beams. In the case of an insufficient input-output isolation, part of the output

signal is fed back into the input overlapping with the input signal. This may lead to signal corruption at the output or even an oscillatory behavior. This typically arises when coupling two microdisk lasers to one waveguide. In this configuration, an isolator should be placed in between two devices to allow propagation of the signal in only one direction. Indeed, for all-optical flip-flops for instance, any back reflection into the microdisk causes extra coupling between the CW and the CCW mode, which can jeopardize bi-stable operation. Also, the light from one of the microdisk can inject lock the other one.

The acronym HISTORIC stood for Heterogeneous InP on Silicon Technology for Optical Routing and LogIC. The EU-FP7 project was a collaboration between four partners, being the Technische Universiteit Eindhoven (TU/e) in the Netherlands, the Laboratoire de Photonique et Nanostructures (LPN, CNRS) in France, IBM Zurich in Zwitzerland and imec-Ghent University. The project started in 2008 and lasted three and a half years. HISTORIC proposed to design, develop and test digital photonic integrated circuits containing a relatively large number of active photonic elements combined with passive elements, for use in e.g. all-optical packet switching for both datacom and telecom. The building blocks for the digital photonic circuits are ultra-compact gates based on microring or microdisk lasers, and photonic crystal lasers lasers. These lasers are fabricated making use of the heterogeneous integration of InP membranes on top of silicon on insulator (SOI) passive optical circuits. Different approaches for the ultra compact lasers were investigated, allowing the use of the high precision growth and processing techniques available to the InP platform, as well as to take advantage of the extreme accuracy of state-of-the-art CMOS processing.

Development and optimizations of the fabrication of microdisk lasers: We have developed and optimized several processing steps of the fabrication of a single microdisk laser. Parallel to the work towards a more reliable standard fabrication procedure relying on contact lithography, a process involving electron-beam lithography has been optimized. We studied optically pumped InP-based microdisks integrated on SOI and processed with e-beam lithography. Detection of e-beam alignment markers has allowed the very accurate definition of microdisk lasers with respect to silicon wire waveguides. The achievable and reproducible standard deviation in their peak lasing wavelengths is lower than 500pm on the same chip, thanks to optimizations of the technology. The deviation in the diameter of the microdisks is as low as a few nanometers. One of the important design parameters for these structures remains the coupling between the access waveguide and the microdisk. Thanks to e-beam lithography, the resulting offset of the microdisk lasers is only tens of nanometers away

from the target design value. The processing optimizations presented here also make the fabrication of complex functionalities for all-optical signal processing possible. Identical gates or logic blocks requiring cascaded microdisk lasers on the same chip can be concatenated without losing signal integrity. Finally, we perform 2D-FDTD and electrical injection simulations that demonstrate that a p-i-n epitaxial structure could be a relevant alternative to the tunnel junction-comprising epitaxy currently implemented for microdisk lasers.

Unidirectionality in microdisk lasers: The effort towards optimization of a single device also involved studying the sensitivity of the microdisk laser to external reflections. A thorough theoretical and numerical study of the unidirectional behavior of microdisk lasers coupled to a bus waveguide with a stronger reflector on one side has been carried out. At low bias levels, the ratio of the powers in clockwise and counter clockwise modes depends on the coupling coefficients that determine the coupling between clockwise and counterclockwise modes, whereas at high bias levels, it also depends strongly on the gain suppression. The feedback sensitivity of such lasers is also theoretically and numerically investigated and we come to the conclusion that microdisk lasers are generally much more sensitive to external reflections than traditional Fabry-Perot, DFB or DBR lasers. At high bias levels, the feedback sensitivity also strongly depends on the gain suppression, and at high enough power levels, it can be better than that of traditional edge-emitting lasers. We demonstrate and quantify experimentally stable unidirectional lasing in microdisk lasers heterogeneously integrated on SOI. Feedback from a passive distributed Bragg reflector is used to achieve stable unidirectional operation. This simple passive design does not add optical losses to the system and does not increase its power consumption. The implementation of this solution is the key to avoid the appearance of a "memory" effect in microdisk lasers. It can be implemented to counteract processing effects, such as sidewall roughness, that threaten unidirectional operation of the lasers. Different devices belonging to the same design can now lase in the same direction with higher efficiency and without switching from one lasing direction to the other depending on the injection current and the temperature. This makes the use of microdisk lasers for optical interconnects applications very attractive.

All-optical signal processing applications of III-V microdisk lasers on SOI: A basic requirement for all-optical logic gates is logic-level restoration. The quality of the logic signal must be restored so that the degradations in signal quality do not propagate through the system. In other words, the signal is "cleaned up" at each stage. For optics, it is mandatory to restore the beam quality and/or the pulse quality as well as signal-level ranges. We demonstrate an

all-optical low-power 2R regenerator of 10Gb/s non-return-to-zero data based on a 10μm-diameter electrically pumped microdisk laser, which is heterogeneously integrated onto the silicon-on-insulator platform and processed in a CMOS pilot line. The scheme results in BER (Bit Error Rate) improvement and works for submilliwatt-level input signals. The laser operates in the continuous-wave regime, and it is single mode at room temperature and consumes 6mW of electrical power. Its regeneration capability is investigated in simulations up to 20Gb/s and experimentally demonstrated at 10Gb/s.

The basic requirements for logic gates listed by D. A. B. Miller can now be adjusted. Cascadability has not been demonstrated, but the fabrication involving the use of electron-beam lithography demonstrated that the diameters of nominally identical microdisk lasers only differ by a few nanometers. The processing improvements also open the door to the collection of a higher output power of the microdisk lasers, which will increase the fan-out. 2R regeneration has been experimentally demonstrated, as well as investigated in simulations. We finally experimentally characterized the sensibility of microdisk lasers towards feedback and external reflections.

“Don’t be a coconut
God is trynna talk to you ”

Julian Casablancas, Ask Me Anything, 2004

1 Introduction

Looking back on the twentieth century, the influence of microelectronics on our society can hardly be overestimated. Telecommunications have grown so much in the twentieth century that they revolutionized every aspect of our lives. Distance is no longer an obstable to communication. The wide-spread use of the radio, the television, of smart phones, and the growth of computer networks have drastically changed our everyday lives and will continue to do so as new internet-based services keep on being implemented. Never in history has it been so easy to communicate and to have access to information so close at hand.

The next scientific revolution after microelectronics could be emerging already. Nanophotonics could have a similar impact on our lives in the next coming decades. Indeed, we can wonder if electrons will still then embody the same hope for processing huge amounts of information. Light, and more precisely photons, could become a valuable alternative for many applications. Light beams have practically unlimited information capacity (very broad bandwidth), very low transmission losses and do not dissipate heat. These qualities make them relevant for the transport of information. However, it must not be overlooked that the speed of photons makes them very difficult to trap over a long period of time in order to construct an optical memory element for instance. Such an optical memory element that could replace the functionality

of an electronic transistor remains one of the most thrilling challenges in the establishment of photonics as a mature technology.

The invention of the laser [1], [2], and of the optical fiber [3] in the 1960′s initiated the research towards optical communication systems. In such systems, the modulated light from a laser source carries information over very long distances and at extremely high bit rates thanks to the use of thin optical fibers made of glass. The underlying physical principle of an optical fiber can be understood from total internal reflection: when light that is travelling in a dense medium hits a boundary at a steep angle, the light will be completely reflected without loss. The glass used for the fabrication of optical fibers is called silica (SiO_2) and has very low losses (0.1-0.2dB/km) around the telecommunication wavelengths of 1.3μm and 1.55μm. Nowadays, optical fibers allow us to transport enormous amounts of information with bitrates up to 640Gb/s that largely exceed the speed that conventional electronics can process (typically 40Gb/s). The mismatch between the available high optical bandwidth and the limited speed of the signals transported by electronic circuits is considered as a major bottleneck in optical network nodes.

In order to process light signals in such a network node, they are first converted to electrical signals by a photodiode. After the electronic processing is done, they are converted again to the optical domain and sent through an optical fiber to the next network node. These opto-electronic and electro-optic conversions are not only power and time consuming, but also the electronics needed to process these signals at such high bitrates is very expensive. There is a clear need for devices that can do the processing partly or completely within the optical domain, leading to the notion of “all-optical networks” or “transparent networks” where not only the transport of signals is done optically, but also their processing. We see that optical telecommunication is not only progressing in long-distance optical networks, but also on a much smaller scale in intra-chip or on-chip interconnects. The high data rates in current information processing machines require connections that can contain much higher densities of information which can only be provided by optical links. Optics can also reduce the energy consumption as there is no need to charge the lines to the signal voltage: we only need to provide enough energy to charge a photodetector at the receiving end. The first commercial products, based on optical interconnects for application in large data-centers and computer clusters, have recently been introduced [4], [5]. Optical interconnects on a chip-scale level are still in their infancy, but their performance can surpass that of electronic interconnects and could allow for future demands to be met [6]. The evolution of optical interconnects raises the idea to implement a transparent computer where all the pro-

cessing and logic are implemented solely within the optical domain. However, for applications with extensive use of photonics such as the above-mentioned optical networks, there will be a clear need to process light signals directly in the optical domain as the demand for higher bitrates increases.

1.1 Silicon photonics

Early work in the field of silicon photonics was mostly related to passive optical devices [7]- [14]. The strong optical confinement resulting from the high index contrast between silicon (n≈3.45) and SiO_2 (n≈1.45) allows scaling down the photonic waveguides to hundreds of nanometers. Silicon also has excellent material properties such as a high thermal conductivity, high optical damage threshold and high third-order optical nonlinearities which are important for photonic devices. The basic requirement for on-chip optical communication devices is a low-loss optical waveguide. This waveguide may be used just as a transmission medium or for advanced functionalities such as modulation. Silicon photonic waveguides are able to fulfill this requirement. Their surface roughness however causes a significant scattering loss. It has been shown that backscattering due to sidewall roughness is one of the most severe limiting factors in state-of-the art SOI nanowires employed in densely integrated photonics [15]. In general, the silicon waveguides are characterized by losses in the range of 0.1-3dB/cm depending upon their dimensions and the processing conditions. Obviously, the losses are higher in smaller waveguides due to the higher optical intensity at the surface. For larger waveguides, the losses decrease as the evanescent tail of the light feels the surface roughness less. There have been two main approaches to reduce the propagation losses of the waveguides. The design of the waveguide can be optimized in order to avoid scattering loss from the waveguide cross-section [16]– [18]. While another approach is based on processing optimizations such as a wet chemical oxidation and thermal oxidation [19]– [21] . A solution to couple light in and out of the photonics chip is the use of inverted tapers where there is a gradual expansion of a core guided mode into a much larger cladding guided mode. Using this approach, coupling losses as low as 0.2dB have been demonstrated from a single-mode fiber to a silicon wire waveguide [22]. Its limitation is that it cannot be implemented for wafer scale testing as the access fibers need to be aligned to the chip facets. Another approach to couple light in and out of the photonics chip is the use of grating couplers [23], [24]. This approach has been used for all the work further presented.

While significant progress has been made on electro-optics modulation [25], [26], [27] and light detection [28] on the SOI platform, electrically-injected light generation and amplification remains difficult. Over the years, researchers have investivated several ways to generate light emission from silicon, including doping with active rare-earth ions such as erbium [29], riddling silicon with an array of nanoscale holes to create porous silicon, or relying on gain from nonlinear processes such as the Raman effect [30], [31]. These schemes, although capable of emitting light and even achieving lasing, either require optical pumping (and thus the presence of another laser) or weakly emit light. They are therefore not considered as practical or satisfactory solutions [32]. Indeed, since silicon has an indirect band gap, its radiative recombination rate is very low and strongly outnumbered by non-radiative recombination. While a lot of functions can be implemented on a Photonic-Integrated-Circuit (PIC) without an on-chip light source, the availability of an integrated silicon laser will add significantly to the impact of silicon photonics. Therefore, the development of an efficient and electrically-injected silicon laser is receiving much scientific interest.

1.2 Methods for the integration of III-V on SOI

To implement these functions, we believe that III-V materials will remain required, at least in the medium term. In this context, an attractive approach is to use silicon as a substrate for passive waveguide functions, and to integrate III-V materials on the silicon platform, where light generation or amplification is needed. However, integrating III-Vs on silicon is far from straightforward. We will discuss the main techniques that are currently being investigated.

1.2.1 Hetero-epitaxy

Direcly growing the III-V material on the silicon substrate could offer the highest electronic-photonics integration density. However, since all III-V alloys emitting in the 1.3-1.55μm wavelength range have a lattice constant in the range 5.7-6.3Å [33] whereas silicon a has a lattice constant of 5.43Å, and since III-V materials and silicon also present a strong mismatch in thermal expansion coefficient, this represents a technological challenge. The defects created during the direct epitaxial growth of InP or GaAs on silicon result in poor material quality, with dislocations and anti-phase domains. These defects act as efficient non-radiative recombination centers, thereby strongly reducing the luminescence quantum efficiency.

Since the lattice constant of GaAs (5.65Å [33]) is closer to that of silicon, most results cover growth of GaAs-based materials on silicon. In [34], continuous-wave lasing was demonstrated in a GaAs-based quantum-well structure directly grown on silicon, with an intermediate buffer layer to accomodate crystal defects. However, the laser stability was very poor due to the growth and migration of crystal defects into the active region. This problem can be tackled by epitaxial growth sequences that result in 2D instead of 3D crystal defects, concentrated at the interface between the silicon and the III-V. More recently, the University College of London has demonstrated very promising results. They reported the first operation of an electrically pumped 1.3μm InAs/GaAs quantum-dot laser epitaxially grown on a silicon (100) substrate. The laser structure was grown directly on the silicon substrate by molecular beam epitaxy. Lasing at 1.302μm has been demonstrated with threshold current density of 725A/cm^2 and output power of 26mW for broad-area lasers with as-cleaved facets at room temperature. These results are directly attributable to the optimized growth temperature of the initial GaAs nucleation layer [35]. In a further optimization [36], the University College of London reports the first room-temperature continuous-wave operation of III-V quantum-dot laser diodes monolithically grown on a silicon substrate. Long-wavelength InAs/GaAs quantum-dot structures were fabricated on Ge-on-Si substrates. Room-temperature lasing at a wavelength of 1.28μm has been achieved with threshold current densities of 163A/cm^2 and 64.3A/cm^2 under continuous-wave and pulsed conditions for ridge-waveguide lasers with as cleaved facets, respectively. The value of 64.3A/cm^2 represents the lowest room-temperature threshold current density for any kind of laser on silicon to date. The Photonics Research Group of Ghent University has demonstrated an InP nano-laser that operates at room temperature and can be selectively grown on a pre-patterned (001) silicon substrate without any complex post-processing. A unique epitaxial scheme combining the defect necking effect with lateral overgrowth is used to grow a short but relatively thick nanowire cavity on silicon for photonic applications. The nanowires are found to consist of a mixture of ZB (Zincblend) and WZ(Wurtzite) crystal phases. Furthermore, the compact size of the nanowire cavity limits the number of possible resonant modes, and a large spontaneous emission factor is experimentally demonstrated [37].

1.2.2 Indium-phosphide Membrane on Silicon

The Technische Universiteit from Eindhoven relies on a platform where active as well as passive components are integrated in one material system: indium phosphide. Research is carried out to develop an Indium-phosphide Membrane on Silicon (IMOS) platform where the silicon membrane is replaced

with an InP-membrane that contains both passive and active regions. As light is kept in a single optical layer, the coupling between active and passive components is greatly alleviated. This coupling does not depend on an intermediate layer and alignment problems with respect to an underlying silicon circuit are reduced. An InP-membrane allows for passive optical devices with fully acceptable performance, and small active components can be integrated with these devices by submicron size selective area growth. An epitaxial stack comprising quaternary layers and quantum wells is etched away, except for the places where an active medium is required. Then, a regrowth of passive material leads to device demonstrating a passive quaternary layer with an embedded local active medium. The processed layer stack is then bonded on SOI with the use of DVS-BCB and the InP substrate is removed. With this technique a number of passive devices have been demonstrated and characterized, which show acceptable performance results. Photonic wires demonstrate losses lower than 1.5dB/mm, 0.6dB excess loss are characterized in a 3dB splitter, and resonator with Q-factor of 15.500 are reported [38]. Furthermore, an ultrasmall polarization converter in InP membrane is demonstrated. Measurements show a very high polarization conversion efficiency of 99% with insertion losses lower than -1.2dB at a wavelength of 1.53μm [39]. The downside of this approach comes from the incompatibility of this process with the silicon CMOS-based platform due to the high temperature (around 600°C reached during the regrowth step. Of course, further developments may overcome such a hurdle for the integration of these devices. Several challenges also remain, such as for instance an efficient current and voltage supply to active devices on the membrane. The thermal management and the mechanical stability of the membranes need to be addressed.

1.2.3 Bonding Technology

Molecular bonding

For direct molecular bonding, two ultra-clean and ultra-flat SiO_2 surfaces are brought together and are bonded through Van der Waals attraction at the intimate surface contact. During subsequent curing at around 300°C, the O-H bonds are replaced by Si-O-Si bonds, providing a high bonding strength. The bonding process for the samples from this work that rely on this method has been developed at CEA-Leti. More details on direct wafer bonding can be found in the PhD. thesis of Stevan Stanković [40]. Direct bonding has already been demonstrated as a viable technology for the fabrication of evanescent hybrid III-V/Si devices [41], [42], [43]. However, direct wafer bonding is very sensitive to surface roughness, particle contamination and organic contamination of

the bonding surfaces. Elaborate cleaning procedures need to be implemented prior to bonding. Also, in order to lower the annealing temperature, plasma-activation of the surface is required. All this might lead to a process that is not robust enough in an industrial environment, providing sufficiently high yield at an acceptable cost.

Adhesive bonding

Divinylsiloxane-benzocyclobutene (DVS-BCB) is one of the most popular polymer materials for adhesive wafer bonding. It was developed in the late 1980′s by Dow Chemical Company as a low dielectric constant (low-k) polymer intended to replace silica as a dielectric in on-chip interconnects [44]. Today, it is a well-known material with a variety of applications in microelectronic packaging and interconnects applications. For commercial applications, the monomer is usually B-staged, i.e. only partially-cured, to form an oligomer that is dissolved in mesitylene. These oligomer mesitylene solutions are commercially available under the name Cyclotene and are used as polymer precursors. Solutions with various oligomer content (i.e. resin content) are available, like Cyclotene 3022-35 (with a 35% resin content).

Adhesive bonding looks more promising as it should offer more relaxed bonding conditions, namely a greater tolerance to particle contamination and surface roughness. Specifically, the use of DVS-BCB is appealing, as it has good optical, electrical and mechanical properties. Also, its planarization properties should enable to bond III-V materials on substrates with a topography. Bonding with DVS-BCB is also a low cost process compared to the direct bonding option. However, the thermal conductivity of the polymer ($0.3 W.m^{-1}.K^{-1}$) might be a major obstacle to the industrial development of this bonding technique.

Preparation of the samples is needed to remove any contamination from the bonding surfaces of the dies and to condition these surfaces so that DVS-BCB can be easily and effectively applied. Although the adhesive bonding is somewhat tolerant to particle contamination, since we want to achieve bonding layers of less than 100nm thickness, it is clear that removing any residual particles from the bonding surfaces is essential. Different cleaning procedures are used for III-V dies and for SOI dies.

1.3 Microdisk lasers

1.3.1 State-of-the-art for microdisk lasers heterogeneously integrated on SOI

A lot of research has been done on the development of microscale lasers over the past 20 years (such as photonic crystal lasers [45], plasmon lasers [46], etc). Though the optical output power of such ultra-small lasers is very low, they can be densely integrated on a chip and are in general expected to have very fast dynamics due to the small cavity roundtrip time. Microdisk lasers have a circular cavity structure and were proposed for the first time in 1992 [47], [48]. The high-quality resonances in such a laser are based on whispering gallery modes. These are modes confined very close to the edges of the microdisk, as presented in section 1.3.2. The whispering gallery mode in a microdisk consists of a clockwise (CW) and counterclockwise (CCW) propagating mode. When the coupling between the two modes is small, a cross-gain saturation will cause one of the two modes to dominate. This directional behaviour of the laser can be used for flip-flop operation. Indeed, injecting a pulse into the microdisk will facilitate lasing in the direction of that pulse. When we inject a pulse in the opposite direction, the laser will start to operate in the other directional mode. This bistable behaviour is therefore useful for set-reset flip-flop operation. The first demonstration of flip-flop operation in ring lasers was done in a structure consisting of two coupled ring lasers [49]. In this structure, the light from one ring laser was used to injection-lock the other. More recently, flip-flop operation was demonstrated in a single ring laser [50]. The ring laser had a racetrack design with a radius of 150μm for the circular sections and straight sections of 200μm. The reported switching speed was 130ps (switch-on) and 190ps (switch-off) at pulse energies of 4pJ. Using short pulses and high pulse energies, the switching times were reduced further to 20ps in later experiments [51]. Recently, the first flip-flop on silicon based on a microdisk laser has been reported [52], [53], [54].

A numerical and experimental system relying on Semiconductor Ring Lasers (SRLs) has been developed to study fully integrated all-optical Spiking Neural Networks, [55]- [58]. SRLs also support two counterpropagating modes, which are both linearly and non-linearly coupled to each other by intermodal coupling and cross-gain saturation, respectively. For a restricted phase range of the intermodal coupling coefficient, alternate oscillations will appear. If the laser is operated in the unidirectional regime with two stable states, near the onset of this alternate oscillations regime, theoretically, excitability is expected. But as a drawback of the symmetry of the system, the attraction basins of both stable states are equal in size. Consequently, there will be a competition between

mode-hopping events between both stable states and excitable excursions [55]. This disadvantage can be solved by inducing an asymmetry in the intermodal coupling [56]- [58]. Microdisk lasers behave phenomenologically identically to SRLs [58], [59]. As a consequence, inducing a reflection asymmetry also reveals the excitability mechanism found in SRLs [60].

The first demonstration of microdisks molecularly bonded on silicon were optically pumped devices [61], [62], as result from the EU-FP6 PICMOS project [63]. Later on, the first electrically pumped microdisk laser heterogeneously integrated with a SOI waveguide was reported [64], [65]. The development of the design and of the fabrication of InP-based microdisks were reported in [66], and further optimizations will be described in this work. Besides flip-flop operation, the microdisks can also be used for other optical signal processing applications. All-optical gating for multiplexing and de-multiplexing purposes has been reported [67], along with all-optical wavelength conversion up to 20Gb/s [68], [69], all-optical format conversion [70], switching of 10Gb/s NRZ signals [71], multi-wavelength lasing [72] and several application in optical interconnects. InP microdisk cavities can indeed be employed in various operational modes to facilitate chip-to-chip and on-chip interconnects. Operation as directly modulated light source [73], resonant cavity modulators at 2.73Gb/s [74] and/or resonant photo detectors [75], [76] have all been explored within the HISTORIC project. More recently, a compact optical interconnect on a silicon-on-insulator platform consisting of a directly modulated microdisk laser and detector connected via a silicon waveguide has been presented [77].

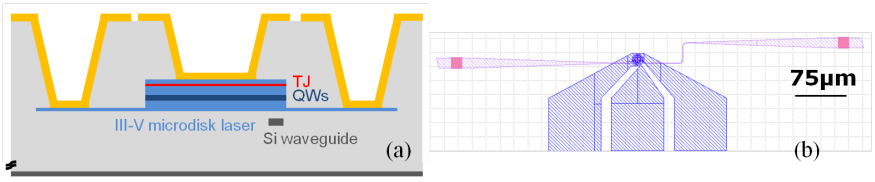

Figure 1.1: (a) Schematic cross-section of the microdisk laser heterogeneously integrated on SOI and embedded in DVS-BCB or a dielectric. (b) Top view of the designed microdisk laser : the SOI waveguide ends on both sides with a fiber-coupler.

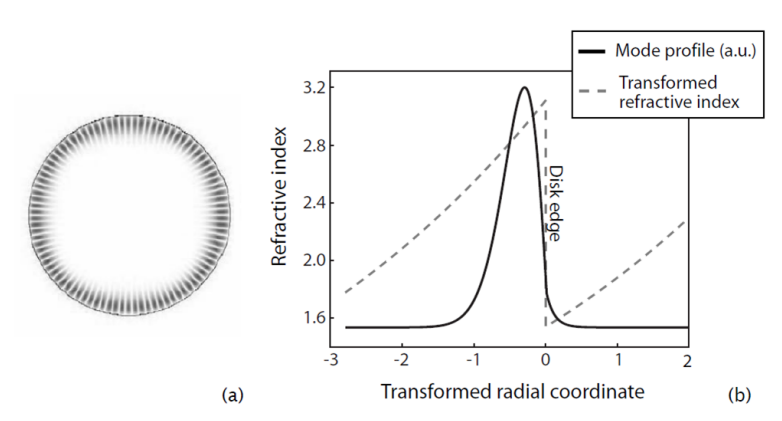

Figure 1.2: (a) FDTD simulation of a whispering gallery mode in a disk laser (top view) and (b) the optical mode depicted after a conformal transformation to an asymmetric, straigh slab waveguide. It can be seen that the light is located near the edge of the disk [65], [78].

1.3.2 Whispering-gallery modes in a microdisk laser

An approximate solution of the whispering gallery modes can be found by solving he Helmholtz equation in cylindrical coordinates. This results in Bessel functions of the first kind inside the microdisk and Hankel functions of the second kind outside the microdisk. The lowest order mode profile corresponds then to the whispering gallery mode as depicted in figure 1.2. Typically, one can apply a conformal transformation of the refractive index profile to calculate the modes as if in an asymmetric, straight slab waveguide [78] (illustrated in figure 1.2). One can see that the lowest order optical mode is confined very close to the edge of the disk. Because disk lasers do not have facets through which the light can be coupled out, an evanescent coupling towards a neighbouring waveguide is assumed in this theoretical approach.

To explain the directional behaviour of the microdisk lasers, we formulate the rate equations now in terms of two counterpropagating modes with electric fields E^+ and E^-. We find [79], [80]:

$$\frac{dE^+}{dt} = \frac{1}{2}(1-j\alpha)\left[G^+ - \frac{1}{\tau_p}\right]E^+ + KE^- \tag{1.1}$$

$$\frac{dE^-}{dt} = \frac{1}{2}(1-j\alpha)\left[G^- - \frac{1}{\tau_p}\right]E^- + KE^+ \tag{1.2}$$

The model includes internal losses in the cavity and losses due to out-coupling through the photon-lifetime parameter τ_{p}. The parameter α is the linewidth enhancement factor that accounts for variations in refractive index due to carrier fluctuations in the semiconductor medium. G is the modal gain factor which will be described further and $K = K_{\mathrm{d}} + jK_{\mathrm{c}}$ represents an explicit linear coupling rate between the two modes where K_{d} is the dissipative coupling and K_{c} the conservative coupling. This coupling term describes the effects of reflection at the end facets of the silicon waveguide, at the grating couplers, and at the fiber facets, as well as the coupling between the clockwise (CW) and the counterclockwise (CCW) modes due to sidewall roughness. For the carrier density rate equation, we find:

$$\frac{\mathrm{d}N}{\mathrm{d}t} = \frac{I}{qV} - \frac{N}{\tau_c} - G^+ \left|E^+\right|^2 - G^- |E^-|^2 \tag{1.3}$$

I denotes the injected current and τ_{c} is the carrier lifetime. The two other terms take into account the carrier depletion due to stimulated emission. The gain experienced in a semiconductor material decreases for high optical intensity. This is due to gain suppression. Gain suppression takes place even when the total carrier density N is constant and reflects the reduction of "resonant carriers" due to carrier heating and spectral hole burning. To account for this effect, the modal gain can be written as:

$$G^+ = \Gamma g_0 v_g (N - N_0)(1 - \epsilon_s \left|E^+\right|^2 - \epsilon_c |E^-|^2) \tag{1.4}$$

$$G^- = \Gamma g_0 v_g (N - N_0)(1 - \epsilon_s |E^-|^2 - \epsilon_c \left|E^+\right|^2) \tag{1.5}$$

where ϵ_{s} reflects the self-gain suppression and ϵ_{c} the cross-gain suppression. The confinement factor Γ is due to the limited height of the active multi-quantum well. N_0 is the transparency carrier density, g_0 is the differential gain, and v_{g} is the group velocity in the microdisk laser. Strain in the quantum wells has a large impact on the band structure of the active material and can have beneficial effects on the gain, by reducing the transparency carrier density and/or improving the differential gain. Calculations have shown that $\epsilon_{\mathrm{c}} = 2\epsilon_{\mathrm{s}}$ [81], [82]. The cross-gain suppression ϵ_{c} will therefore break the symmetry and enforce unidirectional operation of the laser. The gain suppression is, however, only significant when the photon density is high. This means that at lower output powers, normally a bidirectional regime will be present.

The equations can be transformed into a two-dimensional phase-space analysis [83] which can simplify the study of the ring laser dynamics and allow a more intuitive understanding [84], [85]. However, we will not discuss such analyses in this work.

From the above equations, we can conclude that there are two main effects in the coupling between the two modes:

- The linear coupling K due to reflections at the end facets (dissipative) and due to sidewall roughness (conservative). The linear coupling K favors bidirectional operation.
- The nonlinear cross-gain suppression prohibits the counterpropagating cavity mode to build up. This effect is necessary for the unidirectional operation and is present at high values of the photon density.

1.3.3 Typical L-I graph of a microdisk laser

The above equations have been used to implement a simulation tool to study the influence of the laser parameters. More information on this topic can be found in the Master Thesis of Y. De Koninck [78]. In figure 1.3, a typical light-current (L-I) graph of a ring/disk laser structure is depicted. We can distinguish between three different regimes. The first regime, just after threshold, is the bidirectional regime where the two counterpropagating modes are equally present. When the injection current is increased, we can have a bidirectional regime with alternating oscillations [79], [86]. In this regime, the intensities of the two counterpropagating modes are modulated with harmonic sinusoidal oscillations. The modulation is alternate which means that the power in one mode is high when it is low in the other mode. The graph depicts the maximal and minimal values of the mode intensities. The last regime corresponds to the unidirectional operation where the initial conditions determine which of the two modes is dominant [87]. By injecting a pulse in one of the modes, one can switch the lasing direction to that mode which results in flip-flop operation.

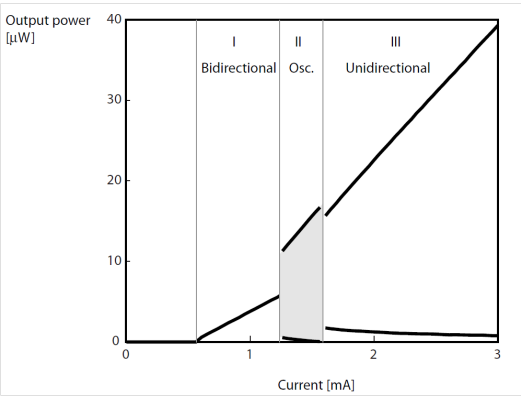

Figure 1.3: Schematic L-I graph of a microdisk/ring laser where different operational regimes can be identified [88].

1.4 EU-FP7 HISTORIC project and basic requirements for all-optical gates

The acronym HISTORIC stood for Heterogeneous InP on Silicon Technology for Optical Routing and LogIC. The EU-FP7 project was a collaboration between four partners, being the Technische Universiteit Eindhoven (TU/e) in the Netherlands, the Laboratoire de Photonique et Nanostructures (LPN, CNRS) in France, IBM Zurich in Zwitzerland and imec-Ghent University. The project started in 2008 and lasted three and a half years. Ghent University-imec was in charge of the fabrication of large Photonic Integrated Circuits (PICs), using the heterogeneous integration of active InP-based components or material on passive SOI structures. The design, the fabrication, the characterization and the results reported in this work were all performed within the framework of the EU-FP7 HISTORIC project.

HISTORIC proposed to design, develop and test digital photonic integrated circuits containing a relatively large number of active photonic elements combined with passive elements, for use in e.g. all-optical packet switching for both datacom and telecom. The building blocks for the digital photonic circuits are ultra-compact gates based on microring or microdisk lasers, and photonic crystal lasers lasers. These lasers are fabricated making use of the heterogeneous integration of InP membranes on top of silicon on insulator (SOI) passive optical circuits. Different approaches for the ultra compact lasers were investigated, allowing the use of the high precision growth and processing techniques available to the InP platform, as well as to take advantage of the extreme accuracy of state-of-the-art CMOS processing. One of the goals of the project was to integrate several all-optical flip-flops and gates on a single chip, so that they would be interconnected by short wire waveguides of the SOI structure. The extremely small dimensions of both the flip-flops, gates and their interconnections would result in a competitive footprint of optical packet switches as compared with electronic switches. The targeted ultra small dimensions (typically less than $100\mu m^2$) of the laser-based all-optical flip-flops were expected to result in record low switching times (< 20ps) and switching energies (< 10fJ). Together with the low propagation losses in the SOI waveguides, this would result in a competitive speed and power consumption for optical packet switches. The possibility of integrating a large number of photonic digital units together, as well as integrating them with compact passive optical routers such as AWGs, opens new perspectives for the design of integrated optical processors or optical buffers. A second goal of the project was to focus on designing new architectures for such optical processing or buffer chips.

Logic systems typically consist of several building blocks (e.g. combinational logic, i.e. gates and sequential logic, i.e. flip-flops), each performing certain logic operations with a limited set of functionality. Complex functions can hence only arise if the gates can be connected and their functionality combined to larger subsystems. To concatenate several identical logic blocks, independent of whether their working principle is electronic or optical, they must fulfil certain requirements. In his commentary letter published in Nature Photonics [89], D. A. B. Miller from Stanford University extensively investigated the device requirements specifically for all-optical systems and lists criteria that need to be fulfilled by photonics to be competitive for optical logic. The prerequisites for building logic systems are cascadability, fan-out, signal refreshing and isolation, which are closely related. The following sections give a short description of the terms.

Cascadability defines the number of identical gates or logic blocks that can be concatenated without losing signal integrity. The output of one stage must be in the correct form to drive the input of the next stage. For instance, if after the second stage, the signal has degraded so much that the following stage cannot process the information, the cascadability is then limited to two gates. It is worth mentioning that in CMOS logic gates, each stage refreshes the signal and assures cascadability. In optics, the output and input wavelengths, beam shapes and pulse shapes should be compatible. It was found in simulations [90] that the switching of the microdisk based all-optical flip-flop is not very sensitive to the power or energy level of the switching pulse, as long as it is larger than a power threshold. The output power from a microdisk laser is also sufficiently large to allow it to switch another microdisk laser. The main challenge is the required wavelength matching between different microdisk lasers. The injection locking range for these lasers is currently a few tens of GHz (or a few hundreds of picometers). This requires very accurate control of the diameters of each microdisk laser.

Fan-out defines the number of identical gates which can be driven with the output of one stage. As the output of the first stage is split into the amount of driven stages, the signal quality also degrades. In electronics, the fan-out is limited to 2-4 due to the ever-more reduced operation voltages. A microdisk laser exhibits a fan-out significantly larger than 10. Simulations have shown that a long-lasting input signal can be as low as 3μW and still change the state of the microdisk laser based flip-flop emitting at an output power of approximately 70μW, resulting in a fan-out of 23 [90]. Experimentally, it has been demonstrated that an injection power of only 360nW is sufficient to switch the state of a flip-flop emitting at 20μW resulting in a fan-out larger than 50 [52].

The quality of the logic signal must be restored so that degradations in signal quality do not propagate through the system. Signal refreshing means that the signal is re-amplified, re-shaped and if necessary also re-timed. In CMOS, inverter chains fulfil this functionality. In optics, we must consider restoring beam quality and/or pulse quality as well as signal-level ranges. Simulations have shown that the signal re-amplification and re-shaping could be achieved with microdisk lasers [90]. A weak signal is injected into the device with low power and a shallow slope. The microdisk laser outputs a strongly amplified signal with a different shape. A gate is needed to perform re-timing.

Signals reflected back into the output can behave as new input signals. Designing a system that isolates reflected signals is a real challenge. In microelectronics, this can be simply achieved by adding an isolating layer between the input and the output of logic blocks (for instance, a gate dielectric). Transistors provide this isolation, but the microscopic physics of nonlinear optical processes and stimulated emission typically does not. Ideally, we want a device with separate input and output beams. In the case of an insufficient input-output isolation, part of the output signal is fed back into the input overlapping with the input signal. This may lead to signal corruption at the output or even an oscillatory behavior. This typically arises when coupling two microdisk lasers to one waveguide. In this configuration, an isolator should be placed in between two devices to allow propagation of the signal in only one direction. Indeed, for all-optical flip-flops for instance, any back reflection into the microdisk causes extra coupling between the CW and the CCW mode, which can jeopardize bi-stable operation. Also, the light from one of the microdisk can inject lock the other one.

The requirements to achieve an all-optical logic system are summarized in Figure 1.4. The table compares the requirements with the status at the beginning of the EU-FP7 HISTORIC project. Also, the potential status at the end of the project is given and compared to the state-of-the-art in CMOS electronics [90].

	Requirement	Current status	Reachable	CMOS
Cascadability	∞	1	10	∞
Fan-out	>2	>20 (Sim) > 50 (Exp)	>50	>2
Signal refreshing	3R	Sim: 2R: Re-shape+Reamplify Exp: 0R	3R	3R
Isolation	>10 dB	Sim: 20 dB Exp: 0 dB	>0 dB	>>30 dB

Figure 1.4: General requirements for all-optical digital systems [90].

1.5 Thesis outline

The prime idea behind carrying out this work was to demonstrate the feasibility of multifunctional and fully-functional photonic chips using the III-V-on-silicon photonics platform. It was envisaged that the III-V-on-silicon platform will be a CMOS compatible platform in the near future. At present III-V material based device fabrication is not widely accepted to be CMOS compatible, but processes can be developed in which III-V-on-silicon will become CMOS compatible. The microdisk was chosen as a building block because it can be fabricated with a small foot-print and different photonic functionalities are possible in it with lower power consumption.

Chapter 2 gives an overview of the standard fabrication procedure of microdisk lasers. Several optimizations have been implemented to combine the expertise available in three different clean-rooms of the partners of the HISTORIC project. We demonstrate the advantages of using an electron-beam lithography based processing for the definition of microdisk lasers and of their top contacts. The uniformity of nominally identical microdisk lasers processed with electron-beam lithography is studied. Simulations are performed to provide alternatives regarding the epitaxial structure used for microdisk lasers.

Chapter 3 theoretically and experimentally demonstrate the sensibility of a microdisk laser to external reflections. A Bragg reflector is added to one side of the waveguide to which the device is coupled.

Chapter 4 demonstrates the use of a microdisk laser for all-optical signal processing applications. We theoretically and experimentally demonstrate 2R-regeneration. Flip-flop operation with optical pulses as short as 25ps is reported and all-optical gating up to 20GHz is investigated.

Chapter 5 draws conclusions of this work and highlights the perspectives of microdisk lasers for optical interconnects applications.

1.6 Publications

The results obtained within this work have been published in several papers and were presented at various conferences. The following list gives an overview.

Publications in international journals

1. K. Vandoorne, P. Mechet, T. Van Vaerenbergh, M. Fiers, G. Morthier, D. Verstraeten, B. Schrauwen, J. Dambre, P. Bienstman. *Experimental demonstration of reservoir computing on a silicon photonics chip* . Accepted for publication in Nature Communications, 2014.
2. P. Mechet, T. Spuesens, S. Werquin, K. Vandoorne, N. Olivier, J.-M. Fedeli, P. Regreny, D. Van Thourhout, G. Roelkens, and G. Morthier. *All-optical low-power 2R regeneration of 10Gb/s NRZ signals using a III-V on SOI microdisk laser*. IEEE Photonics Journal, 5(6), 2013.
3. K. Alexander, T. Van Vaerenbergh, M. Fiers, P. Mechet, J. Dambre, and P. Bienstman. *Excitability in optically injected microdisk lasers with phase controlled excitatory and inhibitory response*. Optics Express, 21(22):26182–26191, 2013.
4. G. Morthier, and P. Mechet. *Theoretical analysis of unidirectional operation and reflection sensitivity of semiconductor ring or disk lasers*. IEEE Journ. Quant. El., 49(12):1097–1101, 2013.
5. P. Mechet, S. Verstuyft, T. De Vries, T. Spuesens, P. Regreny, D. Van Thourhout, G. Roelkens, and G. Morthier. *Unidirectional III-V microdisk lasers heterogeneously integrated on SOI*. Optics Express, 21(16):19339–19352, 2013.
6. P. Mechet, F. Raineri, A. Bazin, Y. Halioua, T. Spuesens, T.J. Karle, P. Regreny, P. Monnier, D. Van Thourhout, I. Sagnes, R. Raj, G. Roelkens, and G. Morthier. *Uniformity of the lasing wavelength of heterogeneously integrated InP microdisk lasers on SOI*. Optics Express, 21(9):10622–10631, 2013.
7. T. Van Vaerenbergh, M. Fiers, P. Mechet, T. Spuesens, R. Kumar, G. Morthier, B. Schrauwen, J. Dambre, and P. Bienstman. *Cascadable excitability in microrings*. Optics Express, 20(18):20292–20308, 2012.
8. K. Van Acoleyen, J. Roels, P. Mechet, T. Claes, D. Van Thourhout, and R. Baets. *Ultra-compact phase modulator based on a cascade of NEMS-operated slot waveguides fabricated in Silicon-On-Insulator*. IEEE Photonics Journal, 4(3):779–788, 2012.
9. J. Hofrichter, T. Morf, A. La Porta, B.J. Offrein, P. Mechet, G. Morthier, T. De Vries, H.J.S. Dorren, O. Raz. *Inverting and non-inverting operation of InP microdisk modulators*. IEEE Electronics Letters, 48(10):586–588, 2012.

10. J. Hofrichter, O. Raz, A. La Porta, T. Morf, P. Mechet, G. Morthier, T. De Vries, H.J.S. Dorren, and B.J. Offrein. *A low-power high-speed InP microdisk modulator heterogeneously integrated on a SOI waveguide.* Optics Express, 20(9):9363–9370, 2012.

11. J. Lloret, R. Kumar, S. Sales, F. Ramos, G. Morthier, P. Mechet, T. Spuesens, D. Van Thourhout, N. Olivier, J.-M. Fedeli, and J. Capmany. *Ultra-compact electro-optic phase modulator based on III-V on silicon microdisk resonator.* Optics Letters, 37(12):2379–2381, 2012.

12. R. Kumar, T. Spuesens, P. Mechet, N. Olivier, J.-M. Fedeli, P. Regreny, G. Roelkens, D. Van Thourhout, and G. Morthier. *10Gbit/s all-optical NRZ-OOK to RZ-OOK format conversion in an ultra-small III-V on silicon microdisk fabricated in a CMOS pilot line.* Optics Express, 19(24):24647–24656, 2011.

13. R. Kumar, T. Spuesens, P. Mechet, P. Kumar, O. Raz, N. Olivier, J.-M. Fedeli, G. Roelkens, R. Baets, D. Van Thourhout, and G. Morthier. *Ultra-fast and Bias-free All-Optical Wavelength Conversion Using III-V on Silicon Technology.* Optics Letters, 36(13):2450–2452, 2011.

Publications in international conferences

1. G. Morthier, P. Mechet, T. Spuesens, D. Van Thourhout, G. Roelkens. *Asymmetric heterogeneously integrated InP microdisk lasers on Si for optical interconnect and optical logic (invited).* Publication in Conference on Lasers and Electro-Optics 2014 (CLEO), San Jose, United States, 2014.

2. G. Morthier, and P. Mechet. *Theoretical and experimental analysis of unidirectionality of asymmetrically-coupled semiconductor ring or disk lasers.* SPIE Photonics West 2014, Volume 8980, Physics and Simulation of Optoelectronic Devices XXII, San Francisco, United States, February 2014.

3. G. Roelkens, S. Keyvaninia, Y. De Koninck, P. Mechet, T. Spuesens, M. Tassaert, S. Stankovic, G. Morthier, R. Baets, D. Van Thourhout, G. Duan, J.-M. Fedeli, and M. Smit. *Heterogeneous III-V/silicon photonic integrated circuits (invited).* Asia Communications and Photonics Conference 2013, Beijing, China, November 2013.

4. P. Mechet, F. Raineri, A. Bazin, T. Spuesens, P. Regreny, P. Monnier, D. Van Thourhout, I. Sagnes, R. Raj, G. Roelkens, and G. Morthier. *Extremely uniform lasing wavelengths of InP microdisk lasers heterogeneously integrated on SOI.* IEEE Photonics Conference 2013 (IPC), ME3.2, Seattle, United States, September 2013.

5. P. Mechet, T. Spuesens, N. Olivier, J.-M. Fedeli, P. Regreny, D. Van Thourhout, G. Roelkens, and G. Morthier. *All-optical, low-power 2R regeneration of*

10Gb/s NRZ signals using a III-V on SOI microdisk laser. 18th OptoElectronics and Communications Conference held jointly with 2013 International Conference on Photonics in Switching (OECC/PS), TuPO-4, Kyoto, Japan, July 2013.

6. G. Morthier, M. Tassaert, P. Mechet, O. Raz, H. Dorren, D. Van Thourhout, and G. Roelkens. *III-V on silicon components for packet switching (invited)*. 18th OptoElectronics and Communications Conference held jointly with 2013 International Conference on Photonics in Switching (OECC/PS), Kyoto, Japan, July 2013.

7. G. Morthier, P. Mechet, T. Spuesens, G. Roelkens, and D. Van Thourhout. *Heterogeneously integrated InP microdisk lasers (invited)*. 7th International Conference on Nanophotonics (ICNP) held jointly with the 3rd Conference on Advances in Optoelectronics and Micro/Nano Optics (AOM) 2013, 111, China, May 2013.

8. T. Van Vaerenbergh, M. Fiers, P. Mechet, T. Spuesens, R. Kumar, G. Morthier, K. Vandoorne, B. Schneider, B. Schrauwen, J. Dambre, and P. Bienstman. *Self-pulsation and excitability mechanism in silicon-on-insulator microrings*. 2012 Asia Communications and Photonics Conference (ACP), 1–3, Guangzhou, China, November 2012.

9. J. Hofrichter, A. La Porta, T. Morf, B.J. Offrein, P. Mechet, G. Morthier, T. De Vries, H.J.S. Dorren, and O. Raz. *Compact high-speed InP microdisk modulators heterogeneously integrated on a SOI waveguide*. IEEE Optical Interconnects, MB6, Santa Fe, United States, May 2012.

10. R. Kumar, T. Spuesens, P. Mechet, N. Olivier, J.-M. Fedeli, P. Regreny, G. Roelkens, D. Van Thourhout, and G. Morthier. *10Gbit/s bias-free and error-free all-optical NRZ-OOK to RZ-OOK Format conversion using a III-V-on-silicon microdisk resonator*. The Optical Fiber Communication Conference and Exposition (OFC) and The National Fiber Optic Engineers Conference (NFOEC) 2012, JW2A.77, Los Angeles, United States, March 2012.

11. G. Roelkens, S. Keyvaninia, S. Stankovic, M. Tassaert, N. Hattasan, A. Gassenq, P. De Heyn, Y. De Koninck, P. Mechet, R. Kumar, M. Muneeb, D. Vermeulen, G. Morthier, R. Baets, and D. Van Thourhout. *III-V on silicon membrane photonics for near-infrared and mid-infrared applications (invited)*. 16th European Conference on Integrated Optics (ECIO 2012), Barcelona, Spain, April 2012.

12. R. Kumar, T. Spuesens, P. Mechet, J.-M. Fedeli, N. Olivier, P. Regreny, G. Roelkens, D. Van Thourhout, and G. Morthier. *All-optical de-multiplexing of 10Gbps data using III-V/SOI microdisk resonators*. 17th Annual Sympo-

sium of the IEEE Photonics Benelux Chapter, 119–122, Delft, the Netherlands, October 2011.

13. G. Morthier, P. Mechet, R. Kumar, G. Roelkens, T. Spuesens, T. De Vries, E. J. Geluk, P. Regreny, R. Baets, and D. Van Thourhout. *Progress in heterogeneously integrated silicon-InP laser diodes for on-chip all-optical networks and signal processing (invited).* Frontiers in Optics 2011, FWBB4, San Jose, United States, October 2011.
14. R. Kumar, T. Spuesens, P. Mechet, J.-M. Fedeli, N. Olivier, P. Regreny, G. Roelkens, D. Van Thourhout, and G. Morthier. *Proof-of-concept demonstration of an all-Optical de-multiplexer using III-V/SOI microdisk resonator fabricated in a CMOS pilot line.* IEEE Photonics Conference 2011 (IPC), 127–128, Arlington, United States, October 2011.
15. G. Roelkens, S. Stankovic, S. Keyvaninia, P. Mechet, R. Kumar, T. Spuesens, G. Morthier, R. Baets, D. Van Thourhout, M. Lamponi, G. Duan, Y. Halioua, F. Raineri, R. Raj. *Laser sources on a heterogeneous III-V/silicon platform (invited).* IEEE Photonics Conference 2011 (IPC), 395–396, Arlington, United States, October 2011.
16. J. Hofrichter, F. Horst, B.J. Offrein, O. Raz, T. De Vries, H.J.S. Dorren, P. Mechet, and G. Morthier. *Microdisc lasers coupled to silicon waveguides as versatile on-chip optical components for light generation, conversion and detection.* 2011 Semiconductor Conference Dresden (SCD 2011), 1–4, Dresden, Germany, September 2011.
17. R. Kumar, T. Spuesens, P. Mechet, P. Regreny, J.-M. Fedeli, N. Olivier, G. Roelkens, D. Van Thourhout, and G. Morthier. *All-optical demultiplexing using III-V/SOI microdisk resonators.* European Semiconductor Laser Workshop (ESLW), Lausanne, Switzerland, September 2011.
18. R. Kumar, T. Spuesens, P. Mechet, P. Regreny, N. Olivier, J.-M. Fedeli, G. Roelkens, D. Van Thourhout, and G. Morthier. *10Gbps bias-free all-optical wavelength conversion using InP-microdisk resonators heterogeneously integrated onto SOI.* European Conference and Exhibition on Optical Communication (ECOC), We.9.LeSaleve.3, Geneva, Switzerland, September 2011.
19. W. Bogaerts, S. Selvaraja, H. Yu, T. Spuesens, P. Mechet, S. Stankovic, S. Keyvaninia, J. Van Campenhout, P. Absil, G. Roelkens, D. Van Thourhout, and R. Baets. *A Silicon Photonics Platform with Heterogeneous III-V Integration (invited).* Integrated Photonics Research, Silicon and Nano-Photonics (IPR), IWC2, Toronto, Canada, June 2011.
20. P. Mechet, L. Liu, R. Kumar, K. Huybrechts, T. Spuesens, G. Roelkens, E.-J. Geluk , T. De Vries, P. Regreny , D. Van Thourhout, R. Baets, and G. Morthier. *Heterogeneously integrated microdisk lasers for optical interconnects*

and optical logic (invited). SPIE Photonics West 2011, 7913, San Francisco, United States, January 2011.

21. G. Roelkens, D. Vermeulen, L. Liu, T. Spuesens, R. Kumar, P. Mechet, K. Huybrechts, S. Keyvaninia, S. Stankovic, M. Tassaert, P. De Heyn, K. Komorowska, S. Selvaraja, D. Van Thourhout, G. Morthier, R. Baets, and R. Halir. *III-V/silicon photonic integrated circuits for FTTH and optical interconnect (invited)*. IB2COM, Malaga, Spain, August 2010.
22. G. Morthier, L. Liu, R. Kumar, P. Mechet, K. Huybrechts, G. Roelkens, T. Spuesens, T. De Vries, E.J. Geluk, P. Regreny, R. Baets, and D. Van Thourhout. *Heterogeneous InP on SOI integration for the realization of all-optical logic devices (invited)*. Integrated Photonics Research, Silicon and Nano Photonics (IPR), Photonics in Switching (PS), IWF2, Monterey, United States, July 2010.
23. D. Vermeulen, T. Spuesens, P. De Heyn, P. Mechet, R. Notzel, S. Verstuyft, D. Van Thourhout, and G. Roelkens. *III-V/SOI photonic integrated circuit for FTTH central office transceivers in a PTP network configuration*. European Conference and Exhibition on Optical Communication (ECOC), Tu.5.C.2, Torino, Italy, May 2010.

Publications in national conferences

1. T. Van Vaerenbergh, M. Fiers, P. Mechet, T. Spuesens, R. Kumar, G. Morthier, K. Vandoorne, B. Schneider, B. Schrauwen, J. Dambre, and P. Bienstman. *Characterization of cascadable excitability in a silicon-on-insulator microring*. 17th Annual Symposium of the IEEE Photonics Benelux Chapter, 119–122, Mons, Belgium, November 2012.
2. P. Mechet, S. Verstuyft, I. Sagnes, G. Roelkens, and G. Morthier. *Numerical and Experimental Study of III-V on SOI Microdisk Lasers with p-i-n Junction*. 117th Annual Symposium of the IEEE Photonics Benelux Chapter, 93–96, Mons, Belgium, November 2012.

References

[1] A. L. Schawlow, and C. H. Townes. *Infrared and Optical Masers.* Physical Review, 112(6):1940–1949, 1958.

[2] T. H. Maiman. *Stimulated optical radiation in ruby.* Nature, 187(4736):493–494, 1960.

[3] K. C. Kao, and G. A. Hockham. *Dielectric-fibre surface waveguides for optical frequencies.* Proceedings of the Institution of Electrical Engineers-London, 113(7):1151–1158, 1966.

[4] C. Gunn. *CMOS Photonics for High-Speed Interconnects.* IEEE Micro, 26(2):58–66, 2006.

[5] A. Narasimha, B. Analui, Y. Liang, T. J. Sleboda, S. Abdalla, E. Balmater, S. Gloeckner, D. Guckenberger, M. Harrison, R. Koumans, D. Kucharski, A. Mekis, S. Mirsaidi, D. Song, and T. Pinguet. *A fully integrated 4x10-Gb/s DWDM optoelectronic transceiver implemented in a standard 0.13µm CMOS SOI technology.* IEEE Journal of Solid-State Circuits, 42(12):2736–2744, 2007.

[6] D. A. B. Miller. *Device requirements for optical interconnects to silicon chips.* Proceedings of the IEEE, 97(7):1166–1185, 2009.

[7] B. Schuppert, J. Schmidtchen, and K. Petermann. *Optical channel waveguides in silicon diffused from GeSi alloy.* Electronics Letters, 25(22):1500–1502, 1989.

[8] R. A. Soref, J. Schmidtchen, and K. Petermann. *Large single-mode rib waveguides in GeSi and Si-on-*SiO_2. IEEE Journal of Quantum Electronics, 27(8):1971–1974, 1991.

[9] P. D. Trinh, S. Yegnanarayanan, and B. Jalali. *Integrated optical directional couplers in silicon-on-insulator.* Electronics Letters 31(24):2097–2098, 1995.

[10] U. Fischer, T. Zinke, and K. Petermann. *Integrated optical waveguide switches in SOI.* Proceedings of IEEE Interantional SOI Conference, 141–142, 1995.

[11] T. T. H. Eng, S. S. Y. Sin, S. C. Kan, and G. K. L. Wong. *Surface micromachined movable SOI optical waveguides.* Proceedings of International Conference on Solid–State Sensers and Actuators,1:348–350, 1995.

[12] C. Z. Zhao, G. Z. Li, E. K. Liu, Y. Gao, and X. D. Liu. *Silicon–on–insulator Mach–Zehnder waveguide interferometers operating at 1.3µm.* Applied Physics Letters, 67(17):2448–2449, 1995.

[13] P. D. Trinh, S. Yegnanarayanan, and B. Jalali. *5X9 integrated optical star coupler in silicon-on-insulator technology.* IEEE Photonics Technology Letters 8(6):794–796, 1996.

[14] P. D. Trinh, S. Yegnanarayanan, F. Coppinger, and B. Jalali. *Silicon–on–insulator (SOI) phased–array wavelength multi-demultiplexer with extremely low-polarization sensitivity.* IEEE Photonics Technology Letters, 9(7):940–942, 1997.

[15] F. Morichetti, A. Canciamilla, C. Ferrari, M. Torregiani, A. Melloni, and M. Martinelli. *Roughness induced backscattering in optical silicon waveguides.* Physical Review Letters, 104(3):33902–1 to 33902–4, 2010.

[16] S. Steven, W. G. Michael, L. Donna, C. W. Richard, and M. L. Theodore. *Hybrid multi-mode/single-mode waveguides for low loss.* Integrated Photonics Research (IPR), paper IThE5, 2004.

[17] P. Dong, W. Qian, S. Liao, H. Liang, C.-C. Kung, N.-N. Feng, R. Shafiiha, J. Fong, D. Feng, A. V. Krishnamoorthy, and M. Asghari. *Low loss shallowridge silicon waveguides.* Optics Express, 18(14):14474–14479, 2010.

[18] E. Cassan, S. Laval, S. Lardenois, and A. Koster. *On-Chip optical Interconnects with compact and low-loss light distribution in silicon-on-insulator rib waveguides.* IEEE Journal of Selected Topics in Quantum Electronics, 9(2):460–464, 2003.

[19] K. K. Lee, D. R. Lim, L. C. Kimerling, J. Shin, and F. Cerrina. *Fabrication of ultralow-loss Si/*SiO_2 *waveguides by roughness reduction.* Optics Letters, 26(23):1888–1890, 2001.

[20] D. K. Sparacin, S. J. Spector, and L. C. Kimerling. *Silicon waveguide sidewall smoothing by wet chemical oxidation.* Journal of Lightwave Technology, 23(8):2455–2461, 2005.

[21] J. Takahashi, T. Tsuchizawa, T. Watanabe, and S. Itabashi. *Oxidation induced improvement in the sidewall morphology and cross-sectional profile of silicon wire waveguides.* Journal of Vacuum Science and Technology B, 22(5):2522–2525, 2004.

[22] W. Bogaerts, P. Dumon, D. Van Thourhout, and R. Baets. *Low-loss, lowcrosstalk crossings for SOI nanophotonic waveguides.* Optics Letters, 32(19):2801–2803, 2007.

[23] D. Taillaert, F. Van Laere, M. Ayre, W. Bogaerts, D. Van Thourhout, P. Bienstman, and R. Baets. *Grating couplers for coupling between optical fibers and nanophotonic waveguides.* Japanese Journal of Applied Physics (invited), 45(8A):6071–6077, 2006.

[24] F. Van Laere, T. Claes, J. Schrauwen, S. Scheerlinck, W. Bogaerts, D. Taillaert, L. O'Faolain, D. Van Thourhout, and R. Baets. *Compact focusing grating couplers for silicon-on-Insulator integrated circuits.* IEEE Photonics Technology Letters, 19(23):1919–1921, 2007.

[25] Q. F. Xu, B. Schmidt, S. Pradhan, and M. Lipson. *Micrometre-scale silicon electro-optic modulator*. Nature, 435(7040):325–327, 2005.

[26] Q. F. Xu, S. Manipatruni, B. Schmidt, J. Shakya, and M. Lipson. *12.5 Gbit/s carrier-injection-based silicon micro-ring silicon modulators*. Optics Express, 15(2):430–436, 2007.

[27] A. S. Liu, L. Liao, D. Rubin, H. Nguyen, B. Ciftcioglu, Y. Chetrit, N. Izhaky, and M. Paniccia. *High-speed optical modulation based on carrier depletion in a silicon waveguide*. Optics Express, 15(2):660–668, 2007.

[28] G. Roelkens, J. Brouckaert, D. Taillaert, P. Dumon, W. Bogaerts, D. Van Thourhout, R. Baets, R. Nötzel, and M. Smit. *Integration of InP/InGaAsP photodetectors onto silicon-on-insulator waveguide circuits*. Optics Express, 13(25):10102–10108, 2005.

[29] A. W. Elshaari, S. F. Preble, C. Cress, R. Raffaelle, and M. A. Abushagur. *Towards a low-Q erbium doped silicon laser*. Frontiers in Optics (FiO), paper FThW5, 2008.

[30] H. Rong, R. Jones, A. Liu, O. Cohen, D. Hak, A. Fang, and M. Paniccia. *A continuous-wave Raman silicon laser*. Nature, 433:725–728, 2005.

[31] B. G. Lee, A. Biberman, A. C. Turner-Foster, M. A. Foster, M. Lipson, A. L. Gaeta, and K. Bergman. *Demonstration of broadband wavelength conversion at 40 Gb/s in silicon waveguides*. IEEE Photonics Technology Letters, 21(3):182–184, 2009.

[32] O. Graydon. *View from... Group IV Photonics: Hope from hybrids*. Nature Photonics, 5:718–719, 2011.

[33] S. Adachi. *Physical properties of III-V semiconductor compounds*. Physical properties of III-V semiconductor compounds, 1992.

[34] D. G. Deppe, N. Holonyak, D. W. Nam, K. C. Hsieh, G. S. Jackson, R. J. Matyi, H. Shichijo, J. E. Epler, and H. F. Chung. *Room-Temperature continuous operation of P-N* $Al_xGa_{1-x}As-GaAs$ *quantum-well heterostructure lasers grown on Si*. Applied Physics Letters, 51(9):637–639, 1987.

[35] T. Wang, H. Liu, A. Lee, F. Pozzi, and A. Seeds . *1.3μm InAs/GaAs quantum-dot lasers monolithically grown on Si substrates*. Optics Express, 19(12):11381–11386, 2011.

[36] A. Lee, Q. Jiang, M. Tang, A. Seeds, and H. Liu. *Continuous-wave InAs/GaAs quantum-dot laser diodes monolithically grown on Si substrate with low threshold current densities* . Optics Express, 20(20):22181–22187, 2012.

[37] Z. Wang, B. Tian, M. Paladugu, M. Pantouvaki, N. Le Thomas, C. Merckling, W. Guo, J. Dekoster, J. Van Campenhout, P. Absil, and D. Van Thourhout. *Polytypic InP nano-laser monolithically integrated on (001) silicon*. Accepted for publication in Nano Letters.

[38] J. van der Tol, R. Zhang, J. Pello, F. Bordas, G. Roelkens, H. Ambrosius, P. Thijs, F. Karouta, and M. Smit. *Photonic integration in Indium-Phosphide membranes on silicon.* IET Optoelectronics, 5(5):2018–2036, 2011.

[39] J. Pello, J. van der Tol, S. Keyvaninia, PJ. van Veldhoven, H. Ambrosius, G. Roelkens, and M. Smit. *High-efficiency ultrasmall polarization converter in InP membrane.* Optics Letters, 37(17):3711–3713, 2012.

[40] S. Stanković. *Hybrid III-V/Si DFB Lasers Based on Polymer Bonding Technology.* Doctoral Thesis, Ghent University, 2013.

[41] H. Park, A. W. Fang, D. Liang, Y.-H. Kuo, H.-H. Chang, B. R. Koch, H.-W. Chen, M. N. Sysak, R. Jones, and J. E. Bowers. *Photonic Integration on the Hybrid Silicon Evanescent Device Platform.* Advances in Optical Technologies, 2008:1–18, 2008.

[42] D. Liang, A. W. Fang, H.-W. Chen, M. N. Sysak, B. R. Koch, E. Lively, O. Raday, Y.-H. Kuo, R. Jones, and J. E. Bowers. *Hybrid silicon evanescent approach to optical interconnects.* Applied Physics A, 95(4):1045–1057, 2009.

[43] M. J. R. Heck, H-W. Chen, A. W. Fang, B. R. Koch, D. Liang, H. Park, M. N. Sysak, and J. E. Bowers. *Hybrid Silicon Photonics for Optical Interconnects.* IEEE Journal of Selected Topics in Quantum Eelectronics, 17(2):333–346, 2011.

[44] Y. H. So, P. Garrou, J. H. Im, and D. M. Scheck. *Benzocyclobutene-based polymers for microelectronics.* Chemical Innovation, 31(12):40–47, 2001.

[45] O. Painter, R. K. Lee, A. Scherer, A. Yariv, J. D. O'Brien, P. D. Dapkus, and I. Kim. *Two-dimensional photonic band-gap defect mode laser.* Science, 284(5421):1819–1821, 1999.

[46] R. F. Oulton, V. J. Sorger, D. A. Genov, D. F. P. Pile, and X. Zhang. *A hybrid plasmonic waveguide for subwavelength confinement and long-range propagation.* Nature Photonics, 2(8):496–500, 2008.

[47] S. L. McCall, A. F. J. Levi, R. E. Slusher, S. J. Pearton, and R. A. Logan. *Whispering-gallery mode microdisk lasers.* Applied Physics Letters, 60(3):289–291, 1992.

[48] A. F. J. Levi, R. E. Slusher, S. L. McCall, T. Tanbun-Ek, D. L. Coblentz, and S. J. Pearton. *Room temperature operation of microdisc lasers with submilliamp threshold current.* Electronics Letters, 28(11):1010–1012, 1992.

[49] M. T. Hill, H. J. S. Dorren, T. de Vries, X. J. M. Leijtens, J. H. den Besten, B. Smalbrugge, Y. S. Oei, H. Binsma, G. D. Khoe, and M. K. Smit. *A fast low-power optical memory based on coupled micro-ring lasers.* Nature, 432(7014):206–209, 2004.

[50] A. Trita, G. Mezosi, F. Bragheri, Y. Jin, S. Furst, W. Elsasser, I. Cristiani, M. Sorel, and G. Giuliani. *Dynamic operation of all-optical flip-flop based*

on a monolithic semiconductor ring laser. Proceedings of the 34th European Conference on Optical Communication (ECOC), 2008.

[51] A. Trita, M.J. Latorre Vidal, M. Zanola, G. Mezosi, J. Javaloyes, M. Sorel, F. Bragheri, I. Cristiani, A. Scire, S. Balle, and G. Giuliani. *All-optical set-reset flip-flop based on semiconductor ring laser: ultrafast response and errorfree bit-error-rate operation*. Proceedings of the International Conference on Photonics in Switching (PS), 2009.

[52] L. Liu, R. Kumar, K. Huybrechts, T. Spuesens, G. Roelkens, E.-J. Geluk, T. de Vries, P. Regreny, D. Van Thourhout, R. Baets, and G. Morthier. *An ultra-small, low-power, all-optical flip-flop memory on a silicon chip*. Nature Photonics, 4:182–187, 2010.

[53] K. Huybrechts, L. Liu, R. Kumar, T. Spuesens, G. Roelkens, E.-J. Geluk, T. de Vries, M. K. Smit, P. Regreny, P. Rojo-Romeo, D. Van Thourhout, R. Baets, and G. Morthier. *Digital photonics using InP microdisk lasers heterogeneously integrated on silicon-on-insulator*. Proceedings of the 15th European Conference on Integrated Optics (ECIO 2010), 2010.

[54] R. Kumar, K. Huybrechts, L. Liu, T. Spuesens, G. Roelkens, E.-J. Geluk, T. de Vries, P. Regreny, D. Van Thourhout, R. Baets, and G. Morthier. *An ultra-small, low-power, all-optical flip-flop memory on a silicon chip*. Proceedings of the Optical Fiber Conference and Exposition (OFC), 2010.

[55] L. Gelens, S. Beri, and J. Danckaert. *Phase-space approach to directional switching in semiconductor ring lasers*. Applied Physics Letters, 1(9), 2009.

[56] S. Beri, L. Mashall, L. Gelens, G. Van der Sande, G. Mezosi, M. Sorel, J. Danckaert, and G. Verschaffelt. *Excitability in optical systems close to Z_2-symmetry*. Physics Letters A, 374:739–743, 2010.

[57] L. Gelens, S. Beri, G. Sande, G. Verschaffelt, and J. Danckaert. *Multistable and excitable behavior in semiconductor ring lasers with broken Z_2-symmetry*. European Physical Journal, D(58):197–207, 2010.

[58] W. Coomans, L. Gelens, S. Beri, J. Danckaert, and G. Van der Sande. *Solitary and coupled semiconductor ring lasers as optical spiking neurons*. Physical Review E(84):1–8, 2011.

[59] Y. De Koninck, K. Huybrechts, G. Van der Sande, J. Danckaert, R. Baets, and G. Morthier. *Nonlinear dynamics of asymmetrically coupled microdisk lasers*. Proceedings of the LEOS Annual Meeting IEEE Conference, 503–504, 2009.

[60] K. Alexander, T. Van Vaerenbergh, M. Fiers, P. Mechet, J. Dambre, and P. Bienstman. *Excitability in optically injected microdisk lasers with phase controlled excitatory and inhibitory response*. Optics Express, 21(22):26182–26191, 2013.

[61] C. Seassal, P. Rojo-Romeo, X. Letartre, P. Viktorovitch, G. Hollinger, E. Jalaguier, S. Pocas, and B. Aspar. *InP microdisk lasers on silicon wafer: CW room temperature operation at 1.6μm.* Electronics Letters, 37(4):222–223, 2001.

[62] H. T. Hattori, C. Seassal, E. Touraille, P. Rojo-Romeo, X. Letartre, G. Hollinger, P. Viktorovitch, L. Di Cioccio, M. Zussy, L. El Melhaoui, and J. M. Fedeli. *Heterogeneous integration of microdisk lasers on silicon strip waveguides for optical interconnects.* IEEE Photonics Technology Letters, 18(1-4):223–225, 2006.

[63] EU–FP6 PICMOS, *http://picmos.intec.ugent.be/.*

[64] J. Van Campenhout, P. Rojo-Romeo, P. Regreny, C. Seassal, D. Van Thourhout, S. Verstuyft, L. Di Cioccio, J. M. Fedeli, C. Lagahe, and R. Baets. *Electrically pumped InP-based microdisk lasers integrated with a nanophotonic silicon-on-insulator waveguide circuit.* Optics Express, 15(11):6744–6749, 2007.

[65] J. Van Campenhout. *Thin-Film microlasers for the integration of electronic and photonic integrated circuits.* Doctoral Thesis, Ghent University, 2007.

[66] T. Spuesens, L. Liu, T. de Vries, P. R. Romeo, P. Regreny, and D. Van Thourhout. *Improved design of an InP-based microdisk laser heterogeneously integrated with SOI.* Proceedings of the 6th IEEE International Conference on Group IV Photonics, 202–204, 2009.

[67] R. Kumar, L. Liu, G. Roelkens, E.-J. Geluk, T. de Vries, F. Karouta, P. Regreny, D. Van Thourhout, R. Baets, and G. Morthier. *10GHz All-Optical Gate Based on a III-V/SOI Microdisk.* IEEE Photonics Technology Letters, 22(13):981–983, 2010.

[68] J. Hofrichter, O. Raz, L. Liu, G. Morthier, F. Horst, P. Regreny, T. De Vries, H.J.S. Dorren, and B.J. Offrein. *All-optical wavelength conversion using mode switching in InP microdisc laser.* Electronics Letters, 47(16):927–929, 2011.

[69] R. Kumar, T. Spuesens, P. Mechet, P. Kumar, O. Raz, N. Olivier, J.-M. Fedeli, G. Roelkens, R. Baets, D. Van Thourhout, and G. Morthier. *Ultra-fast and bias-free all-optical wavelength conversion using III-V on silicon technology.* Optics Letters, 36(13):2450–2452, 2011.

[70] R. Kumar, T. Spuesens, P. Mechet, N. Olivier, J.-M. Fedeli, P. Regreny, G. Roelkens, D. Van Thourhout, and G. Morthier. *10Gbit/s all-optical NRZ-OOK to RZ-OOK format conversion in an ultra-small III-V-on-silicon microdisk fabricated in a CMOS pilot line.* Optics Express, 19(24):24647–24656, 2011.

[71] L. Liu, G. Roelkens, T. Spuesens, R. Soref, P. Regreny, D. Van Thourhout, and R. Baets. *Low-power electro-optical switch based on a III-V microdisk cavity on a silicon-on-insulator circuit.* Proceedings of the Asia Communications and Photonics Conference and Exhibition (ACP), Shanghai, China, 2009.

[72] J. Van Campenhout, L. Liu, P. Rojo-Romeo, D. Van Thourhout, C. Seassal, P. Regreny, L. Di Cioccio, J. M. Fedeli, and R. Baets. *A compact SOI integrated multiwavelength laser source based on cascaded InP microdisks.* IEEE Photonics Technology Letters, 20(13-16):1345–1347, 2008.

[73] O. Raz, H.J.S. Dorren, R. Kumar, G. Morthier, P. Regreny, and P. Rojo-Romeo. *50 FJ-per-bit, high speed, directly modulated light sources for on-chip optical data communications.* Proceedings of OFC 2011, pp. OMM5, 2011.

[74] L. Liu, J. Van Campenhout, G. Roelkens, R. A. Soref, D. Van Thourhout, P. Rojo-Romeo, P. Regreny, C. Seassal, J. M. Fedeli, and R. Baets. *Carrier injection–based electro-optic modulator on silicon-on-insulator with a heterogeneously integrated III-V microdisk cavity.* Optics Letters, 33(21):2518–2520, 2008.

[75] J. Hofrichter, O. Raz, A. La Porta, T. Morf, P. Mechet, G. Morthier, T. De Vries, H.J.S. Dorren, B.J. Offrein. *A low-power high-speed InP microdisk modulator heterogeneously integrated on a SOI waveguide.* Optics Express, 20(9):9363–9370, 2012.

[76] J. Hofrichter, T. Morf, A. La Porta, B.J. Offrein, P. Mechet, G. Morthier, T. De Vries, H.J.S. Dorren, and O. Raz. *Inverting and non-inverting operation of InP microdisk modulators.* Electronics Letters, 48(10):586–588, 2012.

[77] T. Spuesens, J. Bauwelinck, P. Regreny, and D. Van Thourhout. *Realization of a compact optical interconnect on Silicon by heterogeneous integration of III-V.* IEEE Photonics Technology Letters, 25(14):1332–1335, 2013.

[78] Y. De Koninck. *Niet-lineaire dynamica van enkelvoudige en gekoppelde microschijflasers.* Master Thesis, Ghent University, 2009.

[79] M. Sorel, G. Giuliani, A. Scire, R. Miglierina, S. Donati, and P. J. R. Laybourn. *Operating regimes of GaAs-AlGaAs semiconductor ring lasers: experiment and model.* IEEE Journal of Quantum Electronics, 39(10):1187–1195, 2003.

[80] T. Numai. *Analysis of signal voltage in a semiconductor ring laser gyro.* IEEE Journal of QuantumElectronics, 36(10):1161–1167, 2000.

[81] E. J. D′Angelo, E. Izaguirre, G. B.Mindlin, G. Huyet, L. Gil, and J. R. Tredicce. *Spatiotemporal dynamics of lasers in the presence of an imperfect O(2) symmetry.* Physical Review Letters, 68(25):3702–3705, 1992.

[82] M. Sargent. *Theory of a multimode quasi-equilibriumsemiconductor-laser.* Physical Review A, 48(1):717–726, 1993.

[83] G. Van der Sande, L. Gelens, P. Tassin, A. Scire, and J. Danckaert. *Two dimensional phase-space analysis and bifurcation study of the dynamical behaviour of a semiconductor ring laser*. Molecular and Optical Physics, 41(9):095402, 2008.

[84] L. Gelens, S. Beri, G. Van der Sande, J. Danckaert, N. Calabretta, H. J. S. Dorren, R. Notzel, E. Bente, and M. K. Smit. *Optical injection in semiconductor ring lasers: backfire dynamics*. Optics Express, 16(15):10968–10974, 2008.

[85] L. Gelens, G. Van der Sande, S. Beri, and J. Danckaert. *Phase-space approach to directional switching in semiconductor ring lasers*. Physical Review E, 79(1):016213, 2009.

[86] M. Sorel, P. J. R. Laybourn, A. Scire, S. Balle, G. Giuliani, R. Miglierina, and S. Donati. *Alternate oscillations in semiconductor ring lasers*. Optics Letters, 27(22):1992–1994, 2002.

[87] M. Sorel, P. J. R. Laybourn, G. Giuliani, and S. Donati. *Unidirectional bistability in semiconductor waveguide ring lasers*. Applied Physics Letters, 80(17):3051–3053, 2002.

[88] K. Huybrechts. *Digital photonics using single laser diodes for all-optical network nodes*. Doctoral Thesis, Ghent University, 2010.

[89] D.A.B. Miller. *Are optical transistors the logical next step?*. Nature Photonics, 4:3–5, 2010.

[90] HISTORIC project. *Specifications for all-optical flip-flops, gates and digital photonics*. HISTORIC Deliverable D1.2, 2010.

"Parfois on regarde les choses
Telles qu'elles sont
En se demandant pourquoi
Parfois, on les regarde
Telles qu'elles pourraient être
En se disant pourquoi pas"

Gaëtan Roussel, Il y a, 2009

2

Development and optimizations of the fabrication of microdisk lasers

This chapter provides a description of the standard fabrication procedure for microdisk lasers. The main advantages of the microdisk laser are its relatively easy fabrication and its excellent performance as an integrated laser source. The devices from this work were fabricated within the FP7 European project HISTORIC ("Heterogeneous InP on Silicon Technology for Optical Routing and LogIC"). As previously mentioned in chapter 1, three project partners contributed to the process development and optimizations for microdisk lasers. We present the different process flows conducted in the cleanrooms of Ghent University–imec, of the Laboratoire de Photonique et Nanostructures (LPN), and of the Technische Universiteit from Eindhoven (TU/e). The combination of the expertise and experience of each research group has resulted in drastic improvements for the fabrication of microdisk lasers. The collaborations within the project indeed allowed the use of high precision growth and processing techniques available to the InP platform, as well as of the extreme accuracy of state-of-the-art CMOS processing. For instance, the lasers are fabricated making use of the heterogeneous integration of InP membranes on top of Silicon-On-Insulator (SOI) passive optical circuits. Ghent University has demonstrated its expertise in the adhesive bonding technique over the last ten years. Also, the processing know-how on InP at TU/e in Eindhoven is capital to minimize

the sidewall surface roughness of the microdisks. Finally, the electron-beam lithography process from LPN has been adapted and optimized in order to accurately align microdisk lasers to the underlying passive optical waveguides. In a last section of this chapter, we describe the fabrication in Ghent University of microdisk lasers based on a alternative epitaxial stack. For detailed information about the processing of devices from this PhD. work, please refer to appendix A.

2.1 Layout of an integrated microdisk laser

The layout of a microdisk laser heterogeneouly integrated on SOI is shown in Figure 2.1. A microdisk is etched in an InP-based film with a total thickness t. The film is bonded onto a patterned and planarized, passive SOI waveguide structure. The InP etch is incomplete, leaving a thin bottom contact layer with a thickness t_s. The top metal contact is placed above the center of the microdisk, without overlap with the whispering-gallery mode at the edge of the microdisk. The bottom metal contact is deposited on the bottom contact layer. The microdisk edge is laterally aligned to an underlying SOI wire waveguide, with an intermediate SiO_2/DVS − BCB thickness t_{ox}. The wire waveguide has a width w and a heigth of 220nm. The microdisk is embedded in a low-refractive-index polymer or dielectric, which both serves as an optical isolation and planarization layer. For fabricated devices, we typically used a Divinylsiloxane-Benzocyclobutene (DVS-BCB) polymer for this purpose.

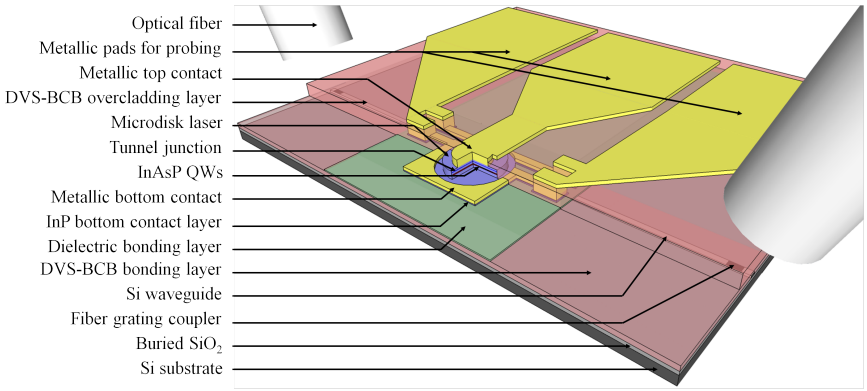

Figure 2.1: Schematic representation of the heterogeneous SOI-integrated microdisk laser.

2.2 Process overview

A global overview of the fabrication procedure of heterogeneously integrated microdisk lasers is shown in Figure 2.2. The main elements are the InP-based epitaxial growth of the laser structure, the adhesive bonding, the III-V processing and the metallization steps defining the electrical contacts of the microdisk laser.

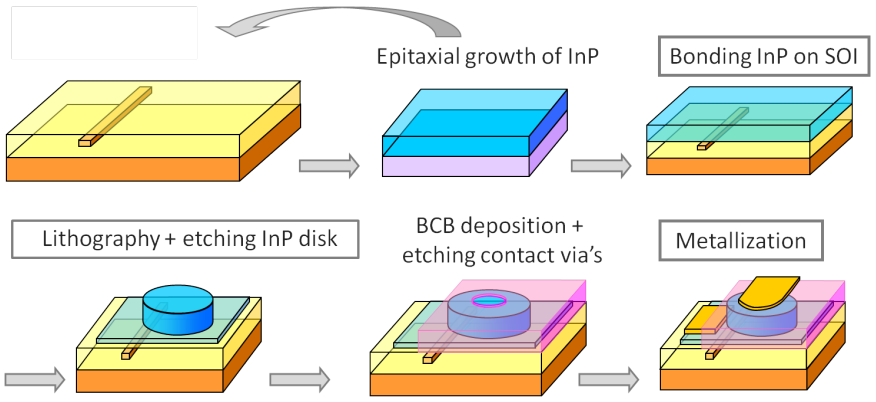

Figure 2.2: Overview of the process flow of a microdisk laser [1].

As described in the introduction of this chapter, the process of microdisk lasers has been split during this work between three different research groups. The main process flow from this PhD. work – from bonding to metal deposition for electrical pumping – has indeed been developed and executed in Ghent University. Bonding is always performed in Ghent, although SOI samples from imec and from CEA-Leti are post-processed. In this section, the standard fabrication procedure is first described. Several optimizations have been implemented in Ghent to improve the yield and the characteristics of the microdisk lasers. Also, further modifications were added to this process flow in order to rely on the expertise of project partners (lithography of the microdisks and reduction of the sidewall roughness). Finally, an alternative epitaxial stack is proposed and sucessfully processed in the cleanroom of Ghent University.

Tables from Figures 2.3 to 2.6 are a chronological summary of the fabrication steps in each cleanroom. We were responsible of every fabrication step carried out in Ghent University. Processing steps in TU/e were performed under the supervision of Ir. Tjibbe de Vries. In LPN, we worked under the supervision and with the help of Dr. Fabrice Raineri. Only the the electron-beam lithography exposure itself has always been performed by Prof. I. Sagnes and Dr. Rémi Braive from LPN. The first process is the one developed in Ghent University,

where samples are bonded on SOI chips fabricated at imec and at CEA-Leti. Also, the fabrication of samples based on the alternative epitaxial stack is fully carried out in Ghent University. Samples for the second process are bonded in Ghent University, but the etching of the microdisk lasers itself is performed at the TU/e. Several optimizations are implemented at LPN, where microdisks and their top metallic contacts are defined with electron-beam lithography and where several III-V etching recipes are proposed.

Step	Process at Ghent University			Process at TU/e
	imec SOI	**CEA-Leti SOI**	**p-i-n microdisks**	**III-V etch**
1	DUV-193nm lithography + Si etch for WG definition	DUV-193nm lithography + Si etch for WG definition	DUV-193nm lithography + Si etch for WG definition	
2	Air cladding	Oxide cladding CMP to the WG level	Air cladding	
3	SOI and III-V clean	SOI and III-V clean	SOI and III-V clean	
4	SiO_2 deposition on III-V	SiO_2 deposition on III-V	Al_2O_3 deposition on III-V	
5	Bonding in the CB6L wafer bonder	Bonding in the CB6L wafer bonder	Bonding in the CB6L wafer bonder	
6	Full wet etch of the substrate	Full wet etch of the substrate	Full wet etch of the substrate	
7	Etch-stop removal	Etch-stop removal	Etch-stop removal	Etch-stop removal
8	300nm-thick SiO_2 hard mask deposition	300nm-thick SiO_2 hard mask deposition	Contact lithography for top metallic contact definition	300nm-thick Si_3N_4 hard mask deposition
9	Contact lithography for disk definition	Contact lithography for disk definition	Top metallic contact deposition (Ti/Pt/Au : 40/50/100nm)	Contact lithography for disk definition
10	RIE etch of the SiO_2 hard mask	RIE etch of the SiO_2 hard mask	ICP etch of the InGaAs top layer	RIE etch of the Si_3N_4 hard mask
11	Surface treatment (H_3PO_4/H_2O + HF)	Surface treatment (H_3PO_4/H_2O + HF)	300nm-thick SiO_2 hard mask deposition	Surface treatment (H_3PO_4/H_2O + HF)
12	ICP etch of the III-V microdisks	ICP etch of the III-V microdisks	Contact lithography for disk definition	ICP etch of the III-V microdisks
13	SiO_2 hard mask thinned to 50nm	SiO_2 hard mask thinned to 50nm	RIE etch of the SiO_2 hard mask	
14	Surface treatment (H_3PO_4/H_2O + HF)	Surface treatment (H_3PO_4/H_2O + HF)	ICP etch of the III-V microdisks	

Figure 2.3: Chronological summary of the different process flows and optimizations of the fabrication of microdisk lasers in Ghent University and at the Technische Universiteit of Eindhoven.

15	Contact lithography for bottom metallic contact definition	Contact lithography for bottom metallic contact definition	Contact lithography for bottom metallic contact definition	
16	Bottom metallic contact deposition (Ti/Pt/Au : 40/50/100nm)	Bottom metallic contact deposition (Ti/Pt/Au : 40/50/100nm)	Bottom metallic contact deposition (Ti/Pt/Au : 40/50/100nm)	
17	Contact lithography for island definition	Contact lithography for island definition	Contact lithography for island definition	
18	ICP etch of the bottom contact layer	ICP etch of the bottom contact layer	ICP etch of the bottom contact layer	
19	DVS-BCB overcladding	DVS-BCB overcladding	DVS-BCB overcladding	
20	DVS-BCB curing	DVS-BCB curing	DVS-BCB curing	
21	Contact lithography for top and bottom vias	Contact lithography for top and bottom vias	Contact lithography for top and bottom vias	
22	Etching of the top and bottom vias in the DVS-BCB	Etching of the top and bottom vias in the DVS-BCB	Etching of the top and bottom vias in the DVS-BCB	
23	Contact lithography for bottom vias only	Contact lithography for bottom vias only	Contact lithography for bottom vias only	
24	Deeper etching of the bottom vias in the DVS-BCB	Deeper etching of the bottom vias in the DVS-BCB	Deeper etching of the bottom vias in the DVS-BCB	
25	Contact lithography for top metal / heat sink definition	Contact lithography for top metal/heat sink definition	Oxygen plasma	
26	Oxygen plasma	Oxygen plasma	Contact lithography for pads definition	
27	Etching of the remaining SiO_2 hard mask	Etching of the remaining SiO_2 hard mask	Metallic pads deposition (Ti/Au : 40/100nm)	
28	Top metallic contact deposition (Ti/Pt/Au : 40/50/100nm)	Top metallic contact deposition (Ti/Pt/Au : 40/50/100nm)	Extra metallic deposition for electrical tests (Au : 800nm)	
29	Contact lithography for pads definition	Contact lithography for pads definition		
30	Metallic pads deposition (Ti/Au : 40/100nm)	Metallic pads deposition (Ti/Au : 40/100nm)		
31	Extra metallic deposition for electrical tests (Au : 800nm)	Extra metallic deposition for electrical tests (Au : 800nm)		

Figure 2.4: Chronological summary of the different process flows and optimizations of the fabrication of microdisk lasers in Ghent University and at the Technische Universiteit of Eindhoven.

Step	Process at LPN			
	1st generation EBL	2nd generation EBL	3rd generation EBL	ICP tests
1	Bonding performed at Ghent University			
2				
3				
4				
5				
6				
7	Contact lithography for opening of SOI markers	Contact lithography for opening of SOI markers	Contact lithography for opening of SOI markers	
8	Wet etching of the III-V layers bonded on top of the SOI markers	Wet etching of the III-V layers bonded on top of the SOI markers	Wet etching of the III-V layers bonded on top of the SOI markers	
9	Wet etching of the SiO_2 or Al_2O_3 from bonding above the markers	Wet etching of the SiO_2 or Al_2O_3 from bonding above the markers	Wet etching of the SiO_2 or Al_2O_3 from bonding above the markers	
10	RIE etch of the DVS-BCB on top of the SOI markers	RIE etch of the DVS-BCB on top of the SOI markers	RIE etch of the DVS-BCB on top of the SOI markers	
11	Wet etching of the BOx layer inside the SOI markers	Wet etching of the BOx layer inside the SOI markers	Wet etching of the BOx layer inside the SOI markers	
12	300nm-thick Si_3N_4 hard mask deposition	300nm-thick Si_3N_4 hard mask deposition	300nm-thick Si_3N_4 hard mask deposition	
13	PMMA spin-coating	PMMA spin-coating	ma-N 2410 spin-coating	
14	EBL exposure for disk definition	EBL exposure for disk definition	EBL exposure for disk definition	

Figure 2.5: Chronological summary of the different process flows and optimizations of the fabrication of microdisk lasers in Ghent University and at the Technische Universiteit of Eindhoven and in Laboratoire de Photonique et Nanostructures.

15	PMMA development	PMMA development	ma-N 2410 development	
16	Nickel deposition and lift-off in trichloroethylene	RIE etch of the Si_3N_4 hard mask	RIE etch of the Si_3N_4 hard mask	
17	RIE etch of the Si_3N_4 hard mask	Contact lithography to remove the remaining Si_3N_4 hard mask	ICP etch of the III-V microdisks performed in TU/e	Chlorine ICP, HBr-ICP, Cl_2H_2-ICP
18	ICP etch of the III-V microdisks	RIE etch of the remaining Si_3N_4 hard mask	PMMA spin-coating	
19		ICP etch of the III-V microdisks	EBL exposure for top and bottom contacts definition	
20			PMMA development	
21			Simultaneous top and bottom metallic contact deposition (Ti/Au : 40/800nm)	
22			DVS-BCB overcladding	
23			DVS-BCB curing	
24			Etching of the top and bottom vias in the DVS-BCB	
25			Contact lithography for bottom vias only	
26			Deeper etching of the bottom vias in the DVS-BCB	
27			Oxygen plasma	
28			Contact lithography for pads definition	
29			Metallic pads deposition (Ti/Au : 40/100nm)	
30				
31				

Figure 2.6: Chronological summary of the different process flows and optimizations of the fabrication of microdisk lasers in Ghent University and at the Technische Universiteit of Eindhoven and in Laboratoire de Photonique et Nanostructures.

2.3 Standard fabrication process for microdisk lasers heterogeneously integrated on SOI

In this section, we present in details the most important technological processes that are used to fabricate heterogeneous SOI-integrated microdisk lasers. They consist of the fabrication of the SOI waveguide circuit, the growth of the InP-based epitaxial structures, the bonding of the InP-based material to the SOI wafer and the III-V processing of the microdisk lasers.

2.3.1 SOI waveguide technology

Silicon-On-Insulator seems to be the ideal substrate for realizing silicon integrated photonic circuits. Figure 2.7 depicts a schematic cross-section of a SOI substrate. Even though it was originally invented to improve device performance in transistors, the material technology was further embraced by integrated photonics. The thickness requirements of the device layer and buried oxide (BOx) are however very different for electronics and photonics applications. Their specifications have been adapted over the years to suit photonic circuits. The thickness of the low index BOx layer should be sufficiently large to avoid leakage of light from the device layer to the silicon substrate. It has been shown by Pieter Dumon in his Doctoral Thesis that a BOx thickness of 2000nm is required for sufficient isolation for both transverse electric (TE) and magnetic (TM) polarized light in the device layer [2]. The thickness of the device layer depends on the waveguide geometry, which could be based either on a thick core layer (1000nm thick) or a thin core layer (200-300nm thick). In addition to the thickness of the device layer, the doping is an important material parameter. Very little is known about doping concentrations in different substrates used in silicon photonics [3]. Since high doping levels can reduce the transmission, it is generally accepted that un-doped or very low doping levels are desirable for photonic applications. SOI wafers are manufactured in a variety of ways: separation by implanted oxygen (SIMOX) [4], [5] , smart cut [6] , wafer bonding [7], and epitaxial layer transfer (ELTRAN) [8].

Among these techniques smart cut SOI wafers are most widely used in silicon photonics because the related device layer is highly transparent for infrared wavelengths. The fabrication process to obtain this SOI takes advantage of the SmartCut technique developed at CEA-Leti [9] ten years ago. In this technique (Figure 2.7) a silicon wafer is first oxidized to create thermal oxide layer and is then implanted with a high dose of hydrogen ions, forming in the silicon substrate a uniform layer of weak lattice bonds between the Si atoms [10]. This wafer is then bonded to a clean silicon wafer. Thermal processing at 1000°C

splits the structure along the cleavage zone created by the ion implantation. In the end, the wafer is polished by chemical mechanical polishing (CMP) down to a 220nm thick Si top layer.

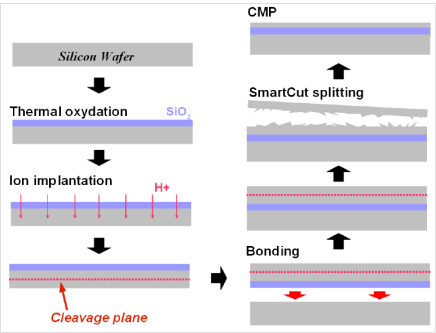

Figure 2.7: Process flow for the SOI fabrication with the SmartCut technique.

In this work, we use smart cut SOI wafers with a 220nm device layer on top of a 2000nm BOx layer, processed either by imec (Leuven, Belgium) or by CEA-Leti (Grenoble, France). After designing the important features of the SOI circuit, the SOI structures are ordered and processed through ePIXfab. Several runs per year allow research groups to obtain affordable SOI samples processed in a CMOS line. The differences between the two fabrication processes from these two foundries are presented below.

SOI waveguide technology in imec

The process to define the waveguide into the silicon depends on which CMOS-line (imec or CEA-Leti) is involved in the fabrication. Both fabrication lines rely on Deep UV lithography [11] followed by Reactive-Ion-Etching (RIE) [12]. In both cases, a thin organic antireflective layer (Bottom Anti-Reflective Coating = BARC) is coated on the silicon in order to limit reflection on the SOI structure of the UV light during deep UV lithography. An intermediate Si_3N_4 hardmask is deposited below the BARC layer. The mask is designed for Deep-Ultra-Violet (DUV) lithography at 193nm in an ASML 1100 equipment. The photoresist layer is coated, and after a baking step, the sample is illuminated with 193nm UV light through the metallic mask pattern. The resist is then developed and the intermediate nitride layer is opened by RIE. The pattern is etched in the silicon using RIE dry etching with a Cl_2/HBr gas mixture [12].

More details about this technology can be found in the PhD thesis of Shankar Selvaraja [3]. After the waveguide definition, a thick layer of oxide can be deposited on top of the wafer. CMP is then performed to planarize and

thin the oxide layer down to the intermediate Si_3N_4 hardmask, which is then used as an etch-stop layer. The resulting planarized surface makes the bonding process more reliable and repeatable in terms of uniformity in the thickness of the bonding layer, as will be discussed in section 2.5. In the case where the silicon waveguides are not cladded by the oxide layer, we need to pay extra attention to the thickness uniformity of the bonding layer. A process ensuring a good uniformity has been developed and will be presented in section 2.5.

SOI waveguide technology in CEA-Leti

Figure 2.8 shows a scheme of the process flow followed for the fabrication of the SOI used at CEA-Leti. Here, the waveguide pattern is defined in the first instance, in an intermediate SiO_2 hardmask layer between the BARC and the photoresist. The mask is designed for DUV lithography at 193nm. The intermediate layer is then patterned by deep UV lithography. The pattern of a unit cell (typically 10 x 10mm^2 large) is repeated over the whole wafer. In the stepping process, the illumination dose and focus can be varied, which results in a variation of the characteristic dimensions of the patterns over the wafer. After exposure, the wafer gets a post-bake treatment, after which the resist is developed and the intermediate layer is opened by RIE. The anti-reflective coating layer is etched using Br/F based chemistry and the hard mask is opened. Finally, the silicon is etched through the hard-mask/photoresist by RIE dry etching with a Cl_2/HBr gas mixture [12]. More information on the SOI waveguide fabrication with DUV lithography can be found in [13]. The wafers delivered by CEA-Leti used in this work were all overcladded with a thick oxide layer that had been thinned down to the waveguide level by CMP.

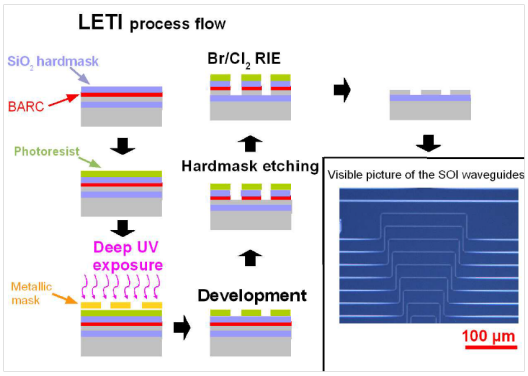

Figure 2.8: SOI fabrication at CEA-Leti and a microscope picture of a few curved waveguides.

2.3.2 Adhesive bonding of the III-V on SOI

The heterostructures are grown at 490°C using solid source molecular beam epitaxy (SSMBE) on a two-inch InP wafer supplied by InPact S.A. An InGaAs sacrificial etch-stop layer, which is removed following bonding, was grown first. The epitaxial stack used for processing microdisk lasers is presented in Table 2.1. Three 6nm-thick compressively strained InAsP quantum wells (QWs) are embedded in 15nm Q1.2 barriers. Metal contacts usually have a poor resistivity on *p*-type InP, and in standard devices, it is necessary to add a *p*-type InGaAs contact layer to improve the contact resistance [14]. This InGaAs layer is highly absorbing around 1.55μm. To overcome this issue, we replace the *p*-contact by a *p*++/*n*++ tunnel junction and add a *n*+ contact layer. A thorough study of the impact of this tunnel junction on the optical and the electrical properties of the microdisk lasers has been carried out in the PhD. thesis of J. Van Campenhout [1].

Layer	*Doping level (cm^{-3})*	*Thickness (nm)*	*Comment*
InP	5.10^{18}Si	95	*n*+-type bottom contact
InGaAsP	1.10^{18}Si	120	Q1.2 *n*-type
InGaAsP		25	Q1.2 spacer
InGaAsP		3 x 15	Q1.2 barriers
InAsP		3 x 6	QWs
InGaAsP		25	Q1.2 spacer
InP	5.10^{17} to 1.10^{18}Be	135	*p*-type
InGaAsP	2.10^{19}Be	20	Q1.3 *p*++-type
InGaAsP	1.10^{19}Si	20	Q1.3 *n*++-type
InP	1.10^{18} to 5.10^{18}Si	80	*n*+-type top contact

Table 2.1: Description of the epitaxial stack used for the fabrication of microdisk lasers

The bonding procedure can be divided into two phases. The first one is the preparation of the SOI and the III-V dies, while the second one is the bonding itself.

First, a solution of diluted DVS-BCB:mesitylene is prepared. The dilution will influence the thickness of the bonding layer. The SOI die is most of the time covered with photoresist deposited prior to dicing at imec or CEA-Leti. The substrate requires a preliminary cleaning procedure with acetone and isopropanol. This strips the resist of the SOI die, and simultaneously removes some particles from the dicing off the surface. We treat the surface of the SOI die further with a well-established organic cleaning recipe from the CMOS-industry,

the Standard Clean 1 (SC-1) solution ($NH_4OH : H_2O_2 : H_2O$) in the proportions 1:1:5. Werner Kern developed the basic procedure in 1965 while working for RCA (Radio Corporation of America) - hence the name RCA-clean 1 [15]. This treatment with the oxidizing ammonia solution results in the formation of a thin "chemical" silicon dioxide layer (about 10Å) on the silicon surface [16]. Without H_2O_2, the silicon would suffer a strong attack by the NH_4OH. Furthermore, NH_4OH complexes many multivalent metal ions (Cu^{2+}, Zn^{2+}, Ag^{+}) [17]. The efficiency of the SC-1 solution on particle removal has been quantitatively demonstrated [18]. At the alkaline pH value of SC-1 solution, most surfaces are negatively charged. Electrostatic repulsion between the removed particle and the oxide surface will then prevent particle redeposition.

Under a well-ventilated wet bench, we first pour 150mL of water in a teflon beaker. The water is heated up to 75°C. When the temperature is stable, we add 30mL of aqueous ammonia to the water. As the reaction between the two agents is endothermic, the temperature usually drops to 60°C. After getting it up back to 75°C, we finally add 30mL of peroxide to the mix. The temperature also drops and needs to be stabilized again to 75°C. Only then can the SOI die be immersed into the mix. Cleaning is effective after a minimum of 15 minutes in the solution [16]. However, when the contact of the wafer surface in the chemistry is extended, the wafer surface is being roughened by the etching effect of SC-1 [19]. The SC-1 solution should not be used longer than 30 minutes. The etching rate then dramatically drops as most active cleaning agents have been consumed in the chemical reaction.

During the 15 minutes needed to clean the SOI, the III-V is prepared for bonding. This combined cleaning procedure reduces the amount of deposited particles on top of the clean III-V surface. The epitaxial wafers for microdisk lasers are coated with two sacrificial layers : 100nm of InP and 100nm of InGaAs. Still under a well-ventilated bench, the first InP sacrificial layer is removed in a 37% aqueous solution of HCl. The first step of the chemical reaction involves a synchronous exchange of bonds. In-Cl and P-H bonds replace the original H-Cl and In-P bonds. Since the Indium and Phosphor atoms at the surface are triply bonded to neighboring atoms, two further bonds must be broken in an analogous manner to remove each atom from the lattice. Indium is therefore dissolved as hydrolyzed $InCl_3$ and PH_3 are released [20]. It is extremely important to etch InP in a well-ventilated wet bench to reduce the contamination of the working environment with Phosphine. The etching rate of InP in a pure HCl solution at room temperature is 5μm per minute [21]. In order to fully etch the InP layer and to remove as many particles as possible, the die is etched for 15 seconds.

The second sacrifical layer is etched with a solution of $H_2O : H_2SO_4 : H_2O_2$ in the proportions 1:3:1 [22]. As the reaction between the 96% aqueous solution of sulfuric acid and water is exothermic, we make sure the beaker is cooled to 20°C before we add the 30% aqueous solution of peroxide. The etching rate of the solution is in the order of several hundreds of nanometers per minute [23]. Only when the temperature is back to 20°C, the III-V die can be etched for 25 seconds and rinced for several minutes under running deionized water.

The SOI is rinced for several minutes under running deionized water in order to remove all remaining traces from SC-1. Inside a class 100 cleanroom dedicated to bonding, it is then very carefully dried on a hot plate to remove all traces of water. As reported by Dow Company itself, the DVS-BCB adhesion to III-V semiconductors (GaAs, InP) tends to be marginal, even with the use of AP3000 adhesion promotor. As with gold, it is best to avoid this interface and employ an intermediate layer (e.g., SiO_2 or Si_3N_4) to which DVS-BCB has good adhesion once an adhesion promoter is applied [24]. In order to enhance the adhesion of DVS-BCB on SOI, we spin-coat a thin layer of adhesion promoter AP3000 on top of all the samples in this PhD–work. The adhesion promotor is spin-coated at the same speed as the DVS-BCB layer and is not baked. The usual spin-coating procedure comprises a spreading step, lasting 5 seconds at 500rpm, followed by a spin-coating step of 40 seconds at 3000rpm.The effect of the adhesion promotor on the quality of the etching of the III-V as well as the effect of a post-bake of the AP3000 prior to the spin-coating of DVS-BCB are reported in the works of T. Spuesens [25] and S. Keyvaninia [26]. In our case, the DVS-BCB is spin-coated right after the AP3000 sequence to prevent it from drying. The dilution of the DVS-BCB is chosen so that the final bonding thickness does not exceed 250nm. After this, the SOI die is baked on a hot plate, for 5 minutes at 150°C, to evaporate mesitylene and to the stabilize the BCB film.

Two adhesive bonding techniques have been used to bond the III-V die on top of the SOI. One of them consists in manually placing and pressing the III-V die above the SOI design of interest after spin-coating the DVS-BCB. The disavantages of this method are multiple. First, as the pressure on the die is not uniform, the resulting thickness of the bonding layer will not be uniform under a single die and will vary from die to die. Also, the bonding is performed at atmospheric pressure, which means that air or evaporated mesitylene might form bubbles under the III-V that will jeopardize the quality of the bonding. The DVS-BCB bonded sample is then cured under a N_2 flow. The temperature profile starts at 150°C for 20 minutes. At this temperature, DVS-BCB is still in a liquid state (as can be seen in Figure 2.9) and can adapt to the topography of the

dies, filling the voids at the bonding interface. Subsequently, the temperature is slowly increased up to 280°C, with a ramp of 1.6°C/min. After reaching 280°C, the dies are kept at this temperature for 1 hour in a N_2 atmosphere, and then slowly cooled down to room temperature.

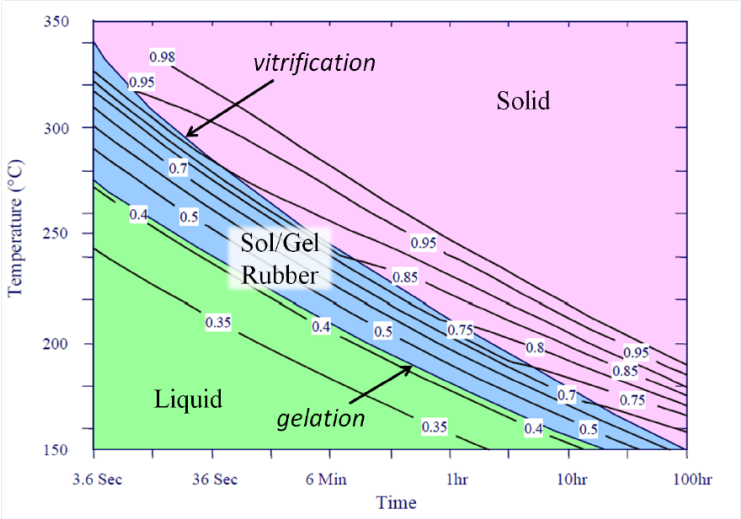

Figure 2.9: Degree of DVS-BCB polymerization and phase diagram, depending on curing time and temperature [27].

The second technique relies on machine bonding. After the pre-curing of the spin-coated DVS-BCB on a hot plate for 15 minutes at 180°C, the SOI die is mounted on a carrier wafer of the Karl Süss CB6L bonder and placed into the transport fixture. The III-V die is then positioned on top of the SOI design of interest, the transport fixture is loaded into the processing chamber of the wafer bonder and the bonding recipe is started. The temperature profile inside the chamber of the wafer bonder is identical to the one applied after manual bonding. Pressure on top of the III-V die is applied during the 20 minutes step at 150°C. At this temperature, the DVS-BCB is still in a liquid state and can accommodate to the topography of the dies, filling the voids at the bonding interface, while the bonding pressure is being applied.

After curing is finished, the bonded samples are in both cases cooled down to room temperature and finally unloaded from the processing chamber. Afterwards, the InP substrate is removed by complete wet etching in HCl(aq. 37%). We stress the fact that it is extremely important to etch InP in a well-ventilated wet bench to reduce the contamination of the working environment with phosphine. In the end, a thin III-V film with the functional layers is obtained, bonded to the SOI die, ready for further processing, as can be seen in Figure 2.10.

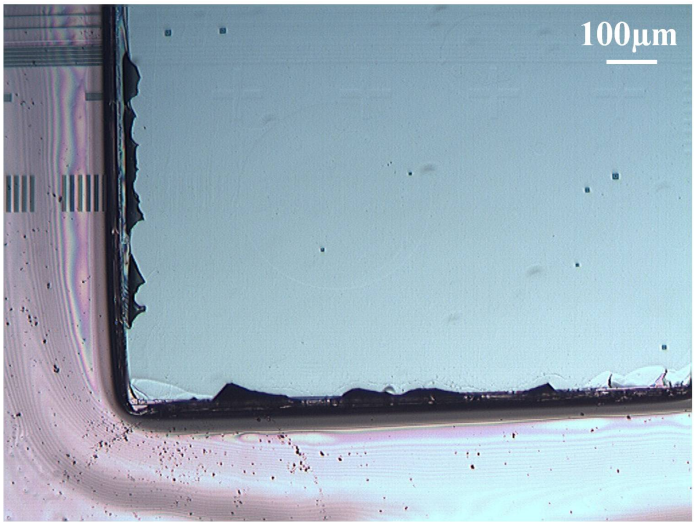

Figure 2.10: Thin III-V film bonded to SOI after substrate removal. Some defects are visible, and the underlying SOI design can be seen through the III-V layers.

2.3.3 Microdisk laser definition

Before any further post-processing, the 300nm-thick InGaAs etch-stop layer is etched using the same solution as previously mentioned: $H_2O : H_2SO_4 : H_2O_2$ in the proportions 1:3:1. A 300nm-thick SiO_2 or Si_3N_4 layer is deposited by Plasma-Enhanced-Chemical-Vapor-Deposition (PECVD). This layer acts as a hard mask for the definition of the microdisk lasers. A standard reversible photoresist AZ5214E is spin-coated on top of the sample to define the mesa of the microdisk lasers by contact lithography. The alignment of this first lithography step is made possible thanks to alignment markers etched in the SOI level. However, a misalignment of the microdisk laser vs. the underlying waveguide will influence the efficiency of the coupling of the light. As presented in section 2.5, we developed a process using electron-beam lithography to improve this alignment accuracy.

After the lithography, the hard mask is etched in a Reactive-Ion-Etching chamber with a SF_6/O_2 plasma. Before etching the III-V layers, the top surface of the epitaxy is cleaned from all particles from the hard mask opening and from a possible native oxide. The sample is etched for 1 minute in a solution of $H_3PO_4 : H_2O$ in the proportions 1:10. This cleaning procedure makes the III-V surface hydrophobic [28]. To reverse its polarity, the sample is dipped for 1 second in a 1% HF solution. The III-V layers are then etched in an Inductively-

Coupled-Plasma Reactive-Ion-Etching (ICP-RIE) chamber. The etching is not complete, and a 100nm-thick *n*+-doped InP layer is left to act as a bottom contact. The quality of the lithography and the ICP etching will determine the roughness of the sidewall of the microdisk. This damage is responsible for a large fraction of non-radiative recombinations. The alignment markers required for the alignment of all the consecutive layers are also etched in the III-V layers. Figure 2.11c is an image taken by Scanning-Electron-Microscope (SEM) of the sidewall of a microdisk laser after ICP etching at TU/e.

2.3.4 Bottom contact deposition

Before the deposition of the bottom metallic contacts, the III-V surface is cleaned from all particles and native oxide with a solution of $H_3PO_4 : H_2O$ in the proportions 1:10. Contact lithography is used to define the metallic bottom contact. The standard recipe for a contact taken on a *n*-doped InP layer in the Photonics Research Group consists of Ti/Pt/Au (40nm:50nm:100nm). Titanium has demonstrated a better adhesion to the *n*-doped InP layer [29]. Platina is used to prevent Gold from migrating to the III-V layers in high temperature steps and under an electrical bias [29]. The metals are deposited by thermal evaporation in a Univex chamber and removed by lift-off, as can be seen on Figure 2.11d.

2.3.5 Island definition

The next step consists in separating each microdisk laser from the next one. This process is called “island definition”, and is performed by etching the remaining 100nm-thick InP bottom contact layer with the ICP after a contact lithography (AZ5214E photoresist), as can be seen in Figure 2.12a. In this PhD. work, the standard fabrication procedure has been modified to allow deposition of the bottom metallic contact prior to island definition, which was not the case in previous works. This ensures the bottom contact is deposited on a flat III-V surface. The ICP etching recipe for island definition has also been optimized to prevent micromasking due to metallic particles.

2.3.6 Overcladding of the microdisk laser

The sample is overcladded with pure DVS-BCB spin-coated so that its thickness above the edge of the microdisk reaches 800 to 900nm. This is performed to electrically isolate the bottom contact from the top one. The DVS-BCB is cured under a N_2 flow following the same temperature profile as the one described in the bonding section.

2.3.7 Opening of vias in the DVS-BCB

In order to reach the bottom contact and to deposit the metallic top contact, vias in the DVS-BCB are defined by contact lithography. The vias are opened after etching the DVS-BCB in the RIE chamber. We etch under low pressure so that the etched sidewalls of the DVS-BCB layer are not straight but slightly inclined to facilitate metal deposition in the vias. First, the vias to reach the metallic bottom contacts are opened, but are not fully etched. A second contact lithography allows us to etch vias to the top InP contact layer and to fully etch vias to the metallic bottom contacts, and the results can be seen in Figure 2.12b. The vias to the top InP layer are intentionnally etched a little longer to remove all possible residue of DVS-BCB that could act as an isolator between the metallic contact and the III-V layers.

2.3.8 Top contact deposition

Before the deposition of the top metallic contacts, the III-V surface is cleaned from all-particles and native oxide in a 10 minutes long oxygen plasma cycle and followed by a solution of $H_3PO_4 : H_2O$ in the proportions 1:10. After a new contact lithography, the vias for the top contact are open. The sample is then loaded in a Univex chamber for thermal evaporation of the same metal recipe used for the bottom contact: Ti/Pt/Au (40nm:50nm:100nm). The top contact is also defined by lift-off, as can be seen in Figure 2.41a.

2.3.9 Metallic pads deposition

Electrical characterization of the sample requires thick metallic pads for probing. The samples are loaded in an electron-gun chamber where extra Ti/Au(40nm:800nm) pads are deposited and defined by lift-off, as visible in Figure 2.12d. After a first electrical characterization, a Rapid-Thermal-Annealing of the contacts can be performed for 15 seconds at 375°C.

In the course of this work, several optimizations have been made to the fabrication procedure of microdisk lasers. We report an improvement of the bonding yield, of the bonding thickness uniformity, a reduction of the contact resistance, an improvement in the heat dissipation in the cavity, and a new fabrication method for the definition of the microdisks.

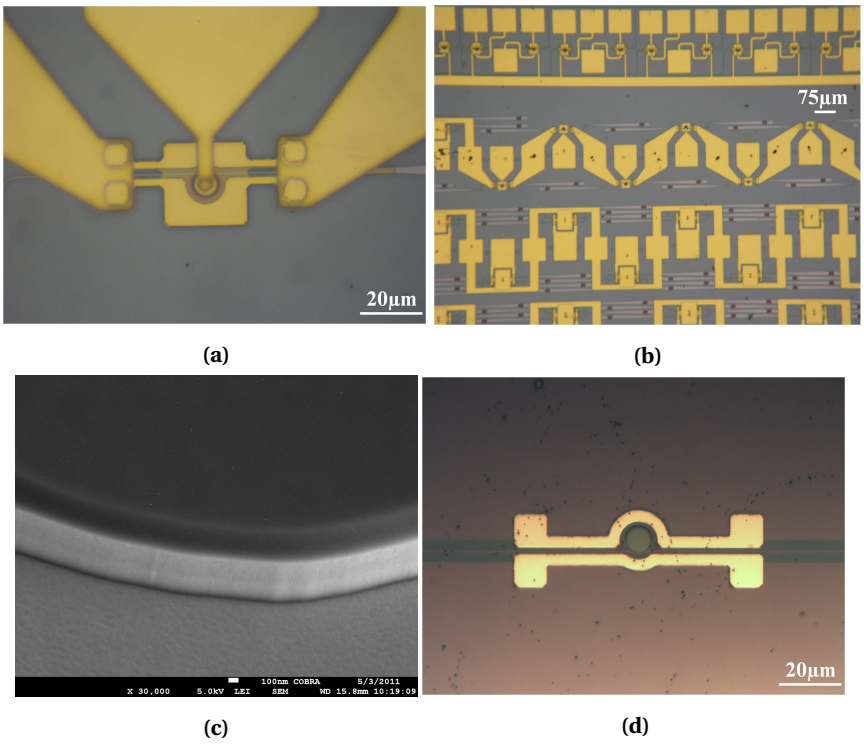

Figure 2.11: Optical microscope images of the density of integration of heterogeneously integrated microdisk lasers on a single chip. (a) Completed microdisk laser. (b) Metallic pads used for electrical characterization of the microdisk lasers. (c) SEM image of the sidewall of a microdisk laser etched with ICP in the clean-room of the Technische Universiteit from Eindhoven. (d) Optical microscope image of the metallic bottom contact definition.

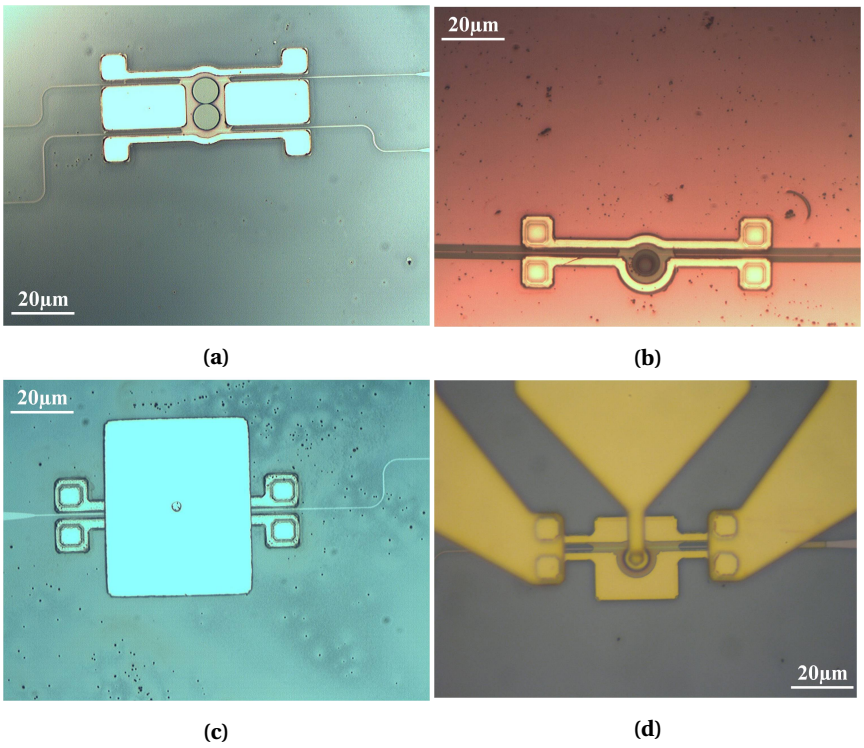

Figure 2.12: Optical microscope images of the density of integration of heterogeneously integrated microdisk lasers on a single chip. (a) Optical microscope image of the definition of the islands of the microdisk lasers. (b) Optical microscope image of the opening of the DVS-BCB vias to reach the bottom metallic contacts. (c) Optical microscope image of the definition of the top metallic contacts. (d) Optical microscope image of a completed microdisk laser.

2.4 Improvement of the bonding yield of III-V layers heterogeneously integrated on SOI

As explained in the previous section, defects from the epitaxy can jeopardize the yield of the bonding, or the quality of the III-V surface after substrate removal. Also, the adhesion of the bonding layer to the III-V material is of primary importance for a high bonding yield. As reported by Dow Company, the DVS-BCB adhesion to III-V semiconductors (GaAs, InP) tends to be marginal, even with the use of the adhesion promotor AP3000. As with gold, it is best to avoid this interface and employ an intermediate layer (e.g., SiO_2 or Si_3N_4) to which DVS-BCB has good adhesion once an adhesion promoter is applied [24]. Depositing a thin layer (10nm is enough) of SiO_2 on top of the III-V prior to bonding has significantly increased the bonding yield and the quality of the bonded layer. Figure 2.13 shows two images of two samples after bonding and substrate removal. The initial III-V dies are from the same wafer, are in both cases 6 x 6mm^2 and are bonded the same day, under the same process conditions. The sample from the right image is bonded without this extra oxide deposition on the III-V. The sample from the left image is bonded with oxide and is a perfect bonding: the initial III-V surface completely remains after substrate removal.

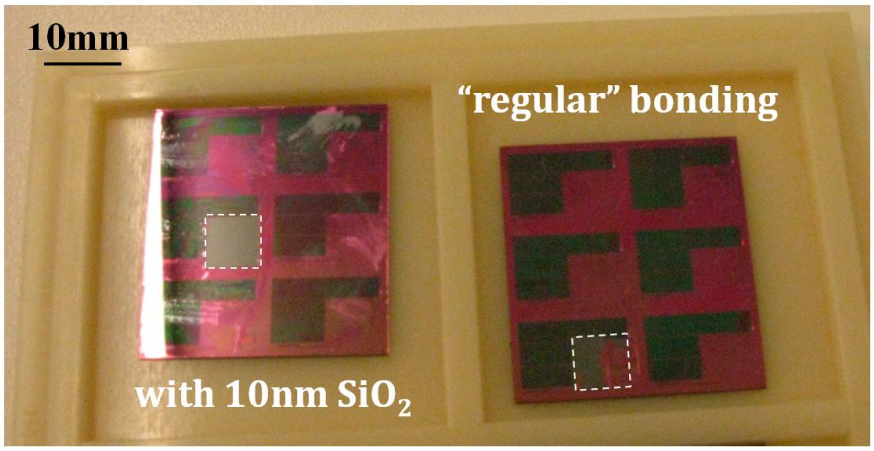

Figure 2.13: Drastic improvement of the III-V bonding yield with the deposition of a thin silica layer on top of the III-V prior to bonding.

In the course of this work, the deposition of a thin (10nm) or thick (150nm) layer of silica became systematic for all studied samples.

2.5 Improvement of the uniformity of the bonding layer thickness of III-V layers heterogeneously integrated on SOI

Effort has been put in improving the uniformity of the bonding layer thickness for the manual bonding method. Several samples from the same SOI design with air cladding have been bonded using different DVS-BCB:mesitylene solutions. The bonding thickness has then been measured using Focused-Ion-Beam (FIB) cross-sections on three different locations per die. An optimum dilution of DVS-BCB:mesitylene has been found for reproducibility from one die to another. The proportions 2:3 result in a uniform bonding layer with a thickness of 250nm. A more diluted solution resulted in air trapping under the III-V. Indeed, as can be seen in Figure 2.15, the spin-coated DVS-BCB does not fill the SOI trenches, and air is trapped under the III-V membrane.

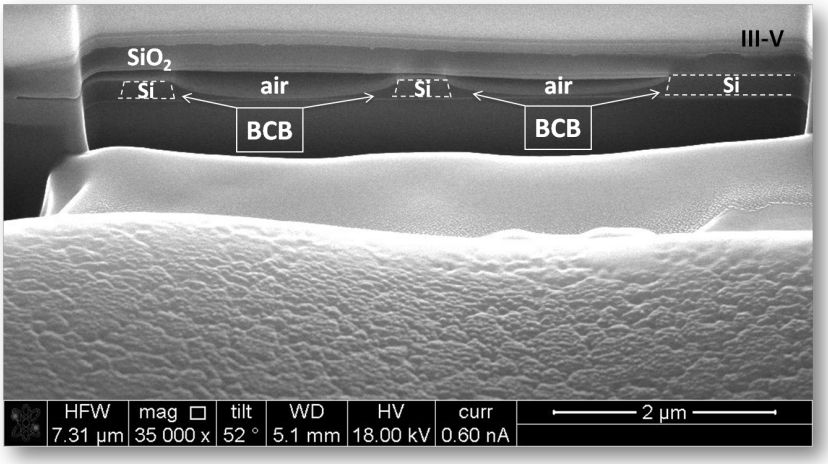

Figure 2.14: Failed bonding due to the presence of air under the III-V membrane after bonding. The DVS-BCB:mesitylene solution is too diluted and does not fill the trenches of the air cladded SOI sample.

To avoid performing this systematically on each SOI-substrate, the wafer bonder (Karl Süss CB6L) has also been used. SEM images of FIB cross-sections of samples bonded with the machine demonstrate that a 120nm-thick DVS-BCB bonding layer is uniform on the same die, and can also be reproduced from one die to another. Figure 2.15 is a SEM image of a sample where 100nm of SiO_2 has been deposited on the III-V prior to bonding.

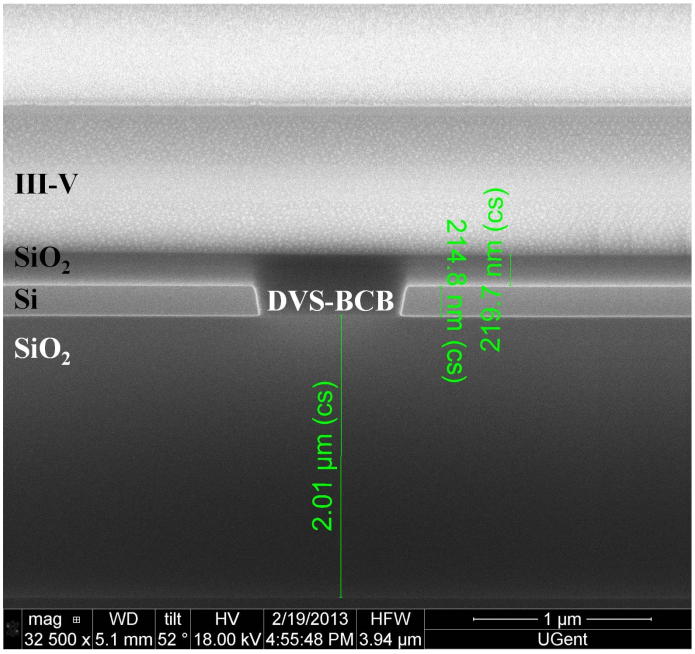

Figure 2.15: SEM image of a FIB cross-section of a device where a 100nm thick SiO_2 layer has been deposited prior to bonding with the wafer bonder. The measured total bonding thickness is then 120nm.

2.6 Improving the definition of microdisk lasers with contact lithography

In the previous section, the standard fabrication process for microdisk lasers relies on the reversible AZ5214E photoresist. The positive AZ-ECI photoresist has been designed to have superior implant and dry etch resistance. Further characterization shows strong adhesion and good thermal stability. It is also a family of photoresists with high resolution capabilities (0.4μm critical dimensions in production). Figure 2.16a illustrates that the diameter of the microdisk lasers after fabrication with the reversible AZ5214E photoresist is wider than the target design. Indeed, the designed microdisk had a diameter of 10.16μm, but the SEM image of a FIB cross-section performed along a diameter of the microdisk indicates that the diameter is actually closer to 10.78μm. The offset of the edge of the microdisk vs. the underlying waveguide is now 220nm larger than designed value on one side of the device and 486nm larger than the designed value on the other side (Figure 2.16b). This leads to a low coupling efficiency of the laser emission from the microdisk to the waveguide.

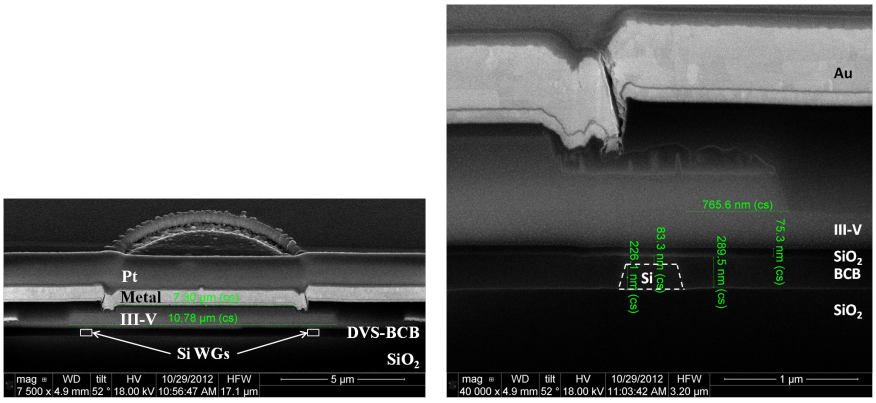

(a) **(b)**

Figure 2.16: Larger diameter of a microdisk laser after processing compared to the design. (a) SEM image of a FIB cross-section: the diameter of the microdisk is 0.6μm larger than the designed diameter. (b) SEM image of a FIB cross-section: the offset of the edge of the microdisk vs. the underlying waveguide is now 486nm larger than designed value.

A new process has then been developed to use the ECI photoresist. The sidewall of the ECI photoresist after baking is smoother than the one of the AZ5214E. This will transfer less roughness to the hard mask and consequently to the III-V layers. Figure 2.17 illustrates that after III-V etching, the diameter of the microdisk is closer to the designed value. Indeed, from top view with the SEM, we measure a diameter of 7.38μm while the targeted value was 7.5μm. Improvement of the post-exposure baking time could help us achieve even better results.

2.7 Improving the definition of microdisk lasers with electron-beam lithography

As discussed in chapter 1, the first basic requirement for logic gates is cascadability, i.e. the number of identical gates or logic blocks that can be concatenated without losing signal integrity. The output of one stage must be in the correct form to drive the input of the next stage. In optics, the output and input wavelengths, beam shapes and pulse shapes should be compatible. Another challenge lies in improving the fan-out, i.e. the number of identical devices which can be driven from one device. This requires a wavelength match between several cascaded microdisk lasers.

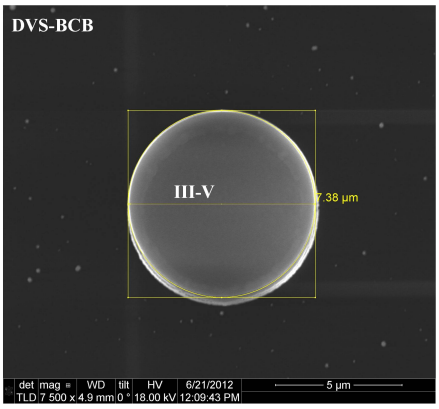

Figure 2.17: SEM top view of a microdisk fabricated with positive ECI photoresist.

In the previous section, we highlighted that the microdisk definition in itself holds most of the challenges of this fabrication. The contact lithography process does not allow us to reproducibly control the alignment between the edge of the microdisk and the edge of the underlying SOI waveguide. Also, the diameter of a microdisk processed with contact lithography is likely to differ from the designed value.

This section presents an alternative to the use of contact lithography. Within the collaboration between the Photonics Research Group of Ghent University and the Laboratoire de Photonique et Nanostructures (LPN) in Marcoussis (France), an electron-beam lithography process has been developed for microdisk lasers heterogeneously integrated on SOI. We report the fabrication procedure, and the excellent results obtained in terms of standard deviation in lasing wavelength of nominally identical devices.

2.7.1 State of the art in lasing uniformity

The mature CMOS fabrication technology makes large-scale integration of functional optical devices on SOI possible. Purely passive features on SOI, such as guiding and filtering, have already been demonstrated [30]. However, the parameters of on-chip nanophotonic structures are sensitive to fabrication-induced process variations across the die. Studies have addressed the reliability challenges that arise from this sensitivity to variations [30], [31]. Even in the tailored process technology of the SOI platform, the uniformity of ring resonators closely placed to one another is of the order of 0.5nm [30].

The uniformity of the lasing wavelength of several laser configurations has been investigated in the past in order to demonstrate an accurate control of the semiconductor source wavelength. These results are useful for applications such as wavelength-division multiplexing (WDM). WDM requires laser sources with wavelengths closely aligned to the passband of demultiplexing optical filters at the receiver end. A common and simple strategy for meeting this demand is the use of wavelength-stabilized discrete sources and passive demultiplexing filters [32]. A 0.59nm standard deviation in the CW lasing wavelength at 20°C has been reported for 1.3μm AlGaInAs-InP monolithic laser arrays with low-pressure MOVPE grown strained multiple-quantum-well active regions [33]. The uniformity is attributed to the homogeneous growth of MOVPE. A study of the wavelength uniformity of a hundred unmounted 1.3μm distributed Bragg reflector (DBR) lasers has also been reported under 1μs pulsed operation [34]. A standard deviation in lasing wavelength of 0.27nm has been demonstrated across the wafer, indicating good thickness and compositional uniformity of the crystal growth. A multiple-wavelength distributed feedback laser diode (DFB-LD) array, with precisely controllable wavelengths is a very attractive light source for use in WDM systems. The use of electron-beam lithography for the definition of the grating pitch allows reaching a standard deviation as low as 0.37nm across 2-inch wafers [35]. The deviations in threshold current and in maximum output power of DFB lasers coupled to SOI have been reported [36]. A strong effort on optimizing the lasing uniformity has been carried out in the field of Vertical-Cavity Surface-Emitting Lasers (VCSELs) [37]. VCSELs make useful light sources in WDM systems because of their two-dimensional array configuration, single-mode operation, and precisely controlled lasing wavelength. Uniform 1.5mW light output of monolithically integrated four-wavelength VCSEL arrays fabricated by molecular beam epitaxy (MBE) was achieved under CW operation at room temperature [38]. A standard deviation in lasing wavelength ranging from 0.27 to 0.38nm for 5x6 arrays of four-wavelength VCSEL units (10 x 12 VCSELs) lasing between 927.4nm and 942.9nm has been demonstrated. This standard deviation can be explained by the natural nonuniformity of MBE thickness over the wafer. A hybrid integration technique based on flip-chip has also been proposed. In this case, each VCSEL is individually prepared by MBE growth and is arrayed by flip-chip bonding. Table 2.2 summarizes the mentioned demonstrations of accurate control of the semiconductor lasing wavelength. Uniformity in lasing wavelength has not yet been reported for heterogeneously integrated laser diodes on SOI.

Even though the fabrication process reported in the previous section already includes several optimizations, contact lithography does not allow us to repeatibly align the edge of the microdisk vs. the edge of the underlying waveguide. As a consequence, the coupling efficiency of the laser emission of nominally

Laser	*Pump*	*Lasing wavelength*	*Standard deviation*	*Technology*
Monolithic lasers	CW	1.3μm	0.59nm	Arrays;MOVPE
DBRs	Pulse	1.3μm	0.27nm	100 lasers
DFB-LDs	PL	1.3μm	0.37nm	2-inch wafer;EBL
VCSELs	CW	927-942nm	0.27-0.38nm	flip-chip

Table 2.2: State of the art on the accurate control of the semiconductor lasing wavelength.

identical microdisk lasers belonging to the same SOI die varies. Also, for digital all-optical signal processing applications, the lasing wavelengths from multiple microdisks must be very accurately controlled. In order to increase the cascadability of the all-optical system, the wavelengths of the microdisk lasers must be aligned to each other. The design and optimization of a semiconductor microdisk laser is critically dependent on the quality-factor of resonant optical modes as well as the spectral and spatial overlap of these modes with the active medium. A theory for quantitative analysis of microdisk laser emission spectra is presented in [39]. While this approach does not allow for an assessment of the bending loss, it is useful to obtain approximate field profiles. The boundary condition results in the resonant frequencies expressed in equation 2.1,

$$\lambda^{LM} = \frac{2\pi}{X^{LM}}.n_{eff}R \tag{2.1}$$

where X^{LM} is the L-th zero of the Bessel function of the M-th order J_{M}. According to equation 2.1, the lasing wavelength of a microdisk laser is related to the effective index and the radius of the device. Uniformity of the lasing wavelength hence depends on deviations in both disk diameter and effective index, the latter being dependent on temperature, layer thicknesses, etc. The diameter of the device is directly influenced by process conditions. To some extent, it is possible to control the lasing wavelength of the microdisks by processing the devices with high accuracy patterning tools, e.g. electron-beam lithography. In this work, we study the room temperature and continuous wave laser emission of InP-based microdisk lasers, fabricated using electron-beam lithography, heterogeneously integrated and evanescently coupled to SOI waveguides. The microdisks are optically pumped from the waveguide or from the top surface. The laser emission is then collected with an optical fiber out of grating couplers etched at the edges of the silicon waveguide. We report the first investigation of the lasing wavelength uniformity of microdisk lasers integrated on the same SOI die. We demonstrate that nominally identical devices lase within a range of 500pm from one another.

2.7.2 First generation of electron-beam defined microdisk lasers

LPN carries out its research activities within the general context of nanosciences, at the cross-roads of quantum optics and electronics, of physics, chemistry and biology, of materials science and device physics. LPN develops the new technologies and the concepts that will initiate innovation both in fundamental and in applied science. Their expertise in the technology of semiconductors and photonic devices relies on excellent fabrication facilities. LPN has a large clean-room of 1000m^2 (700m^2 (class 100/1000)+ 300m^2 epitaxy(class 1000/10000)+ 150m^2 (technical areas)) belonging to the Renatech French national nanofabrication network providing all the necessary tools for the fabrication research and development in micro- and nano- technologies. The research groups in LPN have the technological expertise to develop and optimize ultimate dimension electron-beam lithography processes. Electron-beam lithography (e-beam lithography or EBL) is an essential step for direct writing of nanostructures in the 10-500nm range and for optical mask fabrication. The electron-beam writer is mainly used for direct writing. Advanced processes have been developed for direct writing of nanostructures in PMMA, AZ resists, ZEP520 resist, as well as the negative ma-N 2400 resist.

In the course of this PhD. work, several generations of microdisk lasers have been fabricated using EBL at LPN. The samples are bonded in the clean-room of the Photonics Research Group of Ghent University, and are further processed in LPN for the microdisk definition. Depending on the generation of devices, the hard mask is etched in LPN, at Ghent University, or at the Technische Universiteit Eindhoven (TU/e). The ICP etching of the III-V layers is also performed either in LPN, at Ghent University or at TU/e depending on the generation of devices. The e-beam writer from LPN is a VISTEC EBPG 5000+, purchased in 2003. Here are a few technical specifications from this industrial e-beam writer:

- Thermal field emission gun;
- Acceleration voltage: 20kV, 50kV and 100kV, mainly operating at 100keV;
- Minimum spot diameter: <10nm at 100keV;
- Beam current: 130pA or 200nA;
- Automatic laser focusing for height measurement;
- Interferometric stage positioning with an accuracy: $\lambda/1024$=0.60nm;
- Field stiching accuracy: <30nm;
- Two level superposition accuracy: <30nm;
- Sample sizes: 35mm, 2 , 4 wafers, optical masks 3 and 4;
- Automatic 10-holder airlock for batch processing of multiple substrates;
- Field size : 160x160μm to 1000x1000μm;
- Writing frequency : 25MHz, can be speed up to 50MHz.

The pattern to expose is coded into a GDS-II file generated from a python script with the IPKISS library. Using predefined objects from the library, the patterns (holes, trenches, etc) are written as a combination of more or less complex polygons. The GDS-II is then converted into a procedure file that command the e-beam writer to expose only the areas that will not subsequently be etched. A drastic improvement of the pattern precision of the e-beam writer has been achieved in the course of the PhD of Alexandre Bazin from LPN [40]. One detected flaw at the beginning of this work was the faceting visible on the GDS-II file when the coding resolution of the IPKISS library (used to generate the GDS-II file) was not set low enough. Figure 2.18 shows an example of this facetting on a disk shape and also shows the corrected shape when the meshing resolution was decreased down to 10pm.

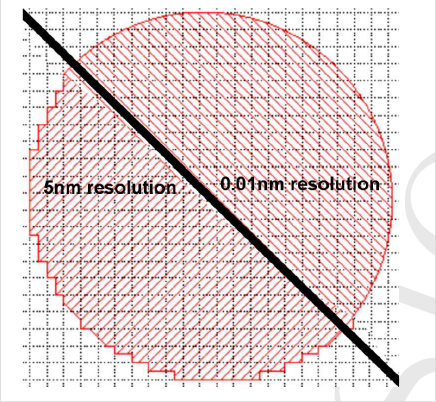

Figure 2.18: Correction of the resolution of the GDS-II code read by the electron-beam writer during exposure to avoid facetting of circular shapes [40].

Figure 2.19 is a block diagram of the e-beam column. The position of the stage inside the e-beam writer is monitored by interferometry, and the accuracy of the position of the stage is as good as 0.60nm. On top of this interferometric monitoring, an exact copy of the writing stage of the e-beam writer can be found outside the machine. The software of the e-beam writer is connected to the software of the microscope positioned above the second stage. The operator can then align the sample as good as possible on the second stage, and accurately note the coordinates of the markers used for the alignment of the design. The sample is loaded on a wafer cassette.

The alignment procedure of the microdisks vs. the SOI circuit inside the e-beam writer is done by a semi-automatic procedure. The e-beam lithography system is set to use markers made at the SOI level to precisely define the

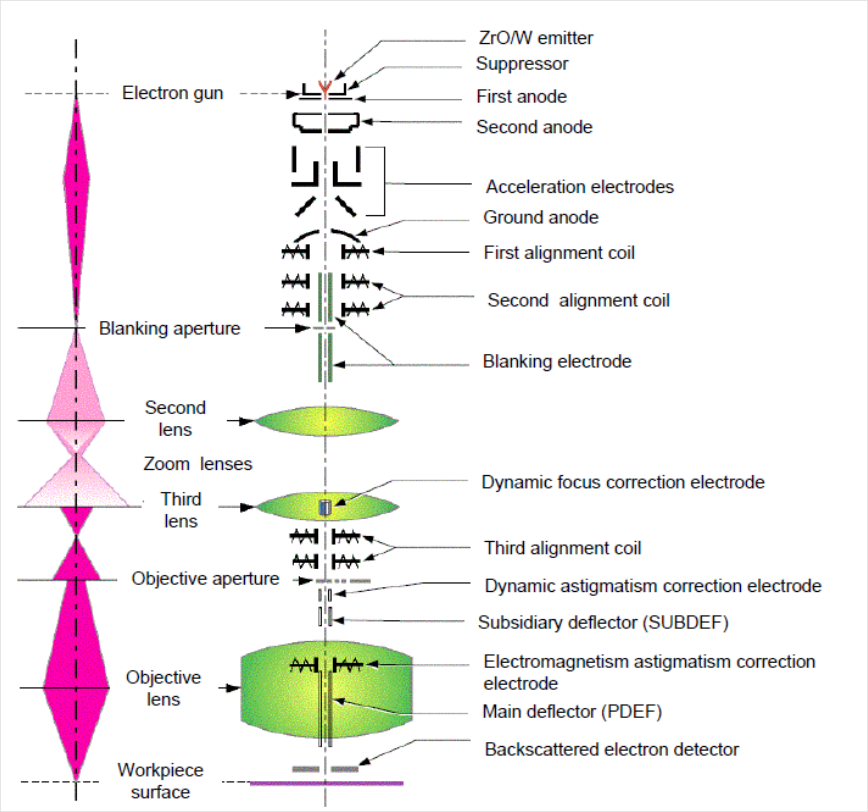

Figure 2.19: Schematic description of the elements of the column of the e-beam writer [41].

reference frame of coordinates used for the alignment of the III-V structures. A centre position of the SOI circuit is defined by detecting at least three markers etched in the SOI. In order to align the microdisks with the waveguides, the rectangular GDS-II pattern includes four markers located at the four edges of the pattern. After optimization of the configuration of exposure and of the geometry of the markers [42], the best option lies in using 10 x 10 μm^2 squares etched through the 220nm Silicon and the 2μm-thick SiO_2 layers. The markers define a center that the e-beam writer identifies as the one of the SOI level. Using this procedure, the e-beam writer can position all the microdisks vs. the waveguides maximum 30nm off the design value, correcting for translation and rotation errors [43]. Between two consecutive exposures, the e-beam writer will automatically correct its alignment after reading again the coordinates of the three markers at the level of the SOI. The machine will offer the possibility to

the user to check the position of the e-beam writer through SEM visualization. Figure 2.20 illustrates that inside the e-beam writer, the beam size spot on the sample will change depending on its position. Intuitively, the smaller the spot, the higher the writing resolution. The SEM can then be used to manually improve the heigth focus.

After substrate removal, the 300nm-thick etch-stop InGaAs layer is etched with the solution $H_2O : H_2SO_4 : H_2O_2$ in the proportions 1:3:1. The markers from the SOI are masked by the bonded III-V layer and the DVS-BCB on top of the SOI. The multilayer semiconductor/dielectric stack is prone to charging, as the DVS-BCB is a very efficient insulating layer. To be able to detect the markers with the SEM, the contrast between the non-etched and the etched surfaces need to be enhanced. We also should remove the DVS-BCB layer around the alignment marker in order to reduce a charging effect under SEM inspection. A preliminary processing step is then needed to "reveal" the markers. The process is described in Figure 2.21.

A layer of AZ9260 photoresist is spin-coated on the sample and then soft-baked on a hot plate at 110°C for 7 minutes and 30 seconds. The sample is then exposed for 2 minutes with a broadband (310-450nm) Mercury-vapour ultraviolet lamp (through a metallic mask to define 500μm-wide trenches). The exposed photoresist is developed with a solution of AZ400K:H_2O in proportions 1:4. The membrane and the bonding layer are then completely etched inside the trenches. Successive wet etch steps with HCl and $H_2O : H_2SO_4 : H_2O_2$ are used to remove the InP and the InGaAs(P) layers respectively. The silica or alumina layer used for bonding is etched during 8 minutes with an ammonium fluoride (AF) solution. The cured DVS-BCB is removed with Reactive-Ion-Etching (RIE) using a Sulphur/Hexafluoride/Oxygen (SF_6/O_2 plasma). A good contrast in the e-beam detection of the markers is obtained after a full etch in the marker of the 2μm thick BOx layer (25 minutes in ammonium fluoride). It is then the abruptness of the edges of the etched markers that ensures a correct measurement of the position of their center. Figures 2.22 are optical microscope images of the SOI markers covered by DVS-BCB and the epitaxy (left) and of the SOI markers after "opening" (right).

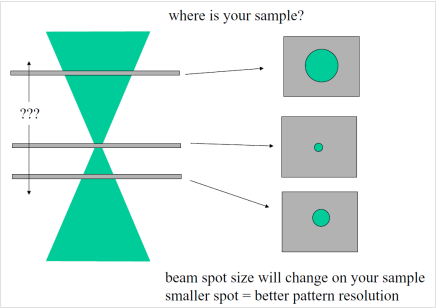

Figure 2.20: Resolution of the electron-beam writing depending on the focus heigth [41].

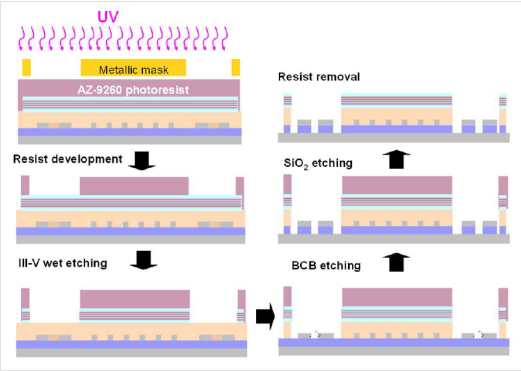

Figure 2.21: Process flow for the preparation of the sample before electron-beam lithography: enhancing the contrast of the SOI alignment markers [40].

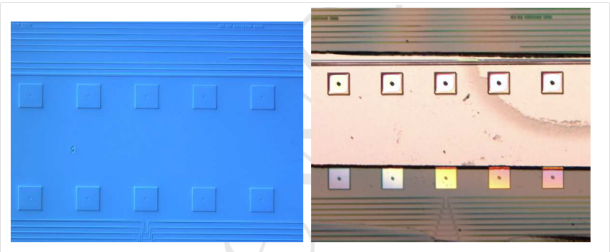

Figure 2.22: SOI alignment markers covered with DVS-BCB and III-V (left). SOI alignment markers after etching to enhance their contrast (right) [40].

2.7.3 First generation of electron-beam processed samples

After the cleaning of the SOI alignment markers, a 300nm-thick Si_3N_4 mask is deposited on top of the epitaxy by Plasma-Enhanced Chemical-Vapor Deposition (PECVD) to act as a hard mask. This layer also protects the DVS-BCB and underlying silicon waveguides in the following processing steps.

The first generation of devices were processed with a positive photoresist, polymethyl-methacrylate (PMMA), spin-coated on top of the Si_3N_4 layer. The process flow with PMMA was the first one developed at LPN for the fabrication of InP pillars, and so far the one with the best results in terms of resolution of processed structures, sidewall roughness, etc. In the case of a positive photoresist, the exposed surface of the resist is removed in the developer, while the non-exposed area remains. In the case of microdisk lasers, the exposed shapes are the disks themselves, which implies that after exposure of the PMMA, the disks would become holes. We need to develop a two-steps process to define disks instead. This is illustrated in Figure 2.23.

The concept relies on exposing a disk or a ring in the 430nm-thick PMMA layer. After a soft bake and 30s of development in AZ400K, the sample is covered in PMMA except where the disk or the ring is defined. The sample is then loaded for metal deposition. A thin layer of Nickel (40nm) is deposited and lifted-off in a bath of Trichloroethylene. The disk or ring is then defined in Nickel on top of the hard mask. Next, the pattern is transferred to the Si_3N_4 layer in the RIE in LPN and the Nickel mask is removed with HNO_3/H_2O. Figure 2.24 is a SEM image (top view) of the sample after the hard mask opening and the Nickel removal. The edge of the Si_3N_4 layer is covered in metallic particles that were re-deposited on the sample during the RIE etching.

Finally, the III-V layers are etched at the Technische Universiteit Eindhoven (TU/e) with Inductively-Coupled-Plasma (ICP). The recipe is based on a CH_4/H_2 chemistry. The III-V is etched during 1 minute-long cycles using 30sccm of CH_4 and 10sccm of H_2 under 200W of ICP power and at 60°C. Each etching cycle is followed by a descum cycle of 10 seconds. The ICP power is kept constant, as well as the temperature, but the cycle is based on 40sccm of O_2. Pearton [21] describes that the CH_4/H_2 chemistry was introduced to overcome the limitations of Chlorine mixtures for In-containing compounds [44]. The role of the CH_4, is to remove the group III species (A) as $(CH_3)_mA_n$ type compounds, while the H_2 removes the group V species (B) as BH_3. This mixture etches all III-V materials at a slow rate, but with very smooth morphologies. The etch rate can be increased by replacing CH_4 with C_2H_6, C_3H_8 and other hydrocarbon gases, and at low biases, the addition of Ar also aids the etch rate by providing more ion-enhanced removal of the etch products. The CH_4/H_2 discharges are remarkably forgiving of the presence of water vapor, which actu-

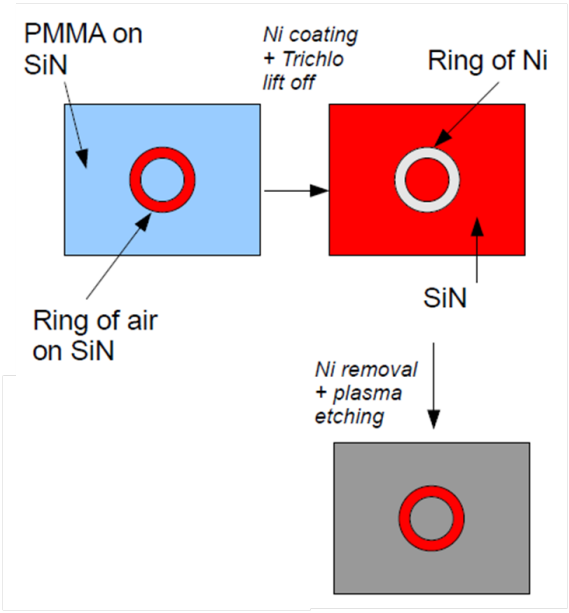

Figure 2.23: Process flow for the first generation of devices fabricated with electron-beam lithography.

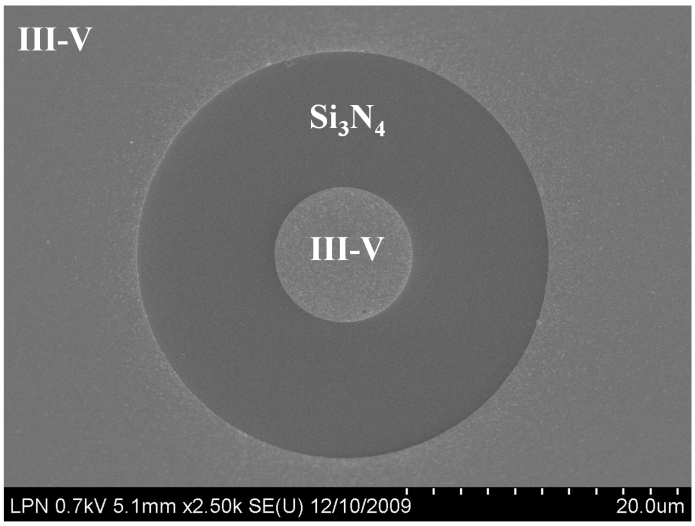

Figure 2.24: SEM image (top view) of the hard mask of the first generation after RIE etching (disk of Si_3N_4 on top of III-V). Metallic particles from the Nickel mask were re-deposited on the sample.

ally enhances dissociation of the gases. The major drawback is the deposition of polymer within the reactor chamber. This can be very heavy at high pressure (>20 mtorr) or high CH_4 flow rates. Under most conditions the polymer can be removed by O_2 plasma cleaning after each etching run. The ratio of CH_4 to H_2 must be kept between 0.1-0.4 to prevent excessive polymer deposition at the high values and preferential loss of the group V species at the low end of the range [45], [46].These effects lead to rough surface morphologies.

Both the RIE and the ICP recipes are standard processing steps, optimized to reduce the roughness of the etched sidewalls. Figure 2.25 is a SEM image of the sidewall of a processed microdisk. The roughness of the metallic mask transferred to the hard mask, and consequently to the III-V layers. Such microdisk was not further processed.

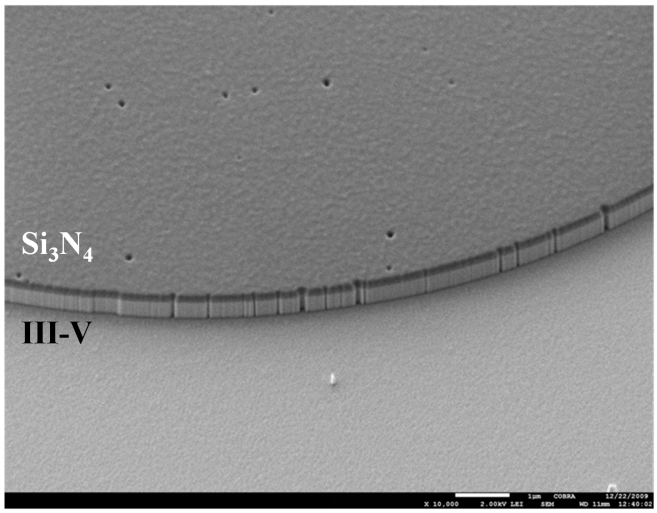

Figure 2.25: SEM image of the sidewall of a microdisk from the first generation: the sidewall roughness is due to the metallic lift-off used for the shape definition.

2.7.4 Second generation of electron-beam defined microdisk lasers

Another alternative to processing microdisks with PMMA is to modify the original design. Instead of exposing the microdisk itself, we expose a rectangular shape in which we open a ring or a disk. Figure 2.26 schematically depicts the process flow of the second generation of devices. The pattern is exposed in the PMMA. After development, the sample is etched with RIE. The microdisk is then a disk of Si_3N_4 on top of the III-V layers, as can be seen in Figure 2.27.

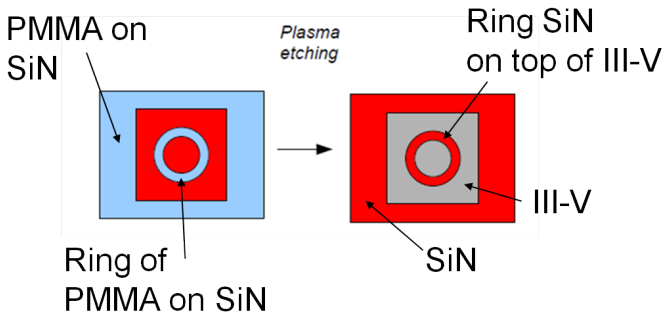

Figure 2.26: Process flow for the second generation of devices fabricated with electron-beam lithography.

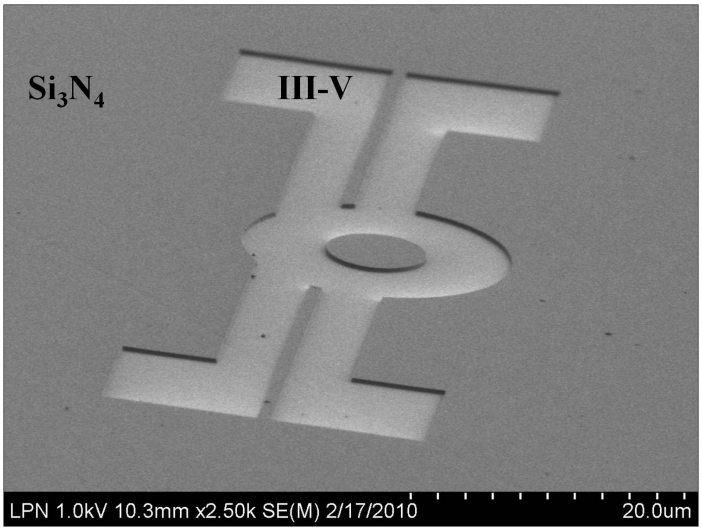

Figure 2.27: SEM image of the hard mask of the second generation after RIE etching (disk of Si_3N_4 on top of III-V).

However, the Si_3N_4 layer remains everywhere around the rectangular exposed shape. This hard mask needs removing for further processing. A contact lithography is then performed in the clean-room of Ghent University and a rectangular structure (smaller than the e-beam exposed one) is covered in photoresist. The remaining hard mask is further etched with the RIE of TU/e, and the III-V layers are also etched with the ICP of TU/e. Under SEM inspection, it is clear that the sample cannot be further processed. Because of micromasking during the contact lithography, pillars of III-V of a few hundreds of nanometers high remain after the ICP etching, as can be seen in Figures 2.28a and 2.28b. Not

only are they present at the edges of the design (Figure 2.29), but they are also present a few nanometers away from the sidewall of the microdisk. This makes further processing impossible. However, the roughness of the sidewall of the disk itself is reduced compared to the first generation.

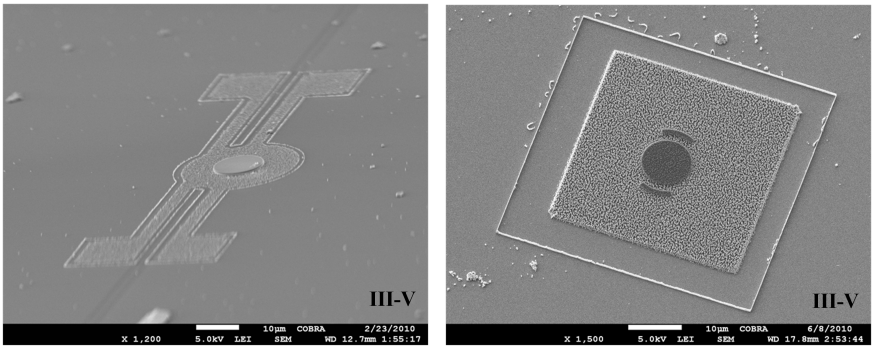

(a) **(b)**

Figure 2.28: SEM image of the sidewall of a microdisk from the second generation: micromasking during the hard mask removal prevents further processing.

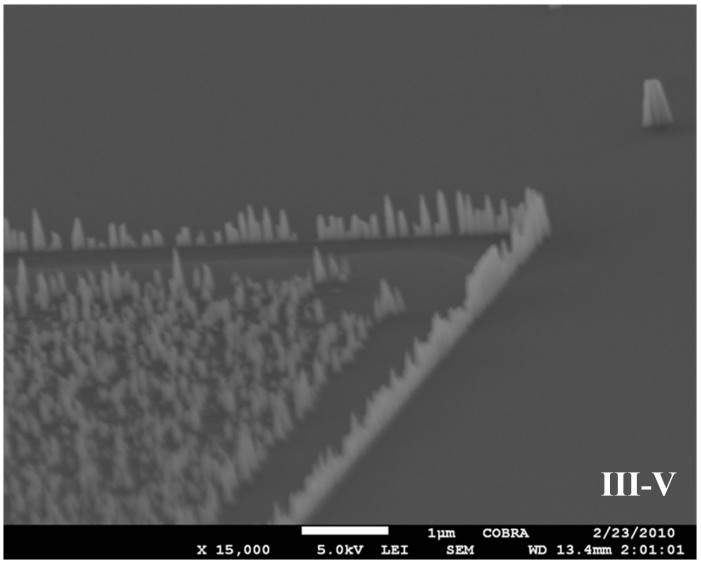

Figure 2.29: SEM image of the III-V pillars at the edges of the design due to micromasking during hard mask etching.

2.7.5 Third generation of electron-beam defined microdisk lasers

Eventually, a process based on a negative resist has been developed for microdisk lasers. In the case of a negative resist, the exposed surface of the resist solidifies while the rest of it is removed with the developer. This implies that the design just consists of microdisk shapes that will be exposed and will remain. It is then possible to pattern microdisks into the bonded InP material in one single e-beam exposure.

A 300nm-thick layer of the negative ma-N 2410 resist is spin-coated on top of the 300nm-thick Si_3N_4 hard mask. The best results were obtained when the microdisks were written with a resolution of 2.5nm. With this resolution, it only takes 4 minutes to expose 50 disks of diameters between 6 and 10μm. As mentioned in the description of the standard fabrication process in the previous section, alignment markers for the following processing steps are defined at the same level as the microdisk lasers. However, the size of the alignment markers is usually in the hundreds of μm^2 range. Exposing the markers with a resolution of 2.5nm could require several hours of exposure. Therefore, the design of the e-beam pattern is split into two different files. The first design only contains the microdisk lasers and will be exposed with a 2.5nm resolution, while the second design contains alignment markers, and will be exposed with a 20nm resolution (already 8 minutes exposure). The two exposures are consecutive and the e-beam writer automatically corrects his position in-between. After development (1min in pure MIF726), the hard mask is etched in LPN with a SF_6/CHF_3 plasma (Figure 2.30a), and the III-V layers are etched at TU/e. To avoid reflow during the subsequent high temperature steps the ma-N is then removed in a RIE dry etch organic cleaning process. Figure 2.30b is a SEM image of the microdisk laser. The roughness of the sidewall is greatly improved, and the sample is clean of pillars or micromasking. A facetting is visible, but this problem has been solved when the resolution of the GDS-II file has been lowered down to 10pm.

Figure 2.30c is a SEM image of the sidewall of a microdisk from the third generation for which the hard mask and the III-V layers have been etched at Ghent University. The roughness of the sidewall of the microdisk is worse than when the microdisk is etched at TU/e. Some etched material is re-deposited along the sidewall of the device.

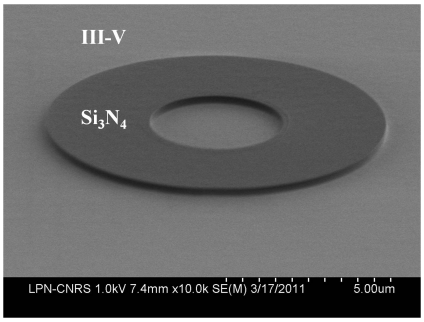

(a)

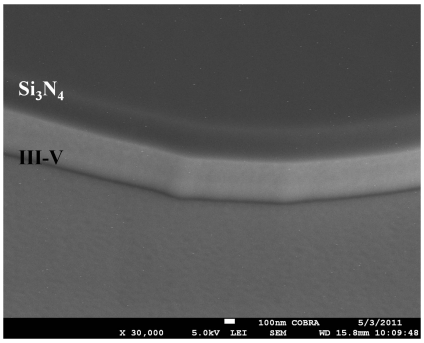

(b)

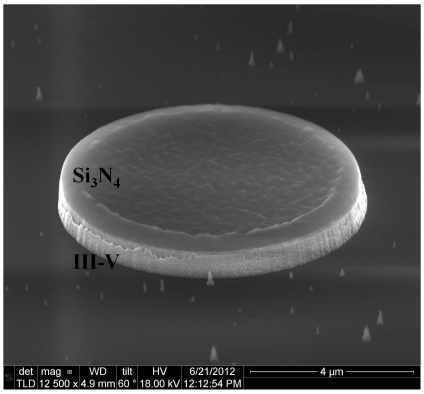

(c)

Figure 2.30: (a) SEM image of the etched hard mask of a microring from the third generation. (b) SEM image of the sidewall of a microdisk from the third generation etched at TU/e. (c) SEM image of the sidewall of a microdisk from the third generation etched at Ghent University.

2.8 Improving the etching of the III-V by Inductively-Coupled-Plasma in LPN

As mentioned in the introduction of this chapter, the process flow for the samples with microdisks is split between three clean-rooms. The bonding is performed at Ghent University, while the e-beam lithography is done in LPN. The hard mask can be opened in LPN, at Ghent University or at TU/e. The III-V layers are etched either at Ghent University or at TU/e. The main reason that the etching of the III-V layers is not performed in LPN after e-beam lithography is that LPN developed III-V etching recipes for samples on which the III-V etch is complete, where no bottom contact should be left. Finally, the metallization steps are performed at Ghent University. In order to avoid these successive commutations, the III-V Reactive-Ion-Etching (RIE) recipes available at LPN have been tested on samples from the third generation. The principle of Reactive-Ion-Etching is presented in appendix C.

The first etching test is performed in a RIE chamber with a recipe based on Chlorine. As visible on Figure 2.31a, the Si_3N_4 hard mask and the InP chemically react with the Chlorine. The sidewall is tilted under a large angle. The surface becomes very rough with more Chlorine in the discharge because of increasing In-enrichment of the surface. One can enhance the volatility of the Indium Chlorides by heating the sample above 130°C to promote desorption, but this is not always a practical solution, as reported in [47]. The sidewall roughness as well as the chemical redeposition prevents us from further processing.

The second etching test is performed with ICP in LPN. The recipe is based on HBr. SEM images of the etched microdisk before hard mask removal (2.31b) and after hard mask etching (2.31c) are presented. A periodic pattern along the sidewall of the microdisk after hard mask removal prevents us from further processing.

A final etching test is performed on samples from the third generation. The pattern from the hard-mask is transferred to the InP-based layer by ICP dry-etch process with a Cl_2/H_2 gaseous source [48]. This etching process was developed at LPN for deep-etching (>5μm) InGa(Al)As/InP heterostructures in order to obtain smooth and vertical sidewalls with no undercut. This high-aspect-ratio etching is possible because of the good anisotropy of the etching mechanism. Bouchoule et al. [49], [50] demonstrated that this anisotropic etching was due to the surface passivation of the sidewalls which are deposited with a thin silicon oxide layer during the etching using a Si cathode. This has also been observed during ICP etching of GaAs using a chlorine-based plasma in presence of Si(cathode). It has been shown that an addition of O_2 gas [51] or N_2 gas [52] could induce the deposition of a SiO_2-like passivation layer on GaAs sidewalls.

Figure 2.31d is a SEM image of the sidewall of a microdisk laser etched with this recipe. Although the good verticality of the structure can be assessed for the Cl_2/H_2 process, there remains some room for improvement in the optimisation of the etching conditions for the etching of the InGaAsP material composing the quantum wells [47].

We demonstrated that it is possible to define microdisks with e-beam lithography and etch the sample with a complete III-V etch in LPN. Samples for the third generation are then processed to evaluate the potential in cascadability of the microdisk lasers.

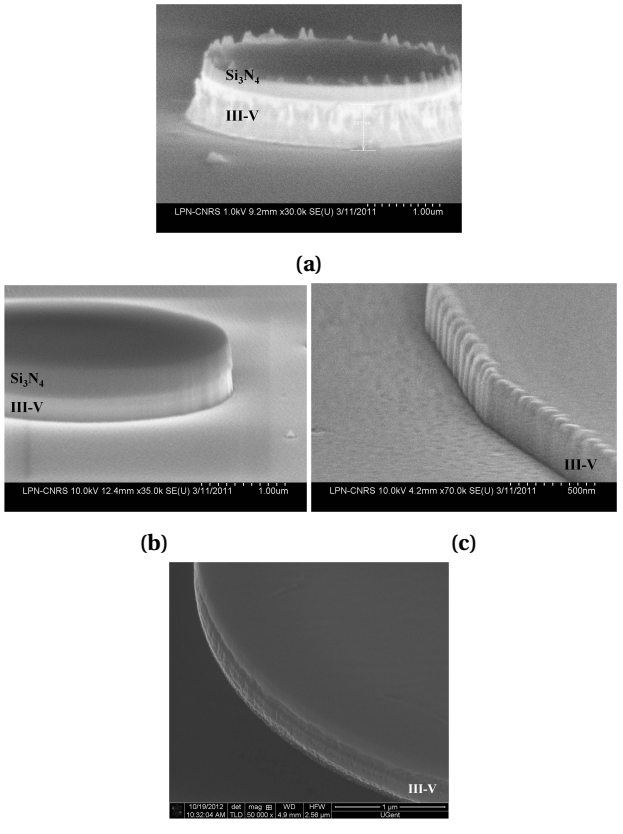

Figure 2.31: SEM images of the sidewalls of microdisks from the third generation etched with different ICP recipes at LPN. (a) Etched with Chlorine-RIE. (b) Etched with HBr-ICP before hard mask removal. (c) Etched with HBr-ICP after hard mask removal. (d) Etched with Cl_2H_2-ICP.

2.9 Improving the standard deviation in lasing wavelength of microdisk lasers heterogeneously integrated on SOI

The layout of an SOI-integrated microdisk laser is shown in Figure 2.32. As presented in the previous sections, two optical levels can be identified in Figure 2.32. The two levels are separated by a thin transparent layer (140nm) of a low refractive index material (n=1.54 for DVS-BCB) and 100nm of Al_2O_3 (n=1.7), allowing evanescent coupling to the underlying waveguide. The goal of processing a device bonded on an Al_2O_3 layer is to improve the heat dissipation from the structure, since the thermal conductivity of sputtered Al_2O_3 is significantly larger than that of DVS-BCB and close to 2 $W.m^{-1}.K^{-1}$ [53], while that of DVS-BCB is close to 0.3 $W.m^{-1}.K^{-1}$, as indicated in Table 2.4 of section 2.12. The InP etch is complete. The microdisks are laterally aligned to an underlying SOI wire waveguide. The designed microdisk lasers have a diameter between 6 and 7.5μm. For the fabricated sample under study, the design of the passive level consists of 5 sections of nominally identical waveguides with a given width w, as depicted on Figure 2.32(b). The smallest value of w is 300nm. w increases with a 50nm-step from one section to another. The largest waveguide width on the sample is then 500nm. The offset between the edge of the microdisk and the edge of the waveguide is kept constant within one section.

The device fabrication relies on the adhesive bonding of the MBE-grown InP-based heterostructure onto the SOI with the use of the planarizing polymer DVS-BCB. The SOI waveguides are fabricated in at CEA-Leti in a CMOS fab using 248nm DUV lithography. The silicon waveguide widths have been confirmed by SEM. Alignment markers for subsequent processing are defined in the Si on the same mask layer and relative to the waveguide structures. This allows the accurate e-beam alignment of microdisk lasers with respect to the waveguides. A diluted DVS-BCB solution is spun onto the SOI wafer in order to achieve a 150nm-thick bonding layer. The InP wafer is coated with a 100nm-thick Al_2O_3 layer before being put in contact with the SOI wafer coated with DVS-BCB. The sample is then pressed and cured following the recipe presented in the previous section. The InP substrate is removed afterwards chemically (using pure HCl).

The process flow from the third generation is then applied to fabricate a sample with e-beam lithography. The microdisks are etched in LPN, which means that the III-V etch is complete and that no bottom contact layer is left. During the InP etch, the Al_2O_3/DVS-BCB layer is slightly thinned and this actually allows us to obtain reasonably contrasted SEM pictures of the edge of

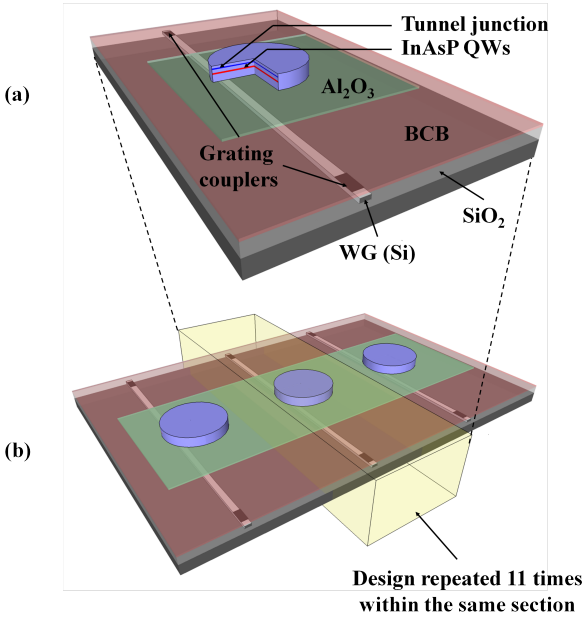

Figure 2.32: Schematic representation of the heterogeneous SOI-integrated microdisk lasers. (a) Microdisk laser structure coupled to underlying waveguide. (b) Array of nominally identical microdisk lasers.

the microdisk and the edge of the underlying waveguides beneath the residual DVS-BCB. SEM measurements show that the microdisk lasers are aligned with respect to the SOI wires with an alignment accuracy better than 40nm compared to the design value. This level of accuracy enables reproducibility in the fabrication and a close control of the evanescent coupling. Figure 2.33 shows a SEM image of the cross-section of a lasing device. From several cross-sections performed with FIB, we can conclude that the DVS-BCB bonding thickness is uniform on the sample. The total thickness above the waveguide is 235nm everywhere on the sample. It is then possible to compare nominally identical devices, as the offset of the devices within one section as well as the total bonding thickness are fixed.

The microdisks are studied under optical pumping at room temperature using the experimental setup depicted in Figure 2.34 [42]. For the first experiment, laser emission from the microdisks is explored using a modulated laser diode as pump source. The pump delivers 50ns long pulses every 740ns. The wavelength of operation is set at 1.18μm where the InGaAsP QW barrier material is absorptive and where silicon is transparent in order to maximize the pumping

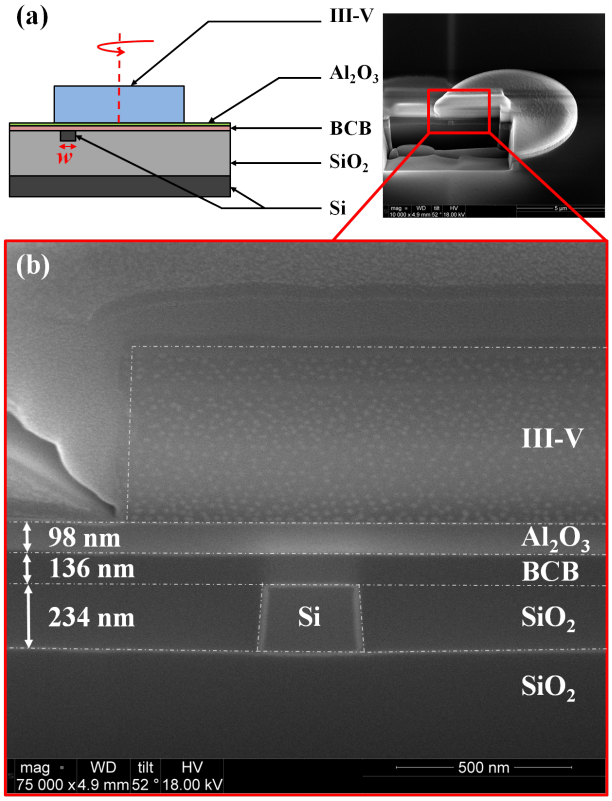

Figure 2.33: (a) Schematic of microdisk cross-section (cylindrical revolution along the dashed line). (b) SEM image of the location of the cross-section on a microdisk laser. (c) SEM image of the cross-section of a lasing device coupled to a 300nm-wide waveguide.

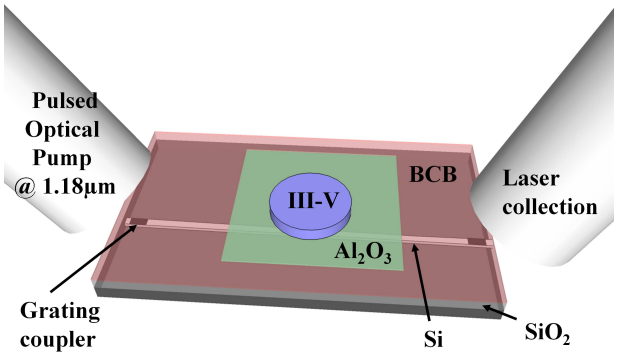

Figure 2.34: Optical pumping of a microdisk through the underlying Si waveguide.

efficiency. The pump is coupled from an optical fiber to the SOI waveguide via one of the two gratings etched at each side of the waveguide. These gratings were originally optimized for operation at 1.55μm. By setting the angle between the fiber and the sample at 12° and by using p polarization, it is possible to couple the pump light at 1.18μm into the TM mode of the SOI waveguide. The pump light is absorbed in the III-V layer through evanescent coupling to the microdisk. Of course, the alignment of the waveguide with respect to the microdisk is of primary importance to ensure maximum efficiency of the optical pumping. Above threshold, the laser emission from the microdisk is coupled to the TE mode of the waveguide, and is collected at the other grating by a fiber positioned at 10° angle in order to maximize the collection at 1.55μm. The laser emission is analyzed using a spectrometer equipped with a cooled array of InGaAs detectors.

We plot on Figure 2.35, in log-log scale, the laser emission output power of a 7μm-diameter microdisk as a function of the pump pulse energy effectively coupled to the SOI waveguide. The resulting curve has a classic S-shape from which a threshold of about 3.9pJ is deduced (2.36.10^7 pump photons).

These results indicate that microdisk lasers can be pumped effectively from the silicon waveguide layer, which can in some cases simplify the fabrication process. We plot in Figure 2.36 the spectral position of the emission peak of this 7μm-diameter microdisk as a function of the pumping energy above threshold. At the point where the carrier level gets clamped, the peak lasing wavelength also gets clamped at a value of 1567.4nm. For higher pump pulse energies,

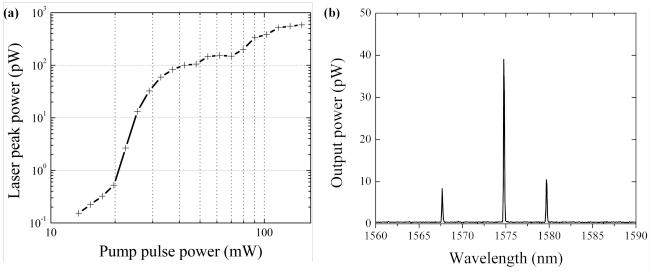

Figure 2.35: (a) S-shape curve of a 7μm-diameter microdisk laser optically pumped through the waveguide at 1.18μm (log-log scale). (b) Measured lasing spectrum of the microdisk under 30pJ of pump energy.

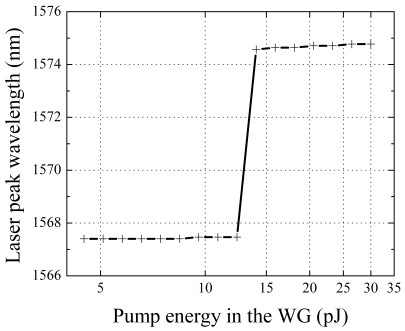

Figure 2.36: Mode competition in 7μm-diameter microdisk laser optically pumped through the waveguide at 1.18μm.

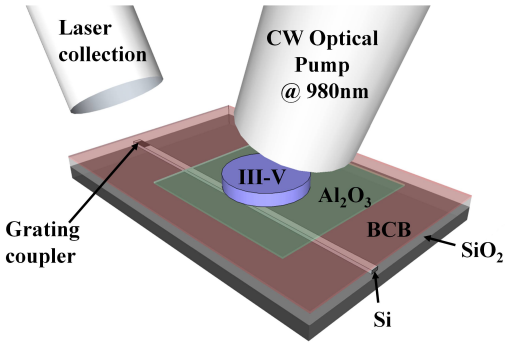

Figure 2.37: Schematic representation of optical pumping of a microdisk laser from the top surface.

mode competition with another radial, azimuthal or vertical mode due to heat generation in the structure results in CW lasing operation at 1574.7nm. For some all-optical signal processing applications, the lasing wavelength of cascaded microdisks must be aligned to each other. Therefore, we will evaluate the spread in emission wavelength between nominally identical devices.

Microdisks with nominally identical designs and coupled to waveguides with the same width are studied under optical pumping. The setup for this second experiment is schematically depicted in Figure 2.37. The CW light of a laser emitting at 980nm is focused on the top surface of the microdisks using a single-mode fiber under a 10° angle. The light emitted from the microdisk lasers couples to the TE mode of the underlying waveguide. Another fiber positioned above one grating coupler collects the laser emission of the microdisks also under a 10° angle. Working at constant pump power for every device of every section, the spectrum of each microdisk above threshold is recorded on an optical spectrum analyzer with a 100pm resolution.

Table 2.3 is a summary of the results for 5 different sections on the same sample. For instance, a standard deviation of 0.37nm on the lasing wavelength of 9 nominally identical 7.5μm-diameter microdisks and coupled to 450nm-wide waveguides is measured. The spectra from the microdisk lasers are plotted together on Figure 2.38. From this characterization, we demonstrate that a standard deviation in lasing wavelength of nominally identical devices on the same chip lower than 500pm is achievable.

Disk diameter	*Number of disks*	*WG width*	σ
7.5μm	10	500nm	0.44nm
7.5μm	9	450nm	0.37nm
7μm	7	400nm	0.67nm
7μm	11	350nm	0.48nm
6μm	11	300nm	0.44nm

Table 2.3: Standard deviation in lasing wavelength of microdisk lasers on the same die

From equation 2.1 can be shown that the uniformity of the lasing wavelength depends on the deviations in both disk diameter and effective index, the latter being dependent on the temperature, the thicknesses of the layers, etc. The measurements are performed in similar conditions of pump power. A 500pm standard deviation in lasing wavelength for 7.5μm-diameter microdisk lasers is to be related to a deviation in the diameter of the processed devices as low as 2.3nm. This deviation can be explained by process variations from one microdisk to the other, during the etching of the hard mask and of the III-

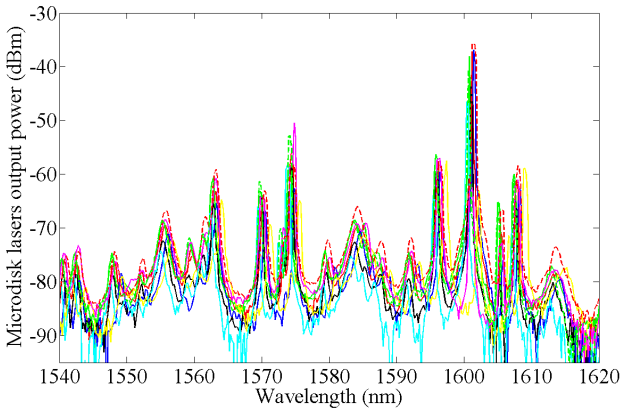

Figure 2.38: Spectra of 9 nominally identical microdisk lasers processed with electron-beam lithography and optically pumped at 980nm. The standard deviation in peak lasing wavelength is 0.37nm.

V layers. Figure 2.39 shows the wavelength distribution of 43 microdisk lasers across the same die. The distribution is centered on λ, being the average lasing wavelength for each section. The size of the bins is $\sigma/2$, σ being the standard deviation in wavelength in each section of microdisks coupled to waveguides with the same width. 16 microdisk lasers on this sample are lasing over a span of σ centered on λ.

Under electrical pumping, a maximal tuning efficiency of the lasing wavelength of 7.5μm-diameter microdisk lasers of 0.35nm.mW^{-1} has been achieved by electrically heating a III-V semiconductor arc closely located to the microdisk cavity [54]. This device is used for compensating wavelength variations resulting from fabrication. Such a technology could very well be implemented to compensate the standard deviation characterized in this paper, with low additional power consumption. Using the same setup as depicted on Figure 2.37, we then study the pump power needed to obtain lasing devices on seven 7.5μm-diameter microdisks belonging to the same section (waveguide width of 500nm). Figure 2.40 shows that mode hopping occurs between a mode at 1574.3nm and a mode at 1600.7nm when the pump power is increased because of heat generation in the structure. Six of the seven microdisk lasers start lasing around 1574.5nm with a standard deviation in pump power of 1.73dBm. As the pump power increases, single-mode operation around 1600.7nm is triggered in the six lasers with a standard deviation in pump power of 2.25dBm. Laser 7 is already lasing at 1600.2nm under low pump power, and remains lasing at this wavelength for higher pump powers. Processing and fiber positioning variations from one microdisk to another explains the deviation in pump power.

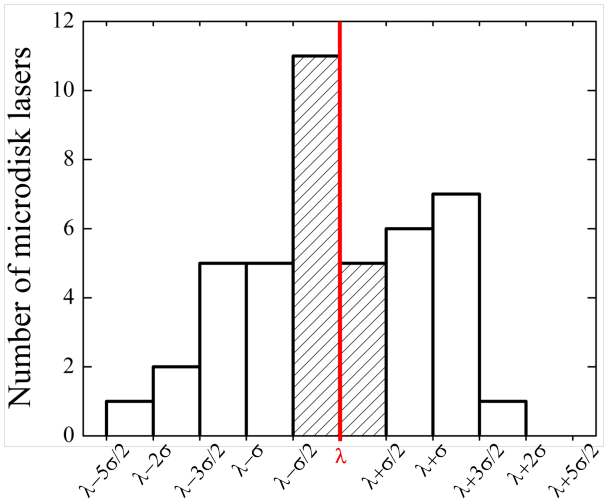

Figure 2.39: Wavelength distribution of 43 microdisk lasers of the same sample centered on λ. The patterned area shows that the peak lasing wavelength of 16 microdisk lasers is between λ-σ/2 and λ+σ/2.

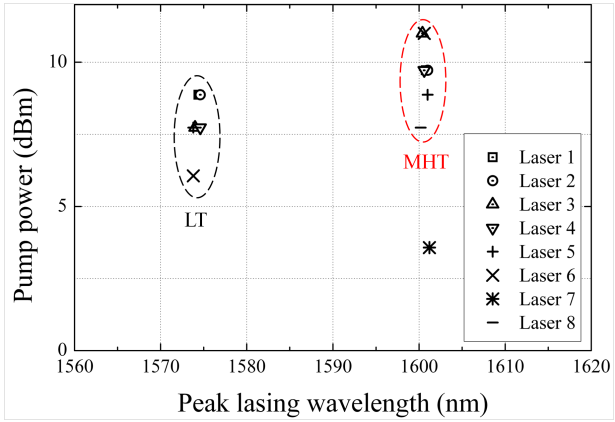

Figure 2.40: Laser threshold (LT) and mode hopping threshold (MHT) in nominally identical microdisk lasers under increasing pump power.

2.10 Improvement of the surface cleaning treatment prior to metal deposition

The surface treatment of the III-V layers before metallic deposition drastically influences the series resistance of the electrical contacts [55]. A surface treatment of the III-V has been implemented in the standard procedure in order to etch a possible native oxide at the surface, and remove particles. The sample is systematically etched for 2 minutes in a solution of $H_3PO_4 : H_2O$ in the proportions 1:10. This cleaning procedure makes the III-V surface hydrophobic. To reverse its polarity, the sample is dipped for 1 second in a 1% HF solution. This surface treatment has resulted in a reduction of the series resistance of the microdisk laser, as will be shown in section 2.16.

2.11 Improvement of the top metallic contact definition with electron-beam lithography

As presented in chapter 1, the coupling efficiency of the light emitted from the microdisk laser to the underlying waveguide strongly depends on three technological features. First, the total bonding thickness must be compatible with an efficient evanescent coupling of the light. Several optimizations of the bonding procedure led to an improvement of the uniformity, the repeatability and the reproducibility of the bonding thickness. Also, the introduction of the e-beam lithography process allows us to accurately control the offset of the edge of the microdisk vs. the underlying waveguide. The last remaining technological challenge is the definition of the top metallic contact. Indeed, a misalignment of this top contact increases the optical losses induced by absorption of the optical mode by the metal [56]. To ensure the alignment of the metallic contact with respect to the already defined microdisk laser, a process with e-beam lithography has been developed.

After the ICP etching of the III-V layers, a 300nm-thick PMMA layer (positive photoresist) is spin-coated on the sample. The design consists in the top metallic contact, and the useful alignment markers are the ones from the SOI-level. This means that the top metallic contact of a disk is aligned with respect to the SOI level and not with respect to the microdisk level as it would be with contact lithography. The metallic contact is deposited in LPN. The contact recipe then only consists of Ti/Au (40nm/800nm), as a Ti/Pt/Au contact has not been developed in LPN. Figures 2.41a and 2.41b are respectively an image under optical microscope inspection and a SEM image of a FIB cross-section of a fabricated device after overcladding with DVS-BCB and opening of vias above the top and the bottom contacts. The top metallic contact looks well-deposited.

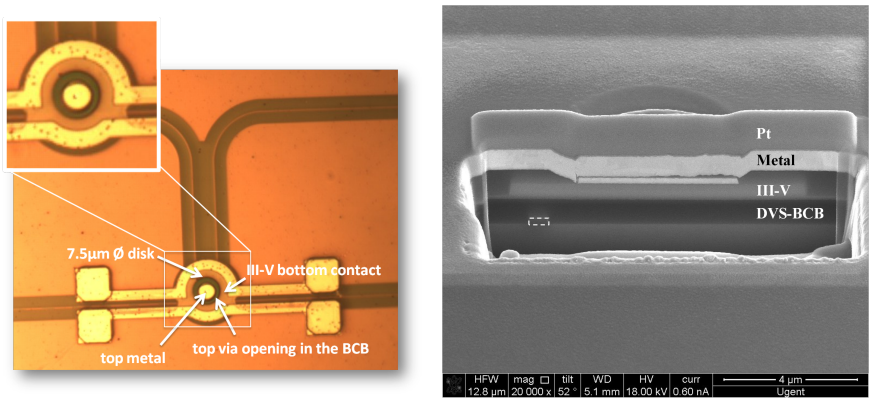

(a) **(b)**

Figure 2.41: Inspection under optical microscope and FIB-cross-section of a sample on which microdisks and top metallic contacts were defined with electron-beam lithography.

Under electrical characterization, the devices are all short-circuited. We relate this to the absence of Platina layer that is normally deposited to prevent migration of Gold to the III-V layers.

2.12 Improving the heat dissipation of a single device

When driving the microdisk laser at a higher bias current, a thermal roll-over of the optical power is visible on the L-I graph as the optical power decreases under increasing bias currents. Several process optimizations can improve the heat dissipation in the microdisk laser. First, the bonding layer material can be changed to evacuate some of the heat to the substrate. Also, another material than DVS-BCB can be used as an overcladding material. Table 2.4 compares the thermal conductivities of several materials.

The thermal conductivity of the DVS-BCB is extremely poor. Nanodiamond particles have been added to DVS-BCB to improve the heat dissipation in the bonding layer. The nanodiamond particles are added to a pure DVS-BCB solution. The mixture needs to be agitated in an ultrasonic bath 30 minutes before being diluted and spin-coated. Two concentrations of nanodiamonds (0.5% and 1%) have been spin-coated on a bare silicon substrate die, and 10nm of SiO_2 has been deposited on the III-V surface before bonding. Figure 2.42a is an image of the bonding layer after spin-coating of the 5%-nanodiamond-BCB and Figure

Material	*Thermal conductivity* ($W.m^{-1}.K^{-1}$)	*Reference*
Si	149	[57]
InP	63	[58]
SiO_2	1.4	[57]
Amorphous Al_2O_3	2	[53]
DVS-BCB	0.29	[27]
Diamond	1000	[59]
MgF_2	14	[60]
Wood	0.4	[61]

Table 2.4: Thermal conductivities of several materials.

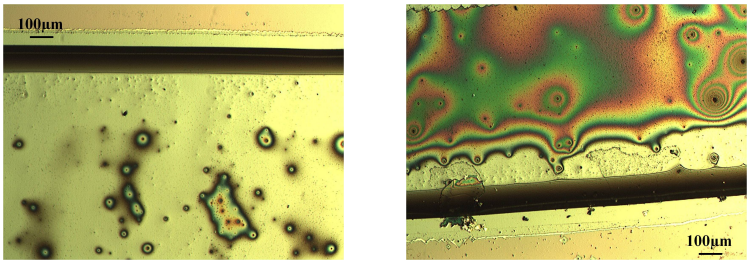

(a) **(b)**

Figure 2.42: Improving the heat dissipation of a microdisk laser with a modified DVS-BCB solution including nanodiamond particles. (a) Optical microscope image of a III-V sample bonded with a 5%-nanodiamond-DVS-BCB solution. (b) Optical microscope image of a III-V sample bonded with a 10% nanodiamond-DVS-BCB solution.

2.42b is an image of the bonding with a 10% solution. The III-V layer remains after substrate removal (the edge of the III-V can be seen at the edge of both images). The bondings have been successful with both solutions.

The investigation of the impact of the nanodiamond particles on the thermal properties of photonic crystal lasers heterogeneously integrated on SOI has been carried out at LPN. After bonding their III-V epitaxy with the modified DVS-BCB solutions on top of SOI dies, they demonstrate that the introduction of nanodiamond particles in the DVS-BCB solution used for bonding does not increase the optical losses in the SOI waveguides. Also, the thermal dissipation of the photonic crystal cavities processed on samples bonded with nanodiamond particles is 10 times improved compared to the one of samples bonded with non-modified DVS-BCB solution. This study is published in the Doctoral Thesis of A. Bazin [40].

Changing the nature of the bonding material, as well as the nature of the

overcladding material, would greatly improve the thermal dissipation of microdisk lasers. From Table 2.4, it is clear that the first modification of the standard procedure towards a better thermal managment consists in reducing the thickness of the DVS-BCB bonding layer. The use of the wafer bonder allows us to reproducibly reach thicknesses of the DVS-BCB bonding layer of a few tens of nanometers. It is then possible to deposit a thicker SiO_2 layer on top of the III-V prior to bonding (100nm for instance), and to spin-coat a DVS-BCB solution so that the total bonding thickness is more dependent on the thickness of the oxide layer than on the thickness of the DVS-BCB layer. The effect of this new bonding method on the thermal dissipation of microdisk lasers needs to be experimentally quantified.

Another amorphous dielectric has been used for bonding microdisk laser on SOI. As can be seen in Table 2.4, the thermal conductivity of amorphous Al_2O_3 is slightly higher than the one of SiO_2. Figure 2.43 is a SEM image of a FIB-cross-section of a microdisk laser bonded with a 85nm-layer of Al_2O_3 deposited by thermal evaporation in a Univex chamber prior to bonding. During the ICP etching of the microdisk laser, the SiO_2 hard mask has been etched at the edges of the microdisk. The sidewall of the III-V microdisk is then also etched and no longer vertical. This can be solved by depositing a better quality and a thicker layer of SiO_2, and by improving the selectivity of the ICP etching recipe.

Also, overcladding microdisk lasers can be performed with another CMOS-compatible material. We study the thermal dissipation in a 7.5μm-diameter microdisk laser with a 2D-simulation in COMSOL, for different overcladding materials. As the structure has a cylindrical symmetry, only half of the microdisk cross-section is simulated. The heat generated by electrical pumping is simulated as a heat source located in the quantum wells of the microdisk laser. The calculation of the temperature therefore only relies on the dissipation of this thermal power in the volume of the microdisk. It does not take injection of carriers into account. The simulation results of four microdisks structures are compared. The power dissipated in the volume of the microdisk laser as well as the thickness of the overcladding layer (500nm on top of the edge of the microdisk) are the same for all four structures. The bonding layer of the first structure (Figure 2.44a) consists of 150nm of SiO_2 and 150nm of DVS-BCB, and the device is overcladded with DVS-BCB. The bonding layer of the second sample (Figure 2.44b) consists of 150nm of SiO_2 and 150nm of DVS-BCB, and the device is overcladded with SiO_2. We also simulate the thermal dissipation in a microdisk laser with a bonding layer consisting of 150nm of Al_2O_3 and 150nm of DVS-BCB, overcladded with DVS-BCB. Finally, we study a fourth sample with a bonding layer consisting of 150nm of Al_2O_3 and 150nm of DVS-BCB and overcladded with SiO_2, as shown in Figure 2.44c. From Table 2.5, we can compare the temperatures at the edge of the four microdisks, where the optical mode is

propagating. They are relative temperatures with respect to the temperature of the substrate (300K).

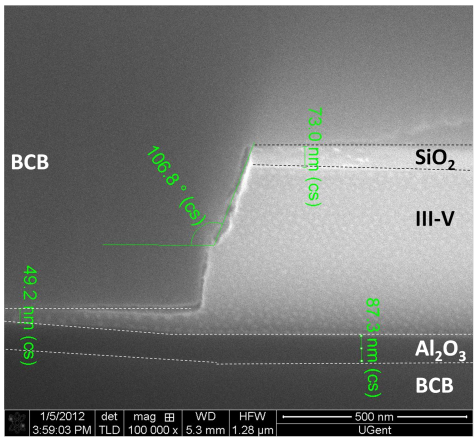

Figure 2.43: Successful bonding of a microdisk laser bonded with Al_2O_3.

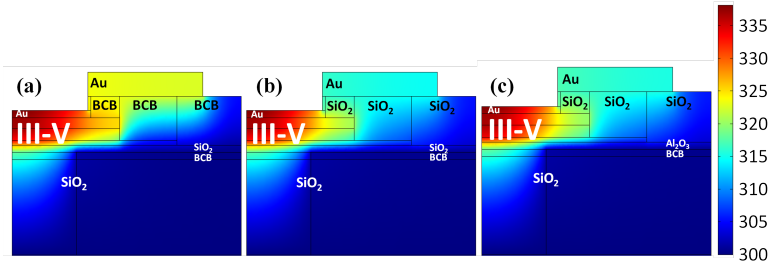

Figure 2.44: Simulation of the temperature at the edge of the microdisk performed with COMSOL for (a) Bonding layer: 150nm DVS-BCB + 150nm SiO_2 ; overcladding DVS-BCB. (b) Bonding layer: 150nm DVS-BCB + 150nm SiO_2 ; overcladding SiO_2. (c) Bonding layer: 150nm DVS-BCB + 150nm Al_2O_3 ; overcladding SiO_2.

Bonding interface	*Thickness*	*Overcladding*	*ΔTemperature (K)*
SiO_2	150	DVS-BCB	33.5
SiO_2	150	SiO_2	21
Al_2O_3	150	DVS-BCB	32
Al_2O_3	150	SiO_2	20

Table 2.5: Temperatures at the edge of the microdisk laser.

2.13 p-i-n epitaxy for the fabrication of microdisk lasers heterogeneously integrated in SOI

The samples described in the previous sections are fabricated with an epitaxy including a tunnel junction (TJ) as top contact (cf. section 2.1). In [1], the performance of a tunnel-junction-based approach for a thin film microdisk laser that has no metal contacts in close proximity with the optical field is investigated. The tunnel junction is assumed to consist of two 20-nm-thick, heavily doped (2.10^{19}cm^{-3}) InGaAsP layers with 1.2μm-bandgap wavelength (Q1.2). The active layer consists of three compressively strained (+1.7%) InAsP quantum wells, embedded in 20-nm-thick Q1.2 barriers, and surrounded with Q1.2 optical confinement layers (OCLs) with to-be-optimized thicknesses. This design allows reducing TJ-related optical absorption loss by reducing optical confinement in the TJ while preserving optical overlap with the quantum wells and the underlying SOI waveguide. It is compared with an approach based on a very thin InGaAs contact layer [62]. The alternative design is identical to the one with first one except for the TJ and the top n-type contact layer which are replaced by a thin 15-nm *p*++-InGaAs contact layer and 100-nm *p*++-Q1.2 layer. The highly *p*-doped layers are in this configuration present in the full diameter of the microdisk laser. The absorption of these layers at the edge of the microdisk causes optical losses. The lowest material gain required to compensate for the internal loss is calculated to be three times lower in the design with the tunnel junction than in the design with the p-i-n epitaxy [1].

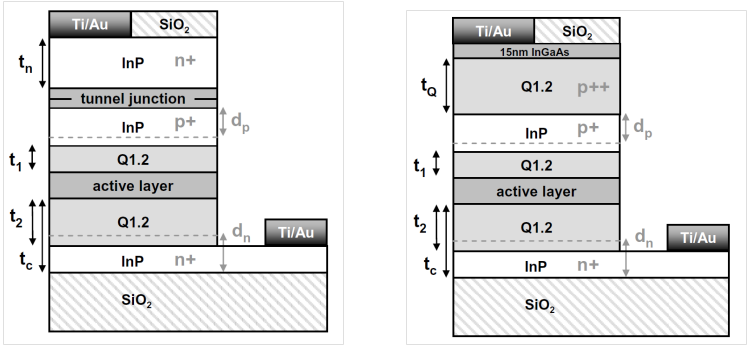

Figure 2.45: Schematic description of alternative epitaxial stacks for the fabrication of microdisk lasers heterogeneously integrated on SOI. (a) Design including a tunnel junction. (b) Design incorporating a thin ternary contact layer.

2.13.1 FDTD simulation of the optical mode in the microdisk laser and simulations of the electrical injection

The growth of the tunnel junction is performed at the Institut des Nanotechnologies de Lyon (INL) in Lyon, France and constitutes in itself a fabrication challenge. The alternative p-i-n epitaxy is much more common to grow, and the resistivity of the Ti/Pt/Au contact on a *p*-doped InGaAs layer is much better than on a *n*-doped InP layer [14]. However, a new process flow must be developed to reduce the optical losses induced by the *p*-doped top contact layers. We propose to etch them above the edge of the microdisk, where the optical mode is propagating. Simulations are needed to study the performance of such a structure. Here is a list of parameters that need varying to quantify their impact on the characteristics of the microdisk laser:

- Size of the top contact metal: the optical mode should not "feel" the metallic top contact;
- Etch depth of the III-V layers at the edge of the microdisk laser: the optical mode should be pushed towards the silicon level for a good coupling efficiency without jeopardizing its optical confinement;
- Doping of the top contact and thickness of the bottom contact layer: as described in section 2.16, the series resistance of a TJ-based device has been improved by depositing the metallic contact on a quaternary bottom contact layer;
- Good electrical injection: etching the top contact layers should not jeopardize the eletrical injection in the microdisk. Simulations need to demonstrate that carriers flow to the edge of the microdisk in order to provide radiative recombinations.

The 2D-simulations are performed with the TCAD-software Silvaco. As the structure has a cylindrical symmetry, only half of the microdisk cross-section is implemented. A 2D-cylindrical Helmholtz solver has been specifically integrated into the "Laser" module of Silvaco for the microdisk laser simulations. The basic steps to optimize the device are:

- Optimize the geometry and the refractive indexes to get the correct optical modes. For this, with the "waveguide" statement from Silvaco, it is possible to print out the actual optical eigen energies and to make sure they are close to the desired range (1.55μm). The output file is a cross-section of the radial mode profile;
- After the modes and optical eigen energies are optimized, it is possible to get the correct lasing energy by adapting the $InAs_yP_{1-y}$ composition and

thickness of the QWs;
- Correct threshold voltages must be obtained when optimizing the affinities of the materials. By changing them, one must make sure that the QWs make equal contributions to the luminous power, and that all QWs have a positive gain. If QWs are not balanced, only one well will amplify, while others will absorb;
- Finally, the device can be run as laser. We consider here a microdisk laser, i.e. a 3D optical cavity without mirrors. However, the code requires the specification of a reflectivity of mirrors. Therefore, the reflectivities of the mirrors in the code is set at 100%, and a parameter is added to specify the losses related to the extraction of the power. It is then possible to plot the LI curve of the device, the dependance of the light power on the voltage, current, photon densities, modal gain and loss.

Layer	*Doping level* (cm^{-3})	*Thickness (nm)*	*Comment*
InGaAs	2.10^{18}Zn	100	*p*++-type top contact
InP	2.10^{18}Zn	150	*p*++-type top contact
InP	4.10^{17}Zn	185	*p*+-type top contact
InGaAsP		90	quaternary barrier
InGaAsP		3 x 20	quaternary barriers
InGaAsP		3 x 10	QWs
InGaAsP		20	quaternary barrier
InGaAsP		90	quaternary barrier
InP	4.10^{17}Si	200	*n*+-type bottom contact
InP	1.10^{18}Si	150	*n*++-type bottom contact

Table 2.6: Description of the epitaxial stack used for the fabrication of microdisk lasers based on the p-i-n epitaxy

The epitaxy is designed as described in Table 2.6. The simulations using ATLAS-Silvaco consider half of a 18.5μm-diameter disk embedded in silica, and rely on the cylindrical symmetry and mesh available in the module. According to the simulation flow previously described, the first step is to optimize the geometry of the device and the refractive indexes to get the correct optical modes. Six designs have been considered in total, but we will focus on the three best options as shown in Figure 2.46. Design (a) is the reference structure. For this implementation, the lowest part of the structure consists of a 335nm-thick *n*-doped InP bottom contact layer. In addition, this design is not etched at its edge. In design (b), the bottom contact consists of 335nm-thick *n*-doped InP layers and the structure is etched for 250nm at its edge. In design (c), the bottom contact consists of 335nm-thick *n*+-doped InP layers and the structure is etched

for 350nm at its edge. The diameter of the metallic top contact is 5.1μm, and the contact is taken on a *p*++-doped InP layer. The doping level of this contact layer is set to 1.10^{18}cm^3. The *p*++-doped InGaAs top contact layer is not considered in the simulation. Regarding optical losses, an imaginary refractive index has been considered to simulate the losses induced by the top metal contact (Au) and by the heavily doped *p*-type (top of the structure) and *n*-type (bottom of the structure) layers.

The first challenge is to make sure the etching of the top contact layers does not jeopardize the optical confinement of the mode in the cavity. With the "waveguide" statement from Silvaco, it is possible to perform 2D-FDTD simulations, to print out the actual optical eigen energies and to make sure they are close to the desired range (1.55μm). The output file is a cross-section of the radial mode profile. In Figure 2.47, the light intensity of the fundamental mode in the microdisk laser is simultaneously plotted for the three different structures. The color scale is identical for the three plots, which allows quantitative comparison of the light intensity inside the different devices.

For the reference structure (design (a)), the maximal intensity of the optical mode nicely overlaps with the QWs. The optical mode also extends in the bottom contact layers, which will facilitate coupling to the underlying waveguide. For design (c), the light intensity is the highest simulated between the three structures. However, because of the etching, the optical mode is pushed downwards and the overlap between the optical intensity and the QWs is poor. Design (b) offers the best compromise between the three devices. The light intensity is higher than inside the reference structure, the overlap between the mode and the QWs is good, and the mode still extends in the bottom contact layers to ensure an efficient coupling to the underlying waveguide.

The FDTD simulations demonstrate that etching the microdisk laser at its edge does not jeopardize the optical confinement of the mode. The electrical injection inside the difference structures is now investigated.

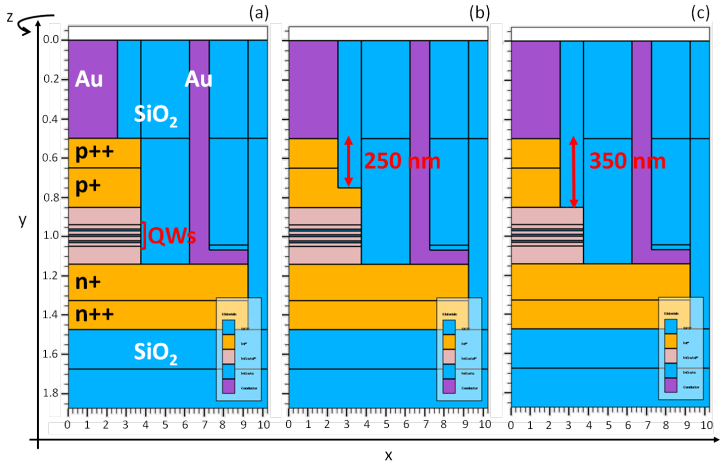

Figure 2.46: Study of the performance of a p-i-n microdisk laser with Silvaco. (a) Reference structure with a 335nm-thick *n*-doped InP bottom contact layer and for which the edge is not etched. (b) Similar structure than (a) where 250nm of III-V at the edge are etched. (c) Similar structure than (a) where 350nm of III-V at the edge are etched.

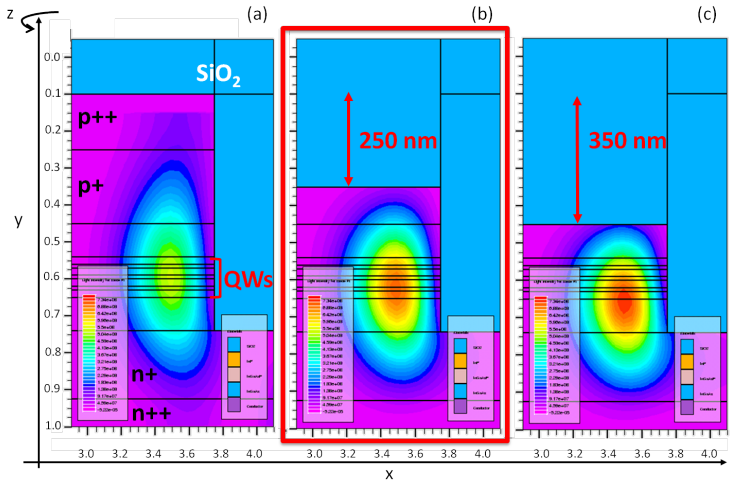

Figure 2.47: Simulation with Silvaco of the optical confinement of the whispering-gallery mode in p-i-n microdisk lasers corresponding to the 3 structures presented in Figure 2.46.

2.13.2 Optimization of the band diagram of a microdisk based on a p-i-n epitaxial stack

The dopings of the *p*-type and the *n*-type layers must be adjusted to enhance the lateral current spreading in the QWs. An extensive library of materials and their characteristics is included in Silvaco. It is however mandatory to check the validity of the band diagram of the simulated structure. At zero bias, this is performed by plotting the band diagram along a cross-section next to the center of the device. Figure 2.48 is the band diagram at zero bias of the structure where 250nm of III-V are etched at the edge of the microdisk.

All the bandgaps measured on Figure 2.48 correspond to the values from literature. The simulated structure can then be electrically injected. It is important to make sure the etching of the III-V layers at the edge of the microdisk laser does not hinder an efficient electrical injection.

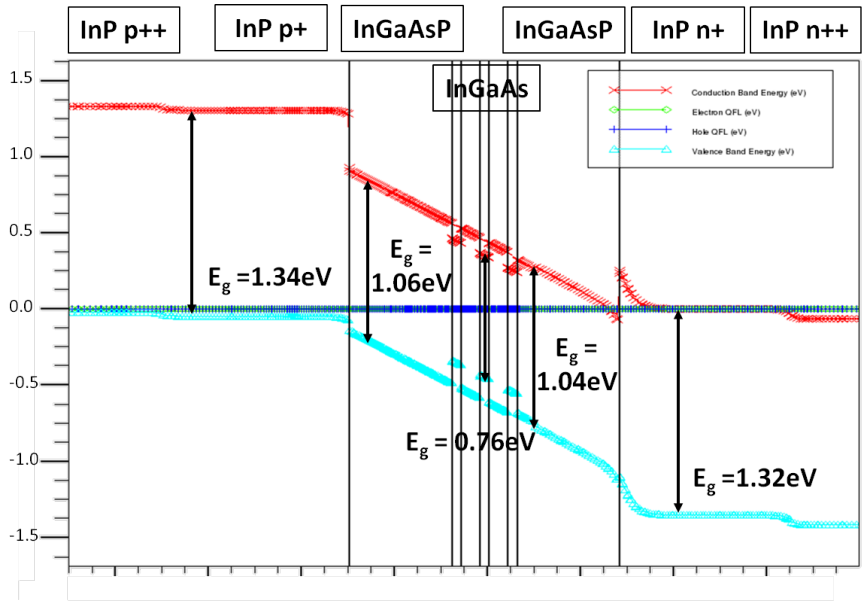

Figure 2.48: Band diagram at zero bias of the microdisk structure where 250nm of III-V are etched at its edge.

2.13.3 Simulation of the electrical injection inside a microdisk based on a p-i-n epitaxial stack

The voltage-current characteristic of a microdisk laser where 250nm of III-V has been etched at its edge is plotted from 0 to 2V. A threshold of 0.8V is measured. As the composition and the bandgaps of each layer are well optimized, the QWs are balanced and the amount of radiative recombinations is similar in the three QWs. The maximum radiative recombination rate is located at the center of the microdisk laser. As visible in Figure 2.49, the gain is positive at 1V in the three QWs between 1.3μm and 1.44μm, while its maximum is located at 1.42μm.

The radiative recombination rate is proportional to the product of the hole concentration and the electron concentration. The limiting factor to the amount of radiative recombinations is the concentration of holes as holes have a lower mobility than electrons. The hole concentration inside the second quantum well when the microdisk is biased at 1V is plotted on Figure 2.50. The hole concentration is the highest under the middle of the metallic top contact, but we focus on the edge of the microdisk where the radiative recombinations overlap with the optical mode. On Figure 2.50, we compare the reference structure (design (a)) to the structure where 250nm of III-V have been etched at the edge of the microdisk (design (b)). The hole concentration integrated over the quantum well of the etched structure is higher than the one of the reference structure. At the edge of the microdisk, the hole concentration is in the same order of magnitude for the two structures. For design (b), the optical losses will be lower as there is no tunnel junction nor overlap with a highly absorping contact layer. Etching the highly *p*-doped III-V layers does not jeopardize the electrical injection in the microdisk laser and improves the radiative recombination rate.

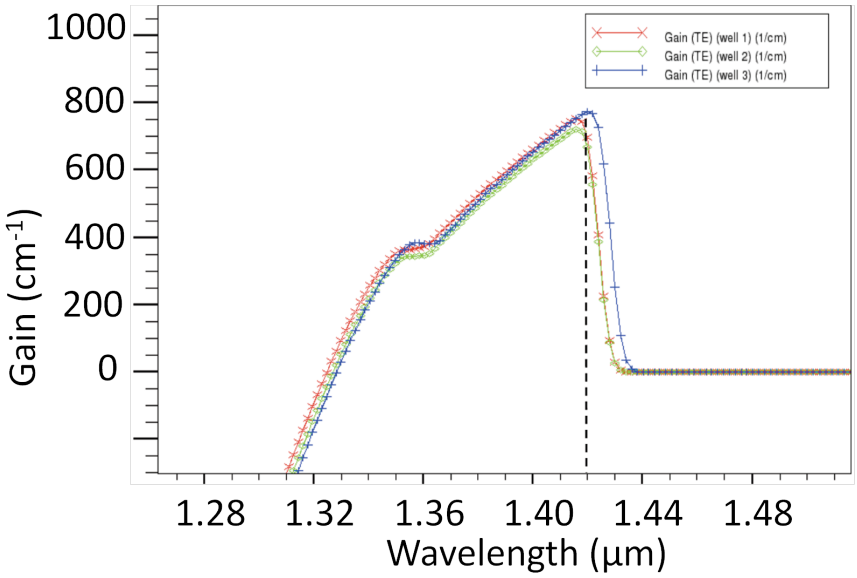

Figure 2.49: Positive gain inside the QWs for a microdisk biased at 1V.

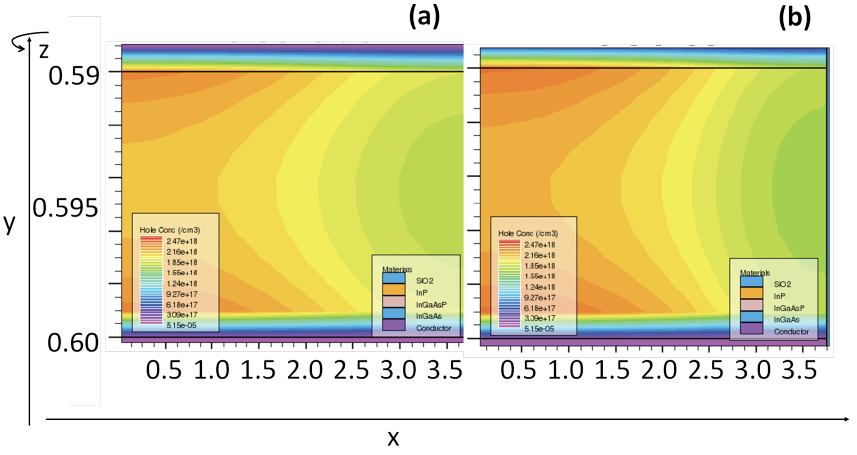

Figure 2.50: Hole concentration inside the second QW and under electrical pumping (1V). (a) For the reference structure. (b) For the structure where 250nm of III-V are etched at the edge of the microdisk laser.

2.13.4 Fabrication of electrically-pumped microdisk lasers based on a p-i-n epitaxial stack

The simulations demonstrate that etching 250nm of InP at the edge of the microdisk offers the best configuration for efficient electrical injection and ensures a better overlap of the optical mode with the quantum wells. Figure 2.51 describes the process flow of the fabrication of microdisk lasers based on the p-i-n epitaxial stack. In the simulations, the metallic top contact is taken on *p*++-doped InP. Experimentally, it has been demonstrated that depositing a Ti/Pt/Au contact on a *p*-doped InGaAs layer instead of a *p*-doped InP results in lower contact resistance. In [14], one of the best contact resistivities of a Ti/Pt/Au contact taken on *p*-doped InGaAs (doped at 2.10^{20}cm^{-3}) is reported. The measured contact resistivity is as low as $1.10^{-6}\Omega.\text{cm}^2$. On the other hand, a contact resistivity of $2.49.10^{-3}\Omega.\text{cm}^2$ of a Ti/Pt/Au contact taken on a p-doped InP (doped at $7.5.10^{18}$cm^{-3}) layer has been reported in [63]. In the process flow described below, the metallic top contact is then taken on the *p*++-doped InGaAs layer, that will also be etched above the edge of the microdisk laser.

An ICP etching recipe of the III-V layers through a metallic mask has been developed. As previously reported in the description of samples from the first e-beam generation in section 2.7.3, etching through a metallic mask results in sidewall roughness and micromasking because of the redeposition of metallic particles. Several tests have been performed to test the quality of the etching through a SiO_2 mask and metallic layers. The thickness of the hard mask has been varied and the metallic stacks with only Ti, Ti/Pt and Ti/Pt/Ti have been investigated. The combination that results in the lowest density of micromasking is 400nm of SiO_2 mask and a Ti/Pt/Ti deposition, as can be seen in Figure 2.53.

The contact resistivities of the top and bottom contacts were measured using the Transmission Line Model (described in section 2.14.3). Two metal recipes are deposited on the *p*++-doped InGaAs top contact layer and on the *n*+-doped InP bottom contact layer, and are not annealed: Ti/Pt/Au (20/25/200nm) and Ti/Pt/Au (40nm/50nm/200nm). A contact resistivity of $1,7.10^{-3}\Omega.\text{cm}^2$ is the best result obtained on *p*++-doped InGaAs with the Ti/Pt/Au (20nm/25nm/200nm) recipe, while a contact resistivity of $6,1.10^{-2}\Omega.\text{cm}^2$ is measured on the *n*+-doped InP layer with the Ti/Pt/Au (40nm/50nm/200nm) recipe.

Before metallization for electrical pumping, the microdisks are optically pumped with a continuous-wave laser emitting at 980nm. At this stage, the metallic contact is present on top of the microdisks. The 980nm laser light is

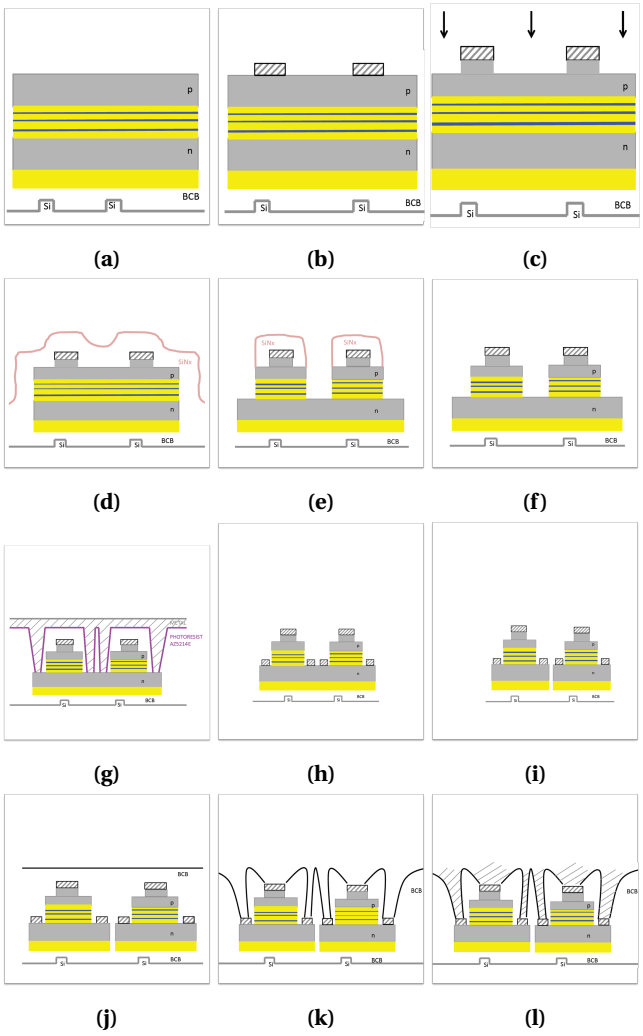

Figure 2.51: Process flow of microdisks fabricated with the p-i-n epitaxial stack. (a) Bonding of the p-i-n epitaxy on SOI. (b) Metallic top contact deposition. (c) ICP etch of the highly *p*-doped top contact layers at the edge of the microdisk. (d) Hard mask deposition. (e) ICP etch of the microdisk lasers. (f) Hard mask removal. (g) Metallic bottom contact deposition. (h) Metallic bottom contact lift-off. (i) ICP etch of the bottom contact layers for island definition. (j) Planarization with DVS-BCB. (k) Top and bottom vias etching in the DVS-BCB to reach. (l) Metallic pads deposition for electrical pumping.

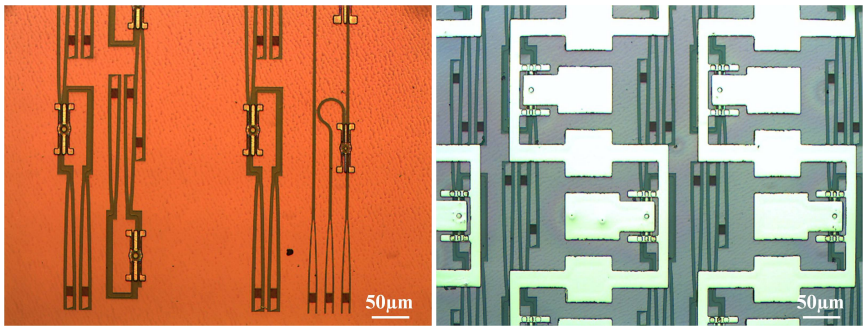

(a) **(b)**

Figure 2.52: Optical microscope image of the fabricated microdisk based on the p-i-n epitaxial stack. (a) Microdisks after lift-off of the bottom contact. (b) Finished sample after extra metallization for electrical pads.

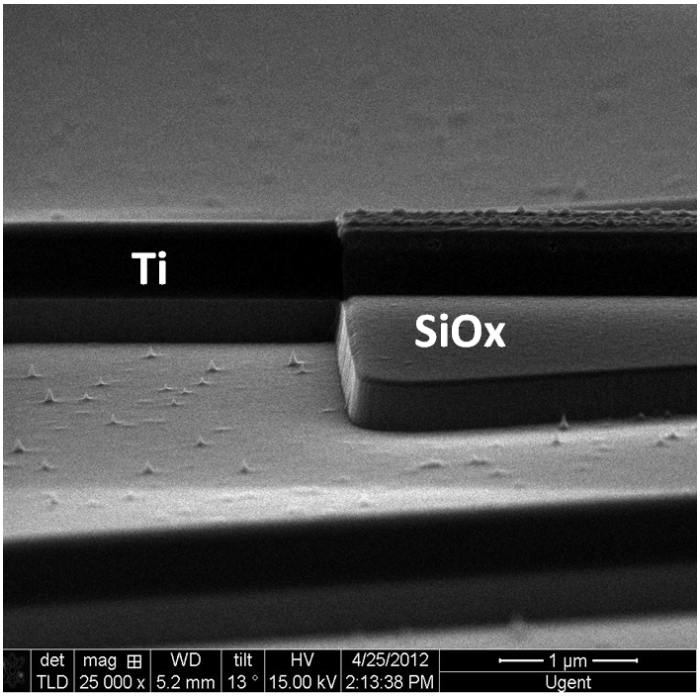

Figure 2.53: Optimization of the micromasking when etching through a metallic mask during the fabrication of p-i-n-based microdisk lasers.

focused on the top surface of the microdisks using a single-mode fiber under a 10° angle. The light emitted from the microdisk couples to the TE mode of the underlying waveguide. Another fiber positioned above one grating coupler collects the laser emission of the microdisks also under a 10° angle. Working at constant pump power for every device, the spectrum of each microdisk above threshold is recorded with an optical spectrum analyzer with a 100pm resolution. Figure 2.54a depicts the optical spectrum of one of the fabricated microdisks. The weak optical output power is explained by the low coupling efficiency between the microdisk and the underlying waveguides. The microdisks were fabricated with AZ5214E photoresist. As explained in section 2.6, the resulting offset of the edge of the microdisk vs. the underlying waveguide is now 220nm larger than designed value on one side of the device and 486nm larger than the designed value on the other side (Figure 2.16b). The optical output power could be improved by using ECI photoresist or e-beam lithography.

The sample are further processed to perform electrical characterization. A voltage-current characteristic of a microdisk laser is plotted in Figure 2.54b. A threshold voltage of 0.8V is visible, but no lasing is recorded under electrical injection.

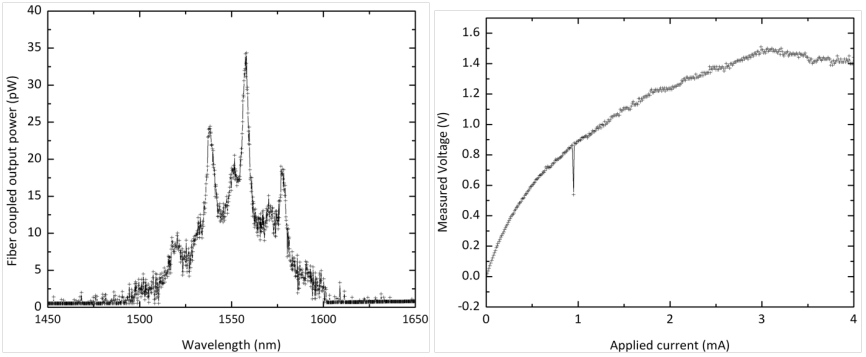

(a) **(b)**

Figure 2.54: (a) Spectrum of a 7.5μm-diameter microdisk fabricated with the p-i-n epitaxial stack under optical pumping. (b) VI characteristic of a fabricated microdisk based on a p-i-n epitaxial stack.

2.14 Systematic tests to perform on the III-V epitaxy before bonding

Integration of III-V epitaxy on top of an SOI waveguide circuit is a time-, effort- and money-consuming process. Processing a complete device without beforehand testing the quality of the epitaxial wafer is risking to be faced with a very low bonding yield, a very high series resistance of the device, and/or very low lasing efficiency. In the course of this work, a set of optical and electrical tests has been developed and systematically performed before any III-V processing (and even before bonding). We report what we consider to be mandatory tests.

2.14.1 Optical inspection of the surface quality of the epitaxial wafer

Scanning the surface of the epitaxial wafer under an optical microscope is already helpful in chosing areas of III-V that will be used for bonding. Indeed, it is possible to see defects in the epitaxy during this optical inspection. Figure 2.55 is a picture of the surface of an epitaxial wafer grown by Molecular-Beam-Epitaxy (MBE) taken with an optical microscope.

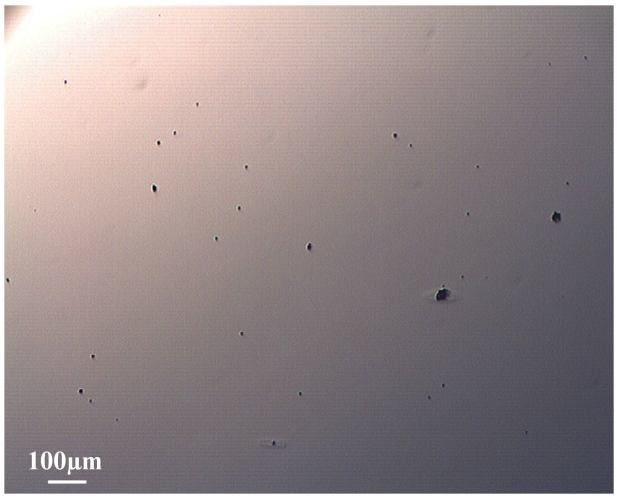

Figure 2.55: Optical microscope image of the surface of an epitaxial wafer grown by MBE prior to bonding. The black dots are particles from the growing chamber, while the biggest defect on the right side of the picture was trapped into the wafer during the epitaxial growth : the defect goes trough the entire epitaxial stack.

Defects in the epitaxy will jeopardize the quality of the bonded layer. Figures 2.56a and 2.56b are microscope pictures of the surface of the III-V epitaxy after bonding and substrate removal. Due to the presence of defects, the bonding yield is very low : large pieces of III-V material detached from the SOI after substrate removal. Also, the surface quality of the remaining bonded area does not allow us to continue with post-processing. In the few cases where the bonding is somehow successful, several epitaxial layers can be chemically under-etched when the etching solution used to remove the substrate penetrates the defects.

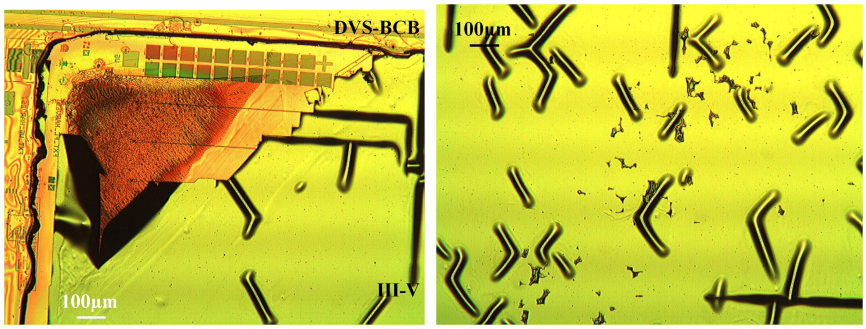

(a) **(b)**

Figure 2.56: Optical microscope image of the low bonding yield when the epitaxy present defects : large pieces of III-V are detaching from the SOI after substrate removal (the black line is the imprint of the corner of the original III-V in the DVS-BCB). Defects have caused the formation of under-etched channels in the middle of the III-V bonded die after substrate removal. (a) Corner of the die. (b) Middle of the die.

In this work, the epitaxial wafers were grown on 2-inches substrates. In order to maximize the use of this expensive and valuable material, the wafer is cleaved in dies of a few mm x mm^2 so that the resulting III-V die covers the SOI design of interest after bonding. It is mandatory to cover the epitaxial wafer with photoresist prior to cleaving. Indeed, most of the resulting particles after cleaving will be rinced off the surface when stripping the photoresist.

2.14.2 Test of the optical properties of the quantum wells

Photoluminescence is an important non-destructive technique for measuring the purity and the crystalline quality of semiconductors. It requires very little sample manipulation or environmental control. In our case, photoluminescence is used prior to check the optical properties of the epitaxial wafer. Variations of the photoluminescence intensity upon change of temperature has been characterized for the microdisk laser epitaxial stack.

The sample is maintained at a given temperature inside a cryostat filled with liquid N_2. Light from a laser at the wavelength of 800nm shines on the surface of the sample. The light emitted by the sample is collected and analyzed with a spectrometer. The temperature of the chuck inside the cryostat is swept from 78.5K to 340K. Figure 2.57 is an example of a photoluminescence spectrum of a III-V epitaxial stack used for microdisk lasers for this range of temperature. The quantum wells emit around 1.55μm at room temperature, while a 300nm-thick InGaAs etch-stop layer emits around 1.6μm. It is possible to calculate the bandgap of each emitting layer and extract their composition from this measurement. The dependence of the bandgap energy as a function of temperature can also be extracted.

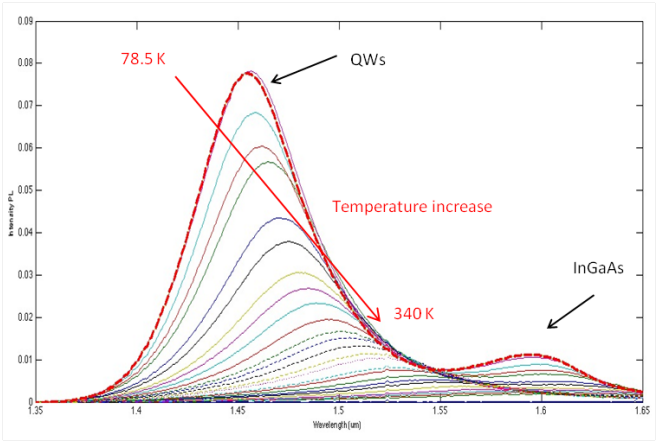

Figure 2.57: Photoluminescence spectrum of an epitaxial stack for microdisk lasers prior to bonding. The quantum wells are emitting at 1.55μm, while a 300nm-thick InGaAs etch-stop layer emits around 1.6μm.

2.14.3 Electrical test of the epitaxy

The contact resistance between the metallic pads and the semiconductor must be very small compared to the resistance in the semiconductor device [64]. This requires the use of "ohmic" contacts. The fabrication of high quality ohmic contacts on both *n*- and *p*-type III-V semiconductors is essential for the successful operation of opto-electronic devices such as semiconductor lasers and semiconductor optical amplifiers. From a practical point of view, a satisfactory ohmic contact should not significantly degrade device performance and can pass the required current with a voltage drop that is small compared with the drop across the active region of the device.

The characteristic quantity to express the quality of a contact is the contact resistivity [64], a parameter of the metal-semiconductor material system. This parameter is measured via planar test structures. Different test methods have been developed for quantitatively assessing the performance of ohmic contacts on a semiconductor: the Cross-bridge Kelvin Resistor (CKR) and the Transmission Line Model (TLM). In both these structures, a current is sourced from the highly doped semiconductor level into the metal level via the contact window. The voltage drop between the two levels is measured. The calculated resistance is linked to the contact resistivity. With refined mathematical models of the resistors, an accurate value of the contact resistivity can be extracted. The TLM originally proposed by Shockley [65] offered a convenient method for determining the specific contact resistance ρ_c for planar ohmic contacts. Shockley also proposed an experiment in which the total resistance R_T between any two contacts (of length d and width w) separated by a distance l could be measured and plotted as a function of l. A detailed description of the principle of the TLM is presented in appendix B.

In the course of this work, systematic TLM measurements have been performed on the III-V wafers in order to test the electrical properties of the epitaxy. After bonding a small piece of the epitaxy to a bare piece of silicon, half of the III-V surface is covered with photoresist. The other half is chemically etched so that only the bottom contact layers remain. Metallic pads are deposited on top of the bottom contact and on top of the top contact. Typically, the width of the mesa was about 100μm for contacts of 100 x 100μm^2. The distance between the electrical pads was doubled between the contacts i and i+1, starting from a 2μm-wide gap. A first deposition with e-gun is performed with the recipe Ti/Pt/Au (25/50/100nm). To be able to probe the metallic pads, a second deposition of Ti/Au (40/300nm) is performed with Joule evaporation. Figure 2.58 illustrates the resulting sample from side and top views. It is then possible to characterize the diode between the top and the bottom contacts, and to evaluate the specific contact resistances on both sides.

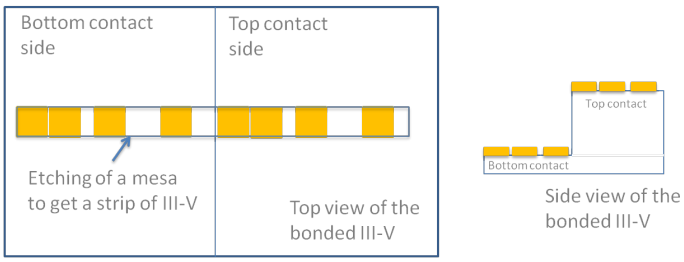

Figure 2.58: Top and side view of defined TLM pattern on a III-V laser epitaxy.

2.15 Description of the processing of the samples presented in Chapter 3 and Chapter 4

The sample studied in chapter 3 was bonded on a SOI chip from CEA-Leti with adhesive bonding in the clean-room of Ghent University. The epitaxial stack is the one presented in Table 2.1. The microdisk lasers were defined by contact lithography using the ECI photoresist in Ghent. We then etched the III-V layers with ICP at TU/e. Finally, the sample was planarized and metallized in Ghent, following the fabrication procedure described in the previous sections. Full characterization has been carried out in Ghent.

The sample studied in chapter 4 was bonded on a SOI chip from CEA-Leti with molecular bonding at the CEA-Leti. The epitaxial stack is the one presented in Table 2.1. After the bonding process, the InP substrate is removed so that only the desired epitaxial structure remains. Alignment markers for subsequent processing are defined in the silicon layer relative to the waveguide structures. This allows the accurate alignment of microdisk lasers with respect to the waveguides. The standard III-V processing steps comply with a 200-mm wafer scale CMOS environment. In particular, 248-nm DUV lithography is used to accurately define the III-V structures. All etching, oxide isolation layer deposition and metallization steps are performed at 200-mm wafer scale. Two dry etching steps are needed, one to define the disk cavity and another one to make the disk laser bottom contact area. SiO_2 is deposited as cladding layer and a CMP step is performed to planarize the surface. The low refractive index of the material ensures good optical confinement of the laser light in the microdisk laser. It also reduces the optical losses induced by the metallic top contact as the distance between the optical mode and the metal can be made large enough. To be able to contact the devices, all vias are etched in a single step where the III-V materials are used as an etch stop. The standard Ti/Pt/Au contacts cannot be used as gold is not allowed in a CMOS environment. A CMOS compatible Ti/TiN/AlCu (10:40:1000nm) metal stack is used [67], and demonstrates a very good specific contact resistance [68]. The 1μm-thick contact also serves as a heat sink as it improves the heat dissipation under continuous-wave bias. Full characterization of the sample has been carried out at Ghent University.

2.16 Discussion: successful fabrication of improved single devices heterogeneously integrated on SOI

The implementation of all the optimizations listed in the previous section has led to the successful fabrication of devices. In order to reduce the series resistance of a single device, the InP etch is intentionally stopping in the bottom contact quaternary layer (cf. Table 2.1). The bottom contact layer is then 100 to 120nm thick. Also, great effort has been dedicated to surface treatment of the III-V layers before metallic deposition. These modifications have led to a drastic reduction of the series resistance of a 7.5μm-diameter microdisk laser, as visible in Figure 2.59.

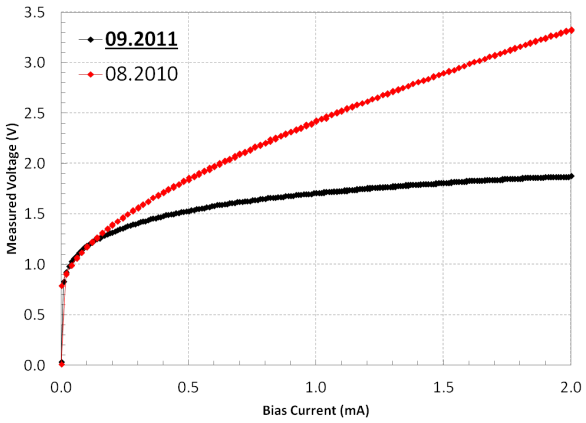

Figure 2.59: Reduction of the series resistance of a single microdisk laser. The red curve is the measured V-I graph of a 7.5μm-diameter microdisk laser processed in 2010, while the black curve is the measured resistance of a 7.5μm-diameter microdisk laser processed in 2011 with process optimization.

Thanks to the development of the ECI photoresist process, we successfully fabricated the smallest InP-based microdisk laser heterogeneously integrated on SOI. Figure 2.60 shows the optical spectrum of the 6μm-diameter microdisk laser. Continuous-wave and single-mode operation of the microdisk is demonstrated at 1546nm. The Free-Spectra-Range (FSR) of the device is 28nm and the Side-Mode-Suppression-Ratio (SMSR) is close to 19.8dB. We also demonstrated single-mode operation of a 7.5μm-diameter microdisk laser with a SMSR of 27.6dB, as depicted in Figure 2.61.

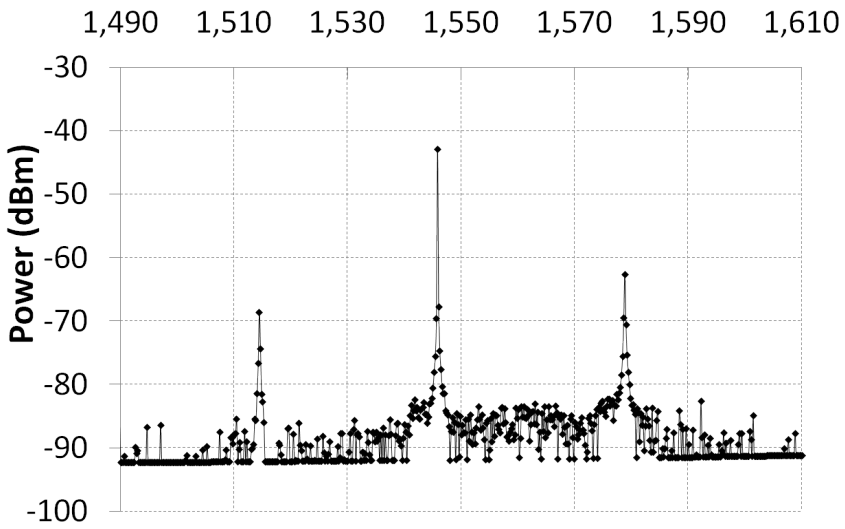

Figure 2.60: Continuous-wave and single-mode operation of a 6μm-diameter microdisk laser after implementation of a series of fabrication optimizations (x-axis: wavelength in nanometers).

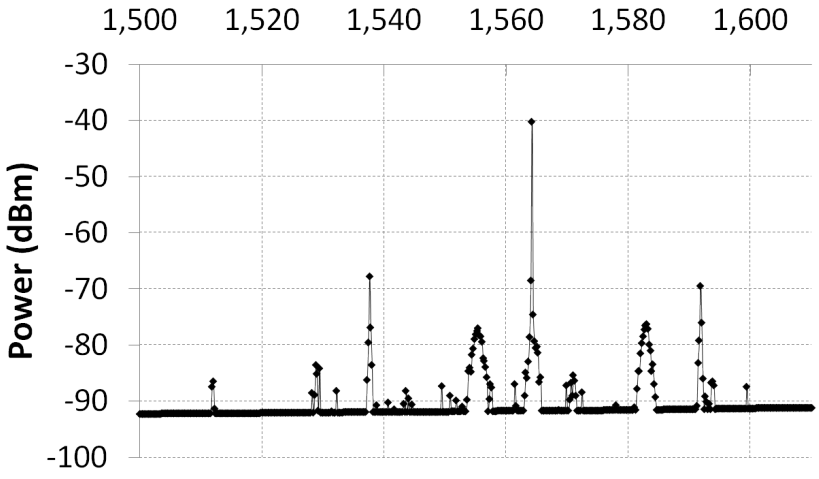

Figure 2.61: Continuous-wave and single-mode operation of a 7.5μm-diameter microdisk laser after implementation of a series of fabrication optimizations (x-axis: wavelength in nanometers).

We also demonstrate optically pumped InP-based microdisks integrated on SOI and processed with e-beam lithography. Detection of e-beam alignment markers has allowed the very accurate definition of microdisk lasers with respect to silicon wire waveguides. The achievable and reproducible standard deviation in their peak lasing wavelengths is lower than 500pm on the same chip, thanks to optimizations of the technology. The deviation in the diameter of the microdisks is as low as a few nanometers. The resulting hybrid structure combines advantages of both the III-V and the SOI platforms, offering the possibility to collect light from the SOI and also enabling optical pumping of the lasers through the very same passive circuit. We demonstrate a very accurate control of the lasing wavelength of the microdisk lasers, for a given offset of the microdisk versus the SOI waveguide and for a given microdisk diameter. One of the important design parameters for these structures remains the coupling between the access waveguide and the microdisk. Thanks to e-beam lithography, the resulting offset of the microdisk lasers is only tens of nanometers away from the target design value. The processing optimizations presented here also make the fabrication of complex functionalities for all-optical signal processing possible. Identical gates or logic blocks requiring cascaded microdisk lasers on the same chip can be concatenated without losing signal integrity.

References

[1] J. Van Campenhout. *Thin-Film microlasers for the integration of electronic and photonic integrated circuits.* Doctoral Thesis, Ghent University, 2007.

[2] M. Sorel, P. J. R. Laybourn, G. Giuliani, and S. Donati. *Ultra-Compact Integrated Optical Filters in Silicon-on-insulator by Means of Wafer-Scale Technology.* Doctoral Thesis, Ghent University, 2007.

[3] S. K. Selvaraja. *Wafer-Scale Fabrication Technology for Silicon Photonic Integrated Circuits.* Doctoral Thesis, Ghent University, 2011.

[4] O. W. Holland, D. Fathy, and D. K. Sadana. *Formation of ultrathin, buried oxides in Si by O[sup+] ion implantation.* Applied Physics Letters, 69(5):674–676, 1996.

[5] Kasamatsu Riyuusuke Aoki Yoshiro Murakami, Yoshio. *Using a rapid thermal process for manufacturing a wafer bonded SOI semiconductor.* 2009.

[6] B. Aspar, M. Bruel, H. Moriceau, C. Maleville, T. Poumeyrol, A. M. Papon, A. Claverie, G. Benassayag, A. J. AubertonHerve, and T. Barge. *Basic mechanisms involved in the Smart-Cut(R) process.* Microelectronic Engineering, 36(1-4):233–240, 1997.

[7] J. S.Raby George Bajor. *Using a rapid thermal process for manufacturing a wafer bonded SOI semiconductor.* 1988.

[8] T. Yonehara and K. Sakaguchi. *ELTRAN: Novel SOI Wafer Technology*. Japan Society of Applied Physics, 4:10–16, 2001.

[9] M. Bruel. *Silicon on insulator material technology*. Electronics Letters, 31:1201–1202, 1995.

[10] A. P. K. Graham T. Reed. *Silicon Photonics: The State of the Art*. 2004.

[11] S. K. Selvaraja, P. Jaenen, W. Bogaerts, D. Van Thourhout, P. Dumon, and R. Baets. *Fabrication of photonic wire and crystal circuits in Silicon-On-Insulator using 193-nm optical lithography*. Journal of Lightwave Technology, 27:4076–4083, 2009.

[12] S. K. Selvaraja, W. Bogaerts, and D. Van Thourhout. *Loss reduction in Silicon nanophotonic waveguide micro-bends through etch profile improvement*. Optics Communications, 284(8):2141–2144, 2011.

[13] W. Bogaerts, R. Baets, P. Dumon, V. Wiaux, S. Beckx, D. Taillaert, B. Luyssaert, J. Van Campenhout, P. Bienstman, D. Van Thourhout. *Nanophotonic Waveguides in Silicon-on-Insulator Fabricated with CMOS Technology*. Journal of Lightwave Technology, 23(1):401–412, 2005.

[14] G. Franz, and M.C. Amann. *Extremely low contact resistivity of Ti/Pt/Au contacts on p+-InGaAs as determined by a new evaluation method*. J. Electrochemical Soc., 140(3):847–850, 1993.

[15] W. Kern, and D. Puitonen. *RCA Review*. 31:187, 1970.

[16] W. Kern, and J. Vossen. *Handbook of semiconductor cleaning technology*. Thin Film Processes, 1993.

[17] S. Raghavan. *Wet etching and cleaning: surface considerations and process issues*. NSF/SRC Engineering Research Center for Environmentally Benign Semiconductor Manufacturing, 1999.

[18] S. K. Sahari, J. C. H. Sing, K. Ab. Hamid. *The effects of RCA Clean variables on particle removal efficiency*. World Academy of Science, Engineering and Technology, 26, 2009.

[19] Heyn. *Cost-effective cleaning and high quality thin gate oxides*. IBM Journal of Research and Development, 1999.

[20] P. H. L. Notten. *The etching of InP in HCl solutions: a chemical mechanism*. Journal of the Electrochemical Society: Solid-State Science and Technology, 131(11):2641–2644, 1984.

[21] S. K. Pearton. *Wet and dry etchings of compound semiconductors*.

[22] F. Fiedler, A. Schlachetzki, G. Klein. *Material-selective etching of InP and an InGaAsP alloy*. Journal of Materials Science, 17(10):2911–2918, 1982.

[23] Biacore, *http://terpconnect.umd.edu/ browns/wetetch.html*.

[24] Dow Company. *CYCLOTENE Advanced Electronic Resins: Processing procedures for BCB adhesion.* CYCLOTENE Advanced Electronic Resins, 2007.

[25] T. Spuesens. *Compact on-chip optical interconnects on silicon by heterogeneous integration of III-V microsources and detectors.* Doctoral Thesis, Ghent University, 2014.

[26] S. Keyvaninia. Doctoral Thesis, Ghent University, 2014.

[27] Dow Company. *Processing Procedures for CYCLOTENE Series Dry Etch Resins.*

[28] D. J. Hymes, M. Ravkin, W. C. Krusell, V. Noorai. *Method and apparatus for cleaning of semiconductor substrates using standard clean 1 (SC1).* US Patent 5858109, 1999.

[29] D. H. Kim, J. A. del Alamo, J. H. Lee, and K. S. Seo. *Logic suitability of 50nm* $In_{0.7}Ga_{0.3}As$ *HEMTs for beyond-CMOS applications.* IEEE Transactions on Electronic Devices, 54:2606–2613, 2008.

[30] W. Bogaerts, P. De Heyn, T. Van Vaerenbergh, K. De Vos, S. Selvaraja, T. Claes, P. Dumon, P. Bienstman, D. Van Thourhout, and R. Baets. *Silicon microring resonators.* Lasers and Photonics Reviews, 6(1):47–73, 2012.

[31] Z. Li, M. Mohamed, X. Chen, E. Dudley, K. Meng, L. Shang, A. R. Mickelson, R. Joseph, M. Vachharajani, B. Schwartz, and Y. Sun. *Reliability modeling and management of nanophotonic on-chip networks.* IEEE Trans. Very Large Scale Integr. (VLSI) Syst., 20(1):98–111, 2012.

[32] M. G. Young, T. L. Koch, U. Koren, D. M. Tennant, B. I. Miller, M. Chien, and K. Feder. *Wavelength uniformity in* $\lambda/4$ *shifted DFB laser array WDM transmitters.* Electron. Lett., 31(20):1750–1752, 1995.

[33] C.-C. Lin, M.-C. W, H.-H. Liao, and W.-H. Wang. *Highly uniform operation of high-performance 1.3*μ*m AlGaInAs-InP monolithic laser arrays.* IEEE J. Sel. Topics Quantum Electron., 36(5):590–597, 2000.

[34] T. L. Koch, P. J. Corvini, and U. Koren. *Wavelength uniformity of 1.3Îijm GaInAsP/InP distributed Bragg reflector lasers with hybrid beam/vapour epitaxial growth.* Electron. Lett., 24(13):822–824, 1988.

[35] Y. Muroya, T. Nakamura, H. Yamada, and T. Torikai. *Precise wavelength control for DFB laser diodes by novel corrugation delineation method.* IEEE Photonics Technol. Lett., 9(3):288–290, 1997.

[36] S. Srinivasan, A. W. Fang, D. Liang, J. Peters, B. Kaye, and J. E. Bowers. *Design of phase-shifted hybrid silicon distributed feedback lasers.* Opt. Express, 19(10):9255–9261, 2011.

[37] W. Yuen, G. S. Li, and C. J. Chang-Hasnain. *Multiple-wavelength vertical-cavity surface-emitting laser arrays.* IEEE J. Sel. Topics Quantum Electron., 3(2):422–428, 1997.

[38] H. Saito, I. Ogura, and Y. Sugimoto. *Uniform CW operation of multiple-wavelength vertical-cavity surface-emitting lasers fabricated by mask molecular beam epitaxy.* IEEE Photonics Technol. Lett., 8(9):1118–1120, 1996.

[39] N. C. Frateschi, and A. F. J. Levi. *Resonant modes and laser spectrum of microdisk lasers.* Appl. Phys. Lett., 66(22):2932–2934, 1995.

[40] A. Bazin. *III-V Semiconductor Nanocavities on Silicon-On-Insulator Waveguide: Laser Emission, Switching and Optical Memory.* Doctoral Thesis, Universite Paris VII - Denis Diderot, 2013.

[41] Gatech, *http://nanolithography.gatech.edu/training/focus_height.ppt.*

[42] Y. Halioua, T. Karle, F. Raineri, P. Monnier, I. Sagnes, R. Raj, G. Roelkens, and D. Van Thourhout. *Hybrid InP-based photonic crystal lasers on silicon on insulator wires.* Appl. Phys. Lett., 95(20):201119, 2009.

[43] T. J. Karle, Y. Halioua, F. Raineri, P. Monnier, R. Braive, L. Le Gratiet, G. Beaudoin, I. Sagnes, G. Roelkens, F. Van Laere, D. Van Thourhout, and R. Raj. *Heterogeneous integration and precise alignment of InP-based photonic crystal lasers to complementary metal-oxide semiconductor fabricated silicon-on-insulator wire waveguides.* Journal of Applied Physics, 107(6):063103, 2010.

[44] U. Niggebrugge, M. Klug, and G. Garus. . Inst. Phys. Conf Series, 79:367–372, 1985.

[45] T. R. Hayes, M. Dreisbach, P. Thomas, W. Dautremont-Smith, and L. A. Heimbrook. *Reactive ion etching of InP using* CH_4/H_2 *mixtures: Mechanisms of etching and anisotropy.* J. Vac. Sci. Technol., B(7):1130–1410, 1989.

[46] S. J. Pearton , U. K. Chakrabarti , A. Katz, A. P. Perley, W. S. Hobson, and C. Constantine *Comparison of* CH_4/H_2/Ar *reactive ion etching and electron cyclotron resonance plasma etching of In-based III-V alloys.* J. Vac. Sci. Technol., B(9):1421–1432, 1991.

[47] S. C. McNevin. *Chemical etching of GaAs and InP by chlorine: The thermodynamically predicted dependence on* Cl_2 *pressure and temperature.* J. Vac. Sci. Technol., B(4):1216, 1986.

[48] S. Guilet, S. Bouchoule, C. Jany, C. S. Corr, and P. Chabert. *Optimization of a* Cl_2/H_2 *inductively coupled plasma etching process adapted to nonthermalized InP wafers for the realization of deep ridge heterostructures.* Journal of Vacuum Science and Technology B: Microelectronics and Nanometer Structures, 24(5):2381–2387, 2006.

[49] S. Bouchoule, G. Patriarche, S. Guilet, L. Gatilova, L. Largeau, and P. Chabert. *Sidewall passivation assisted by a silicon coverplate during*

Cl_2/H_2 *and HBr inductively coupled plasma etching of InP for photonic devices.* Journal of Vacuum Science and Technology B: Microelectronics and Nanometer Structures, 26(2):666–674, 2008.

[50] L. Gatilova, S. Bouchoule, S. Guilet, and P. Chabert. *Investigation of inp etching mechanisms in a* Cl_2/H_2 *inductively coupled plasma by optical emission spectroscopy.* Journal of Vacuum Science and Technology A: Vacuum, Surfaces, and Films, 27(2):262–275, 2009.

[51] S. Bouchoule, S. Azouigui, S. Guilet, G. Patriarche, L. Largeau, A. Martinez, L. Le Gratiet, A. Lemaitre, and F. Lelarge. *Anisotropic and Smooth Inductively Coupled Plasma Etching of III-V Laser Waveguides Using HBr-*O_2 *Chemistry.* Journal of The Electrochemical Society, 155(10):778–785, 2008.

[52] M. Volatier, D. Duchesne, R. Morandotti, R. Ares, and V. Aimez. *Extremely high aspect ratio GaAs and GaAs/AlGaAs nanowaveguides fabricated using chlorine ICP etching with N2-promoted passivation.* Nanotechnology, 21(13):134014, 2010.

[53] S. M. Lee, D. G. Cahill, and T. H. Allen. *Thermal-conductivity of sputtered oxide-films.* Phys. Rev. B: Solid State, 52(1), 253–257, 1995.

[54] L. Liu, T. Spuesens, G. Roelkens, D. Van Thourhout, P. Regreny, and P. Rojo Romeo. *A thermally tunable microdisk laser built on a III-V/silicon-on-insulator heterogeneous integration platform.* IEEE Photonics Technol. Lett., 22:1270, 2010.

[55] S. Arafin, A. Bachmann, K. Kashani-Shirazi, S. Priyabadini, M.-C. Amann. *Low-resistive sulphur-treated ohmic contacts to n-type InAsSb.* IET Optoelectron., 3(6):259–263, 2009.

[56] T. Spuesens, D. Van Thourhout. *Analysis of loss contributions in InP-based microdisk lasers heterogeneously integrated with SOI.* Annual Symposium of the IEEE Photononics Benelux Chapter, 209–212, 2010.

[57] Carl L. Yaws. *Handbook of Thermal Conductivity.* 3:1–398, 1995.

[58] T. P. Pearsall. *Properties, processing and applications of Indium Phosphide.* IEE Inspec, 21, 2000.

[59] H. D. Young *University Physics 7th Ed.*. Addison Wesley:15–5, 1992.

[60] K. Koyama. *Thermal Conductivity of Magnesium Fluoride Between* 25° *and* 900°. Journal of the American Ceramic Society, 52(4):222–224, 1969.

[61] Hukseflux, *http://www.hukseflux.com/.*

[62] M. Vanwolleghem, P. Gogol, P. Beauvillain,W. Van Parys, and R. Baets. *Design and optimization of a monolithically integratable InP-based optical waveguide isolator.* Journal of the Optical Society of America B-Optical Physics, 24(1):94–105, 2007.

[63] Y. Lv, H. Tang, B. Han, X. Wu, K. Zhang, X. Li, and H. Gong. *Extremely low contact resistivity of Ti/Pt/Au contacts on p+-InGaAs as determined by a new evaluation method.* Proc. SPIE 6835, Infrared Materials, Devices, and Applications, 68350D, 2008.

[64] S. M. Sze. *Physics of Semiconductor Devices.* 1969.

[65] W. Shockley. *Research and investigation of inverse epitaxial UHF power transistors.* Report No. A1-TOR-64-207, Air Force Atomic Laboratory, 1964.

[66] F. Mandorlo, P. Rojo Romeo, N. Olivier, L. Ferrier, R. Orobtchouk, X. Letartre, J.- M. Fedeli, and P. Viktorovitch. *Controlled multi-wavelength emission in full CMOS compatible micro-lasers for on-chip interconnections.* J. Lightwave Technol., 30(19):3070–3080, 2012.

[67] L. Grenouillet, A. Bavencove, T. Dupont, J. Harduin, P. Philippe, P. Regreny, F. Lelarge, K. Gilbert, P. Grosse, and J. Fedeli. *CMOS compatible contacts and etching for InP-on-silicon active devices.* 6th IEEE Int. Conf. Group IV Photon. (GFP), 196–198, 2009.

[68] T. Spuesens, F. Mandorlo, P. Rojo-Romeo, P. Regreny, N. Olivier, J.M. Fedeli, and D. Van Thourhout. *Compact integration of optical sources and detectors on SOI for optical interconnects fabricated in a 200 mm CMOS pilot line.* J. Lightwave Technol., 30(11):1764–1770, 2012.

"It's time to wake up, it's time to change
Let's get it started, I feel like there's so much to rearrange"

The Futureheads, The Beginning Of The Twist, 2008

3

Unidirectionality in microdisk lasers

Directional bistability, i.e. the ability of a laser to operate either in the clockwise (CW) or counter-clockwise (CCW) mode, is a unique characteristic of ring and disk lasers [1]. The bistability of microring lasers was used to demonstrate optical switching and logic applications [2], [3]. This feature has also been observed in racetrack ring lasers and microring lasers built on a hybrid silicon platform [4], [5]. Bistability is useful for some applications, but is undesirable for microdisk lasers used in optical interconnects. Indeed, different devices belonging to the same design can lase in different directions or switch from one lasing direction to the other depending on the injection current and the temperature. Stable unidirectional lasing ensures a higher efficiency of the laser and has been demonstrated using several approaches. In this chapter, unidirectional lasing of single-mode hybrid silicon microdisk lasers operating in continuous-wave is demonstrated. Unidirectionality is achieved without extra power consumption or added complexity to the design as the system relies on a distributed Bragg reflector integrated in the silicon-on-insulator (SOI) circuit.

The acronyms CW and CCW are respectively referring to clockwise and counter-clockwise along this chapter.

3.1 State of the art in unidirectional lasers

A study of the multistable and excitable behavior in semiconductor ring lasers (SRL) with broken Z_2-symmetry has been performed by the Applied Physics Research Group of the Vrije Universiteit Brussel [6]. Bifurcation diagrams of the relative modal intensity as a function of the injection current are plotted. When operating close to the threshold, at low power, the laser operates bidirectionally with CW and CCW operating either in-phase or out-of-phase according to the difference in backscattering phase [7]. For large values of the pump parameter, the nonlinear gain saturation becomes the dominant coupling mechanism between the counterpropagating modes and two out-of-phase (inphase) new solutions can be found. In this region, the optical output power is mainly concentrated in one propagation direction, called unidirectional operation. When the device is symmetric two unidirectional solutions exist and the device exhibits bistability. For intermediate values of the pump parameter, the linear and nonlinear coupling are comparable and the dynamics of the system depends on the value of the difference in backscattering phase. Only for higher values of the pump current, the bidirectional solution disappears in a pitchfork bifurcation, after which it is demonstrated that a bistability between both unidirectional modes remains. When introducing asymmetry in the linear coupling between the two counter-propagating fields of the SRL, it has been demonstrated that the purely bidirectional solution does not exist anymore and that the pitchfork bifurcation (creating the unidirectional solutions in the symmetric case) is replaced by a fold bifurcation. The absence of the pitchfork bifurcation in the asymmetric case is of immediate relevance in the experimental measurements of light-current characteristics. When the asymmetry is non-negligible, it is shown that it is always either the CW or the CCW that is first created in a fold bifurcation.

Unidirectionality has been investigated and demonstrated in different configurations. “S-shape” ring resonator cavities are designed to introduce asymmetric coupling between the clockwise (CW) and the counter-clockwise (CCW) modes [8]. In order to increase the net modal gain in one direction, the injection of an optical pulse from an external laser or light emitting diode (LED) has also been used [1], [5], [9]. These approaches require an external light source or introduce additional optical loss, which either degrades the laser performance or increases the complexity of the total system and its power consumption. Another approach is to break the rotational symmetry by using deformed optical microcavities to increase the directionality of emission and power collection efficiency [10]. However, all deformed cavities have the problem that the quality factor (Q factor) significantly decreases as the deformation increases [11].

Highly unidirectional laser action from whispering-gallery modes has been demonstrated with an elliptical-shape quantum cascade laser microcavity with a wavelength-size notch at the boundary [12].

Another experimental approach is to rely on an integrated optical reflector, such as a teardrop reflector, at one end of the bus waveguide. The reflector induces the laser to emit light toward the other end. Compared with external injection from another laser, this approach does not require additional power consumption or additional complexity and is free of mismatch in wavelength between the two lasers. Unidirectional operation of a hybrid silicon microring laser coupled to a waveguide with such a teardrop reflector is investigated in [13]. However, the hybrid microring laser in that work had a diameter of 50μm, and was operated at 30mA bias current. Under these experimental conditions, unidirectionality was qualitatively demonstrated although the laser does not necessarily operate in single-mode operation.

In this chapter we demonstrate unidirectional lasing of single-mode hybrid silicon microdisk lasers operating in continuous-wave at room temperature. We provide quantitative experimental results as well as a numerical analysis. The devices have a diameter of 7.5μm and are electrically pumped. Extra power consumption and added complexity to the design are not necessary to achieve unidirectionality as the system relies on a distributed Bragg reflector integrated in the SOI circuit.

3.2 Device design and integration technology

We fabricated the unidirectional microdisk laser shown schematically in Figure 3.1. A microdisk is etched into an InP-based film that is bonded onto a patterned SOI waveguide structure. The InP etch is not complete so that an electrical bottom contact can be defined. The disk edge is laterally aligned to an underlying SOI wire waveguide (WG) with contact lithography.

The epitaxy consists of the 583nm thick InP-based membrane described in chapter 2. The microdisk lasers consist of a 483 nm thin disk cavity on top of a 100 nm thin InP bottom contact layer. The two levels are separated by a 50nm-thick DVS-BCB layer and 65nm of SiO_2 (n=1.47), allowing evanescent coupling to the underlying waveguide. The designed microdisk lasers have a diameter of 7.5μm. The SOI waveguides are fabricated in CEA-Leti using 248nm deep ultra-violet (DUV) lithography. The design of the passive SOI circuit for the considered device consists of a 600nm-wide waveguide (height of 220nm), embedded in SiO_2, tapered down on both sides to a 500nm-wide waveguide,

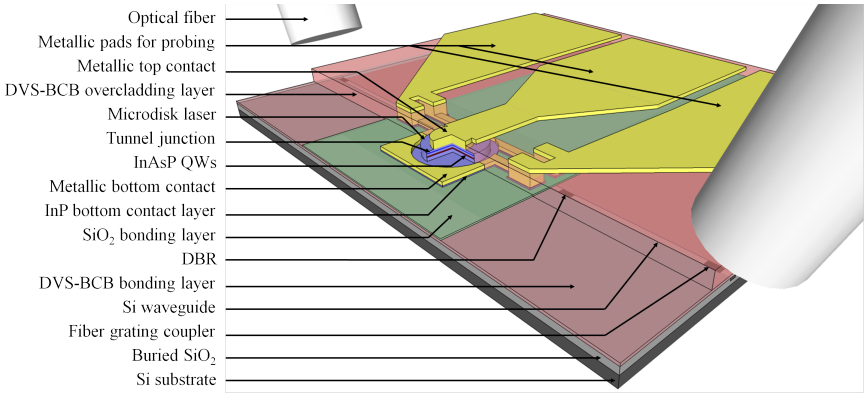

Figure 3.1: Schematic representation of an electrically-pumped heterogeneous SOI-integrated microdisk laser.

as depicted in Figure 3.2. The 500nm-wide waveguide is on one side tapered up to a 2μm-wide waveguide, itself tapered up to a shallow-etch (etching depth : 70nm out of the 220nm) grating coupler (GC) used to collect the laser emission from the microdisk out of the chip in a single-mode optical fiber [14]. The 500nm-wide waveguide is on the other side tapered up to a 2μm-wide waveguide, where a Distributed Bragg Reflector (DBR) structure is defined. A DBR implemented at one end of the bus waveguide forces the laser to emit light towards the other end. If the DBR structure is implemented in the CCW emission direction of the system, light emitted in the CCW mode is partially coupled back to the CW mode inside the microdisk laser. The power coupled back into the cavity leads to a photon density increase and unidirectional lasing in the desired direction. Compared with external injection from another laser this approach does not require additional power consumption and does not suffer from a potential mismatch in wavelength between the two lasers. Two DBR configurations are implemented. They are both shallow-etched and their fill-factor is 50%, but they differ in period. One of them has a period of 290nm, while the other one has a period of 300nm. The waveguide after the DBRs is in both cases further tapered to be able to define another grating coupler, used to collect the laser emission from the microdisk in a single-mode optical fiber. The fiber grating couplers are optimized to demonstrate a maximum coupling efficiency at 1.55μm. Above threshold, the laser emission from the microdisk is coupled to the TE mode of the waveguide, and is simultaneously collected out of both grating couplers in optical fibers under a 10° angle in order to maximize the collection at 1.55μm. The DBR is in both cases designed to be 55μm away from the middle of the 600nm-wide waveguide section.

Prior to bonding, 65nm of SiO_2 is deposited on the unprocessed InP die. The III-V die is positioned upside down on top of the SOI waveguide circuit, on which DVS-BCB has been spin-coated, and the resulting bonded structure is cured. After the bonding process, the InP substrate is wet etched until only the desired epitaxial structure remains. Alignment markers for subsequent processing are defined in the Silicon layer relative to the waveguide structures. This allows the accurate alignment of the microdisk lasers with respect to the waveguides. A nitride hard mask is deposited by PECVD on top of the epitaxy. This layer also protects the DVS-BCB and underlying silicon waveguides in the following processing steps. The pattern is transferred into the nitride mask using Reactive Ion Etching and the microdisks are patterned in the III-V membrane using Inductively Coupled Plasma (ICP) etching. The etching is monitored in order to leave 100nm of n+-doped InP as a bottom contact layer.

The next step consists in defining the metallic bottom contact with lift-off. A thin layer of Ti (40nm) is first deposited to enhance the adhesion of the metal on top of the III-V material. 50nm of Platinum and a thick Gold layer (100nm) are further deposited to finish the bottom contact definition. In order to separate two adjacent microdisk lasers, the InP bottom contact layer between them is etched with ICP. The sample is then planarized by spin-coating and curing undiluted DVS-BCB. The low refractive index of this material ensures good optical confinement of the laser light in the microdisk laser. It also reduces the optical losses induced by the metallic top contact as the distance between the optical mode and the metal can be made large enough. The next steps consist in opening vias in the overcladding DVS-BCB layer in order to access the metallic bottom contact and to deposit the metallic top contact with lift-off (similar recipe as for the bottom contact). Finally, a layer of gold, 800nm thick, is deposited on the sample to define metallic pads that will be used to individually probe each microdisk laser. The thick contact also serves as a heat sink as it improves the heat dissipation under continuous-wave bias. From several cross-sections performed with Focused-Ion-Beam (FIB), we can conclude that the total bonding thickness is uniform everywhere on the sample (115nm above the waveguides). The DVS-BCB overcladding layer above the edge of the microdisk laser is 900nm thick. Figure 3.3 is a microscope image of the sample where the processed microdisk lasers can be seen. The image also illustrates the high potential for dense integration of microdisk lasers on a silicon photonic integrated circuit.

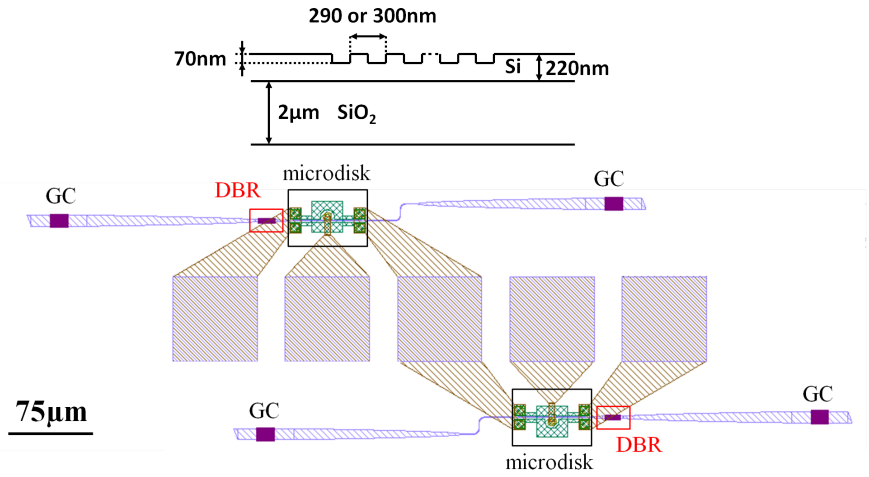

Figure 3.2: Schematic cross-section of the DBR (up) and top view of the design of the fabricated unidirectional microdisk lasers (down). The DBR structure on the top WG has a period of 300nm, while the one on the bottom WG has a period of 290nm.

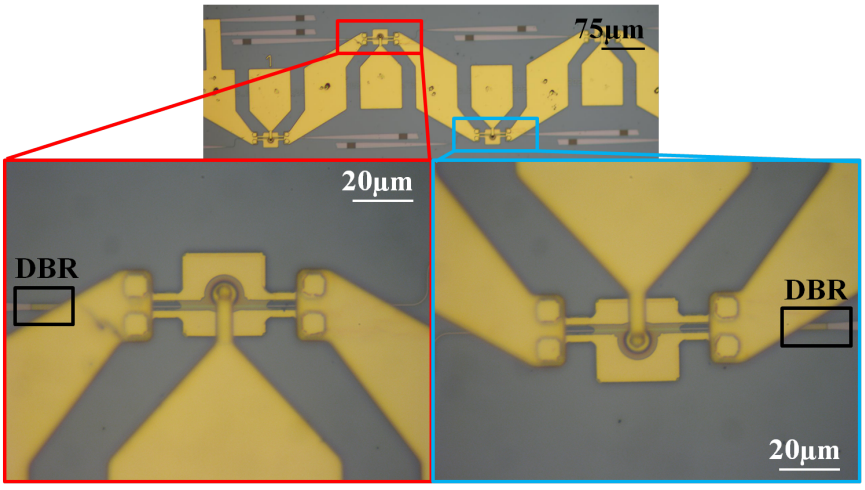

Figure 3.3: Microscope pictures of the fabricated unidirectional devices. The DBR structure can be seen on one side of the waveguide.

3.3 Simulation of the unidirectional behavior

We calculate the reflection and the transmission characteristics of the two DBR structures using CAMFR [15], a fully-vectorial solver based on eigenmode expansion and mode propagation with perfectly matched layer (PML) boundary conditions. We studied in both cases a one-dimensional planar DBR under TE polarization (electric field parallel to the grating lines), with a groove depth of 70nm, a fill-factor of 50%, and 50 periods. For our simulations, we used refractive indices n_{Si} = 3.476 and n_{SiO_x} = 1.444 for silicon and silicon oxide respectively. For both DBRs, the top cladding consists of 200nm of SiO_x. One DBR is simulated with a pitch of 300nm, while the other one is simulated with a pitch of 290nm. The simulations presented in Figure 3.4 demonstrate that the scattering losses at the lasing wavelength of the microdisk lasers are not different between the two DBR structures.

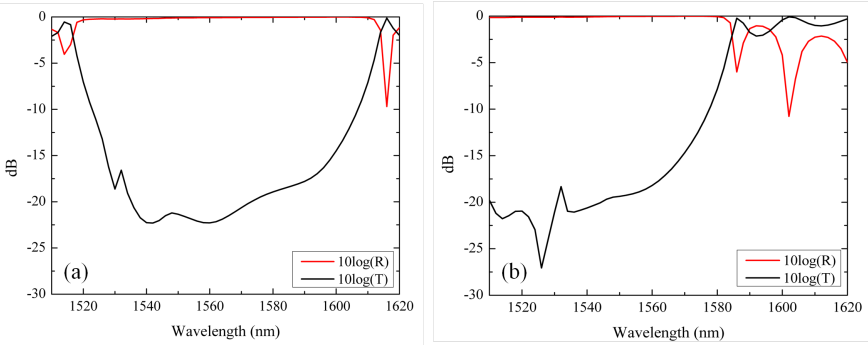

Figure 3.4: Simulated reflection and transmission characteristics of the two DBR structures using CAMFR : (a) DBR with a pitch of 300nm, (b) DBR with a pitch of 290nm.

An approximate analytical solution of the whispering gallery modes can be found by solving the Helmholtz equation in cylindrical coordinates. Because microdisk lasers do not have facets through which the light can be coupled out, an evanescent coupling towards a neighboring waveguide is assumed in this theoretical approach. To explain the directional behavior of the microdisk lasers, we formulate the rate equations in terms of two counterpropagating whispering gallery modes with electric fields E^+ and E^-. The spontaneous emission of the microdisk laser is implemented in two electric fields E_{noise1} and E_{noise2} where E_{noise}=$RR.n.e^{2j\pi n'}$, with RR representing the spontaneous emission amplitude and n and n' random numbers between 0 and 1. Referring to section 1.3.2 for a detailed description of the parameters, we find [16], [17]:

$$\frac{dE^+}{dt} = \frac{1}{2}(1-j\alpha)\left[G^+ - \frac{1}{\tau_p}\right]E^+ + E_{noise1} + KE^- \tag{3.1}$$

$$\frac{dE^-}{dt} = \frac{1}{2}(1-j\alpha)\left[G^- - \frac{1}{\tau_p}\right]E^- + E_{noise2} + KE^+ \tag{3.2}$$

For the carrier density rate equation, we find:

$$\frac{dN}{dt} = \frac{I}{qV} - \frac{N}{\tau_c} - G^+\left|E^+\right|^2 - G^-|E^-|^2 \tag{3.3}$$

I denotes all injected current and τ_c is the carrier lifetime. The gain experienced in a semiconductor material decreases for high optical intensity. This is due to gain suppression. Gain suppression takes place even when the total carrier density N is constant and reflects the reduction of "resonant carriers" due to carrier heating and spectral hole burning. To account for this effect, a gain suppression is added in the denominator of the expression of the modal gain, that is linearized to:

$$G^+ = \Gamma g_0 v_g (N-N_0)(1-\epsilon_s\left|E^+\right|^2 - \epsilon_c|E^-|^2) \tag{3.4}$$

$$G^- = \Gamma g_0 v_g (N-N_0)(1-\epsilon_s|E^-|^2 - \epsilon_c\left|E^+\right|^2) \tag{3.5}$$

where ϵ_s reflects the self-gain suppression and ϵ_c the cross-gain suppression. Calculations have shown that $\epsilon_c = 2\epsilon_s$ [18], [19]. The cross-gain suppression ϵ_c will therefore break the symmetry and enforce unidirectional operation of the laser. The gain suppression is, however, only significant when the photon density is high. This means that at lower output powers, normally a bidirectional regime will be present.

Table 3.1 summarizes the parameters implemented in the numerical solving of the above set of equations. The value for the linear coupling coefficient K is chosen so that the simulation matches the experimental results.

After finding local extrema and stable solutions, the bifurcation diagram as a function of bias current is depicted in Figure 3.5. We can distinguish between three different regimes. The first regime, just after threshold, is the bidirectional regime. As the optical power is low, non-linear effects can be neglected and inter-modal coupling is the dominant effect, causing the two counterpropagating modes to be equally present. When the injection current is increased, we can have a bidirectional oscillating regime. The competition between linear coupling and non-linear gain suppression results in an oscillating behavior [16], [21]. In this regime, the intensities of the two counterpropagating modes are modulated with harmonic sinusoidal oscillations and share the same oscillation frequency which lies in the GHz range. The modulation is out of phase

Symb.	*Name of the parameter*	*Value*	*Unit*	
τ_p	Photon lifetime	4.17	ps	[20]
τ_c	Carrier lifetime	600	ps	[20]
α	Linewidth enhancement factor	4		
v_g	Group velocity in the microdisk	$3x10^8/3.4$	m/s	[20]
ϵ_s	Self-gain suppression	$0.1x10^{-18}$	cm^{-3}	
ϵ_c	Cross-gain suppression	$2 \times 0.1x10^{-18}$	cm^{-3}	
g_0	Differential gain	$1x10^{-16}$	cm^2	
N_0	Transparency carrier density	$1.5x10^{18}$	cm^{-3}	[20]
RR	Spontaneous emission amplitude	2	s^{-1}	
K	Explicit normalized linear coupling rate CW and CCW	$(1.4+7.1j)\frac{v_g}{2\pi R}.10^{-5}$	s^{-1}	[20]

Table 3.1: Parameters considered for the simulation of the bifurcation diagrams of the microdisk lasers

on both outputs which means that the power in one mode is high when it is low in the other mode. The graph depicts the maximal and minimal values of the mode intensities. The last regime corresponds to the unidirectional operation where the initial conditions determine which of the two modes is dominant [1]. Non-linear gain suppression is now dominant and one mode suppresses the other, resulting in unidirectional behavior. The CW mode becomes dominant in Figure 3.5a, while the CCW mode becomes dominant in Figure 3.5b, depending on the initial conditions. The noise generated by the spontaneous emission, and represented by the fields E_{noise1} and E_{noise2} in equations 3.1 and 3.2, will determine if the laser lases preferentially in the CW or the CCW mode.

Figure 3.6 illustrates the simulated bifurcation diagram of the microdisk laser, calculated with the parameters from Table 3.1, except that no gain suppression has been taken into account this time. Without gain suppression in the microdisk cavity, the laser will not lase unidirectionally.

A passive optical reflector is now added to the CCW emission direction of the system, feeding laser emission propagating in the CCW direction back into the laser cavity. To simulate this effect, a new term is added to the calculation of the field propagating in the CW direction.

$$\frac{dE^+}{dt} = \frac{1}{2}(1-j\alpha)\left[G^+ - \frac{1}{\tau_p}\right]E^+ + E_{noise1} + (K + r.e^{j\phi})E^- \quad (3.6)$$

$$\frac{dE^-}{dt} = \frac{1}{2}(1-j\alpha)\left[G^- - \frac{1}{\tau_p}\right]E^- + E_{noise2} + KE^+ \quad (3.7)$$

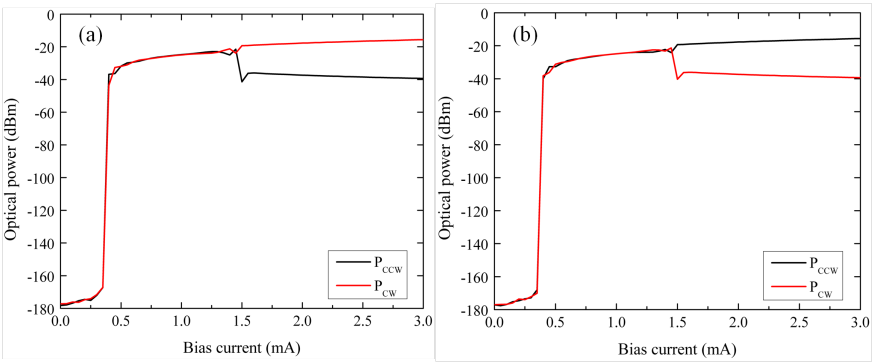

Figure 3.5: Simulated bifurcation diagrams of a 7.5μm-diameter disk when gain suppression is taken into account. The optical power in the CW mode is plotted in red, and the optical power in the CCW mode is plotted in black. Depending on initial conditions, one of the modes becomes dominant and suppresses the other at high bias current ((a) The CW mode becomes dominant, (b) The CCW mode becomes dominant.

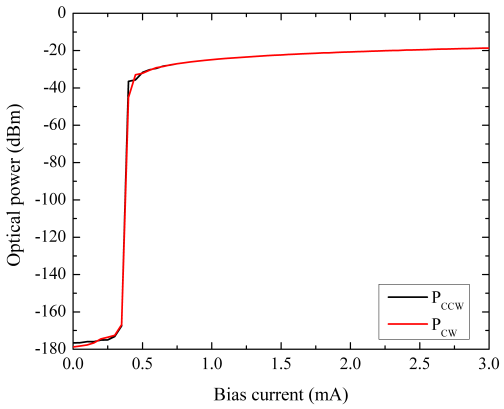

Figure 3.6: Simulated bifurcation diagrams of a 7.5μm-diameter disk : no gain suppression has been taken into account in the simulation. The optical power in the CW mode is plotted in red, and the optical power in the CCW mode is plotted in black. Unidirectional operation of the laser is not achieved without gain suppression in the microdisk cavity.

The reflectivity from the bus waveguide is implemented so that the reflection induced by the DBR structure is simulated as $r.e^{j\phi}$, where r represents the amplitude of the field reflection ($\frac{r_{DBR}\kappa^2}{\tau_{rnd}}$, with r_{DBR} is the reflection of the DBR structure and τ_{rnd} is the roundtrip time in the cavity equal to $\frac{2\pi R}{v_g}$). ϕ represents the phase of the reflected signal. Figure 3.7 illustrates the resulting bifurcation diagrams for different values of r and ϕ. On Figure 3.7a, the phase is kept constant ($\phi = 2\pi$) and the parameter r is swept amongst the values (0; 0.01; 0.1; 1). For r=0, the typical bifurcation diagram plotted in Figure 3.5 is obtained. Even for the lowest value of r, all the optical power is coupled to the CW mode of the microdisk laser and a unidirectional regime is present. As the value of r increases, the extinction ratio of the optical power in the CW mode and the optical power in the CCW mode increases. On Figure 3.7b, the phase is kept constant ($\phi = \frac{\pi}{2}$) and the parameter r is swept amongst the same previous values. We observe that all the optical power is also coupled to the CW mode of the microdisk laser as soon as an external reflection is added to the simulation. The extinction ratio of the optical power in the CW mode and the optical power in the CCW mode increases as a function of r.

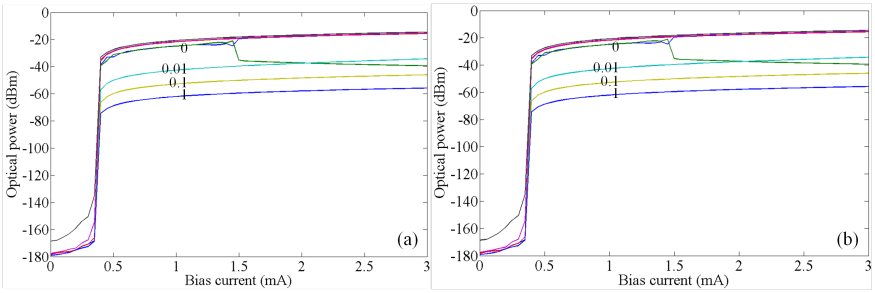

Figure 3.7: Simulated bifurcation diagrams of a 7.5μm-diameter disk coupled to a straight waveguide where a Bragg reflector is implemented on the CCW propagation direction of the system. All the power is coupled to the CW mode as soon as an external reflection is added to the system. (a) Bifurcation diagrams with a phase $\phi = 2\pi$ for increasing values of r. (b) Bifurcation diagrams with a phase $\phi = \frac{\pi}{2}$ for increasing values of r.

The feedback as well as the extra phase introduced by the DBR structure do not have a large impact on the threshold of the microdisk laser, as visible on Figure 3.7. This can be theoretically demonstrated in the static case by calculating the threshold gain of a microdisk laser from the coupled rate equations for the complex field amplitudes E_{CW} and E_{CCW} of the clockwise and counter clockwise propagating laser modes. We have normalized the optical fields such that their squared amplitude is equal to the photon number S. The coupling coefficients

K_i are the total field reflection (including phase) seen by the CW and the CCW mode divided by the roundtrip time of the microdisk. They include scattering due to sidewall roughness as well as reflections from facets or gratings in the bus waveguide.

$$\frac{dE_{CW}}{dt} = \frac{1}{2}(1-j\alpha)\left[G_{CW}-\frac{1}{\tau_p}\right]E_{CW}+K_1E_{CCW} \tag{3.8}$$

$$\frac{dE_{CCW}}{dt} = \frac{1}{2}(1-j\alpha)\left[G_{CCW}-\frac{1}{\tau_p}\right]E_{CCW}+K_2E_{CW} \tag{3.9}$$

with

$$E_{CW} = \sqrt{S_{CW}}e^{j\varphi_{CW}} \tag{3.10}$$

$$E_{CCW} = \sqrt{S_{CCW}}e^{j\varphi_{CCW}} \tag{3.11}$$

$$K_i = |K_i|exp^{j\phi_i} \tag{3.12}$$

$$\Delta\varphi = \varphi_{CW}-\varphi_{CCW} \tag{3.13}$$

$$\frac{S_{CW}}{S_{CCW}} = \mu^2 \tag{3.14}$$

In the static case, this results in:

$$j\frac{d\varphi_{CW}}{dt} = \frac{1}{2}(1-j\alpha)\left[G_{CW}-\frac{1}{\tau_p}\right]+\frac{K_1}{\mu}e^{-j\Delta\varphi} \tag{3.15}$$

$$j\frac{d\varphi_{CW}}{dt} = \frac{1}{2}(1-j\alpha)\left[G_{CW}-\frac{1}{\tau_p}\right]+\frac{|K_1|}{\mu}e^{j(\phi_1-\Delta\varphi)} \tag{3.16}$$

and

$$j\frac{d\varphi_{CCW}}{dt} = \frac{1}{2}(1-j\alpha)\left[G_{CCW}-\frac{1}{\tau_p}\right]+K_2\mu e^{j\Delta\varphi} \tag{3.17}$$

$$j\frac{d\varphi_{CCW}}{dt} = \frac{1}{2}(1-j\alpha)\left[G_{CCW}-\frac{1}{\tau_p}\right]+|K_2|\mu e^{j(\Delta\varphi+\phi_2)} \tag{3.18}$$

We can now decompose the equations for the complex electrical fields into amplitude and phase equations. As we consider the static case, the field amplitudes (and photon numbers S) are constant in time.

$$G_{CW}-\frac{1}{\tau_p} = -2\frac{|K_1|}{\mu}\cos(\Delta\varphi-\phi_1) \tag{3.19}$$

$$G_{CCW}-\frac{1}{\tau_p} = -2|K_2|\mu\cos(\Delta\varphi+\phi_2) \tag{3.20}$$

One important characteristic of ring or disk lasers is that the gain for the CW and CCW mode experiences different gain suppression.

$$G_{CW} = \frac{G_0(N)}{1+\epsilon S_{CW}+2\epsilon S_{CCW}} \tag{3.21}$$

$$G_{CCW} = \frac{G_0(N)}{1+2\epsilon S_{CW}+\epsilon S_{CCW}} \tag{3.22}$$

This gain suppression is typically symmetric around the laser line, such that there is no effect on the refractive index (or on the phase). We then take a look at the phase equations resulting respectively from 3.15 and 3.17 and $\Delta\omega$ equals:

$$\frac{d\varphi_{CW}}{dt} = \Delta\omega = \frac{\alpha}{2}\left[G_0 - \frac{1}{\tau_p}\right] - \frac{|K_1|}{\mu}\sin(\Delta\varphi - \phi_1) \tag{3.23}$$

$$\frac{d\varphi_{CCW}}{dt} = \Delta\omega = \frac{\alpha}{2}\left[G_0 - \frac{1}{\tau_p}\right] + |K_2|\mu\sin(\Delta\varphi + \phi_2) \tag{3.24}$$

In a microdisk laser coupled to a reflector on one side of the bus waveguide, one can assume that K_2 is due to the sidewall roughness and residual facet reflection, while K_1 also includes reflection from the passive reflector (e.g. Bragg reflector) in the bus waveguide and is much larger than K_2. With κ being the coupling between the ring/disk and the bus waveguide and r_1 the field reflection in the bus waveguide, one can write:

$$K_1 = K_2 + \kappa^2 \frac{r_1 v_g}{\pi D} \tag{3.25}$$

where D is the diameter of the ring/disk and v_g is the group velocity in the laser cavity. The parameter r_1 should also include the phase delay due to the propagation between the microdisk and the reflector.

We will first derive $\Delta\varphi$ and μ from the equations for bias currents close to the threshold current, where gain suppression can be neglected (G_{CW}=G_{CCW}=$G_0(N)$). From 3.23, 3.24, and while substracting 3.19 and 3.20 for ϵ =0, one finds respectively:

$$|K_1|\sin(\Delta\varphi - \phi_1) = -|K_2|\mu^2\sin(\Delta\varphi + \phi_2) \tag{3.26}$$

$$|K_1|\cos(\Delta\varphi - \phi_1) = |K_2|\mu^2\cos(\Delta\varphi + \phi_2) \tag{3.27}$$

Dividing the equations 3.26 and 3.27 results in:

$$\tan(\Delta\varphi - \phi_1) = -\tan(\Delta\varphi + \phi_2) \tag{3.28}$$

$$\Delta\varphi = \frac{\phi_1 - \phi_2}{2} + m\pi, m \in \|0,1\| \tag{3.29}$$

Substituting $\Delta\varphi$ in 3.26 and 3.27 readily gives:

$$\mu^2 = \frac{S_{CW}}{S_{CCW}} = \frac{|K_1|}{|K_2|} \tag{3.30}$$

which shows that the powers in the CW and the CCW modes are in the same ratio as their respective field reflection coefficients. Finally, substituting equations 3.29 and 3.30 in equations 3.19 and 3.20 for bias currents close to the threshold current, one finds:

$$G_0 = \frac{1}{\tau_p} - 2\sqrt{|K_1||K_2|}\left|\cos\left(\frac{\phi_1+\phi_2}{2}\right)\right| \tag{3.31}$$

The photon lifetime in the simulations is 4.17ps. The first term of the threshold gain is then in the order of $10^{12}\mathrm{s}^{-1}$. On the other hand, the second term of the threshold gain is in the order of 10^9 to $10^{10}\mathrm{s}^{-1}$ in case of strong back reflection, which makes its influence, including the one from the phase factor, negligible.

For the frequency deviation caused by the noise and the external feedback, we find from 3.23 and 3.24:

$$\Delta\omega = -\sqrt{|K_1K_2|}\left\{\alpha\cos\left(m\pi - \frac{\phi_1+\phi_2}{2}\right) + \sin\left(m\pi - \frac{\phi_1+\phi_2}{2}\right)\right\} \tag{3.32}$$

$$\Delta\omega = -\sqrt{|K_1K_2|(1+\alpha^2)}\sin\left(m\pi - \frac{\phi_1+\phi_2}{2} + \arctan\alpha\right) \tag{3.33}$$

A typical value for K_2 is $6{,}29.10^9\mathrm{s}^{-1}$ [3]. For a microdisk laser with a diameter of 10μm diameter, a group index of 3 and 2% of coupling between the microdisk and the bus waveguide, we find for K_1 the value of 0,02. $10^{14}\mu\mathrm{m/s}/(\pi 10\mu\mathrm{m})$, i.e. $6{,}36.10^{10}\mathrm{s}^{-1}$. This gives a ratio $|\frac{K_1}{K_2}|$ of about 10.

Simulations demonstrate that integrating a reflector on one side of the waveguide to which the microdisk is coupled feeds laser emission back into the laser cavity. This introduces an extra unidirectional gain and results in unidirectional emission of the laser. From the above equations, we can conclude that there are two main effects in the coupling between the two modes. The cross-gain suppression prohibits the counterpropagating cavity mode to build up. This effect is necessary for unidirectional operation, but a low value of the linear coupling K ($K = K_\mathrm{d} + jK_\mathrm{c}$) also favors unidirectional operation. The dissipative coupling K_d and the conservative coupling K_c describe the effects of parasitic reflection due to sidewall roughness. We can simulate the effect of the linear coupling K on the bifurcation diagram of a microdisk laser. In Figure 3.8, we plot the extinction ratio in dB of the optical powers $P_\mathrm{CW}/P_\mathrm{CCW}$ as a function

of the ratio of $|K|$ expressed in table 3.1 over the reflection from the bus waveguide r, when the microdisk is biased at 1mA. The phase ϕ is kept constant while the amplitude of the field reflection r is swept.

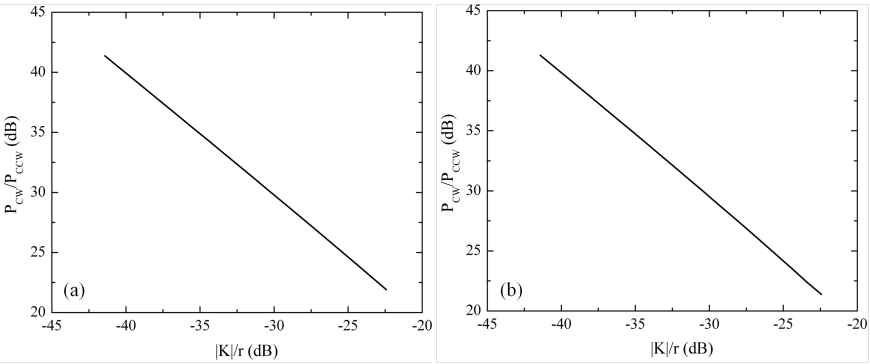

Figure 3.8: Ratio of optical powers in the CW and the CCW modes as a function of the ratio of linear coupling between the modes over the amount of external reflection from the bus waveguide induced by the DBR. (a) For a phase $\phi = 2\pi$ and values of r between 0.01 and 1. (b) For a phase $\phi = \frac{\pi}{2}$ for values of r between 0.01 and 1.

3.4 Analytical description above threshold, including gain suppression

In this section, a theoretical derivation that allows to derive the ratio of the powers in the CW and the CCW directions is given. We also provide, form the same analysis, useful expressions for the feedback sensitivity of a microdisk laser diodes. Studies of the feedback sensitivity of microring or microdisk laser diodes have not been reported so far. Below is the analysis reported for microdisk laser diodes, but the theoretical conclusions are also valid for microring laser diodes.

3.4.1 Low power limit

In section 3.3, we demonstrate that for bias currents close to the threshold current the feedback and the extra phase introduced by the DBR structure do not have a large impact on the threshold gain. Gain suppression is then indeed neglected. At higher bias currents, gain suppression must be included in the calculations. Relying on the definition of variables as described in 3.3, equation

3.26 is in this case not modified, but equation 3.27 must be replaced by, considering ϵ' equal to $\frac{\epsilon}{1+3\epsilon S_{CW}+3\epsilon S_{CCW}}$:

$$\epsilon' G_0(S_{CW}-S_{CCW}) = 2|K_2|\mu\cos(\Delta\varphi+\phi_2)-\frac{2}{\mu}|K_1|\cos(\Delta\varphi-\phi_1) \quad (3.34)$$

$$\epsilon' G_0(S_{CW}-S_{CCW}) = 2|K_2|\mu\frac{\sin(2\Delta\varphi+\phi_2-\phi_1)}{\sin(\Delta\varphi-\phi_1)} \approx \epsilon' G_0 S_{CW} \quad (3.35)$$

We now consider the case with μ»1, i.e. $|K_1|$»$|K_2|$, and thus can neglect S_{CCW}. To take into account the gain suppression, we introduce the approximations:

$$\mu^2 = \frac{|K_1|}{|K_2|}(1+\delta) \quad (3.36)$$

$$\Delta\varphi = \frac{\phi_1-\phi_2}{2}+\delta\varphi \quad (3.37)$$

with δ and $\delta\varphi$ being small. When substituting these expansions to equation 3.26, it is possible to express $\delta\varphi$ as:

$$\delta\varphi = -\frac{\delta}{2}\tan\left(\frac{\phi_1+\phi_2}{2}\right) \quad (3.38)$$

Substituting this result in equation 3.35 gives:

$$\epsilon' G_0 S_{CW}\cos\left(m\pi-\frac{\phi_1+\phi_2}{2}\right) = 2\delta\sqrt{|K_1||K_2|} \quad (3.39)$$

and thus:

$$\mu^2 = \frac{|K_1|}{|K_2|}\left(1+\frac{\epsilon' G_0 S_{CW}\cos\left(m\pi-\frac{\phi_1+\phi_2}{2}\right)}{2\delta\sqrt{|K_1||K_2|}}\right) \quad (3.40)$$

$$\Delta\omega = \epsilon' G_0 S_{CW} - \sqrt{\frac{|K_1K_2|(1+\alpha^2)}{1+\delta}}\sin\left(m\pi-\frac{\phi_1+\phi_2}{2}+\arctan\alpha+\delta\varphi\right) \quad (3.41)$$

For a numerical example, we consider a microdisk with a diameter of 10μm, where $|K_1|$ and $|K_2|$ are $6{,}36.10^{10}s^{-1}$ and $6{,}36.10^{9}s^{-1}$ respectively. In Figure 3.9, we plot the values of μ^2 obtained for two different values of ϵ, $1.10^{-18}cm^3$ (squares) and $2.10^{-18}cm^3$ (rhombuses), and for two different values of (ϕ_1,ϕ_2), $(0,0)$ (squares and rhombuses) and $(0,\frac{\pi}{2})$ (triangles) respectively. The solid lines with symbols represent the values obtained from a numerical time domain simulation of the coupled equations 3.1 and 3.2, while the dashed lines represent

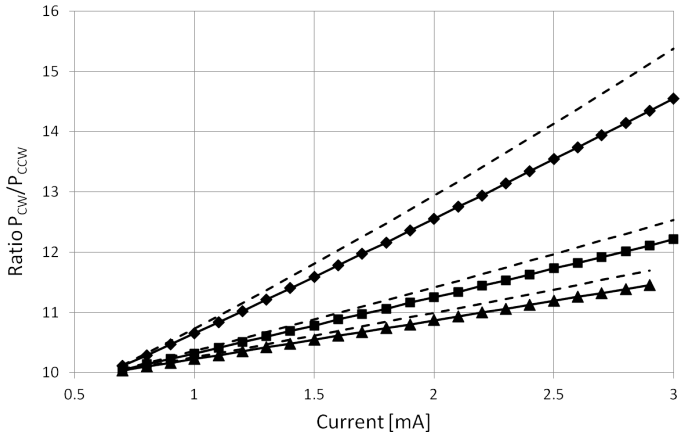

Figure 3.9: Ratio of power in the CW and CCW modes of a microdisk laser at low powers, obtained from a numerical solution of the coupled rate equations, for a microdisk laser with coupling coefficients K_1=6.10^{10}s^{-1}, and K_2=6.10^{9}s^{-1} (rhombuses) for (ϕ_1,ϕ_2)=(0,0) and ϵ=2.10^{-18}cm^3, (squares) for (ϕ_1,ϕ_2)=(0,0) and ϵ=1.10^{-18}cm^3, (triangles) for (ϕ_1,ϕ_2)=(0,π/2) and ϵ=1.10^{18}cm^3. The dashed lines are the approximation as obtained by equation 3.41.

the values obtained using equation 3.41. The approximation can be made even better by replacing S_{CW} by $S_{CW}(1-\left|\frac{K_2}{K_1}\right|)$.
For the special case $\phi_1+\phi_2$ equals π, and for ϵ equal to 0, one finds from equation 3.27 that:

$$\Delta\varphi-\phi_1 = \pm\frac{\pi}{2} \tag{3.42}$$

$$\cos(\Delta\varphi-\phi_1) = 0 \tag{3.43}$$

Although one finds from equation 3.26 that μ^2 equals $\left|\frac{K_1}{K_2}\right|$, we obtain from the time domain numerical analysis a self-pulsating behaviour irrespective of the value of ϵ. It is emphasized that the above approximations are only valid as long as δ is small, i.e. as long as $\epsilon G_0 S_{CW}$ is smaller than $2\sqrt{|K_1||K_2|}$.

3.4.2 High power limit

For high power levels or low coupling constants K_1 and K_2, the factor $\epsilon G_0 S_{\mathrm{CW}}$ is much larger than $2\sqrt{|K_1||K_2|}$, and in this case we can assume that μ^2 is much larger than $\frac{|K_1|}{|K_2|}$. From equation 3.26, it then follows that:

$$\Delta\varphi + \phi_2 = 0 \tag{3.44}$$

$$\Delta\varphi - \phi_1 = -(\phi_1 + \phi_2) \tag{3.45}$$

When substituting in equation 3.34, we have:

$$\epsilon' G_0 S_{CW} = 2|K_2|\mu - \frac{2}{\mu}|K_1|\cos(\phi_1 + \phi_2) \tag{3.46}$$

$$\mu = \frac{\epsilon' G_0 S_{CW}}{4|K_2|} + \frac{\sqrt{(\epsilon' G_0 S_{CW})^2 - 8|K_2|\epsilon' G_0 S_{CW} + 16|K_2 K_1|\cos(\phi_1 + \phi_2)|}}{4|K_2|} \tag{3.47}$$

$$\mu \approx \frac{\epsilon' G_0 S_{CW}}{2|K_2|} \tag{3.48}$$

$$\Delta\omega = \epsilon' G_0 S_{CW} + \frac{2|K_1 K_2|}{\epsilon' G_0 S_{CW}}\sqrt{(1+\alpha^2)}\sin(\phi_1 + \phi_2 - \arctan\alpha) \tag{3.49}$$

Figure 3.10 shows μ^2 obtained from a time domain numerical solution of the coupled wave equations 3.1 and 3.2 up to higher current levels for the case, K_1 equals 6,36.$10^8 s^{-1}$, K_2 equals to 3,18.$10^8 s^{-1}$, and ϵ equals to 1.$10^{-18} cm^3$ as well as the results for currents above 2.5mA obtained using equation 3.49. Although the ratio K_1 over K_2 is only 2, one obtains much higher μ^2 values and they correspond quite well to the values obtained using equation 3.49.

We demonstrate that the external reflection induced by the DBR along the CCW direction clearly influences the behavior of the microdisk laser. The linear dependence of the ratio of optical powers in dB to the ratio in dB of the linear coupling and the reflectivity indicates that the higher the external reflection from the bus waveguide, the higher the extinction ratio between the optical powers in the CW and the CCW modes. The phase of the external reflection, as well as the linear coupling, do not have a significant impact on the slope of the linear dependence between the two ratios.

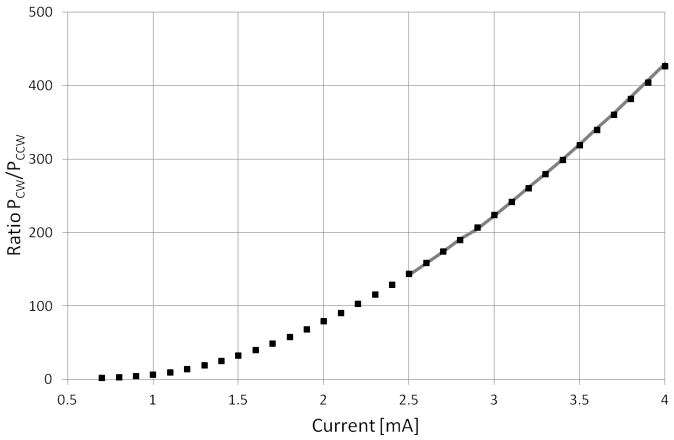

Figure 3.10: Ratio of power in CW and CCW modes in a microdisk laser at high powers, (squares) obtained from a numerical solution of the coupled rate equations, for a microdisk laser with coupling coefficients K_1=6,36.10^8s^{-1}, and 3,18.10^8s^{-1}. The line (–) is calculated from equation 3.49, with $\epsilon = 1.10^{-18}$cm^3.

3.5 Sensitivity of an ideal microdisk laser to feedback

In a Fabry-Perot or a DFB laser of length L, with one 100% reflecting facet and one partly or non-reflecting facet, the feedback sensitivity parameter C can be expressed as [22], [23]:

$$|C| = \frac{2}{\tau_L}\alpha_{end} L\sqrt{K_z} \tag{3.50}$$

where $\alpha_{\text{end}}L$ is the normalized facet loss and K_{z} is the longitudinal Petermann factor. For a Fabry-Perot laser with one 100%-reflecting facet, one can write:

$$\frac{|C|\tau_L}{\alpha_{end}L} = \frac{1-(r_2)^2}{-r_2 ln(r_2)} \tag{3.51}$$

The change in optical pulsation $\Delta\omega$ due to an external field reflection r_{e} is given by:

$$\Delta\omega = |C||r_e|\sqrt{1+\alpha^2}\sin(\omega\tau_e - \arctan\alpha) \tag{3.52}$$

The definition of the feedback sensitivity parameter C implies that the reflection sensitivity of a DFB laser is, apart from a possibly different K_{z} factor, identical to that of a Fabry-Perot laser with identical facet loss. In what follows,

we will therefore only compare the reflection sensitivity of ring/disk lasers with that of Fabry-Perot lasers.

3.5.1 Low power limit

From equation 3.41, we can derive that for a prefect microdisk laser (i.e. without any scattering or residual facet reflection) without gain suppression, the equivalent of 3.52 is (using K_2 equal to $|\kappa|^2 r_e/\tau_L$):

$$\Delta\omega = \sqrt{\left|K_1 \frac{\kappa^2}{\tau_L} r_e\right|} \sqrt{1+\alpha^2} \sin\left(\frac{\phi_1 + \omega\tau_e}{2} - \arctan\alpha\right) \tag{3.53}$$

Assuming a 100% reflection on one side of the bus waveguide, we have K_1 is then equal to $\frac{|\kappa^2|}{\tau_L}$ and equation 3.53 now becomes:

$$\Delta\omega = \frac{|\kappa^2|}{\tau_L} \sqrt{|r_e|} \sqrt{1+\alpha^2} \sin\left(\frac{\phi_1 + \omega\tau_e}{2} - \arctan\alpha\right) \tag{3.54}$$

For such a microdisk laser, the normalized facet loss is (for a relatively small κ):

$$\alpha_{end}\pi D = \ln\left(\frac{1}{1-|\kappa|^2}\right) \approx |\kappa|^2 \tag{3.55}$$

Hence, we can write in analogy with equation 3.50 and with L equal to πD:

$$\Delta\omega = |C| \sqrt{|r_e|} \sqrt{1+\alpha^2} \sin\left(\frac{\phi_1 + \omega\tau_e}{2} - \arctan\alpha\right) \tag{3.56}$$

$$\frac{|C|\tau_L}{\alpha_{end} L} = \frac{\kappa^2}{-\ln(1-\kappa^2)} = \frac{1-t^2}{-2\ln(t)} \tag{3.57}$$

$$t = \sqrt{1-\kappa^2} \tag{3.58}$$

The normalized values of $|C|$ given by 3.51 and 3.58 are plotted and compared in Figure 3.11 as a function of r_2, respectively t.

Although the normalized values are seen to be smaller for microdisk lasers, the square root dependence on the external reflection r_e implies that microdisk lasers generally will have a higher feedback sensitivity. This is especially the case for external reflections of -40dB or less, for which r_e is smaller than 0.01 and thus where the square root of r_e is larger than $10r_e$. Equation 3.56 also holds for non-ideal microdisk lasers, provided that the coupling K_2 due to scattering (or residual facet reflections) is much smaller than that due to the external reflection. For microdisk lasers as in [3], the value of t is typically of the order of 0.98–0.99.

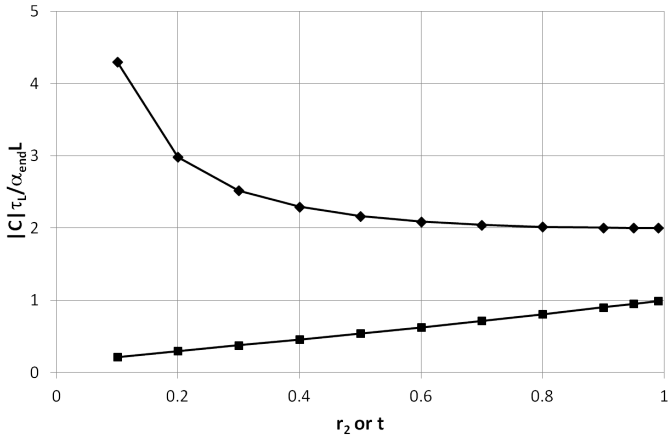

Figure 3.11: Normalized external reflection sensitivity of a Fabry-Perot laser with one 100% reflecting facet and one facet with field reflection r_2 (rhombuses) and of a microdisk laser with one perfectly AR-coated facet, one 100% reflecting facet and a coupling κ^2 ($t^2 = 1-\kappa^2$) between microdisk and bus waveguide (squares).

3.5.2 High power limit

In this case, we can use equation 3.49. We first consider an ideal ring or disk laser, for which K_2 is equal to 0 and K_1 is equal to $\frac{|\kappa|^2}{\tau_L}$ and without the external feedback. From equation 3.49 we find:

$$\Delta\omega = |C|\sqrt{|r_e|}\sqrt{1+\alpha^2}\sin(\phi_1+\omega\tau_e-\arctan\alpha) \tag{3.59}$$

$$\frac{|C|\tau_L}{\alpha_{end}L} = \frac{2\kappa^4}{-\ln(1-\kappa^2)\tau_L}\frac{1}{\epsilon' G_0 S_{CW}} = \frac{(1-t^2)^2}{-2\ln(t)}\frac{1}{\epsilon' G_0 S_{CW}\tau_L} \tag{3.60}$$

Since τ_L is typically of the order of ps or sub-ps, and $\epsilon' G_0 S_{CW}$ is of the order of $10^{10}s^{-1}$, the last factor in equation 3.60 is 100 or more. For values of t^2 larger than 99% (i.e. κ^2 smaller than 1%), the normalized value of C can be smaller than that of an equivalent Fabry-Perot laser (in both cases at the expense of the efficiency). For larger values of κ, ring or disk lasers will have a worse feedback sensitivity though. The approximate equation 3.60 is valid as long as r_e is smaller than $\frac{\epsilon G_0 S_{CW}\tau_L}{2\kappa^2}^2$. For a microdisk laser where κ^2 equals 1%, with a diameter of 10μm and for which $\epsilon G_0 S_{CW}$ is equal to $10^{10}s^{-1}$, we can calculate that r_e is smaller than 0.025 or R_e is smaller than 6.10^{-4}.

Figure 3.12 shows $\Delta\omega$ obtained from a numerical time domain solution of the rate equations as a function of the bias current for microdisk lasers with

a 10μm-diameter and κ^2 equal to 0.01. The bus waveguide has on one side a 100% reflecting facet and on the other side a perfectly AR-coated facet. Two values for r_e are considered : 10^{-2} and 5.10^{-3}. We used ϕ_1 and ϕ_2 equal to 0 and an α-factor of -5 to obtain the maximum $\Delta\omega$. One can see that the reflection sensitivity decreases with increasing bias current (or power) in both cases, and that at low bias $\Delta\omega$ increases proportional with the square root of r_e while at higher bias $\Delta\omega$ is rather proportional with r_e. For values of r_e of 10^{-2} or below, there is of course an order of magnitude or more difference between r_e and its square root.

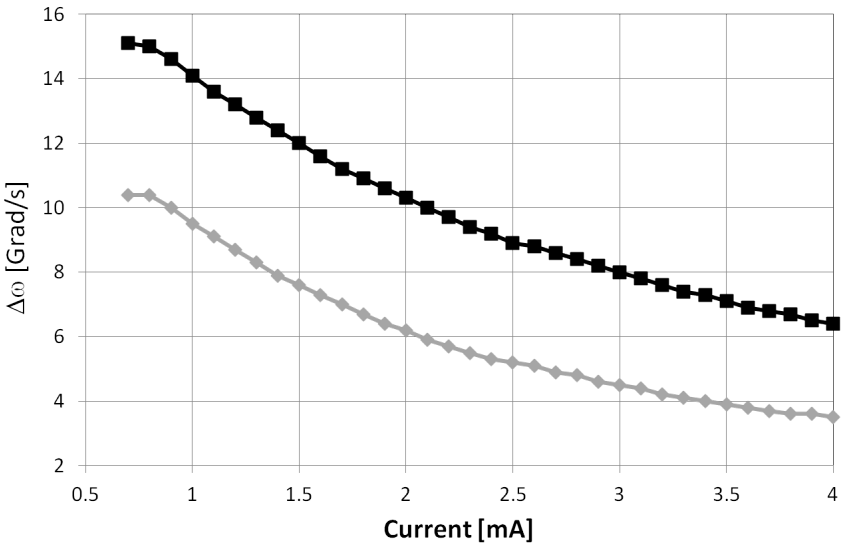

Figure 3.12: Change in optical pulsation ($\Delta\omega$) due to external reflections as a function of bias current. Black curve: r_e is equal to 10^{-2}, grey curve: r_e is equal to 5.10^{-3}.

It can also be remarked that since $\Delta\omega$ is proportional with K_1K_2 at higher power levels, one can also decrease the feedback sensitivity of these microdisk lasers (without affecting the unidirectionality) by decreasing K_1, i.e. by decreasing the reflection R_1 (which we assumed to be 100%) so far.

In the case of a non-negligible K_2 (e.g. caused by a facet reflection r_2), a reflection sensitivity can be derived by expanding K_2 as:

$$K_2 = \frac{|\kappa^2|}{\tau_L}\left[r_2 + (1-|r_2|^2)r_e \exp(-2j\omega\tau_e)\right] \tag{3.61}$$

3.6 Experimental demonstration of the unidirectionality of microdisk lasers

The optical power-current (LI) characteristics of two 7.5μm-diameter lasers lasing in continuous-wave operation at room temperature are plotted in Figure 3.13. The effective DBR length in both designs was chosen to be about 15μm, with 50 periods. The microdisk laser characterized in Figure 3.13a, named Laser A, is coupled to a waveguide where a DBR with a period of 300nm is implemented in the CCW emission direction of the system. The microdisk laser characterized in Figure 3.13b, named Laser B, is coupled to a waveguide where a DBR with a period of 290nm is implemented in the CW emission direction. Thermal roll-over appears in both devices for a bias current higher than 1.5mA.

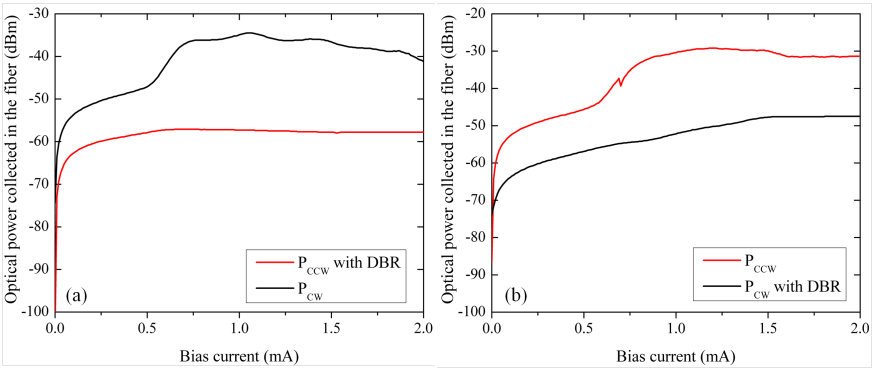

Figure 3.13: Measured LI characteristics of microdisk lasers A and B with a diameter of 7.5μm. The plotted optical power is collected in optical fibers on both sides of the WGs. (a) Microdisk laser A coupled to a WG where the DBR has a period of 300nm. (b) Microdisk laser B coupled to a WG where the DBR has a period of 290nm.

The spectra of the microdisk lasers coupled to a waveguide with a DBR with a period of 300nm and a DBR with a period of 290nm are plotted in Figures 3.14a and 3.14b respectively for 1.2mA bias (continuous wave operation at room temperature). Single-mode operation in continuous wave regime at 1554.0nm and at 1555.8nm is demonstrated for both devices respectively. A side-mode suppression ratio of 18.6dB is measured for laser A on Figure 3.14a and is higher than 25dB for laser B on Figure 3.14b. The free-spectral range is around 27nm for both devices. At the peak lasing wavelength of the microdisk laser, the extinction ratio between the optical powers coupled out of the waveguide on the side of the DBR structure and on the side without DBR is respectively 46.1dB and 39.9dB.

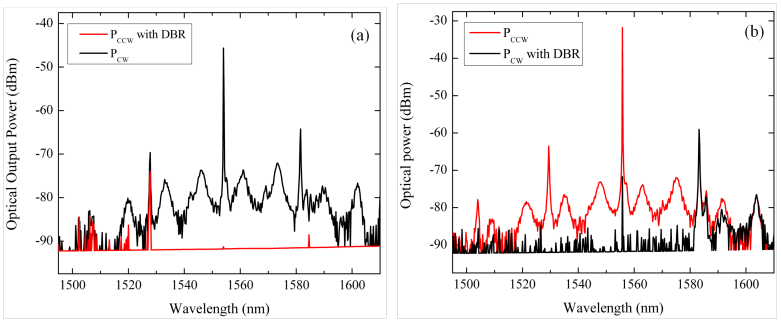

Figure 3.14: Measured spectra of 7.5μm-diameter microdisk lasers A and B. The optical power is collected on both sides of the WGs. (a) Laser A coupled to a WG where the DBR has a period of 300nm. (b) Laser B coupled to a WG where the DBR has a period of 290nm.

Table 3.2 summarizes the wavelengths of each of the longitudinal modes, and their measured optical powers coupling out of the grating couplers on the side of the DBR and on the side without DBR.

Mode	λ *(nm)*	*OP no DBR (dBm)*	*OP DBR (dBm)*	λ *(nm)*	*OP no DBR (dBm)*	*OP DBR (dBm)*
-2				1504.0	-77.8	-88.5
-1	1527.8	-69.7	-73.9	1529.4	-63.5	-92.0
0	**1554.0**	**-45.6**	**-91.7**	**1555.8**	**-31.8**	**-71.7**
+1	1581.6	-64.2	-91.5	1583.2	-59.5	-59.0
+2	1610.2	-76.9		1612.0	-72.9	-72.4

Table 3.2: Spectral characteristics of microdisk lasers A and B: "OP no DBR" stands for "Optical power measured on the side without DBR", and "OP DBR" stands for "Optical power measured on the side with DBR".

The passive characterization of the DBR is performed on a nominally identical passive SOI design covered in DVS-BCB. Light from a tunable laser is coupled into the chip with a 10°-angled single-mode optical fiber through a grating coupler to a waveguide where a DBR with a period of either 290nm or 300nm is present. The optical power at the output of the waveguide, i.e. after the DBR structure, is collected out of another grating coupler in a single-mode optical fiber under a 10° angle. The characterization of the DBR structure with a period of 300nm is presented in Figure 3.15a, and the characterization of the DBR structure with a period of 290nm is presented in Figure 3.15b. In both cases, the transmission measurement is plotted together with the transmission through a straight SOI waveguide without DBR structure.

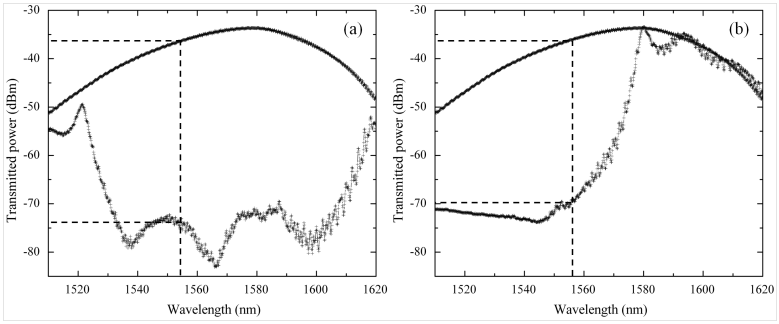

Figure 3.15: Transmission characteristics of a WG where the DBR has a period of 300nm (a), and of a WG where the DBR has a period of 290nm (b). The transmission characteristic of a straight WG of the same sample, acting as reference, is systematically plotted.

The peak efficiency of the grating couplers on this sample is located at 1580.5nm due to the BCB top cladding layer. On Figure 3.15a, an extinction ratio at the peak lasing wavelength of the microdisk laser (1554.0nm) of 38.1dB is measured between the reference transmission and the transmission through the DBR structure. In the case of Figure 3.15b, an extinction ratio at the peak lasing wavelength of the microdisk laser (1555.8nm) of 33.1dB is measured. Even though the reflection induced by the DBR structure is close to 100%, the low coupling efficiency between the microdisk laser and the silicon waveguide lowers the amount of reflection actually felt by the microdisk laser. Comparing the extinction ratios measured on Figures 3.15a and 3.15b to the ones extracted from the spectral measurements from Figures 3.14a and 3.14b, we demonstrate an 8dB difference in lasing power between the CW and the CCW modes for laser A, and a 6.9dB difference for laser B.

3.7 Experimental demonstration of the stability of the unidirectionality of microdisk lasers as a function of temperature

One important requirement for the use of microdisk lasers in optical interconnects is to demonstrate that devices do not lase in different directions or switch from one lasing direction to the other depending on the injection current and the temperature. In [25], the LI curves of a microdisk laser at elevated temperatures remain smooth and unidirectional under pulsed driving conditions,

in contrast to the case where continuous wave drive conditions were applied. Most likely this is because when the ambient temperature is changed, it affects both the silicon waveguide and the InP-based microdisk cavity, while the self heating effect in continuous wave mode only heats up the disk cavity. In this study, we investigate the influence of the DBR on the unidirectionality of the laser over a broad range of temperatures. The sample was heated by means of a Peltier element, under continuous drive conditions. The temperature was increased from 10°C to 35°C with steps of 5°C. As the DBR structure is designed to be 55μm away from the microdisk laser, this corresponds to approximately a 2 radian phase change for the reflected light. Figure 3.16 shows the optical power-current (LI) characteristic of laser B for the different ambient temperatures of the stage. Optical powers coupling out of the grating couplers in the CCW and the CW directions are simultaneously recorded. We demonstrate that due to the presence of the DBR on one side of the waveguide the LI curves remain unidirectional under continuous drive conditions, over a broad range of temperature. Lasing in the CCW direction is measured up to 35°C and a maximum output power of 3μW is measured in the fiber at 10°C (this corresponds to 15μW in the silicon waveguide).

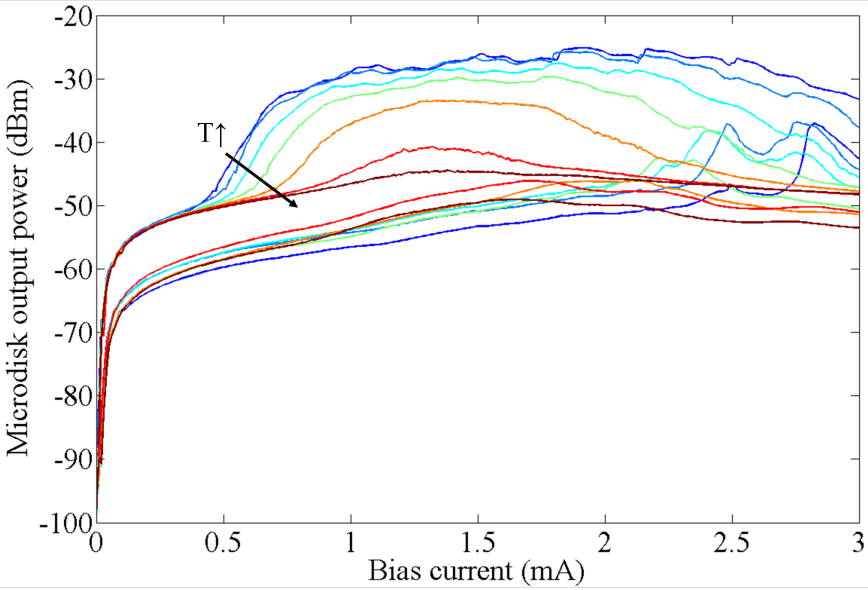

Figure 3.16: LI curves of laser B under continuous wave operation at elevated temperatures. The slope efficiency decreases and the threshold current increases at higher temperatures. The power is the fiber coupled output power.

As expected, the threshold current gradually increases with increasing temperature as can be seen in Figure 3.16, and the slope efficiency drops. The characteristic temperature of the microdisk laser can be extracted by fitting the natural log of the threshold current versus the ambient temperature. A value of 55K was found, which indicates that the laser is highly sensitive to temperature variations. Some optical power is collected out of the grating coupler above 2.5mA after the DBR in the CW direction of the system. The DBR structure is limited in bandwidth. Heat generated in the microdisk laser leads to a red-shift of its optical spectrum. Because of this red-shift, the longitudinal mode around 1580nm in the CW direction starts to fall out of the bandwidth of the DBR structure. Therefore, optical power is collected in the CW direction for wavelengths outside the bandwidth of the DBR.

The spectra of laser B in the CCW and the CW direction of the system for different ambient temperatures of the stage are plotted in Figure 3.17. The thermal resistance of laser B was determined by measuring the wavelength as a function of the ambient temperature ($d\lambda/dT$) and the wavelength change as a function of the injected power ($d\lambda/dP$). We found a value of 80pm/K for $d\lambda/dT$, and a value of 2.0nm/mW. The thermal resistance then becomes 25K/mW, which is very far from the value of 95.3K/W reported for hybrid DFB lasers on SOI [24]. Special attention should be paid to improve heat dissipation of the microdisk lasers. For instance, overcladding the device with SiO_2 instead of DVS-BCB has already reduced the thermal resistance of microdisk lasers to a value of 7.8K/mW [25].

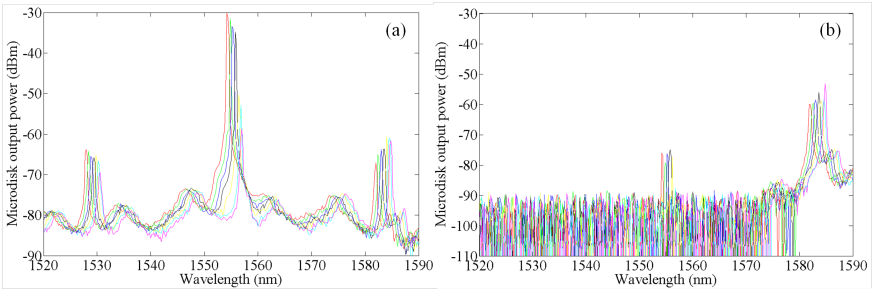

Figure 3.17: (a) Laser B spectra in the CCW direction under continuous wave operation at elevated temperatures. (b) Laser B spectra in the CW direction under continuous wave operation at elevated temperatures. The power is in both cases the fiber coupled output power.

3.8 Discussion

In conclusion, we demonstrated and quantified stable unidirectional lasing in microdisk lasers heterogeneously integrated on SOI. Feedback from a passive distributed Bragg reflector is used to achieve stable unidirectional operation. This simple passive design does not add optical losses to the system and does not increase its power consumption. The implementation of this solution is the key to avoid the appearance of a "memory" effect in microdisk lasers. It can be implemented to counteract processing effects, such as sidewall roughness, that threaten unidirectional operation of the lasers. Different devices belonging to the same design can now lase in the same direction with higher efficiency and without switching from one lasing direction to the other depending on the injection current and the temperature. This makes the use of microdisk lasers for optical interconnects applications very attractive.

We have theoretically shown that microdisk lasers with a strong reflection from one side and weak reflection from the other side can be operating in a unidirectional mode. At low power levels, the ratio of powers in clockwise and counter clockwise mode is approximately equal to the ratio of the coupling coefficients between clockwise and counter clockwise modes, while at high power levels this ratio is determined by gain suppression and the lowest coupling coefficient.

Using the same analysis, we were also able to derive the external feedback sensitivity of unidirectional microdisk lasers in different configurations and compare it to the feedback sensitivity of Faby-Perot lasers with one 100% reflecting facet and one partially reflecting facet. In general, disk laser diodes seem to be more sensitive to external feedback than Fabry-Perot or DFB/DBR laser diodes. At high power levels though, the feedback sensitivity of ring/disk lasers decreases considerably due to gain suppression and under certain conditions it can be better than that of conventional edge-emitting laser diodes.

References

[1] M. Sorel, P. J. R. Laybourn, G. Giuliani, and S. Donati. *Unidirectional bistability in semiconductor waveguide ring lasers.* Appl. Phys. Lett., 80(17):3051–3053, 2002.

[2] M. T. Hill, H. J. S. Dorren, T. de Vries, X. J. M. Leijtens, J. H. den Besten, B. Smalbrugge, Y.-S. Oeil, H. Binsma, G.-D. Khoel, and M. K. Smit. *A fast low-power optical memory based on coupled micro-ring lasers.* Nature, 432:206–209, 2004.

[3] L. Liu, R. Kumar, K. Huybrechts, T. Spuesens, G. Roelkens, E.-J. Geluk, T. de Vries, P. Regreny, D. Van Thourhout, R. Baets, and G. Morthier. *An ultra-small, low-power, all-optical flip-flop memory on a silicon chip*. Nature Photonics, 4:182–187, 2010.

[4] D. Liang, M. Fiorentino, T. Okumura, H.-H. Chang, D. T. Spencer, Y.-H. Kuo, A. W. Fang, D. Dai, R. G. Beausoleil, and J. E. Bowers. *Electrically-pumped compact hybrid silicon microring lasers for optical interconnects*. Opt. Express, 17(22):20355–20364, 2009.

[5] A. W. Fang, R. Jones, H. Park, O. Cohen, O. Raday, M. J. Paniccia, and J. E. Bowers. *Integrated AlGaInAs silicon evanescent race track laser and photodetector*. Opt. Express, 15(5):2315–2322, 2007.

[6] L. Gelens, S. Beri, G. Van der Sande, G. Verschaffelt, and J. Danckaert. *Multistable and excitable behavior in semiconductor ring lasers with broken Z_2-symmetry*. Eur. Phys. Journal D 58, 197–207, 2010.

[7] L. Gelens, G. Van der Sande, S. Beri, and J. Danckaert. *Phase-space approach to directional switching in semiconductor ring lasers*. Phys. Rev. E 79, 016213, 2009.

[8] J. P. Hohimer, G. A. Vawter, and D. C. Craft. *Unidirectional operation in a semiconductor ring diode laser*. Appl. Phys. Lett., 62(11):1185–1187, 1993.

[9] C. J. Born, S. Yu, M. Sorel, and P. J. R. Laybourn. *Controllable and stable mode selection in a semiconductor ring laser by injection locking*. Proceedings of the Conference on Lasers and Electro-Optics CLEO '03, 1–3, paper PWK4, 2003.

[10] A. F. J. Levi, R. E. Slusher, S. L. McCall, J. L. Glass, S. J. Pearton, and R. A. Logan. *Directional light coupling from microdisk lasers*. Appl. Phys. Lett., 62:561–564, 1993.

[11] J. Nockel, A. Stone, and R. Chang. *Q-spoiling and directionality in deformed ring cavities*. Opt. Letters, 19:1693–1695, 1994.

[12] Q. J. Wang, C. Yan, N. Yu, J. Unterhinninghofen, J. Wiersig, C. Pflugl, L. Diehl, T. Edamura, M. Yamanishi, H. Kan, and F. Capasso. *Whispering-gallery mode resonators for highly unidirectional laser action*. PNAS, 107(52):22407–2412, 2010.

[13] D. Liang, S. Srinivasan, D. A. Fattal, M. Fiorentino, Z. Huang, D. T. Spencer, J. E. Bowers, and R. G. Beausoleil. *Teardrop Reflector-Assisted Unidirectional Hybrid Silicon Microring Lasers*. IEEE Photonics Technol. Lett., 24(22):1988–1990, 2012.

[14] F. Van Laere, G. Roelkens, M. Ayre, J. Schrauwen, D. Taillaert, D. Van Thourhout, T. F. Krauss, and R. Baets. *Compact and highly efficient grating*

couplers between optical fiber and nanophotonic waveguides. J. Lightwave Technol., 25(1):151–156, 2007.

[15] CAvity Modelling FRamework, *http://camfr.sourceforge.net.*

[16] M. Sorel, G. Giuliani, A. Scire, R. Miglierina, S. Donati, and P. J. R. Laybourn. *Operating regimes of GaAs- AlGaAs semiconductor ring lasers : experiment and model.* IEEE J. Sel. Topics Quantum Electron., 39(10):1187–1195, 2003.

[17] T. Numai. *Analysis of signal voltage in a semiconductor ring laser gyro.* IEEE J. Sel. Topics Quantum Electron., 36(10):1161–1167, 2000.

[18] E. J. D′Angelo, E. zaguirre, G. B. Mindlin, G. Huyet, L. Gil, and J. R. Tredicce. *Spatiotemporal dynamics of lasers in the presence of an imperfect O(2) symmetry.* Phys. Rev. Lett., 68(25):3702–3705, 1992.

[19] M. Sargent. *Theory of a multimode quasi-equilibrium semiconductor-laser.* Physical Review A, 48(1):717–726, 1993.

[20] J. Van Campenhout. *Thin-Film microlasers for the integration of electronic and photonic integrated circuits.* Doctoral Thesis, Ghent University, 2007.

[21] M. Sorel, P. J. R. Laybourn, A. Scire, S. Balle, G. Giuliani, R. Miglierina, and S. Donati. *Alternate oscillations in semiconductor ring lasers.* Opt. Letters, 27(22):1992–1994, 2002.

[22] O. Nilsson, J. Buus. *Linewidth and Feedback Sensitivity of Semiconductor Diode Lasers.* IEEE Journ. Quant. El., 26:2039–2042, 1990.

[23] G. Morthier. *Feedback sensitivity of Distributed-Feedback Laser Diodes in Terms of Longitudinal Field Integrals.* IEEE Journ. Quant. El., 38:1395–1397, 2002.

[24] S. Stanković. *Hybrid III-V/Si DFB Lasers Based on Polymer Bonding Technology.* Doctoral Thesis, Ghent University, 2013.

[25] T. Spuesens, F. Mandorlo, P. R.-Romeo, P. Regreny, N. Olivier, J.-M. Fédeli, and D. Van Thourhout. *Compact integration of optical sources and detectors on SOI for optical interconnects fabricated in a 200mm CMOS pilot line.* J. Lightwave Technol., 30(11):1764–1770, 2012.

"I'm just tryin' to find
A mountain I can climb"

Julian Casablancas, Machu Picchu, 2011

4

All-optical signal processing applications of III-V microdisk lasers on SOI

As discussed in chapter 1, another important but basic requirement for logic gates is logic-level restoration. The quality of the logic signal must be restored so that the degradations in signal quality do not propagate through the system. In other words, the signal is "cleaned up" at each stage. For optics, it is mandatory to restore the beam quality and/or the pulse quality as well as signal-level ranges [1]. With the advances in photonic integration technology, an integrated optical solution for interconnects has become feasible. Optical wavelength-division-multiplexed (WDM) network links were already able to fulfill the bandwidth capacity requirements in the past. However, due to the increasing demand, the logical next step in optical network evolution would be to implement the routing and switching in the optical domain. As systems consist of an increasing number of components working together, the amount of data that needs to be sent across a chip and between different system components increases as well. The drawback of such all-optical approaches is the limited cascadability of all-optical network nodes due to the accumulation of noise from optical amplifiers and cross-talk from switches [1]. Indeed, the opto-electro-optic (O/E/O) conversions also act as repeaters in the network and they

significantly decrease the noise on the signals. Therefore, there is a clear need for all-optical regenerators that operate at low power consumption and at high bitrates.

In this chapter, we demonstrate an all-optical low-power 2R regenerator of 10Gb/s NRZ data based on a 10μm-diameter electrically pumped microdisk laser, heterogeneously integrated onto Silicon-On-Insulator and processed in a CMOS pilot-line. The scheme results in BER improvement and works for sub-milliWatt level input signals. The laser operates in continuous wave regime, is single mode at room temperature and consumes 6mW of electrical power. Its regeneration capability is investigated in simulations and experimentally demonstrated. We also investigate the response of a 10μm-diameter microdisk laser used as an all-optical gate. For 10Gb/s NRZ-signals, we report a rise time and fall times of 8.0 and 41.0ps respectively, which suggests that the device can operate up to 20GHz. Experiments with 20Gb/s NRZ signals are performed and demonstrate that this solution could be good enough to be used in combination with Forward-Error-Correction (FEC). In another section of this chapter, we demonstrate the all-optical flip-flop operation of a 20μm-diameter and electrically-pumped microdisk laser fabricated in a CMOS pilot-line and working in continuous wave regime. Switching is performed with 25ps-long pulses, and switching times lower than 60ps are reported. Finally, in appendix D, we describe the measurement facilities that were implemented in this PhD. work to allow characterization of devices up to 67GHz.

4.1 All-optical regeneration of 10Gb/s NRZ signals with low-power consuming microdisk laser on SOI

All-optical signal regeneration has so far mainly been explored for applications in long distance links. There are different noise mechanisms that can degrade optical signals in wavelength-division-multiplexed (WDM) networks. The main cause of degradation is the attenuation by propagation in the optical fiber. This attenuation can be overcome by using erbium-doped fiber amplifiers (EDFAs) which will re-amplify the signal. EDFAs are therefore also refered to as “1R regenerators” in some cases. The amplification by EDFAs will, however, also add noise to the signal. Other sources of signal degradation are rather distortions than noise and can be described to the nonlinearities in the fiber (such as self-phase modulation, cross-phase modulation, four wave mixing, etc) and dispersion effects (chromatic as well as polarization dispersion). The combination of all these different degradation effects can influence the shape of the

pulses and add intensity noise to the signal. This distortion can be reduced by using "2R regenerators" in the network (comprising re-amplifying and reshaping functionality). When there are also distortions in the time domain (timing jitter), a "3R regenerator" is needed which performs a re-timing in addition to the 2R functionality.

In this work, we will limit ourselves to 2R regeneration techniques on intensity modulated non-return-to-zero (NRZ) signals. Most of the concepts for regeneration at high speeds solely offer the ability to handle return-to-zero (RZ) signals while most commercial systems are currently still deployed as NRZ. The retiming used by 3R regeneration has been demonstrated to be a reliable technique for transmission over practically unlimited distances (1 000 000 km with 2500 hops [2]). However, this requires clock extraction/recovery techniques which become complicated in all-optical packet switched networks since the packets arrive at burst rates. 2R regeneration is far simpler and more cost-effective. Experiments have shown that even without correcting the time degradations, it is still possible to achieve all-optical packet switching at 10 Gb/s by cascading up to 16 optical nodes and using multistage 2R regeneration [3], [4], [5]. It has also been demonstrated that transmission over large distances (100 000 km) is possible without performing a retiming [6], [7]. All-optical 2R regenerators are typically based on elements with a very steep nonlinear transmission characteristic, ideally resembling a step-like function. This steep transition will act as the decision level between the logical zeros and logical ones. When a bit pattern with noise is inserted, there will be a much lower amplification for the logical zeros than for the logical ones. This will reduce the noise on the signal and thus increase the optical signal-to-noise ratio (OSNR).

Different techniques have been proposed for 2R regeneration, for instance devices based on interferometric structures such as all-optical SOA-based Mach-Zehnders [8] and devices based on self-phase modulation [9], [10]. The limitations of these schemes are their complex structures, their high power consumption or their ability to only regenerate return-to-zero (RZ) signals. Stand-alone semiconductor optical amplifiers (SOAs) are more attractive in terms of switching, gating, wavelength conversion and regeneration due to their optical gain, their strong nonlinear behavior, and their integrability in photonic circuits. Error and pattern dependence-free 40 Gb/s 3R regeneration has been demonstrated using a single semiconductor optical amplifier in a delayed-interference configuration [11]. Bistable semiconductor ring lasers have proven to be good candidates for all-optical signal regeneration (2R) and Re-timing [12]. In the 2R operation, the extinction ratio of the optical data pulse

is significantly improved when the input extinction ratio is as low as 1dB. Passive signal regeneration based on a membrane InP switch has been reported [13]. Because of the high confinement of light in the active region of the membrane switch, the device acts as a saturable absorber with a highly non-linear response. Improvement of the extinction ratio and regenerator operation up to 5 Gb/s have both been shown. Finally, a broadband optical colorless 2R regenerator based on a single distributed feedback laser is also able to regenerate 25 Gb/s non-return-to-zero (NRZ) signals, as reported in [14]. Semiconductor microring or microdisk lasers are suitable as bistable lasers for optical switching or signal processing applications [15]. Microring lasers with very low threshold currents have been demonstrated, making these lasers good candidates for light sources for e.g. on-chip optical interconnects [16], [17]. Microdisk lasers are moreover very versatile devices, used as wavelength converters [18], modulators and resonant photodetectors [19], all with minimal power consumption.

In the coming sections, we present a new signal processing application of the microdisk laser, used as regenerator. We demonstrate the regeneration of 10Gb/s NRZ signals based on a microdisk laser heterogeneously integrated on the Silicon-On-Insulator (SOI) platform and fabricated in a CMOS pilot-line. The regenerator only requires 6mW of operational power and works for sub-milliWatt level input signals, which makes the scheme simpler and more power efficient than opto-electronic regeneration, that typically requires several Watts.

4.1.1 Device design and integration technology

The device fabrication in the CMOS pilot-line of the CEA-Leti relies on the molecular bonding of a 2-inch wafer of the molecular-beam-epitaxy-grown InP-based heterostructure onto SOI [20], [21]. The epitaxial stack is the one described in 2.1. The design of the passive SOI circuit for the considered device consists of a 800nm-wide waveguide, tapered down on both sides to a 450nm-wide waveguide. The 450nm-wide waveguides themselves are tapered up to shallow-etch (etch depth : 70nm out of the 220nm) grating couplers used to collect the laser emission from the microdisk out of the chip in a single-mode optical fiber [22]. The fiber grating couplers (GCs) are optimized for operation at 1.55μm.

The device is schematically depicted in Figure 4.1. The two levels are then separated by a 130nm-thick layer of SiO_2 (n=1.47), allowing evanescent coupling to the underlying waveguide. The coupling section between the microdisk and the passive circuit is in the middle of the 800nm-wide waveguide. The microdisk lasers has a diameter of 10μm and consists of a 483nm thin disk cavity on top of a 100nm thin InP bottom contact layer. A CMOS compatible Ti/T-

iN/AlCu (10:40:1000nm) metal stack is used [23], and demonstrates very good specific contact resistances [24]. The 1μm-thick contact also serves as a heat sink as it improves the heat dissipation under continuous-wave bias. Above threshold, the laser emission from the microdisk is coupled to the TE mode of the waveguide, and is simultaneously collected out of both grating couplers in optical fibers positioned at 10° angle in order to maximize the collection at 1.55μm. Section 2.15 of chapter 2 describes the process flow of this sample in detail.

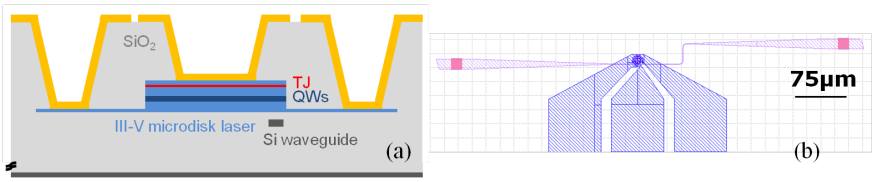

Figure 4.1: (a) Schematic representation of the cross-section of the microdisk laser heterogeneously integrated on SOI and embedded in SiO_2. (b) Top view of the designed microdisk laser : the SOI waveguide ends on both sides with a fiber-coupler.

4.1.2 Static microdisk laser performance

The microdisk laser considered here has a diameter of 10μm, and the emitted light evanescently couples to one underlying waveguide. The light-current (LI) characteristic of the microdisk laser, measured simultaneously at the two ends of the SOI waveguide, is depicted in Figure 4.2a. This measurement was undertaken under continuous wave operation at room temperature. As the bias current of the microdisk laser increases, the temperature inside the cavity increases. This red-shifts the lasing wavelength of the microdisk laser. The phase of the reflected light then changes under increasing bias current and this phenomenon explains the ripples visible on the LI characteristic.

When the threshold current of 1.6mA is surpassed, the microdisk laser is unidirectional. The asymmetry in field reflectivity on both sides of the waveguide leads to different back reflection levels in the laser cavity, as will be discussed below. This difference is responsible for the difference in output power between the two sides. The maximum optical power collected in the fiber is 8μW (this corresponds to 40μW in the silicon waveguide). Figure 4.2b shows the output power spectrum of the biased microdisk laser (under continuous-wave bias at 4.0mA) which illustrates single-mode lasing at 1561.6nm. The free-spectral range of the laser is 22nm, and a side-mode suppression ratio of 25dB is measured on Figure 4.2b.

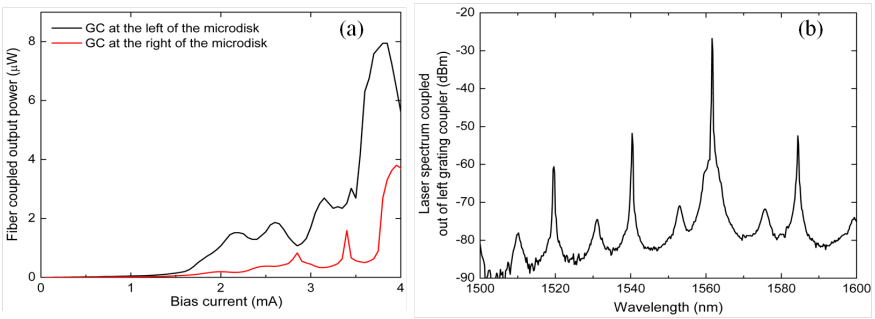

Figure 4.2: (a) LI characteristic of a microdisk laser with a diameter of 10μm. The optical power coupling out of the grating couplers on both sides of the waveguide is simultaneously collected in optical fibers. (b) Single-mode operation of a 10μm-diameter microdisk laser under continuous-wave bias (at 4mA).

4.1.3 Simulation of the regeneration behavior

We formulate the rate equations in terms of two counterpropagating whispering gallery modes with electric fields E^+, propagating in the clockwise (CW) direction, and E^-, propagating in the counterclockwise (CCW) direction. The spontaneous emission of the microdisk laser is implemented in two electric fields E_{noise1} and E_{noise2} where E_{noise}=$RR.n.e^{2j\pi n'}$, with RR representing the spontaneous emission amplitude and n and n' random numbers between 0 and 1. Referring to section 1.3.2 for a detailed description of the parameters, we find [25], [26]:

$$\frac{dE^+}{dt} = \frac{1}{2}(1-j\alpha)\left[G^+ - \frac{1}{\tau_p}\right]E^+ + E_{noise1} + KE^- \tag{4.1}$$

$$\frac{dE^-}{dt} = \frac{1}{2}(1-j\alpha)\left[G^- - \frac{1}{\tau_p}\right]E^- + E_{noise2} + KE^+ \tag{4.2}$$

For the carrier density rate equation, we find:

$$\frac{dN}{dt} = \frac{I}{qV} - \frac{N}{\tau_c} - G^+\left|E^+\right|^2 - G^-\left|E^-\right|^2 \tag{4.3}$$

I denotes all injected current and τ_c is the carrier lifetime. The gain experienced in a semiconductor material decreases for high optical intensity. This is due to gain suppression. Gain suppression takes place even when the total carrier density N is constant and reflects the reduction of "resonant carriers" due to carrier heating and spectral hole burning. To account for this effect, the modal gain is linearized to:

$$G^+ = \Gamma g_0 v_g (N - N_0)(1 - \epsilon_s |E^+|^2 - \epsilon_c |E^-|^2) \quad (4.4)$$

$$G^- = \Gamma g_0 v_g (N - N_0)(1 - \epsilon_s |E^-|^2 - \epsilon_c |E^+|^2) \quad (4.5)$$

where ϵ_s reflects the self-gain suppression and ϵ_c the cross-gain suppression. Calculations have shown that $\epsilon_c = 2\epsilon_s$ [27], [28]. The cross-gain suppression ϵ_c will therefore break the symmetry and enforce unidirectional operation of the laser. The gain suppression is, however, only significant when the photon density is high. This means that at lower output powers, normally a bidirectional regime will be present.

Table 4.1 summarizes the parameters implemented in the numerical solving of the above set of equations. The simulation is performed at the resonance wavelength of the microdisk laser (1561.6nm). The value for the linear coupling coefficient is chosen so that the simulation matches the experimental results presented in section 4.1 below. In order to model the asymmetry in reflection from both sides of the waveguide, an extra term is explicitly added to the rate equation in equation 4.6 and equation 4.7 to calculate the field propagating in the CW direction and the CCW direction respectively. The normalized field reflectivity from the bus waveguide is implemented with a coefficient $T_i = r_i |\kappa|^2 \frac{v_g}{2\pi R}$, where r_i represents the field reflection coefficient from the left/from the right side of the silicon waveguide measured at the microdisk/bus waveguide interface and $|\kappa|^2$ is the power coupling coefficient between the silicon waveguide and the microdisk laser. Finally, in equation 4.7, the calculation of the CCW field takes the injection of optical pulses on the left side of the waveguide into account (represented by E_{in}).

$$\frac{dE^+}{dt} = \frac{1}{2}(1 - j\alpha)\left[G^+ - \frac{1}{\tau_p}\right]E^+ + E_{noise1} + KE^- + T_1 E^- \quad (4.6)$$

$$\frac{dE^-}{dt} = \frac{1}{2}(1 - j\alpha)\left[G^- - \frac{1}{\tau_p}\right]E^- + E_{noise2} + KE^+ + T_2 E^+ + \kappa \frac{v_g}{2\pi R} E_{in} \quad (4.7)$$

Symbol	*Name of the parameter*	*Value*	*Unit*	
R	Microdisk radius	5.0	μm	
τ_p	Photon lifetime	0.47	ps	[29]
τ_c	Carrier lifetime	600	ps	[29]
α	Linewidth enhancement factor	4		
v_g	Group velocity in the microdisk	$3x10^8/3.4$	m/s	[29]
ϵ_s	Self-gain suppression	$1.1x10^{-17}$	cm^{-3}	
ϵ_c	Cross-gain suppression	$2 \times 1.1x10^{-17}$	cm^{-3}	
g_0	Differential gain	$7x10^{-17}$	cm^2	
N_0	Transparency carrier density	$1.0x10^{18}$	cm^{-3}	[29]
κ	Field coupling disk-WG	0.29		
RR	Spontaneous emission amplitude	2	s^{-1}	
T_1	Normalized field reflectivity from the right side of the waveguide	$0.25\|\kappa\|^2$	s^{-1}	
T_2	Normalized field reflectivity from the left side of the waveguide	0	s^{-1}	
K	Symmetric coupling between the 2 modes due to sidewall roughness	$(0.56+2.8j).\frac{v_g}{2\pi R}10^{-4}$	s^{-1}	
P	Average power of the injected optical pulses in the microdisk laser	0.35	mW	

Table 4.1: Parameters considered for the simulation of the regeneration behavior of a microdisk laser

We simulate the injection of a noisy 10Gb/s pseudo-random bit-sequence (PRBS) in the waveguide, along the CCW direction of propagation. The microdisk laser in the simulation is operated at 4mA under continuous-wave bias, and is originally lasing in the CW direction. Gaussian white noise is added to the electrical field of the input signal, both in the logical "1" level and the logical "0" level. The input signal is then filtered using a band-pass filter with a bandwidth of 61GHz. The average input power coupled to the microdisk is then 0.35mW. The optical power of the noisy and filtered input pattern in the waveguide before the microdisk laser is plotted in Figure 4.3a. In the simulation, the optical power traveling in the cavity and in the bus waveguide is obtained from a conversion of the photon density $|\mathrm{E}|^2$. The photon density is implemented in cm^{-3}. The optical power is then (with S the number of photons in the cavity):

$$P = \frac{S\hbar\omega v_g}{L} \tag{4.8}$$

where v_g is the group velocity in the microdisk laser and L is the cavity length. For the CW propagating mode,

$$P_{CW} = \frac{S_{CW}\hbar\omega v_g}{2\pi R} \tag{4.9}$$

$$P_{CW} = |E_{CW}|^2 2\pi R \frac{\hbar\omega v_g w d}{2\pi R} \tag{4.10}$$

$$P_{CW} = |E_{CW}|^2 \hbar\omega v_g A_{eff} \tag{4.11}$$

where A_eff is the effective area of the optical mode. The same equation is valid for the CCW mode. In both cases, $\hbar\omega$ is equal to 0.8eV. The value of v_g is indicated in table 4.1. The width of the optical mode w in the disk is approximated to be 1μm, and finally, d is the thickness of the microdisk laser (around 500nm). In the bus waveguide, the effective area of the optical mode will be different than in the microdisk, but the equation 4.11 is still valid. Since E^+, E^- and E_in are all normalized this way, the field coupling disk-waveguide κ considered in the simulation is dimensionless. The resulting eye diagram of the noisy input signal is depicted in Figure 4.3b.

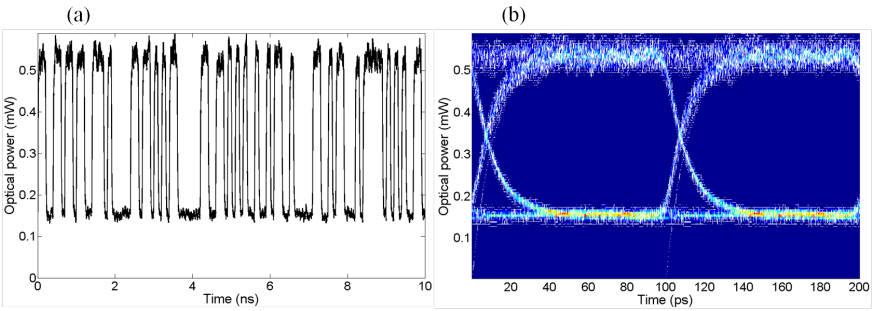

Figure 4.3: Simulation of the injection of a noisy 10Gb/s pseudo-random bit-sequence (PRBS) in the waveguide. (a) Degraded pseudo-random-bit-sequence (PRBS) in the waveguide after filtering with a 61GHz band-pass filter : Gaussian white noise is visible on the trace of the optical power of the input signal. (b) Resulting eye diagram of the degraded and filtered signal in the waveguide before the microdisk laser.

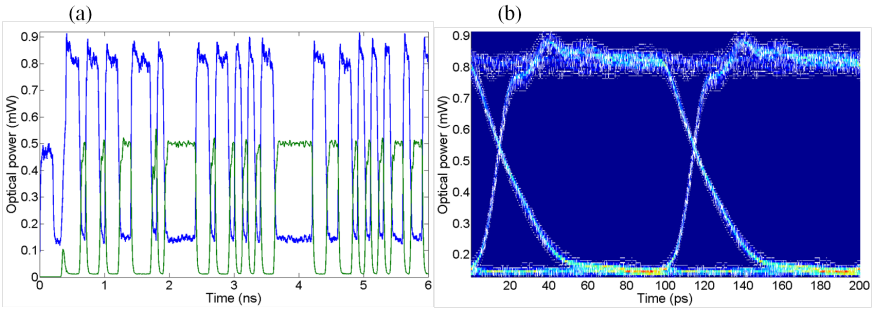

Figure 4.4: Simulation of the regeneration of a noisy 10Gb/s pseudo-random bit-sequence (PRBS) in the waveguide. (a) Optical powers at the output of the microdisk laser, in the waveguide, after filtering with a 61GHz band-pass filter. Above threshold, the microdisk is lasing in the CW dominant state (green) (t<400ps), but as soon as an optical pulse is injected on the left side of the waveguide, the microdisk switches to lase in the CCW dominant state (blue). After the pulse has passed through, the microdisk laser switches back to the CW mode (green). (b) Resulting eye diagram of the regenerated and filtered signal in the waveguide after the microdisk laser.

We calculate the amplitude of the field at the output of the microdisk laser. Figure 4.4a shows what happens when the 10Gb/s data stream is injected from the left side (at t=0). The field propagating on the right side of the waveguide (blue trace in Figure 4.4a) consists of the transmitted input field and of the CCW laser emission of the microdisk laser coupled to the waveguide. The destructive interference between the CCW laser emission of the microdisk laser and the transmitted input field is taken into account in the simulation. The field propagating in the left side of the waveguide (green trace in Figure 4.4a) consists of the CW laser emission of the microdisk laser coupled to the waveguide. From t=0 to t=300ps, the microdisk laser threshold is not yet reached. Only the transmitted input field is measured on the right side of the waveguide. At t=300ps, we observe that the microdisk laser starts lasing in the CW dominant state, in which the CCW mode is suppressed. The power measured on the left side of the SOI is increasing. From t=400ps and for the rest of the PRBS sequence, we see that the injected external pulses couple into the microdisk cavity. As the injected pulses are strong enough, they switch the laser to operate in the CCW mode. In this case, the power at the left side of the SOI waveguide becomes low. But after the pulses have passed through, the asymmetry in the reflectivity from the right side of the bus waveguide forces the microdisk laser to switch back to the CW mode. To suppress transient oscillations of the laser, we also implement a band-pass filter with a bandwidth of 61GHz at the right output of the microdisk laser. The eye diagram of the optical power in the waveguide after the bandpass filter is depicted in Figure 4.4(b). It is plotted above threshold of the microdisk laser. The optical power then consists of the transmitted input power and of the CCW laser emission of the microdisk laser coupled to the waveguide. The noise level of the signal after the microdisk laser is reduced compared to the noise level of the input PRBS. The extinction ratio (ER) measurement is carried out by measuring the logical “0” and “1” levels of the data waveform. The calculated ER of the eye diagram of the input signal (Figure 4.3b) is 5.6dB, while the calculated ER of the eye diagram of the regenerated signal (Figure 4.4b) is 7.5dB.

We simulate the ER of the regenerated signal in the waveguide as a function of the input pulse power. The regenerated signal consists of the transmitted input field and of the CCW laser emission of the microdisk laser coupled to the waveguide. The parameters for this simulation are identical to the ones listed in table 4.1. The microdisk laser is still operated at 4mA under continuous-wave bias. The ER of the PRBS signal is kept constant and equal to 5.6dB. In Figure 4.5, it is clear that for low input pulse powers (lower than 0.1mW in the waveguide), the ER of the signal after the microdisk laser is greatly improved. The influence of the laser emission of the microdisk laser on the eye diagram of the regenerated signal is strong. For higher input pulse powers, the contribution of the

transmitted input field in the regenerated signal is stronger and the effect of the laser emission from the microdisk on the regeneration is less significant. The advantage of the regenerator lies in the fact that it is effective for sub-milliWatt input signals, which makes it more power efficient than opto-electronic regeneration.

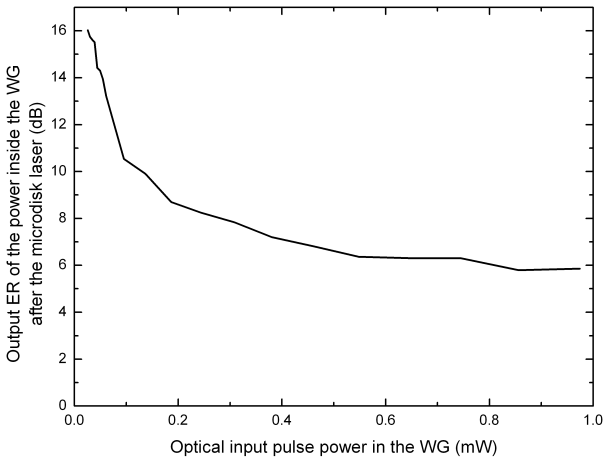

Figure 4.5: Simulation of the evolution of the ER of the optical power in the waveguide after regeneration as a function of the input pulse power in the waveguide.

4.1.4 Regenerator demonstration : results at 10Gb/s

For the experiment, we use the setup depicted in Figure 4.6. Light from a tunable laser source at the resonance wavelength of the microdisk laser (1561.6nm) is sent through a modulator, which is driven by a 10Gb/s pulse pattern generator (PPG). The PPG generates a pseudo-random bit-sequence (PRBS) of 2^{31}-1 bits. We use polarization controlling wheels after the laser source as the modulator only works in TE mode. The original signal is being attenuated, amplified using an erbium-doped fiber amplifier (EDFA), and filtered with a 3nm optical band-pass filter to decrease the optical signal-to-noise ratio. The resulting signal has an average power of 3.5dBm after degradation, and is injected with an optical fiber under a 10° angle into the waveguide through the left grating coupler. Due to a 20% coupling efficiency of the grating couplers, the optical power coupled to the microdisk laser is in the sub-milliWatt range. Light coupling out of the right grating coupler after the microdisk laser is collected in an optical fiber under a 10° angle. Amplification after the microdisk 2R regeneration was needed to increase the signal power. The optical amplification

was implemented in combination with an optical band-pass filter (bandwidth of 0.50nm) to remove amplified spontaneous emission and to emulate the simulated band-pass filter implemented in the simulations. A variable attenuator is used to change the received optical power on the receiver in order to plot BER-diagrams. The microdisk laser is operated at 4mA under continuous-wave bias.

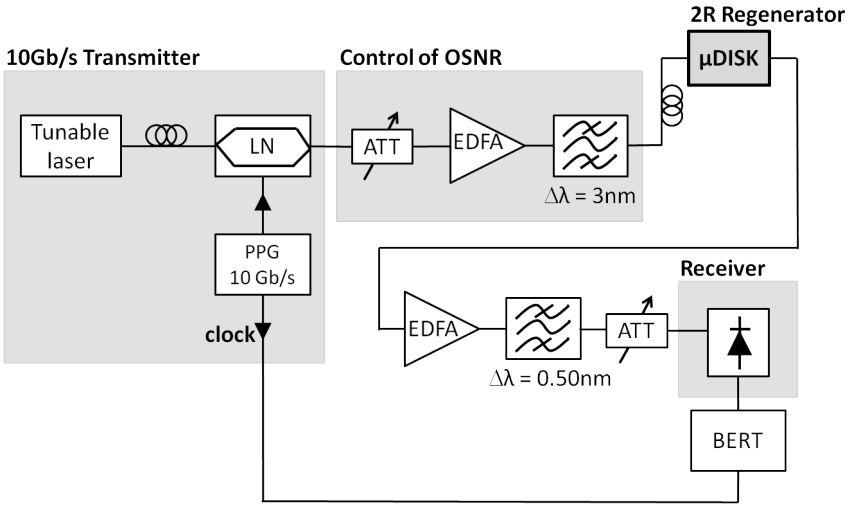

Figure 4.6: Schematic of the setup (LN: Lithium-Niobate modulator; PPG: Pulse Pattern Generator; ATT: attenuator; EDFA: Erbium-Doped Fiber-Amplifier; μDISK: microdisk laser; BERT: Bit-Error-Rate-Tester).

The regenerative capabilities of the regenerator under dynamic operation at 10Gb/s are demonstrated. Figure 4.7 shows the BER measurement results of the degraded signal and the regenerated signal. To measure the BER of the degraded signal, the modulated light out of the 3nm optical band-pass filter is directly sent to the second EDFA. Figures 4.8a and 4.8b show the eye diagrams with and without the 2R regenerator. Clearly, the signal is regenerated. An improvement of the ER is demonstrated. For an input signal with a 13dB-ER, a 2.9dB-improvement in ER is measured. The relatively low experimental ER improvement is due to the presence of the EDFA before the photoreceiver and to a high receiver noise. The amplified spontaneous emission from the EDFA considerably increases the level of the logical "0". Also, the input ER is already very high. The regeneration is also visible on Figure 4.9 where the distributions of the logical "0" and logical "1" levels from the two eye diagrams are plotted. The noise is significantly reduced after regeneration, even though we still suffer from the amplified spontaneous emission from the EDFA located before the re-

ceiver. The eye becomes more open after the 2R regenerator. Less data points are present between the two logical levels on the distribution related to the regenerated signal (Figure 4.9b) that on the distribution related to the degraded one (Figure 4.9a). The distribution of logical "1" level is also narrower after regeneration. We demonstrate an improvement of the Q-factor, from 3.93 for the eye of the degraded signal (Figure 4.8a) to 4.24 for the eye of the regenerated signal (Figure 4.8b).

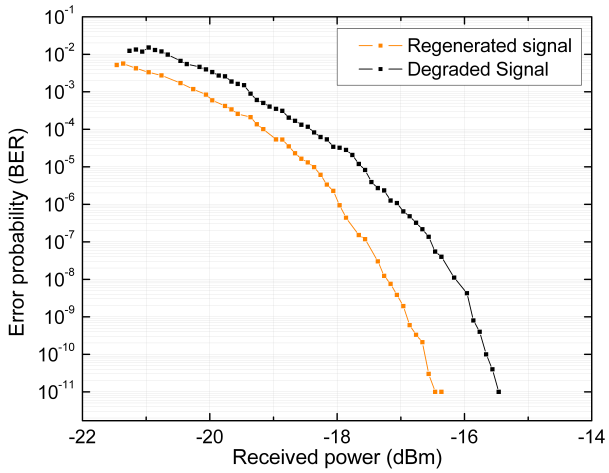

Figure 4.7: BER measurement results with and without 2R regeneration at 10Gb/s. The average power of the degraded signal coupled to the microdisk laser is in the sub-milliWatt range.

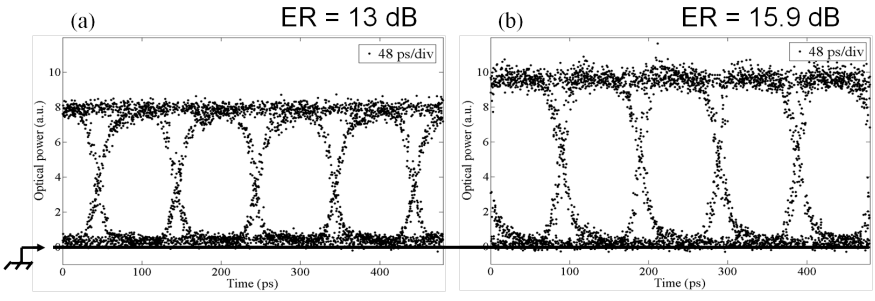

Figure 4.8: (a) Eye diagram of the degraded signal. (b) Eye diagram of the regenerated signal.

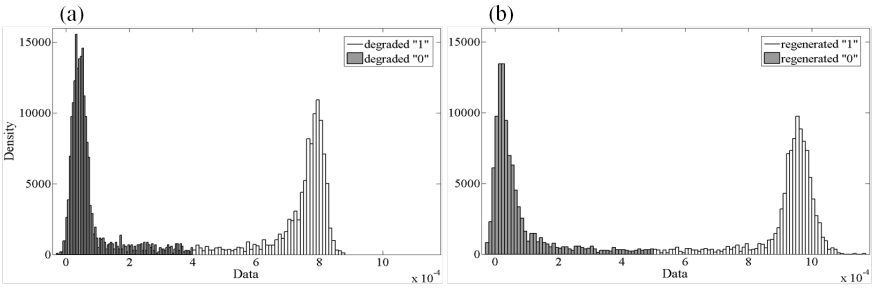

Figure 4.9: Distributions of the logical "1" and the logical "0" levels from (a) the eye diagram of the degraded signal and (b) the eye diagram of the regenerated signal (from Figure 4.8).

4.1.5 Simulation of the regeneration behavior : results at 20Gb/s

The experimental eye diagram from Figure 4.8 shows that operation at a higher speed could be tested on the same sample. However, it was not possible to further test the device under 20Gb/s operation. Experimentally, in [15], the switch-off time of a 7.5μm-diameter microdisk laser based on the same epitaxy has been measured when performing flip-flop operation. A switching time of 60ps was measured. Figures 4.10 and 4.11 depict the simulation results for operation at 20Gb/s. The simulation parameters are identical to the ones presented in table 4.1. We still observe an improvement of the ER of the signal after regeneration, which indicates that the experiment could indeed be carried out at 20Gb/s.

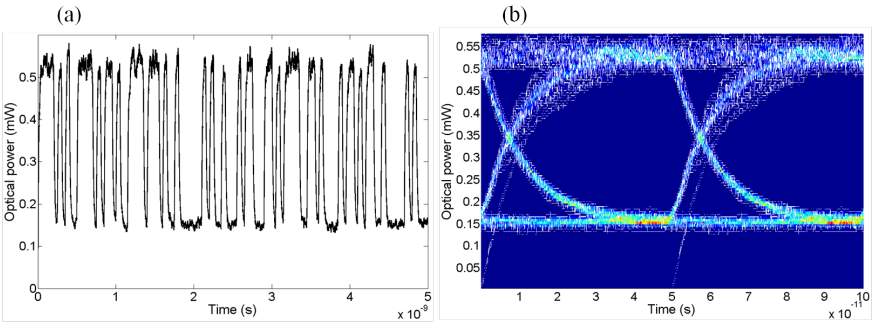

Figure 4.10: Simulation of the injection of a noisy 20Gb/s pseudo-random bit-sequence (PRBS) in the waveguide. (a) Degraded pseudo-random-bit-sequence (PRBS) at 20Gb/s in the waveguide after filtering with a 61GHz band-pass filter : Gaussian white noise is visible on the trace of the optical power of the input signal. (b) Resulting eye diagram of the degraded and filtered signal in the waveguide before the microdisk laser.

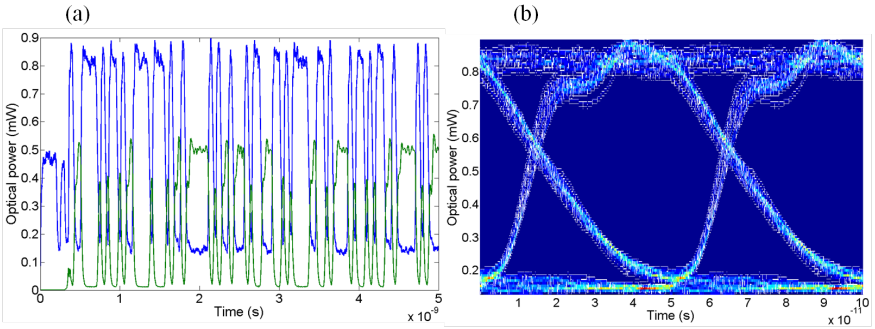

Figure 4.11: Simulation of the regeneration of a noisy 20Gb/s pseudo-random bit-sequence (PRBS) in the waveguide. (a) Optical powers at the output of the microdisk laser, in the waveguide, after filtering with a 61GHz band-pass filter. Above threshold, the microdisk is lasing in the CW dominant state (green) (t=400ps), but as soon as an optical pulse is injected on the left side of the waveguide, the microdisk switches to lase in the CCW dominant state (blue). After the pulse has passed through, the microdisk laser switches back to the CW mode (green). (b) Resulting eye diagram of the regenerated and filtered signal in the waveguide after the microdisk laser.

4.2 Microdisk resonator as an all-optical gate: operation at 10Gb/s

An optical gate is a device in which an optical probe signal output is controlled by a control signal. The control signal can be in the electrical or optical domain. In an electrically controlled gate, the applied voltage decides the output level of the optical probe signal. While in an optically controlled optical gate, the probe as well as the control signal are in the optical domain. An integrated all-optical gate was reported in 1983 in [30]. Using a CMOS compatible platform, all-optical control of light by light was reported in 2004 in [31]. Afterwards, all-optical gates or modulators on III-V or Si based platforms have been reported by different research groups [32], [33], [34]. Due to their smaller achievable size and enhanced nonlinearity originating from the resonant behavior along with high optical confinement, microdisks/rings are considered to be promising for compact and integrated wavelength conversion devices along with many other applications. Wavelength conversion in III-V microdisk using FWM was reported in [35]. On a pure silicon platform, the same was reported in [36] using all-optical modulation. Wavelength conversion in III-V-on-silicon microdisks can be achieved with or without application of an electrical bias. Using electrically biased III-V-on-silicon microdisk, the working principle is based on the fact that the natural lasing from the microdisk can be suppressed when an external control beam is injected into the microdisk cavity. Therefore, the information carried on the injected beam will be copied inversely to the natural lasing wavelength of the microdisk [37], [38], [39]. The experimental demonstration of optical gating based on a microdisk molecularly bonded on SOI and fabricated at CEA-Leti has also been reported [18].

The concept of wavelength conversion in III-V-on-silicon microdisk without using any electrical bias is illustrated in Figure 4.12. The information at a wavelength λ_1 can be transferred to another wavelength λ_2 if λ_1 and λ_2 correspond to the transmission resonances of the microdisk resonator. This concept is based on the refractive index and hence transmission modulation of the resonance, to which the probe beam is tuned, in response to the logic level of data (pump) stream tuned at another resonance.

4.2.1 Concept of an all-optical gate based on a microdisk resonator

An all-optical gate can be realized with a microdisk resonator in a pump-probe configuration [32]. When a high-intensity pump beam is tuned to one of the transmission resonances of the microdisk, the change in the transmittance

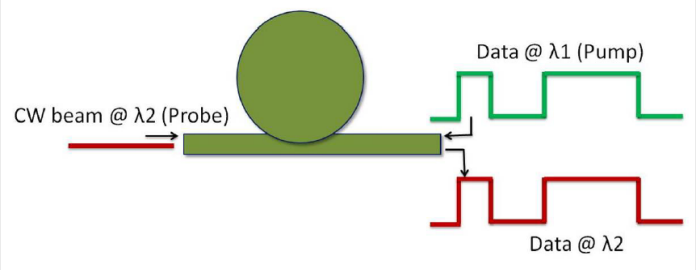

Figure 4.12: Illustration of wavelength conversion concept in a microdisk resonator using pump-probe configuration.

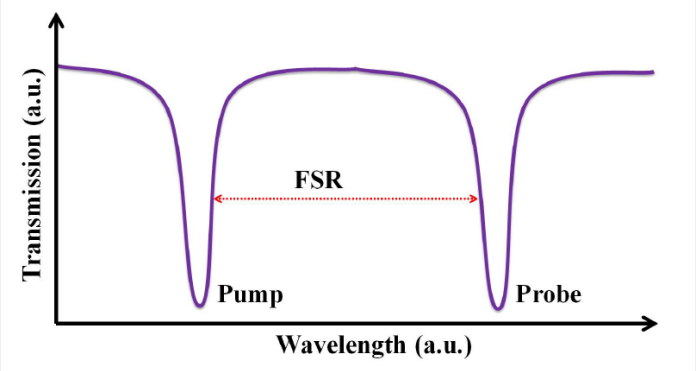

Figure 4.13: Transmission resonance characteristics of a microdisk and the selection of pump and probe wavelengths [40].

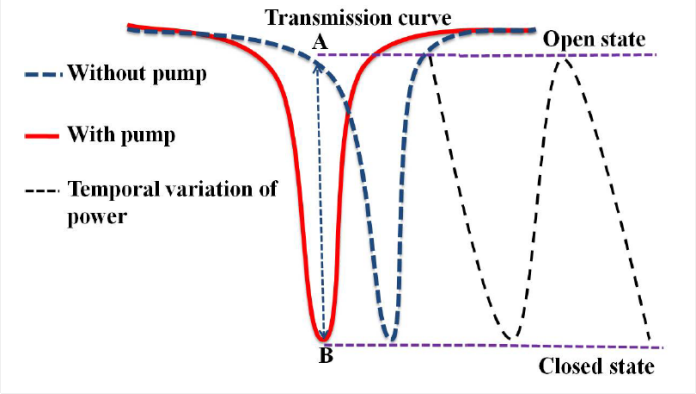

Figure 4.14: Illustration of the concept of an all-optical gate [40].

allows to switch a continuous wave (CW) probe beam tuned to the next resonance as shown in Figure 4.13. For a given band gap of the active material used for fabricating the resonator, the switching can be achieved by exploiting either single photon absorption (SPA) or two photon absorption (TPA) depending upon the wavelength chosen for of the pump. In SPA, each absorbed photon generates an electron-hole pair and these generated carriers change the absorption coefficient and the refractive index of the active layer of the microdisk.

Figure 4.14 schematically illustrates the gating concept. The dotted blue curve shows the transmission dip of the microdisk around the probe wavelength. When pump light is injected into the microdisk at another resonance of the microdisk, free carriers are generated which causes a blue shift in the transmission dip as shown by the solid red curve. Using a pulse train as a pump results in high or low output of the probe beam due to a periodic shifting of the resonance around the probe wavelength. If the probe wavelength is slightly blue tuned off the transmission dip then in the absence of the pump pulse the output is high and the gate is said to be in the open state. In the presence of the pump pulse, due to blue shift of the resonance, the output will be low and the gate is said to be in the closed state. In this way, the power level varies between points A and B in the time domain as represented by the dotted black line. During this whole process, the variation in the power level of the output of the gate follows the pattern of the pump pulses.

Experiments on gating are carried out using III-V material bonded with adhesive bonding process on top of a SOI waveguide circuit as described in section 2.15. The particular microdisk used for the experiment has a diameter of 10μm and was fabricated in a CMOS-compatible fab at CEA-Leti. To find the microdisk resonances, the transmission spectra are measured with transverse electric (TE) polarized light from a continuous-wave (CW) tunable laser. The transmission characteristic of the microdisk resonator is presented in Figure 4.15. Two resonances, one at 1561.8nm and another at 1583.65nm, are measured. Weakers resonances corresponding to other radial modes are also visible on Figure 4.15. The large change in the resonance behavior (extinction ratio, Q-factor) at two wavelengths is due to the fact that the shortest wavelength (1561.8nm) has higher absorption as it lies further away from the bandgap wavelength of the microdisk than the longest wavelength (1583.65nm).

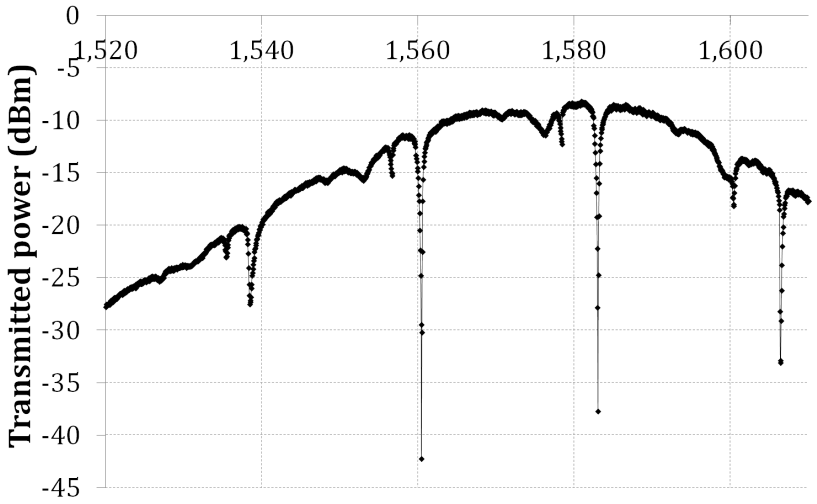

Figure 4.15: Transmission spectrum of the microdisk resonator (x-axis: wavelength in nanometers).

4.2.2 Dynamic all-optical gating measurements at 10Gb/s

Dynamic all-optical gating measurements are performed in a pump-probe configuration. The experimental setup used is sketched in Figure 4.16. A tunable laser (TL) provides the probe beam while a short pulse source provides a pulse train which acts as a pump. The repetition rate of the short pulse source is set by the frequency of a RF output signal from the RF generator. The gate output is collected at the drop port of a circulator. The gate output is amplified using a L-band Erbium-Doped Fiber Amplifier (EDFA). A band pass filter (BPF) follows the EDFA to suppress the amplified spontaneous emission noise generated in the EDFA. The gate output is finally fed to a high speed photodetector (HSPD) connected to a scope. The trigger signal to the scope is provided by the RF generator using a 3dB RF splitter whose other output is connected to the short pulse source. The wavelength of the pump light is set at the lower resonance (1561.8nm), while the wavelength of the probe light is set slightly below the longest resonance (1583.55nm). The pump light is a train of 7.5ps-long pulses at a repetition rate of 10GHz and with an extinction ratio of more than 20dB.

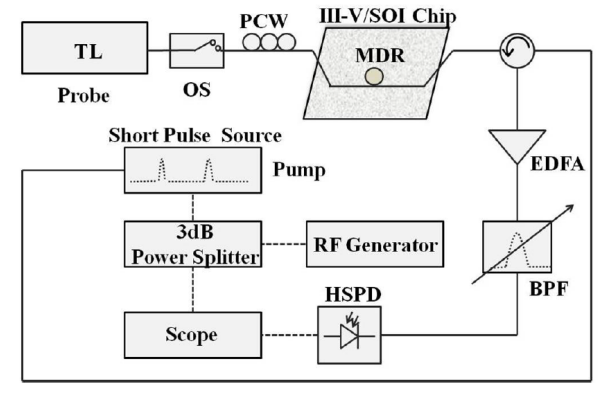

Figure 4.16: Schematic of the experimental setup used for dynamic all-optical gating measurements. MDR : microdisk resonator; OS : optical switch; PCW : polarization controlling wheels [40].

Probe and average pump power in the SOI waveguide are 170μW and 1.5mW, respectively. While carrying out the measurements, the microdisk is kept under a reverse bias of -1V to reduce the fall time by sweeping away the generated carriers from the active region [42].The gate output corresponding to the pulse train (Figure 4.17) is plotted in Figure 4.18. When the pump pulse has a high/low power level, the gate is in the closed/open state, as previously discussed. The extinction ratio between the closed state and the open state is

4.5dB.

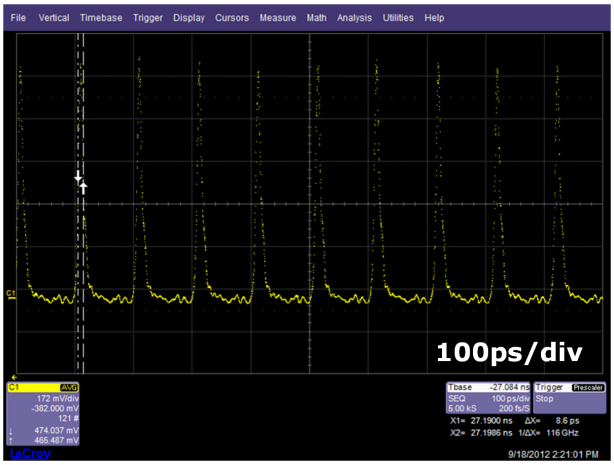

Figure 4.17: All-optical gating: pattern of the pulse train.

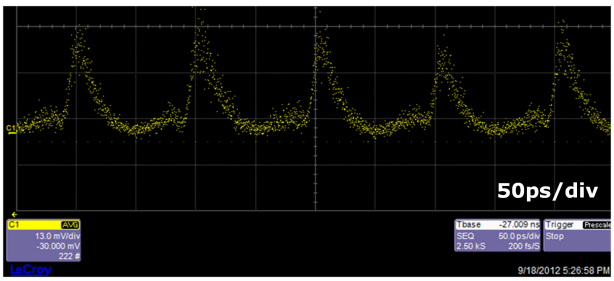

Figure 4.18: All-optical gating: corresponding gating output.

To estimate the gating speed of the device under investigation, transient responses are measured and are plotted in Figure 4.19a and Figure 4.19b. The rise time and fall time are 8.0 and 41.0ps respectively, which suggests that this device can operate up to 20GHz. The low dynamic extinction ratio, as compared to the static extinction ratio (10dB (Figure 4.17)), can be attributed to the spontaneous emission noise generated in the EDFA used to amplify the gate output before feeding it to the oscilloscope, and to the fact that the gate might simply not be fast enough. The speed of the gate is believed to be related to the surface-state recombinations at the sidewalls of the microdisk, along with a contribution from the reverse bias. It seems that by increasing the pump power, the rise time can be reduced but it also requires increasing the reverse bias (to -2V) to compensate the increased fall time. Under the same pump power and increasing the reverse bias to -2V, no improvement in the fall time has been seen. This

can be explained by the saturation of drift velocity as a function of the applied electrical field. When the microdisk is biased at -2V, it is in drift velocity saturation regime [43]. The bandwidth of the pump pulse used is 1nm while the bandwidth of the transmission resonance at 1561.8nm is 0.4nm. This implies that the pump power can be further reduced by matching the bandwidth of the pump signal to that of the microdisk resonance.

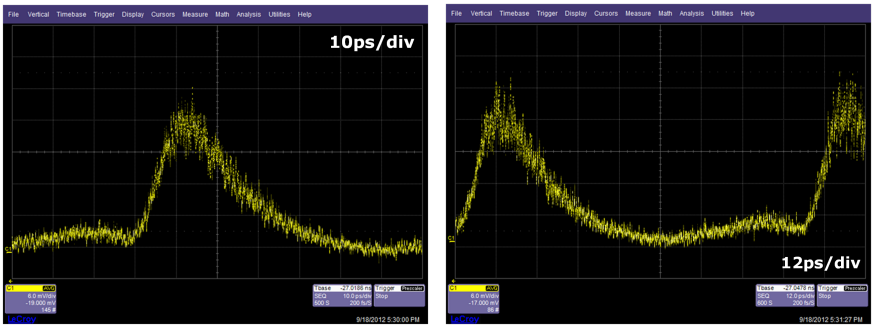

(a) **(b)**

Figure 4.19: Transient response of the gate output. (a) Rise edge. (b) Fall edge.

4.3 Microdisk resonator as an all-optical gate: operation at 20Gb/s

As reported in section 4.2, transient responses suggest that the device can operate up to 20GHz. Dynamic all-optical gating measurements are performed in a pump-probe configuration keeping the probe wavelength around the shortest wavelength resonance and nearly critically coupled. All-optical wavelength conversion is done for 20Gb/s Pseudo-Random-Bit-Sequence (PRBS) data having a pattern length of 2^{31}-1 as the control (pump) signal. The experimental setup used is sketched in Figure 4.20. TL1 is used to provide a probe signal slightly detuned from the longest resonance wavelength of the microdisk (1583.55nm). An electrical PRBS signal at the speed of 20Gb/s generated from the pulse pattern generator driven by a RF source at 20GHz is converted into optical PRBS data using an electro-optic $LiNbO_3$ Mach-Zehnder modulator and a CW optical signal from TL2 tuned at the shortest resonance wavelength of the microdisk (1561.8nm). The generated optical PRBS control signal has an average power of 5mW (in the SOI waveguide). The pulse duration is 25 ps (Full-Width-at-Half-Maximum) for a logic "1" level. A circulator is used to collect the probe signal. The backreflected control signal is suppressed with a wideband

bandpass optical filter (bandwidth of 10 to 15nm) tuned around the wavelength of the probe signal. Afterwards, the signal is amplified with a *L*-band EDFA and the ASE caused by the EDFA is filtered with a 0.5nm-wide filter before being detected by the photodiode connected to a high-speed oscilloscope.

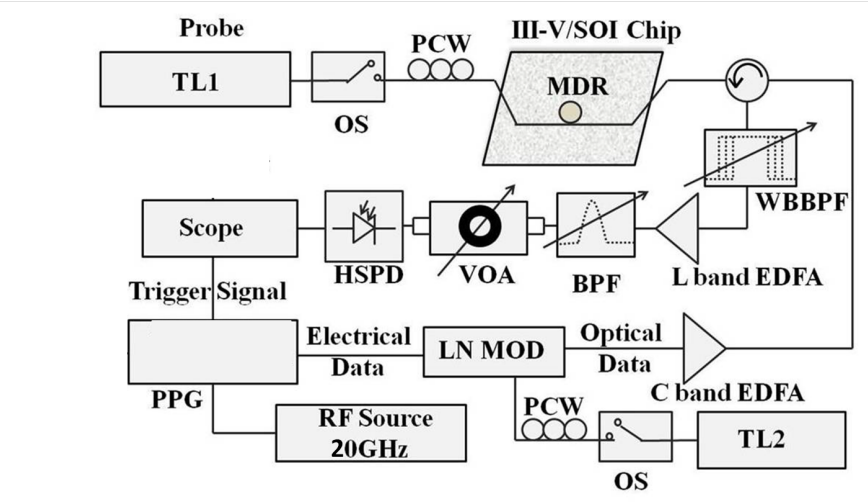

Figure 4.20: Schematic of the experimental setup used for all-optical wavelength conversion at 20Gb/s. TL1 and TL2: tunable lasers; OS: optical switch; PCW: polarization controlling wheels; MDR: microdisk resonator; WBBPF, wideband bandpass filter; BPF: bandpass filter; HSPD: high-speed photodiode (30 GHz); LN MOD: Lithium Niobate Mach-Zehnder modulator; PPG: pulse pattern generator; VOA: variable optical attenuator [40].

Figure 4.21 is the original 20Gb/s PRBS signal at the wavelength of 1561.8nm out of the modulator. The information contained in the control signal at the lower resonance wavelength is transferred to the higher resonance wavelength (CW probe beam) and is plotted in Figure 4.22a. The microdisk laser is reversed bias at -0.2V. The eye diagram corresponding to the wavelength converted signal is shown in Figure 4.22b. The eye is noisy and closing, but could be good enough to be used in combination with Forward-Error-Correction (FEC). FEC is a technique used for controlling errors in data transmission over unreliable or noisy communication channels. The central idea is that the sender encodes their message in a redundant way by using an error-correcting code. The redundancy allows the receiver to detect a limited number of errors that may occur anywhere in the message, and often to correct these errors without retransmission. FEC gives the receiver the ability to correct errors without needing a reverse channel to request retransmission of data, but at the cost of a fixed, higher

forward channel bandwidth. An explanation for the noisy and closing eye could be that the pump beam is injected at a very sharp resonance (with a high Q-factor). The fall time of the optical power inside the microdisk might then be larger than the fall time of the pump signal that is injected in the Silicon waveguide. The pump light then keeps on propagating in the disk (with a decay time given by $\frac{\omega_0}{Q}$) and so the resonance might shift slower. Trying to inject the pump beam at a lower resonance wavelength (1538.70nm), with a lower Q resonance and consequently a shorter carrier lifetime, did not improve the results. Also, reverse biasing the microdisk more did not lead to improvement of the quality of the eye diagram.

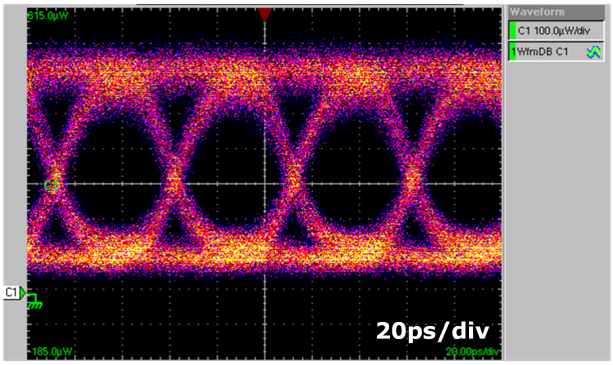

Figure 4.21: Eye diagram of the 20Gb/s PRBS signal.

4.4 All-optical flip-flop triggered with 25ps-long optical pulses

In optical packet switching networks, all-optical flip-flops (AOFFs) are necessary for holding decisions from the optical header processors and for providing control signals to the optical switches [44]. Compact AOFFs have been demonstrated with a number of InP-based active devices, usually bistable laser diodes [46], ring lasers [47], or VCSELs [48]. However, the footprint (several tens of μm), the power consumption (several tens of mW) and the pulsed regime of operation of such devices are still holding these technologies back for certain applications. The heterogeneous integration of III-V material on SOI is a CMOS-compatible alternative that provides dense, large-scale integration of devices. The results leading to flip-flop operation in a microdisk laser heterogeneously bonded on SOI [15] were obtained within the European FP7 Historic project. Flip-flop operation at 10Gb/s in ultra-small microdisk lasers that were integrated on silicon is described in [49]. The devices have a diameter of only

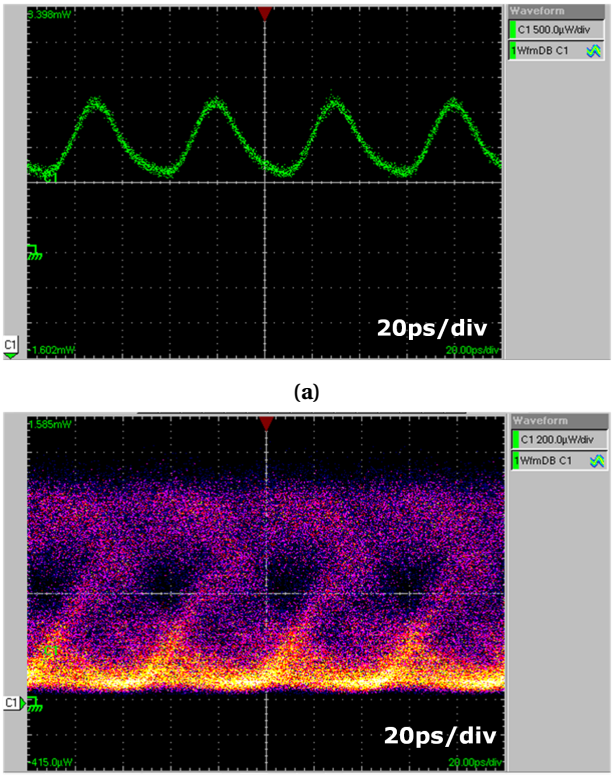

(a)

(b)

Figure 4.22: (a) Waveform of the wavelength converted signal. (b) Corresponding eye diagram.

7.5μm and require a bias current of only 3.5mA. The switching energies can be as low as 1.8fJ. The small footprint and power consumption of these devices make them interesting for large-scale integration with applications such as optical shift registers or random access memories (RAMs). The principle relies on the unidirectional operation of the microdisks due to the nonlinear gain suppression from spectral hole burning and carrier heating.

The switching is performed with 100ps-long optical pulses at a repetition rate of 10Gb/s [15]. The measured switch-off transient of 60ps was measured. On the other hand, the set pulses could not be removed because of the design, as they were at the same wavelength as the microdisk output, and were also propagating in the same direction. Nevertheless, it is obvious from the measurements that the switch-on time should be less than 100ps. In this section,

we perform an all-optical flip-flop experiment on a 20μm-diameter microdisk laser with 25ps-long optical pulses (FWHM). The light-current (LI) characteristic of the microdisk laser, measured at the two ends of the SOI waveguide, is depicted in Figure 4.23. This measurement was undertaken under continuous wave operation at room temperature.

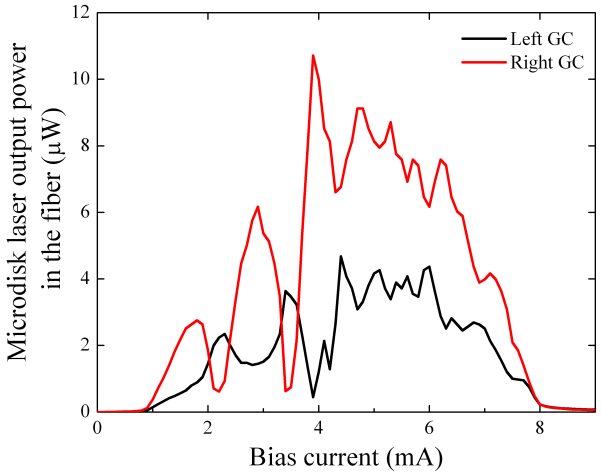

Figure 4.23: L-I curves for the two competing modes (CW and CCW) of a 20μm-diameter microdisk laser.

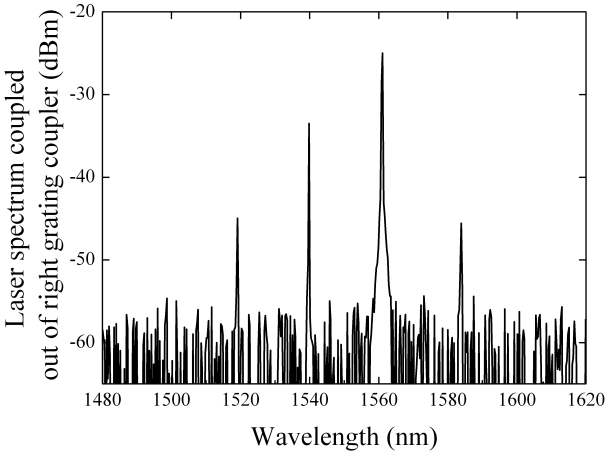

Figure 4.24: Lasing spectrum for the CW mode a 20μm-diameter microdisk laser at a bias of 4.64mA.

When the threshold current of 0.9mA is surpassed, a bidirectional regime is observed. The clockwise and the counter clockwise modes are equally present in this bidirectional regime. A different attenuation by the waveguides as well as small alignment mismatches are responsible for the difference in output power between the two sides. Between 2.0mA and 3.6mA, the reflection feedback from the grating coupler and/or the fiber facet causes a small periodic oscillating regime. The unidirectional, bistable operation starts at 3.6mA. The maximum measured optical output power in the fiber is 11μW. Due to the improved thermal management, the thermal roll-over only starts at 6.2mA. Figure 4.24 shows the output power spectrum of the biased microdisk laser (4.64mA) and illustrates lasing at 1561.86nm.

The measurement setup is schematically depicted in Figure 4.25. Light from a tunable laser source is sent through a modulator which is driven by a 40Gb/s pulse pattern generator. The width of the pulses is then 25ps. We use polarization controlling wheels after the laser source because the modulator works only in TE mode. The pulses are split by a 3dB coupler and a variable optical delay line (ODL) is placed in one of the arms to adjust the relative arrival time between the set and reset pulses. Variable optical attenuators allow to adjust the pulse power. Because the grating couplers are polarization dependent, we use again polarization controlling wheels, before the pulses are sent into the chip. With circulators on both sides, we can monitor the output power of the microdisk on a high-speed optical sampling scope. To overcome the dark current of the detector, the signal power is boosted with an EDFA to increase the signal power (25dB amplification) in combination with an optical band-pass filter (OBPF) with a bandwidth of 0.9nm to remove amplified spontaneous emission.

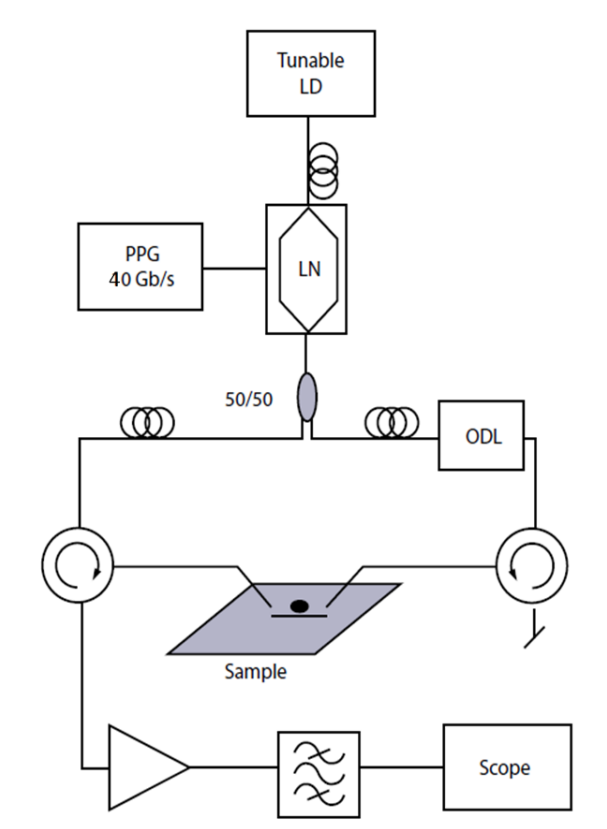

Figure 4.25: Schematic of the measurement set-up for the dynamic all-optical flip-flop experiment with 25ps-long pulses (LN: Lithium-Niobate modulator; PPG: Pulse Pattern Generator; ODL: Optical Delay Line) [14].

The high-speed measurement result of the flip-flop operation is depicted in Figure 4.26b. The microdisk is biased at 4.64mA. When a pulse is injected on the right side of the microdisk, the laser starts operating in clockwise dominant state. This state will remain, even after the pulse has passed through. Injection of a (reset) pulse at the other side 1.2ns later (Figure 4.26a) suppresses the clockwise mode and induces the counter clockwise dominant state. The measured switch-on transient is presented in Figure 4.26c. The set pulse can first be seen, but it is clear the microdisk laser switches after the set pulse. A switching time lower than 60ps was measured. From Figure 4.26d, the injected reset pulse covers the transient of the microdisk output, but the measured switch-off time is also lower than 60ps. However, since the set pulses are at the same wavelength than the microdisk output, and are propagating in the same direction, they cannot be removed in the current design.

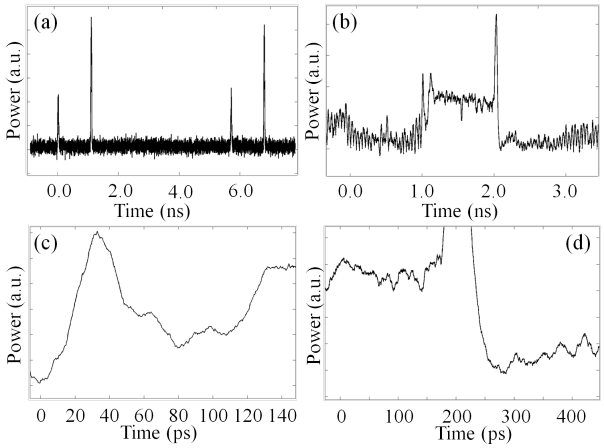

Figure 4.26: High-speed measurement of the switching characteristics for an all-optical flip-flop experiment with 25ps-long pulses. (a) Waveform of the injected optical pulses (central wavelength: 1561.86nm). (b) Waveform of the measured optical signal at one side of the SOI waveguide (averaging over spans of 91 samples). Details of the switch-on (c) and switch-off (d) transients.

We demonstrate the all-optical flip-flop operation of a 20μm-diameter microdisk laser fabricated in a CMOS pilot-line and working in continuous-wave regime. Switching is performed with 25ps-long pulses, and we demonstrate switching times lower than 60ps.

4.5 Discussion

A new concept for 2R regeneration is proposed using a microdisk laser. Improvement in ER and noise reduction have been experimentally demonstrated. We reported bit error rate improvement of 10Gb/s NRZ signals. We explain the relatively low re-amplification of the signal after the microdisk laser by the low photon lifetime in the cavity. Simulations demonstrate optical output powers in the milliWatt range in the waveguide after the microdisk laser when the photon lifetime is increased to a few picoseconds. The parameters taken into account in the simulation (differential gain, etc) are parameters tabled at room temperature. Experimentally, at a continuous bias current of 4mA, heat is already generated inside the microdisk laser, which affects its characteristics. Also, the experimental coupling efficiency between the microdisk laser and the underlying waveguide is unknown. The value implemented in the simulation is what we believe is a relevant value. This can explain the discrepancy in terms of optical output powers between the simulations and the experimental results. Improving the etching process of the microdisk (improvement of the sidewall roughness) will increase the photon lifetime and allow the combination of the noise reduction to a stronger re-amplification of the signal. Table 4.2 compares our technology to other integrated solutions for regeneration. The advantage of the regenerator lies in the fact that it is effective for sub-milliWatt input signals, which makes it more power efficient than opto-electronic regeneration. The regenerators presented in [8], [10], and [14] all require optical input powers of several milliWatt, and are biased above 100mA. This CMOS compatible scheme is promising for all-optical regeneration in future optical networks.

Device	*Footp.* (μm^2)	*Bias current*	*2R speed*	*Input power*	*Signal type*	*Ref.*
Active MZs	>100x100	>250mA	40Gb/s	mW	RZ	[8]
SOAs–LOAs	100x100	250mA	10Gb/s	mW	NRZ	[10]
DFB laser	400x100	150mA	25Gb/s	mW	NRZ	[14]
InP switch	2x100	/	5Gb/s	mW	NRZ	[13]
Microdisk laser	7.5x7.5	4mA	10Gb/s	100μW	NRZ	[50]

Table 4.2: Comparison of the microdisk laser on SOI regenerator with other integrated solutions in terms of footprint, bias current, achievable speeds, nature of signal and power consumption

We demonstrate all-optical gating at 10Gb/s, with switching times compatible with operation at 20Gb/s. The results at 20Gb/s are noisy, but could be good enough to be used in combination with Forward-Error-Correction (FEC).

An explanation for the closing eye could be that the pump beam is injected at a very sharp resonance (with a high Q-factor). The fall time of the optical power inside the microdisk might then be larger than the fall time of the pump signal that is injected in the Silicon waveguide. The pump light then keeps on propagating in the disk (with a decay time given by $\frac{\omega_0}{Q}$) and so the resonance might shift slower. Trying to inject the pump beam at a lower resonance wavelength (1538.70nm) in another device, with a lower Q resonance and consequently a shorter carrier lifetime, could improve the results.

Finally, we report flip-flop operation of a 20μm-diameter microdisk laser, triggered with 25ps-long optical pulses. Switching times lowers than 60ps are recorded. Further optimisation of the speed of the microdisk AOFF so as to allow operation at 40Gb/s will result in energy consumption which is actually very competitive with CMOS solutions [15].

References

[1] D. A. B. Miller. *Are optical transistors the logical next step?*. Nature Photonics, 4:3–5, 2010.

[2] J. Leuthold, G. Raybon, Y. Su, R. Essiambre, S. Cabot, J. Jaques, and M. Kauer. *40 Gbit/s transmission and cascaded all-optical wavelength conversion over 1 000 000 km*. Electronics Letters, 38(16):890–892, 2002.

[3] G. Puerto, B. Ortega, M. D. Manzanedo, A. Martinez, D. Pastor, J. Capmany, and G. Kovacs. *Dimensioning of 10 Gbit/s all-optical packet switched networks based on optical label swapping routers with multistage 2R regeneration*. Optics Express, 14(22):10298–10306, 2006.

[4] M. Yong-Jeon, Z. Pan, J. Cao, Y. Bansal, J. Taylor, Z. Wang, V. Akella, K. Okamoto, S. Kamei, J. Pan, and S.J.B. Yoo. *Demonstration of all-optical packet switching routers with optical label swapping and 2R regeneration for scalable optical label switching network applications*. Journal of Lightwave Technology, 21(11):2723–2733, 2003.

[5] P. Zakynthinos, G. T. Kanellos, D. Klonidis, D. Apostolopoulos, N. Pleros, A. Poustie, G. Maxwell, I. Tomkos, and H. Avramopoulos. *Cascaded operation of a 2R burst-mode regenerator for optical burst switching network transmission*. IEEE Photonics Technology Letters, 19(21-24):1834–1836, 2007.

[6] Z. J. Huang, A. Gray, I. Khrushchev, and I. Bennion. *10Gb/s transmission over 100mm of standard fiber using 2R regeneration in an optical loop mirror*. IEEE Photonics Technology Letters, 16(11):2526–2528, 2004.

[7] J. Mork, F. Ohman, and S. Bischoff. *Analytical expression for the bit error rate of cascaded all-optical regenerators.* IEEE Photonics Technology Letters, 15(10):1479–1481, 2003.

[8] D. Wolfson, A. Kloch, T. Fjelde, C. Janz, B. Dagens, and M. Renaud. *40-Gb/s all-optical wavelength conversion, regeneration, and demultiplexing in an SOA-based all-active Mach-Zehnder interferometer.* IEEE Photon. Technol. Lett., 12(3):332–334, 2000.

[9] P. V.Mamyshev. *All-optical data regeneration based on self-phase modulation effect.* 24th European Conference Optical Communication (Spain), 475–476, 1998.

[10] M. Rochette, L. B. Fu, V. Taeed, D. J. Moss, and B. J. Eggleton. *2R optical regeneration: An all-optical solution for BER improvement.* IEEE J. Sel. Topics Quantum Electron., 12(4):736–744, 2006.

[11] J. Leuthold, B. Mikkelsen, R. E. Behringer, G. Raybon, C. H. Joyner, and P. A. Besse. *Novel 3R Regenerator Based on Semiconductor Optical Amplifier Delayed-Interference Configuration.* IEEE Photon. Technol. Lett., 13(8):860–862, 2001.

[12] B. Li, M. Irfan Memon, G. Mezosi, Z. Wang, M. Sorel, and S. Yu. *Characterization of all-optical regeneration potentials of a bistable semiconductor ring laser.* J. Lightwave Technol., 27(19):4233–4239, 2009.

[13] M. Tassaert, H. J. S. Dorren, G. Roelkens, and O. Raz. *Passive InP regenerator integrated on SOI for the support of broadband silicon modulators.* Opt. Express, 20(10):11383–11388, 2012.

[14] K. Huybrechts, T. Tanemura, K. Takeda, Y. Nakano, R. Baets, and G. Morthier. *All-optical 2R regeneration using the hysteresis in a distributed feedback laser diode.* IEEE Journal in Quantum Electronics, 16(5):1434–1439, 2010.

[15] L. Liu, R. Kumar, K. Huybrechts, T. Spuesens, G. Roelkens, E.-J. Geluk, T. de Vries, P. Regreny, D. Van Thourhout, R. Baets, and G. Morthier. *An ultra-small, low-power, all-optical flip-flop memory on a silicon chip.* Nature Photonics, 4:182–187, 2010.

[16] D. Liang, M. Fiorentino, S. Srinivasan, S. T. Todd, G. Kurczveil, J. E. Bowers, and R. G. Beausoleil. *Optimization of Hybrid Silicon Microring Lasers.* IEEE Photonics Journ., 3:580–587, 2011.

[17] T. Spuesens, J. Bauwelinck, P. Regreny, D. Van Thourhout. *Realization of a compact optical interconnect on Silicon by heterogeneous integration of III-V.* IEEE Photonics Technology Letters, 25(14):1332–1335, 2013.

[18] R. Kumar, T. Spuesens, P. Mechet, P. Kumar, O. Raz, N. Olivier, J.-M. Fedeli, G. Roelkens, R. Baets, D. Van Thourhout, and G. Morthier. *Ultra-fast and*

Bias-free All-Optical Wavelength Conversion Using III-V on Silicon Technology. Opt. Lett., 36(13):2450–2452, 2011.

[19] J. Hofrichter, T. Morf, A. La Porta, O. Raz, H. J. S. Dorren, and B. J. Offrein. *A single InP-on-SOI microdisk for high-speed half-duplex on-chip optical links.* Opt. Express, 20(26):365–370, 2012.

[20] J. B. Lasky. *Wafer bonding for silicon-on-insulator technologies.* Appl. Phys. Lett., 48(1):78–80, 1986.

[21] M. Kostrzewa, L. Dicioccio, M. Zussy, J. Roussin, J. Fedeli, N. Kernevez, P. Regreny, C. Lagaheblanchard, and B. Aspar. *InP dies transferred onto silicon substrate for optical interconnects application.* Sensors and Actuators A: Physical, 125(2):411–414, 2006.

[22] F. Van Laere, G. Roelkens, M. Ayre, J. Schrauwen, D. Taillaert, D. Van Thourhout, T. F. Krauss, and R. Baets. *Compact and highly efficient grating couplers between optical fiber and nanophotonic waveguides.* J. Lightwave Technol., 25(1):151–156, 2007.

[23] L. Grenouillet, A. Bavencove, T. Dupont, J. Harduin, P. Philippe, P. Regreny, F. Lelarge, K. Gilbert, P. Grosse, and J. Fedeli. *CMOS compatible contacts and etching for InP-on-silicon active devices.* 6th IEEE Int. Conf. Group IV Photon. (GFP), 196–198, 2009.

[24] T. Spuesens, F. Mandorlo, P. Rojo-Romeo, P. Regreny, N. Olivier, J.M. Fedeli, and D. Van Thourhout. *Compact integration of optical sources and detectors on SOI for optical interconnects fabricated in a 200 mm CMOS pilot line.* J. Lightwave Technol., 30(11):1764–1770, 2012.

[25] M. Sorel, G. Giuliani, A. Scire, R. Miglierina, S. Donati, and P. J. R. Laybourn. *Operating regimes of GaAs- AlGaAs semiconductor ring lasers : experiment and model.* IEEE J. Sel. Topics Quantum Electron., 39(10):1187–1195, 2003.

[26] T. Numai. *Analysis of signal voltage in a semiconductor ring laser gyro.* IEEE J. Sel. Topics Quantum Electron., 36(10):1161–1167, 2000.

[27] E. J. DAngelo, E. Zaguirre, G. B. Mindlin, G. Huyet, L. Gil, and J. R. Tredicce. *Spatiotemporal dynamics of lasers in the presence of an imperfect O(2) symmetry.* Phys. Rev. Lett., 68(25):3702–3705, 1992.

[28] M. Sargent. *Theory of a multimode quasi-equilibriumsemiconductor-laser.* Physical Review A, 48(1):717–726, 1993.

[29] J. Van Campenhout. *Thin-Film microlasers for the integration of electronic and photonic integrated circuits.* Doctoral Thesis, Ghent University, 2007.

[30] A. Lattes, H. Haus, F. Leonberger, and E. Ippen. *An ultrafast all-optical gate.* IEEE Journal of Quantum Electronics. 19(11):1718–1723, 1983.

[31] V.R. Almeida, C.A. Barrios, R.R. Panepucci, and M. Lipson. *All-optical control of light on a silicon chip.* Nature, 431:1081–1084, 2004.

[32] V. Van, T.A. Ibrahim, K. Ritter, P.P. Absil, G.G. Johnson, R. Grover, J. Goldhar, and P.-T. Ho. *All-optical nonlinear switching in GaAs-AlGaAs microring resonators.* IEEE Photonics Technology Letters, 14(1):74–76, 2002.

[33] T.B. Jones, M. Hochberg, and A. Scherer. *All-optical modulation in a silicon waveguide based on a single-photon process.* IEEE Journal of Selected Topics in Quantum Electronics, 14(5):1335–1342, 2008.

[34] M. Först, J. Niehusmann, T. Plötzing, J. Bolten, T. Wahlbrink, C. Moormann, and H. Kurz. *High-speed all-optical switching in ion-implanted silicon-on-insulator microring resonators.* Optics Letters, 32(14):2046–2048, 2007.

[35] P. P. Absil, J. V. Hryniewicz, B. E. Little, P.S. Cho, R.A. Wilson, L.G. Joneckis, and P.-T. Ho. *Wavelength conversion in GaAs micro-ring resonators.* Optics Letters, 25(8):554–556, 2000.

[36] Q. Xu, V. R. Almeida, and M. Lipson. *Micrometer-scale all-optical wavelength converter on silicon.* Optics Letters, 30(20):2733–2735, 2000.

[37] L. Liu, J. Van Campenhout, G. Roelkens, D. Van Thourhout, P. Rojo-Romeo, P. Regreny, C. Seassal, J.-M. Fédéli, and R. Baets. *Ultralow-power all-optical wavelength conversion in a silicon-on-insulator waveguide based on a heterogeneously integrated III-V microdisk laser.* Applied Physics Letters, 93(6):061107(1)–061107(3), 2008.

[38] O. Raz, L. Liu, R. Kumar, G. Morthier, D. Van Thourhout, P. Regreny, P. Rojo-Romeo, T. de Vries, and H.J.S. Dorren. *Compact, low power and low threshold electrically pumped micro disc lasers for 20Gb/s non return to zero all optical wavelength conversion.* The Optical Fiber Communication Conference and Exposition (OFC) and TheNational FiberOptic Engineers Conference (NFOEC), p.OMQ5, 2010.

[39] J. Hofrichter, O. Raz, L. Liu, G. Morthier, F. Horst, P. Regreny, T. de Vries, H.J.S. Dorren, and B.J. Offrein. *All-optical wavelength conversion using mode switching in InP microdisc laser.* Electronics Letters, 47(16):927–929, 2011.

[40] R. Kumar. *Applications of InP-on-Silicon Microdisks in All-Optical Signal Processing.* Doctoral Thesis, Ghent University, 2012.

[41] R. Kumar, L. Liu, G. Roelkens, E.-J. Geluk, T. de Vries, F. Karouta, P. Regreny, D. Van Thourhout, R. Baets, and G. Morthier. *10GHz All-Optical Gate Based on a III-V/SOI Microdisk.* IEEE Photonics Technology Letters, 22(13):981–983, 2010.

[42] S.F. Preble, Q. Xu, B.S. Schmidt, and M. Lipson. *Ultrafast all-optical modulation on a silicon chip.* Optics Letters, 30(21), 2891–2893, 2005.

[43] J.M.T. Pereira. *Frequency response analysis of InGaAs/InP photodiodes.* 6th Conference on Telecommunications, Peniche, Portugal, pp. 287–290, 2007.

[44] R. Van Caenegem, J. A. Martinez, D. Colle, M. Pickavet, P. Demeester, F. Ramos, and J. Marti. *From IP over WDM to all-optical packet switching: conomical view.* Journ. Lightw. Techn., 24, 1638–1645, 2006.

[45] H. J. S. Dorren, M. T. Hill, Y. Liu, N. Calabretta, A. Srivatsa, F. M. Huijskens, H. de Waardt, and G. D. Khoe. *Optical packet switching and buffering by using all-optical signal processing methods.* Journ. Lightw. Techn., 21, 2–12, 2003.

[46] M. T. Hill, H. J. S. Dorren, T. de Vries, X.J.M. Leijtens, J.H. den Besten, B. Smalbrugge, Y.-S. Oei, H. Binsma, G.-D. Khoe, M. K. Smit. *A fast low-power optical memory based on coupled micro-ring lasers.* Nature 432, 206–209, 2004.

[47] A. Trita, G. Mezosi, M.J. Latorre Vidal, M. Zanola, I. Cristiani, M. Sorel, P. Ghelfi, A. Bogoni, and G. Giuliani . *10 Gb/s Operation of monolithic all-optical set-reset flip-Flop based on semiconductor ring laser.* Conference on Lasers and Electro-Optics, San Jose, United States, 2010.

[48] S.-H. Lee, H.-W. Jung, K.-H. Kim, and M.-H. Lee. *All-optical flip-flop operation based on polarization bistability of conventional-type 1.55μm wavelength single-mode VCSELs.* Journal of the Optical Society of Korea, 14(2), pp. 137–141, 2010.

[49] K. Huybrechts. *Digital Photonics Using Single Laser Diodes for All-Optical Network Nodes.* Doctoral Thesis, Ghent University, 2010.

[50] P. Mechet, T. Spuesens, S. Werquin, K. Vandoorne, N. Olivier, J.-M. Fedeli, P. Regreny, D. Van Thourhout, G. Roelkens, and G. Morthier. *All-optical low-power 2R regeneration of 10Gb/s NRZ signals using a III-V on SOI microdisk laser.* IEEE Photonics Journal, 5(6), 2013.

"Raise your glass to the nighttime and the ways
To choose a mood and have it replaced"

Balthazar, Blood Like Wine, 2011

5 Conclusions and perspectives

5.1 Conclusions

In this PhD. work, we have developed and optimized several processing bottlenecks of the fabrication of a single microdisk laser. Parallel to the work towards a more reliable standard fabrication procedure relying on contact lithography, a process involving electron-beam lithography has been optimized. We studied the continuous wave laser emission of microdisk lasers processed with electron-beam lithography in [1]. The laser emission coupling out of the SOI via a grating coupler etched at one side of the waveguide is collected, and we demonstrate a standard deviation in lasing wavelength of nominally identical devices on the same chip lower than 500pm. The deviation in the diameter of the microdisks is as low as a few nanometers. Finally, we perform 2D-FDTD and electrical injection simulations that demonstrate that a p-i-n epitaxial structure could be a relevant alternative to the tunnel junction-comprising epitaxy currently implemented for microdisk lasers.

The effort towards optimization of a single device also involved studying the sensitivity of the microdisk laser to external reflections. A thorough theoretical and numerical study of the unidirectional behavior of microdisk lasers coupled to a bus waveguide with a stronger reflector on one side has been carried out in [2]. At low bias levels, the ratio of the powers in clockwise and counter clock-

wise modes depends on the coupling coefficients that determine the coupling between clockwise and counterclockwise modes, whereas at high bias levels, it also depends strongly on the gain suppression. The feedback sensitivity of such lasers is also theoretically and numerically investigated and we come to the conclusion that microdisk lasers are generally much more sensitive to external reflections than traditional Fabry-Perot, DFB or DBR lasers. At high bias levels, the feedback sensitivity also strongly depends on the gain suppression, and at high enough power levels, it can be better than that of traditional edge-emitting lasers. In [3], we demonstrate and quantify experimentally stable unidirectional lasing in microdisk lasers heterogeneously integrated on SOI. Feedback from a passive distributed Bragg reflector is used to achieve stable unidirectional operation. This simple passive design does not add optical losses to the system and does not increase its power consumption. The implementation of this solution is the key to avoid the appearance of a "memory" effect in microdisk lasers. It can be implemented to counteract processing effects, such as sidewall roughness, that threaten unidirectional operation of the lasers. Different devices belonging to the same design can now lase in the same direction with higher efficiency and without switching from one lasing direction to the other depending on the injection current and the temperature. This makes the use of microdisk lasers for optical interconnects applications very attractive.

A basic requirement for all-optical logic gates is logic-level restoration. The quality of the logic signal must be restored so that the degradations in signal quality do not propagate through the system. In other words, the signal is "cleaned up" at each stage. For optics, it is mandatory to restore the beam quality and/or the pulse quality as well as signal-level ranges [4]. We demonstrate an all-optical low-power 2R regenerator of 10Gb/s non-return-to-zero data based on a 10μm-diameter electrically pumped microdisk laser, which is heterogeneously integrated onto the silicon-on-insulator platform and processed in a CMOS pilot line. The scheme results in BER improvement and works for submilliwatt-level input signals. The laser operates in the continuous-wave regime, and it is single mode at room temperature and consumes 6mW of electrical power. Its regeneration capability is investigated in simulations up to 20Gb/s and experimentally demonstrated at 10Gb/s [5].

The basic requirements for logic gates listed by D. A. B. Miller [4] can now be adjusted according to the results achieved in this work, as shown in Figure 5.1. Cascadability has not been demonstrated, but the fabrication involving the use of electron-beam lithography demonstrated that the diameters of nominally identical microdisk lasers only differ by a few nanometers. The processing improvements also open the door to the collection of a higher output power of

the microdisk lasers, which will increase the fan-out. 2R regeneration has been experimentally demonstrated, as well as investigated in simulations. We finally experimentally characterize the sensibility of microdisk lasers towards feedback and external reflections.

	Requirement	Current status	Reachable	CMOS
Cascadability	∞	1	10	∞
Fan-out	>2	>20 (Sim) > 50 (Exp)	>50	>2
Signal refreshing	3R	Sim: 2R: Re-shape+Reamplify Exp: 2R	3R	3R
Isolation	>10 dB	Sim: 20 dB Exp: 0 dB	>0 dB	>>30 dB

Figure 5.1: Adapted basic requirements for logic gates.

5.2 Perspectives

5.2.1 Inproving the performance of InP microdisk lasers on SOI

The output power of microdisk lasers depends on several parameters. First, the alignment of the InP towards the underlying waveguide is critical and significantly influences the laser properties [6]. Thanks to the development of an electron-beam lithography process, we demonstrate an accuracy of the alignment of the microdisk with respect to the underlying waveguide compared to the design value as good as 40nm [1].

Also, in [6], it is demonstrated that the output power gradually drops as the coupling from the microdisk to the waveguide decreases. The coupling between microdisk and waveguide also depends on the total bonding thickness, which comprises DVS-BCB, a dielectric layer and III-V layers. The optimal coupling constant α_c that garantees the maximal output power for a desired bias current can be used to compute the optimal bonding thickness. To perform 3D-FDTD simulations of the structure and identity the optimum bonding thickness, it is crucial to compute the correct mode in the cavity. The considered optical mode must be the actual dominant lasing mode and the optical mode must couple to the waveguide. In our case, the microdisk lasers are fabricated in an epitaxy with a total height of 583nm. The microdisk lasers are then multi-mode in the vertical direction.

The used epitaxial material contains three strained InAsP quantum wells, in which the light emission takes place [7]. For this particular material, it is well-known that the photon emission process is very temperature dependent and that lasers fabricated using this material system suffer from thermal instability. A future direction for the research on InP-based microdisk lasers may therefore be directed towards improving the quantum-well material. For example, implementing quantum-wells using the GaInAs/AlInAs material system can greatly improve the thermal stability of the lasers, as demonstrated in [8]. An alternative to the challenging growth of the highly-doped tunnel junction in the present system has been suggested in this work. The corresponding 2D-FDTD simulations and electrical injection simulations demonstrate that, with the development of an appropriate fabrication process, the use of a p-i-n epitaxial structure is possible for microdisk lasers heterogeneously integrated on SOI.

The metallic top contact is of crucial importance in the optimization of the devices. The positioning of the top contact with respect to the perimeter of the microdisk needs to be monitored to obtain high Q-factor cavities. The size of the metal contact must also be accurately defined [6]. For a 7.5μm-diameter microdisk, it was simulated with 2D FDTD performed with MEEP [9] that a clearance of at least 1.1μm is to be sustained to prevent absorption-induced reduction of the Q-factor. A metal to edge clearance of more than 1.7μm would result in radial multi-mode behavior and is also not desirable.

The speed of an electrically-pumped InP microdisk laser is governed by current flowing through the active region in which the laser emission takes place. First, we demonstrated in this work that the series resistance of the device can be greatly reduced by using larger electrical vias from the microdisk to the pads, and by leaving a thicker bottom contact layer. Increasing the doping of the III-V layers and consequently the conductivity of the bottom contact island would also reduce the series resistance of the device. Investigation of the reduction of electrical parasitics is carried out in [10], and are to be seen as design guidelines for large microdisk lasers (diameter larger than 10μm) for which the device speed is clearly limited by the parasitics.

5.2.2 Towards the reduction of reflections induced by the passive SOI circuit

Grating couplers were used in this work to fibre-to-chip coupling. The performance of the grating couplers thus strongly influences the measurements. The grating couplers used in the work are standard grating couplers. They consist of a partially etched grating coupler with a 250μm long parabolic taper. The grating coupler ridges are partially etched with an etch depth of 70nm and a period of 630nm. The grating couplers are centred around 1550nm and are designed to operate at a coupling angle of 10° from the surface normal [11]. The peak efficiency of the grating couplers is measured to be between -6 and -8dB, varying from SOI fabrication run to run. These grating couplers are used as a standard means of optical measurements, but their performance is in this case not ideal:

- The center wavelength of the grating is designed to be 1550nm to be compatible for applications in optical interconnects. The targeted peak of the photoluminescence must then be shifted to a lower wavelength instead of being aligned at 1550nm. Indeed, under electrical pumping of the structure, the electronic bands are tilted resulting in a reduction of the bandgap. This corresponds to a red-shift of about 30nm of the lasing spectrum. The targeted peak of the photoluminescence spectrum must then be close to 1520-1530nm to be compatible with the designed grating couplers.
- As mentioned in chapter 3, microring and microdisk lasers are generally much more sensitive to external reflections than traditional Fabry-Perot, DFB or DBR lasers. The standard grating couplers have a relatively high back reflection of around -20dB, which is translated to a ripple in the frequency response of the grating couplers. These reflections jeopardize passive transmission measurements through the silicon waveguides. These reflections also cause bi-stable devices such as optical flip-flops to switch by introducing feedback inside the cavity. An index matching fluid can be applied between the cleaved fiber facet and the grating coupler to reduce the back-reflection between the fiber facet and the grating coupler;

A reflectionless grating coupler has been simulated with 3D-FDTD and developed within the Photonics Research Group of Ghent University. A reflectionless grating is curved and refocuses the reflection away from the entrance waveguide thereby realizing a 5dB to 10dB reflection reduction down to -40dB for shallow etched gratings, the same back reflection performance of a typical optical fiber connector, without introducing a coupling efficiency penalty.

Furthermore, it has been shown that this method can be used to reduce the reflection of highly reflective (-7dB) deeply etched grating couplers to useful reflections of -28dB [12]. The combination of a tilted grating coupler design, which strongly suppresses the back-reflection for light incident on the grating coupler from a waveguide, and a silicon overlay locally deposited on top of the grating region, which enhances the coupling efficiency of the grating coupler, is reported by means of simulations and experiment. The fabricated tilted focusing grating couplers with silicon overlay show a coupling efficiency of -2.2dB in combination with a back-reflection of around -40dB when excited from the silicon waveguide. The tilted design also provides an alternative approach to enhance the transmission of a grating coupler when the thickness of the silicon overlay is not optimized [13]. These reflectionless grating couplers have been implemented in following designs including microdisk lasers, as visible in Figure 5.2, for straight waveguides. The SOI wafers including designs for microdisk lasers with reflectionless grating couplers are ready to be post-processed at Ghent University. A comparative study of the characteristics of microdisk lasers coupled to standard grating couplers and to reflectionless grating coupler could now be experimentally carried out.

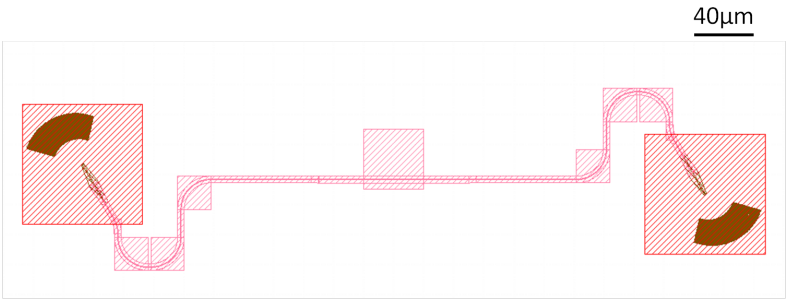

Figure 5.2: Implementation of a reflectionless grating coupler in designs including microdisk lasers

5.2.3 Towards all-optical applications using microdisk lasers

A data flip-flop can be constructed using an all-optical gate and a set-reset flip-flop. The output of the gate serves as a control input for changing the state of the set-reset flip-flop. A simplified diagram of a data flip-flop formed as a result of cascading the optical gate and the set-reset flip-flop is drawn in Figure 5.3. The optical data is tuned to one resonance wavelength of the gate while the optical clock is tuned to another resonance wavelength. The optical power

of the optical clock is chosen to be weaker than the one of the optical data. It passes to the upper waveguide coupled to the set-reset flip-flop when the data has low (logic "0") level. This combination of clock and low level of data acts as set input to set-reset flip-flop. When the data has a high level (logic "1"), it blue shifts the transmission resonance of the gate. The clock becomes off-resonance to the gate and it directly couples to the set-reset flip-flop. This combination of the clock and high level of data serves as a reset input to set-reset flip-flop. The design of the SOI waveguide circuit is depicted in Figure 5.4. While designing the waveguide circuit and the III-V contact mask special emphasis was given to solve the possible difficulties which could arise during the measurements. Since access fibers will be needed at different inputs and outputs, input and output waveguides were ended with the reflectionless grating couplers at a pitch of 127μm corresponding to the pitch of an standard fiber array.

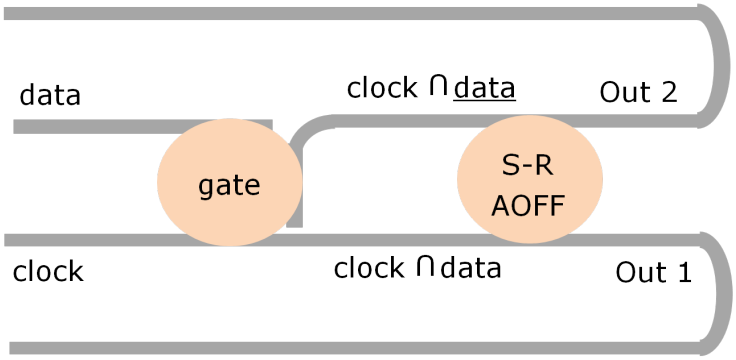

Figure 5.3: Schematic representation of a data flip-flop, comprising two cascaded microdisk lasers, one acting as a gate and another acting as a set-reset flip-flop.

The implementation of such a data flip-flop design is very challenging. First, the microdisk acting as a gate must have exactly the same diameter as the set-reset flip-flop. Also, the microdisk acting as a gate is aligned with respect to three waveguides, as visible in Figure 5.3 and Figure 5.4. Thanks to the use of the developed electron-beam process at LPN, the fabrication of such a data flip-flop is made possible, as the diameter of the microdisks will only differ by a few nanometers, and as the offset between the microdisk and the waveguide will only differ by a tens of nanometers from the target value. This fabrication cannot be performed with contact lithography, for which the achievable alignment risks jeopardizing an efficient coupling between the microdisk lasers and the underlying waveguides, which would result in poor performance of the data flip-flop.

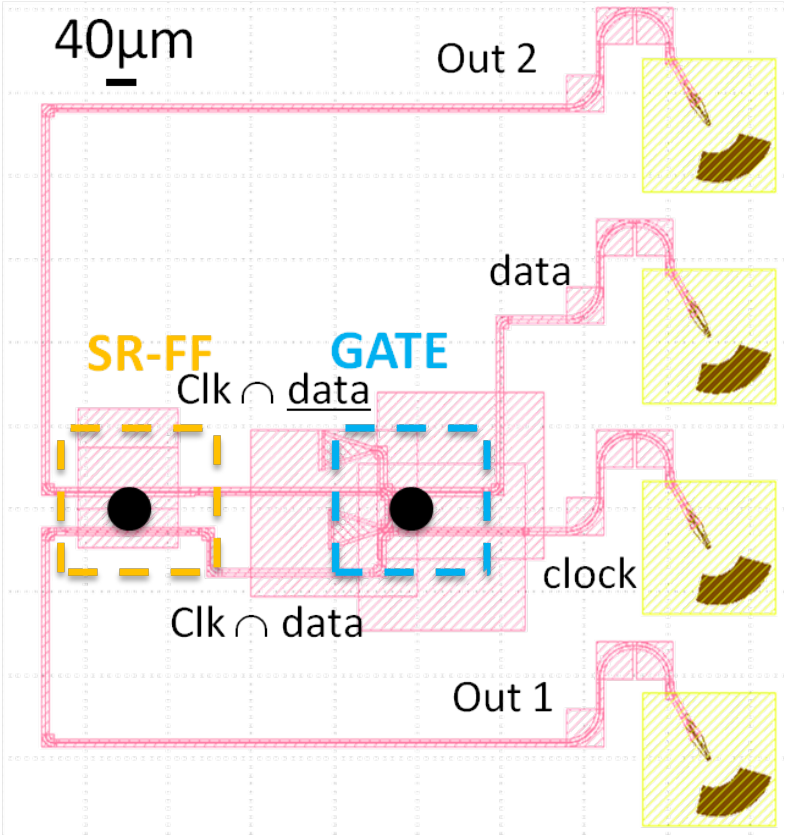

Figure 5.4: Schematic representation of the implemented design of a data flip-flop, comprising two cascaded microdisk lasers, one acting as a gate and another acting as a set-reset flip-flop, with reflectionless grating couplers.

An alternative passive design has also been implemented with reflectionless grating couplers. In this solution, the microdisk lasers are both aligned with respect to two waveguides. Only their diameters must be identical, as visible in Figure 5.5.

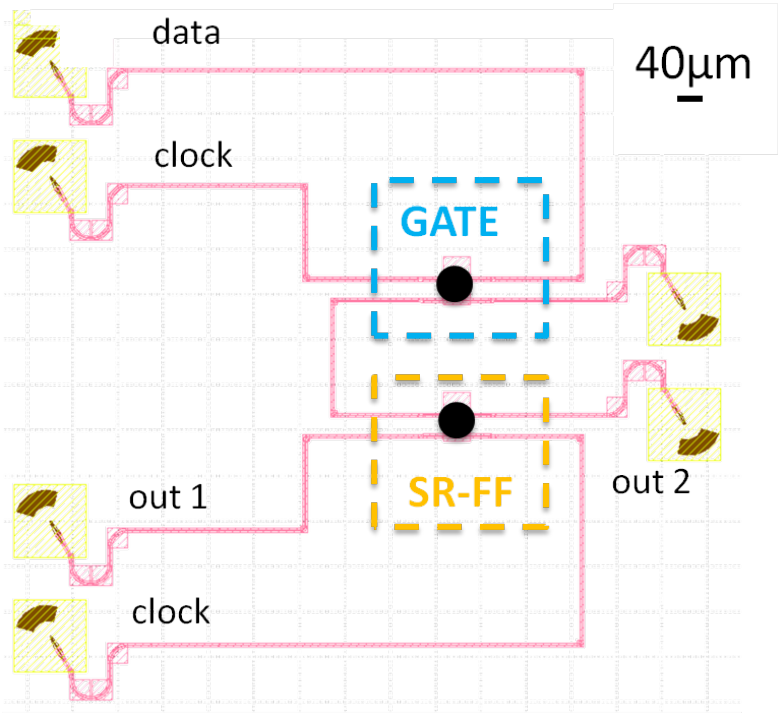

Figure 5.5: Schematic representation of an alternative implemented design of a data flip-flop, comprising two cascaded microdisk lasers, one acting as a gate and another acting as a set-reset flip-flop, with reflectionless grating couplers.

A third passive design is implemented with standard grating couplers, and is depicted in Figure 5.6. A microdisk laser is coupled to two waveguides, and acts as a set-reset flip-flop. Two small footprint integrated Membrane InP Switches (MIPS) are used as gates. The gates consists of an optically pumped III-V membrane waveguide of only 100nm thick, coupled to the underlying SOI waveguide circuit [14]. Because of its limited thickness, the optical confinement in the active layers is maximized, allowing for high extinction ratio of over 30dB when applying a low power optical pump signal, over the entire C-band. The switch has 400/1300ps on/off switching times and no measurable pattern dependence or switching related power penalties for a bitrate up to 40Gb/s, using a switching power of only 2dBm. A pump-probe system is used to trigger the thin-film gates. A pattern data signal acts as a pump beam tuned at 1505nm. It is combined in the thin-film with a CW clock signal acting as a probe beam and tuned at one of the resonant wavelengths of the microdisk laser. When the pump power is increased, more photons are absorbed in the thin-film and therefore more free carriers are generated. Because of these free carriers the absorption of the probe beam will decrease and eventually a net gain of 2dB is reached. When the top gate is open, the bottom gate is closed, and the clock signal forces the set-reset flip-flop to operate in the CCW direction. When the top gate is closed, the bottom gate is open, and the clock signal switches the set-reset flip-flop to operate in the CW direction.

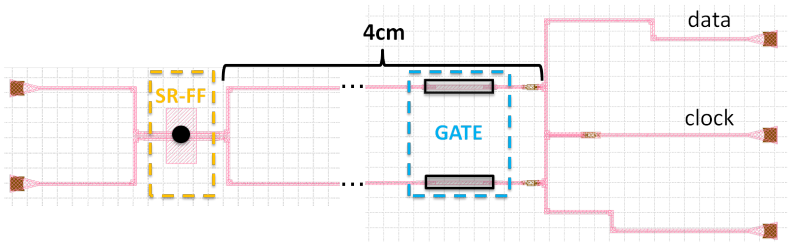

Figure 5.6: Schematic representation of an alternative implemented design of a data flip-flop, comprising one microdisk laser, acting as a set-reset flip-flop, and a two thin-film gates.

Several challenges remain. First, the speed of the gate can be improved to reach 10Gb/s or faster operation, by narrowing the mesa of the device. Also, short carrier lifetimes in InP materials have been obtained by growing an InGaAs QW at the very surface of the heterostructure and by structuring the matter at scales smaller than 200nm. It has been demonstrated that surface growth of QWs reduces the carrier lifetime from 1ns down to about 50ps [15]. InP membranes with InGaAs surface QWs constitute an ideal system for achieving ultrafast all-optical gates activated with low energies. Indeed, the recovery

time of such gates is measured to be as fast as 12ps and can be activated with pulses with energies as low as 40fJ.

The fabrication of such a system relies on the bonding of two different epitaxial stack. In Figure 5.6, the waveguide between the set-reset flip-flop and the thin-film gates is 4cm long, which would allow us to bond the two epitaxies next to each other. In terms of processing, the epitaxy of the thin-film switches would be first bonded on the SOI waveguide circuit. The bonding thickness obtained with machine bonding can be as low as a few tens of nanometers. For instance, in [14], the obtained DVS-BCB bonding thickness is as low as 40nm. The mesa of the thin-film switches would later be defined by contact lithography and etched so that the thin-film switches are completely processed. Afterwards, another layer of DVS-BCB would be spin-coated on top of it to act as the bonding layer for the epitaxy of the microdisk lasers. That way, a die of the epitaxy for the microdisk lasers would be bonded above the thin-film switches. The total bonding thickness for the epitaxy of the microdisks would not be larger than 200nm.

5.2.4 Towards the use of microdisk lasers for optical interconnects

When assessing the performance of single microdisk cavity from a system point of view, the above and the following demonstrations have been carried out: all-optical photonic flip-flop [16], all-optical gating for multiplexing and de-multiplexing purposes [17], all-optical wavelength conversion [18], [19], all-optical format conversion [20], regeneration [5], application in interconnects. InP microdisk cavities can indeed be employed in various operational modes to facilitate chip-to-chip and on-chip interconnects. Operation as directly modulated light source [21], resonant cavity modulators and/or resonant photo detectors [23], [24] have all been explored within the EU-FP7 HISTORIC project. More recently, a compact optical interconnect on a silicon-on-insulator platform consisting of a directly modulated microdisk laser and detector connected via a silicon waveguide has been presented [25]. A single III-V epitaxial structure that contains layers for both the laser and detector ensures that dense integration becomes possible. All fabrication steps for the laser and detector, except for the detector mesa, are carried out simultaneously. The microdisk laser has a threshold current of 0.45 mA and a slope efficiency of 57μW/mA. The responsivity of the detectors is 0.69 A/W. The full optical link has a static efficiency of 3% and a bandwidth of 7.6 GHz. A large signal modulation is applied and a 10Gb/s bit pattern could be resolved.

In all these demonstrations, possible limitations of membrane microdisk lasers for all-optical logic have been identified, such as the isolation of reflected signals and the fan-out capability. These challenges are making their use for all-optical digital photonics questionable. When it comes to optical interconnects, it has been successfully shown that the microdisks can operate as lasers, modulators and detectors for on-chip optical interconnects. The versatility in the applications of this hybrid structure for optical interconnects is remarkable. And for several applications such as wavelength up- and down- conversion or electro-optic modulation, its performance is close to be competitive with that of state-of-the-art components.

References

[1] P. Mechet, F. Raineri, A. Bazin, Y. Halioua, T. Spuesens, T.J. Karle, P. Regreny, P. Monnier, D. Van Thourhout, I. Sagnes, R. Raj, G. Roelkens, and G. Morthier. *Uniformity of the lasing wavelength of heterogeneously integrated InP microdisk lasers on SOI.* Optics Express, 21(9):10622–10631, 2013.

[2] G. Morthier, and P. Mechet. *Theoretical analysis of unidirectional operation and reflection sensitivity of semiconductor ring or disk lasers.* IEEE Journ. Quant. El., 49(12):1097–1101, 2013.

[3] P. Mechet, S. Verstuyft, T. De Vries, T. Spuesens, P. Regreny, D. Van Thourhout, G. Roelkens, and G. Morthier. *Unidirectional III-V microdisk lasers heterogeneously integrated on SOI.* Optics Express, 21(16):19339–19352, 2013.

[4] D. A. B. Miller. *Are optical transistors the logical next step?.* Nature Photonics, 4:3–5, 2010.

[5] P. Mechet, T. Spuesens, S. Werquin, K. Vandoorne, N. Olivier, J.M. Fedeli, P. Regreny, D. Van Thourhout, G. Roelkens, and G. Morthier. *All-optical low-power 2R regeneration of 10Gb/s NRZ signals using a III-V on SOI microdisk laser.* IEEE Photonics Journal, 5(6):7802510, 2013.

[6] T. Spuesens, and D. Van Thourhout. *Analysis of loss contributions in InP-based microdisk lasers heterogeneously integrated with SOI.* Proceedings of the Annual Symposium of the IEEE Photononics Benelux Chapter, Netherlands, p.209–212, 2010.

[7] P. Rojo Romeo, J. Van Campenhout, P. Regreny, A. Kazmierczak, C. Seassal, X. Letartre, G. Hollinger, D. Van Thourhout, R. Baets, J.-M. Fedeli, and L. Di Cioccio. *Heterogeneous integration of electrically driven microdisk based laser sources for optical interconnects and photonic ICs.* Optics Express, 14(9):3864–3871, 2006.

[8] Y. Kawamura, K. Nokana, and O. Nikami. *Low threshold current GaInAs/AlInAs ridge MQW lasers with InP cladding layers.* IEEE Electronics Letters, 24(10):637–638, 1998.

[9] Python binding for MEEP (FDTD solver by MIT), *https://launchpad.net/python-meep.*

[10] J. Hofrichter. *InP microdisk for all-optical signal processing and data transmission.* Doctoral Thesis, Technische Universiteit Eindhoven, 2012.

[11] F. Van Laere, G. Roelkens, M. Ayre, J. Schrauwen, D. Taillaert, D. Van Thourhout, T. F. Krauss, and R. Baets. *Compact and highly efficient grating couplers between optical fiber and nanophotonic waveguides.* J. Lightwave Technol., 25(1):151–156, 2007.

[12] D. Vermeulen, Y. De Koninck, Y. Li, W. Bogaerts, R. Baets, and G. Roelkens. *Reflectionless grating couplers for SOI photonic integrated circuits.* Optics Express, 20(20):22278–22283, 2012.

[13] Y. Li, L. Li, B. Tian, G. Roelkens, and R. Baets. *Reflectionless tilted grating couplers with improved coupling efficiency based on a silicon overlay.* IEEE Photonics Technology Letters, 25(13):1195–1198, 2013.

[14] M. Tassaert, G. Roelkens, H.J.S. Dorren, D. Van Thourhout, and O. Raz. *Bias-free, low power and optically driven membrane InP switch on SOI for remotely configurable photonic packet switches.* Optics Express, 19(26):817–824, 2011.

[15] F. Raineri, A. Bazin, P. Monnier, I. Sagnes, and R. Raj. *All-Optical ultrafast gates with surface grown QWs in photonic crystals heterogenously integrated on SOI.* Proceedings of the Advanced Photonics Congress, IW3C.3, 2012.

[16] L. Liu, R. Kumar, K. Huybrechts, T. Spuesens, G. Roelkens, E.-J. Geluk, T. de Vries, P. Regreny, D. Van Thourhout, R. Baets, and G. Morthier. *An ultrasmall, low-power, all-optical flip-flop memory on a silicon chip.* Nature Photonics, 4:182–187, 2010.

[17] R. Kumar, L. Liu, G. Roelkens, E.-J. Geluk, T. de Vries, F. Karouta, P. Regreny, D. Van Thourhout, R. Baets, and G. Morthier. *10GHz All-Optical Gate Based on a III-V/SOI Microdisk.* IEEE Photonics Technology Letters, 22(13):981–983, 2010.

[18] J. Hofrichter, O. Raz, L. Liu, G. Morthier, F. Horst, P. Regreny, T. De Vries, H.J.S. Dorren, and B.J. Offrein. *All-optical wavelength conversion using mode switching in InP microdisc laser.* Electronics Letters, 47(16):927–929, 2011.

[19] R. Kumar, T. Spuesens, P. Mechet, P. Kumar, O. Raz, N. Olivier, J.-M. Fedeli, G. Roelkens, R. Baets, D. Van Thourhout, and G. Morthier. *Ultra-fast and*

bias-free all-optical wavelength conversion using III-V on silicon technology. Optics Letters, 36(13):2450–2452, 2011.

[20] R. Kumar, T. Spuesens, P. Mechet, N. Olivier, J.-M. Fedeli, P. Regreny, G. Roelkens, D. Van Thourhout, and G. Morthier. *10Gbit/s all-optical NRZ-OOK to RZ-OOK format conversion in an ultra-small III-V-on-silicon microdisk fabricated in a CMOS pilot line*. Optics Express, 19(24):24647–24656, 2011.

[21] O. Raz, H.J.S. Dorren, R. Kumar, G. Morthier, P. Regreny, and P. Rojo-Romeo. *50 FJ-per-bit, high speed, directly modulated light sources for on-chip optical data communications*. Proceedings of OFC 2011, pp. OMM5, 2011.

[22] O. Raz, L. Liu, R. Kumar, G. Morthier, P. Regreny, and H.J.S. Dorren. *A Single InP Membrane Disc Cavity for Both Transmission and Detection of 10 Gb/s Signals in On Chip Interconnects*. Proceedings of ECOC 2010, P2.12, 2010.

[23] J. Hofrichter, O. Raz, A. La Porta, T. Morf, P. Mechet, G. Morthier, T. De Vries, H.J.S. Dorren, B.J. Offrein. *A low-power high-speed InP microdisk modulator heterogeneously integrated on a SOI waveguide*. Optics Express, 20(9):9363–9370, 2012.

[24] J. Hofrichter, T. Morf, A. La Porta, B.J. Offrein, P. Mechet, G. Morthier, T. De Vries, H.J.S. Dorren, and O. Raz. *Inverting and non-inverting operation of InP microdisk modulators*. Electronics Letters, 48(10):586–588, 2012.

[25] T. Spuesens, J. Bauwelinck, P. Regreny, and D. Van Thourhout. *Realization of a compact optical interconnect on Silicon by heterogeneous integration of III-V*. IEEE Photonics Technology Letters, 25(14):1332–1335, 2013.

A

Detailed description of the processing of microdisk lasers

A.1 Process with ECI photoresist

A.1.1 Microdisk definition with ECI photoresist

- Spin-coat Ti-prime (40s, acc. 10, 4000rpm)
- Bake Ti-prime (120°C, 3min)
- Spin-coat ECI-3027 (40s, acc. 10, 4000rpm) : expected thickness of 1.2μm
- Bake ECI-3027 (90°C, 1min30s)
- Exposure for 40s
- Post-exposure bake (110°C, 1min30s)
- Development in pure MIF726 for 40s
- Rincing for 1min with DI-water
- Hard-bake (110°C, 3min)

A.1.2 Bottom contact definition

- Spin-coat Ti-prime (40s, acc. 10, 2500rpm)
- Bake Ti-prime (122°C, 3min)

- Spin-coat AZ-5214E (40s, acc. 10, 2500rpm) : expected thickness of 1.6μm
- Bake AZ-5214E (100°C, 3min)
- Exposure for 12s
- Wait 5min
- Post-exposure bake (122°C, 5min)
- Wait 2min
- Flood-exposure for 42s
- Development in AZ400K/H_2O (1:3) for 25s
- Rincing for 3min with DI-water

A.1.3 Island definition

- Spin-coat Ti-prime (40s, acc. 10, 3000rpm)
- Bake Ti-prime (122°C, 3min)
- Spin-coat AZ-5214E (40s, acc. 10, 3000rpm) : expected thickness of 1.5μm
- Bake AZ-5214E (100°C, 3min)
- Exposure for 20s
- Wait 5min
- Development in AZ400K/H_2O (1:3) for 30s
- Rincing for 3min with DI-water

A.1.4 Overcladding with DVS-BCB

- Spin-coat adhesion promotor AP3000 (5s, acc. 10, 500rpm followed by 40s, acc. 10, 5000rpm)
- Spin-coat DVS-BCB (5s, acc. 10, 500rpm followed by 40s, acc. 10, 2000rpm) : expected thickness of 1μm

A.1.5 Top and bottom vias opening

Ti-prime is not necessary anymore. The sample has been planarized with DVS-BCB, and the adhesion of photoresist on the polymer is better than on III-V.

- Spin-coat AZ-5214E (40s, acc. 10, 2500rpm) : expected thickness of 1.6μm
- Bake AZ-5214E (100°C, 3min)
- Exposure for 9s
- Post-exposure bake (122°C, 5min)
- Wait 2min
- Flood-exposure for 42s

- Wait 5min
- Development in AZ400K/H_2O (1:3) for 20s
- Rincing for 3min with DI-water

A.1.6 Bottom vias opening

- Spin-coat AZ-5214E (40s, acc. 10, 2500rpm) : expected thickness of 1.6μm
- Bake AZ-5214E (100°C, 3min)
- Exposure for 9s
- Post-exposure bake (122°C, 5min)
- Wait 2min
- Flood-exposure for 42s
- Wait 5min
- Development in AZ400K/H_2O (1:3) for 18s
- Rincing for 3min with DI-water

A.1.7 Top metal definition

- Spin-coat AZ-5214E (40s, acc. 10, 3000rpm) : expected thickness of 1.5μm
- Bake AZ-5214E (100°C, 3min)
- Exposure for 10 to 12s
- Post-exposure bake (122°C, 5min)
- Wait 2min
- Flood-exposure for 42s
- Wait 5min
- Development in AZ400K/H_2O (1:3) for 25s
- Rincing for 3min with DI-water

A.1.8 Metallic pads definition

- Spin-coat AZ-5214E (40s, acc. 10, 2000rpm) : expected thickness of 1.6μm
- Bake AZ-5214E (100°C, 3min)
- Exposure for 12s
- Post-exposure bake (122°C, 5min)
- Wait 2min
- Flood-exposure for 42s
- Wait 5min
- Development in AZ400K/H_2O (1:3) for 20s
- Rincing for 3min with DI-water

– Metallic deposition Ti/Au (40nm:900nm)

B

Transmission Line Model (TLM)

The TLM originally proposed by Shockley [1] offered a convenient method for determining the specific contact resistance ρ_c for planar ohmic contacts. Shockley also proposed an experiment in which the total resistance R_T between any two contacts (of length d and width w) separated by a distance l could be measured and plotted as a function of l. The resulting equation between R_T and l provided an estimate of ρ_c through the so-called "transfer length" L_T, measured from the intersection of the l curve for $R_T = 0$ as shown in figure B.1b [2]:

To determine the ohmic contact parameters with the TLM, resistance measurements R_1 and R_2 are made between adjacent contacts as depicted in figure B.1a. The total resistance R_T between any two contacts is given by [2]:

$$R_T = 2R_C + \frac{R_{SH}.l}{w} \tag{B.1}$$

where R_{SH} if the sheet resistance of the semiconductor layer outside the contact region and where w is the width of the contact. However, R_C, the contact resistance, can be shown to be equal to [3]:

$$R_C = \frac{R_{SK}.L_T}{w} coth\left(\frac{d}{L_T}\right) \tag{B.2}$$

where

$$L_T = \sqrt{\frac{\rho_c}{R_{SK}}} \tag{B.3}$$

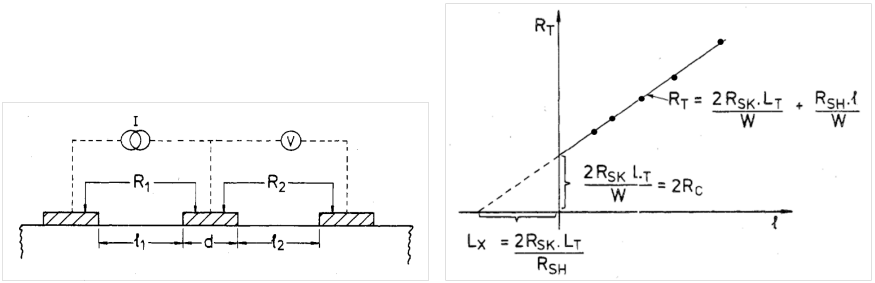

(a) **(b)**

Figure B.1: Transmission Line Model structure and method of evaluation of the resistance values. (a) Experimental measurements for obtaining total resistance and contact resistance values. (b) Plot of total contact to contact resistance as a function of l to obtain transfer length and contact resistance values.

Hence, for $d \geq 2L_T$,

$$R_T = \frac{2R_{SK}.L_T}{w} + \frac{R_{SH}.l}{w} \tag{B.4}$$

where R_{SK} is the modified sheet resistance under the contact.

The relationship of B.4 is plotted in figure B.1b and shows that if the sheet resistance under the contact is significantly modified, then $L_X \neq L_T$ [2]. In this case, the correct value of ρ_c can be found by performing an additionnal measurement - the contact end resistance R_E measurement where the standard technique is to pass a constant current between two contacts (broken line on B.1a)and to measure the potential between one of these contacts and an opposited outside contact pad. The value of R_E is then V/I.

In practice, electrical testing structures must be designed on the lithographical mask used for III-V post-processing. There are three important geometric parameters to consider: the width of the contact level, which is equal to the width of the mesa w, the length of the contacts d and the distance between the contacts i and $i+1$, called l_i, l_{i+1}.

References

[1] W. Shockley. *Research and investigation of inverse epitaxial UHF power transistors.* Report No. A1-TOR-64-207, Air Force Atomic Laboratory, 1964.

[2] G. K. Reeves, and H. B. Harrison. *Obtaining the specific contact resistance from Transmission Line Model measurements.* IEEE Electronic Device Letters, 3(5):111–113, 1982.

[3] H. B. Harrison. *Characterizing metal semiconductor ohmic contacts.* Proceedings IREE Aust., 41:95, 1980.

C

Reactive-Ion-Etching (RIE)

The term RIE is generally applied to discharges contained between two parallel plates, one of which is powered at RF frequencies through a coupling capacitor. The much higher mobility of electrons in the discharge allows them to respond to the alternating field applied across the electrodes, while the massive ions cannot, generally, be swept to the electrodes. The metal plates will charge up to a negative potential relative to the body of the discharge. This potential will stabilize at the value where the electron and ion fluxes are equal. When one of the electrodes is smaller than the other, a larger voltage is developed across the smaller sheath capacitance associated with the small electrode. Since the large electrode is usually the chamber itself, most of the potential difference between plasma and electrode is dropped across the sheath region above the small powered electrode. Since electrons are repelled from this electrode by its negative potential, there are fewer electron-gas molecule collisions, and therefore, less optical emission from this sheath, or space-charge region. It therefore appears as a dark space relative to the more intense glow from the body of the plasma. Ions which stray near the edge of the sheath are accelerated across it and strike the small electrode at near-vertical incidence. The sample to be etched is placed on this electrode and is subject to this ion bombardment as well as a constant flux of neutral gas atoms and molecules.

A schematic of the RIE process is shown in figure C.1. The average electron

temperature is much higher than the ion temperature because of their response to the AC field and the fact they cannot lose much energy in collisions with the much more massive neutral gas molecules. By contrast, energy transfer between ions and neutrals is much more efficient, so the average ion temperature is much lower than that of the electrons. At a pressure of 1mTorr, the neutral gas molecule density is $3x10^{13}cm^{-3}$, while the electron (and ion) density is usually around 10^{10}-$10^{11}cm^{-3}$, and may approach $10^{12}cm^{-3}$ in enhanced discharges. Reactive gas atoms (e.g., Cl) adsorb on the unmasked areas of the sample and form volatile species, whose removal is enhanced by the ion bombardment. In general, the reactive atoms and the physical sputtering by the ions would each individually give rise to a finite etch rate of the sample, but there is a synergy between the two which leads to an etch rate faster than the sum of the two components. At high pressures and low sheath voltages, chemical etching of the substrate is dominant, whereas at low pressure and high sheath biases, ion sputtering is dominant. The former produces lower damage but poorer anisotropy relative to the latter. Almost all RIE processes involve a trade-off of these parameters [1].

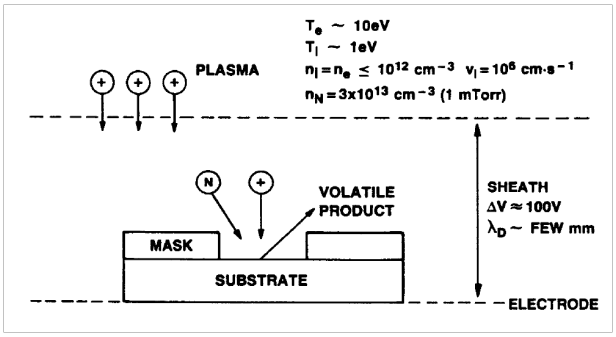

Figure C.1: Schematic of typical RIE parameters.

References

[1] S. K. Pearton. *Wet and dry etchings of compound semiconductors.*

D

High-speed connectors description and handling precautions

D.1 Characterization of devices with signal speeds higher than 20GHz

Going from an insfrastructure that allows performing measurements up to 10Gb/s to a measurement setup that is able to analyze signals whose speeds are up to 40Gb/s or more is a sensitive evolution. This upgrade was already started before this PhD. work, with the purchase of a 100Gb/s Lecroy Digital Oscilloscope to acquire electrical signals, and the corresponding 112Gb/s Fraunhofer photodiode, mounted on the oscilloscope, to convert optical signals into the electrical domain. With the purchase of 40Gb/s compatible signal generators, modulators and detectors, introduction to high-speed equipment was mandatory. In this section, we describe a new characterization setup allowing measurements up to 67GHz.

In this PhD. work, we have been investigating the available technologies for high-speed characterization. Probe-stations are state-of-the-art for wafer-scale measurements. The samples are loaded and maintained thanks to vacuum on a central chuck. High-speed probes are positioned on a circular plate above

the wafer and can be aligned with respect to devices thanks to an optical microscope adapted above the probe-station. In the Photonics Research Group, vertical characterization setups are usually designed so that optical characterization is first performed, and is followed by an electrical characterization if necessary. But as the design of most commercial probe-stations is thought for the semiconductor industry, it does not allow mounting and positioning of optical fibers. Therefore, a new setup had to be designed and implemented in the Photonics Research Group to allow simultaneous optical and electrical characterizations. We gathered feedback from users of the high-speed equipment, and designed together with Jeroen Allaert a new setup that he later implemented and that takes into account input from other group members. To start with, the table is grounded and all electrical equipment related to the measurement setup are ESD-free as long as the operator is wearing an ESD-discharging bracelet. The central chuck of the setup has been modified compared to a usual vertical characterization setup to avoid damaging high-speed GSG probes. Before loading and unloading a sample, the central chuck can be lowered of a few centimeters thanks to a motorized micrometric screw. The design of the chuck is also optimized. The sample, a contact substrate and a calibration substrate can be positioned next to each other during the characterization. This is mimicking a real probe station where the quality of the contact of the high-speed probe is first tested on a contact and a calibration substrates before characterizing actual devices. First, the high-speed probe is put in contact with a contact substrate (Figure D.1a). It consists of a thick metallic layer (soft Gold) that imprints the pins from the high-speed probe. Under visual inspection of the imprint on the contact substrate, it is possible to know if the pins of the high-speed probe are equally contributing to the electrical contact. Then, the high-speed probe is put in contact with a calibration substrate, which consists of several pre-defined electrical test structures. By electrically testing the response of the probe, it is possible to evaluate the quality of the electrical contact. Finally, a last translation of the high-speed probe is necessary to put it in contact with the devices that need charactetization. Also, a Peltier element (visible in Figure D.1b) is added to the chuck and combined with a temperature controller from Thorlabs so that devices can be characterized for different temperatures (Figure D.1b).

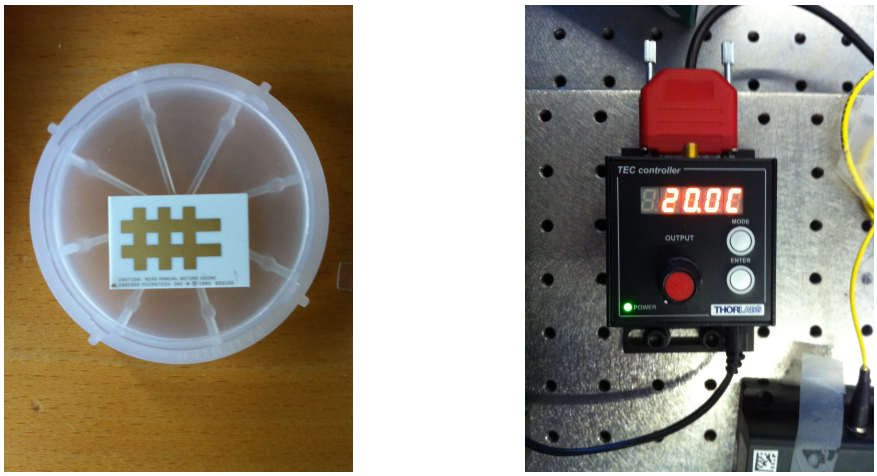

(a) **(b)**

Figure D.1: Contact substrate and temperature controller for the high-speed setup.

Four stages are positioned at cardinal points around the central chuck. Two stages at the North (N) and the South (S) of the setup are dedicated to electrical probing. Each stage consists of XYZ translation stages mounted with micrometric screws, as visible in Figure D.2a. A goniometer is fixed on top of the translation stages. A metallic plate has been designed to be able to adjust the position of the high-speed probe. Four screws are fixed on the goniometer and adapt the height of the high-speed probe to the height of the central chuck. The position of the high-speed probe is chosen so that the rotation center of the goniometer coincides with the rotation center of the tip of the high-speed pins. Figure D.2b is an image of the resulting arm for electrical characterization.

Two stages at the West (W) and the East (E) of the setup are dedicated to optical fibers. The base also consists of XYZ translation stages with micrometric screws. A vertical arm is made of a metal, and a goniometer is adapted on it to ensure the optical fiber can be tilted if it is required to reach the optimum efficiency of the grating couplers. Figure D.3a is a close-up image of the setup when a high-speed probe and two optical fibers are mounted on the chuck. Also, Figure D.3b is a picture from the opposite side of the measurement setup, where the vacuum and the Peltier connections can be seen, but also where the optical fibers are visible.

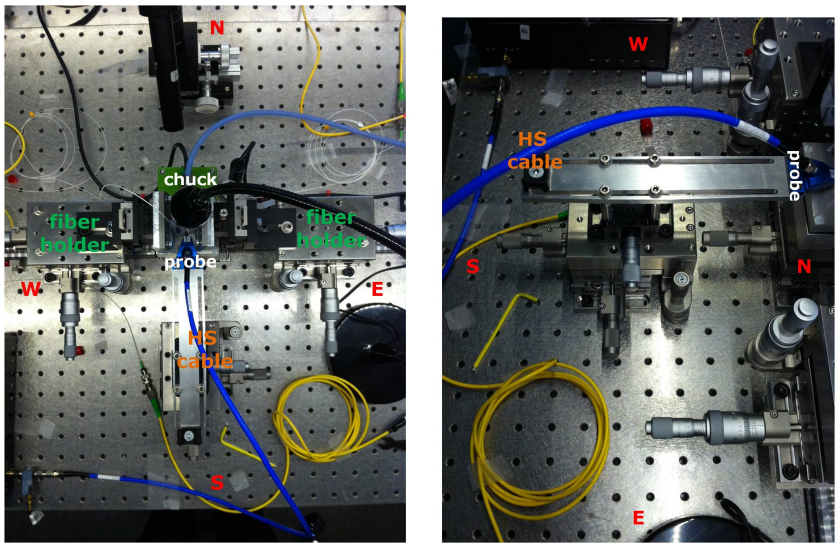

(a) **(b)**

Figure D.2: Customized setup and probe arm for high-speed measurements.

D.2 High-speed connectors description and handling precautions

In our measurement laboratory, three types of RF connectors can be used. The SMA connector is the most common one. It is the workhorse of the RF and microwave industries. The basic design uses a 4.2mm-diameter outer coaxial, filled with PTFE dielectric. Their upper frequency limit is anywhere from 18 to 26GHz, depending on the tolerances held during manufacturing. SMAs, like many other coaxial connector families, are sized to fit a 5/16 inch wrench. SMA connectors will mate with 3.5mm and 2.92mm connectors. Figures D.4a are two images of a male SMA connector and a female SMA connector [1].

There are several precision connectors. The first ones we will present are called 3.5mm and 2.92mm connectors. Their style uses air dielectric, and they will mate with each other as well as with the cheapest SMA style. The 3.5mm connector is the next upgrade from using SMA, as it performs well up to 26 GHz. The 2.92mm connector (often called “2.9mm”) works up to 40GHz. The so-called *K*-connector is Anritsu’s version of the 2.92mm connector. One of these connector usually costs less than 100euros in 2013. As you can see from the images on Figures D.5a, the outer diameter of the coax decreases slightly from a 3.5 to a 2.92mm coax.

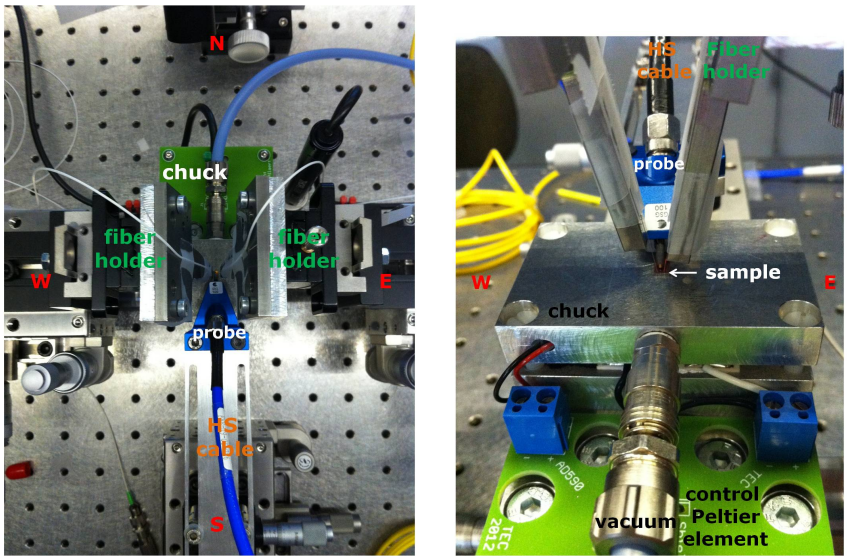

(a) **(b)**

Figure D.3: Image of the chuck of the high-speed setup when a sample is loaded, contacted with a high-speed probe and light is collected from the chip with optical fibers.

(a) **(b)**

Figure D.4: Images of SMA male and female connectors. Their upper frequency limit is anywhere from 18 to 26 GHz, depending on the tolerances held during manufacturing [1].

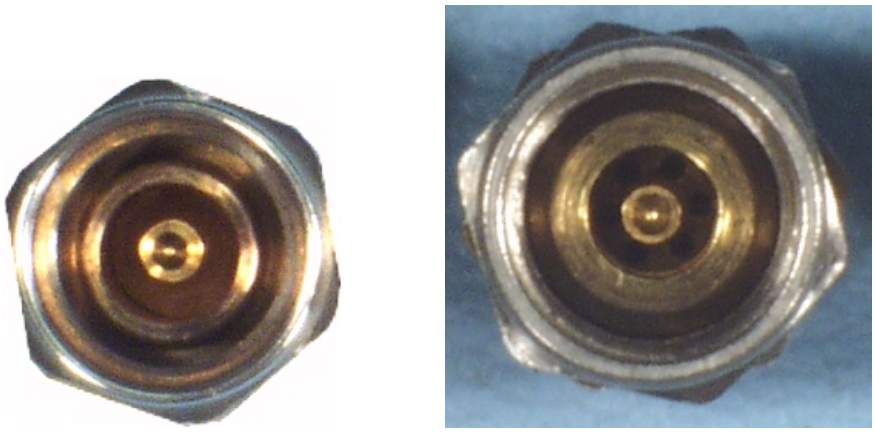

(a) **(b)**

Figure D.5: (a) Image of a 3.5mm connector male. (b) Image of a 2.92mmm connector female [1].

Higher precision connectors are the 2.4mm and 1.85mm connectors (Figure D.6a). They are mechanically compatible with each other, but neither one will thread onto a SMA, a 3.5 nor a 2.92mm connector. These expensive connectors would be harmed by less precise connectors such as SMA. The 1.85mm connector is often called the "*V* connector". Both the 2.4 and 1.85mm connectors require a 5/16 inch wrench. As the price of high-speed connectors keeps climbing as you go up in frequency, one should keep in mind that a *V*-connector costs up to 500 euros in 2013.

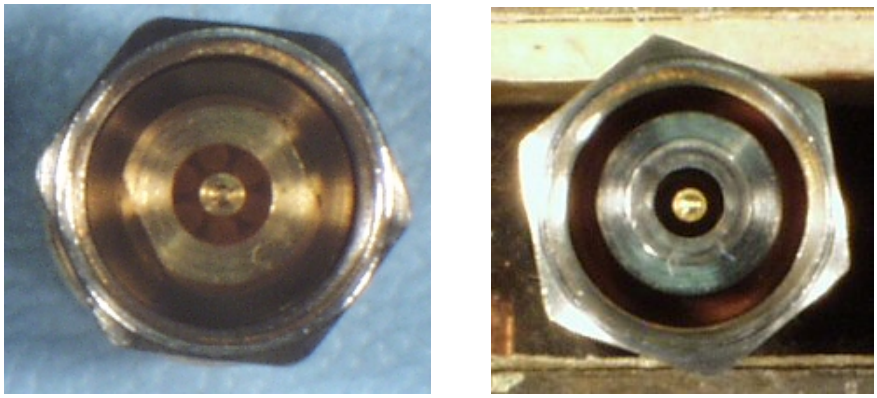

(a) **(b)**

Figure D.6: (a) Image of a 2.4mm connector male. (b) Image of a 1.85mmm connector male [1].

Finally, the 1mm connector (Figure D.7a) is the highest-frequency millimeterwave connector on the market. It performs up to 110GHz. A single 1mm connector costs more than 1500 euros in 2013.

The following table D.1 is a non-exhaustive list of the major connector families.

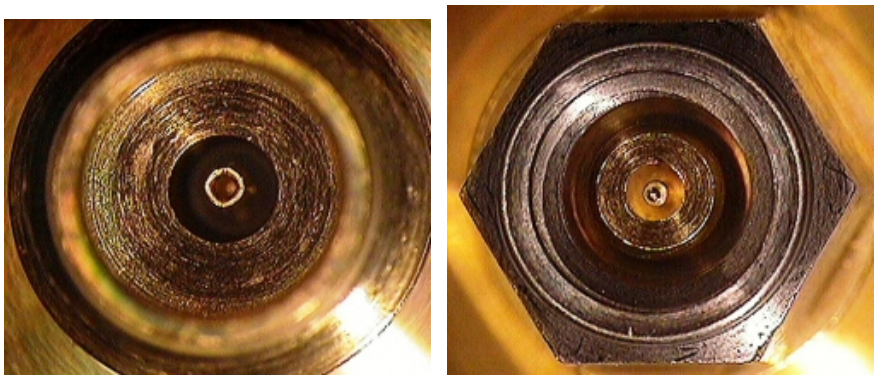

(a) **(b)**

Figure D.7: (a) Image of a 1mm connector female. (b) Image of a 1mmm connector male [1].

Connector type	*Frequency limit*	*Dielectric*	*Comment*
BNC	4GHz	PTFE	
SMB	4GHz	PTFE	Available in 50 or 75Ω
SMC	10GHz	PTFE	
SMA	25GHz	PTFE	Most common connector
3.5mm	26.5GHz	Air	Precision connector mates to SMA
2.92mm	40GHz	Air	Precision connector threads to SMA and 3.5mm Often called “2.9 mm”
K	40GHz	Air	Covers all the *K* freq. band
2.4mm	50GHz	Air	2.4mm and 1.85mm will mate with each other without damage
1.85mm	60GHz	Air	Mechanically compatible with 2.4mm connectors
V	60GHz	Air	Anritsu’s term for 1.85mm connectors as they span the *V* freq. band
1mm	110GHz	Air	Costs a fortune

Table D.1: Non-exhaustive list of the major connector families [1]

Another way is to classify the RF connectors depending on their frequency usage, as done in Figure D.8 [1].

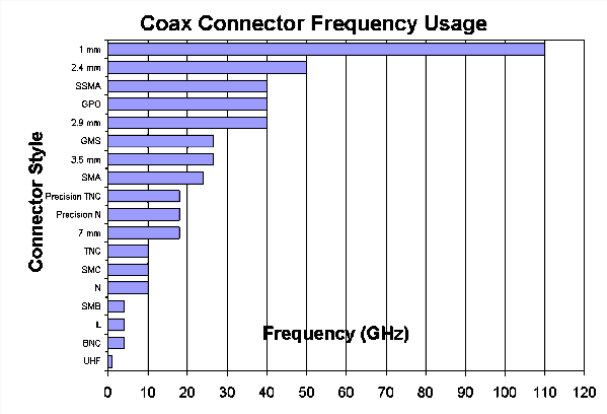

Figure D.8: Frequency usage of the major connector families.

Within any connector family there are three adapters you can use. A male-to-male adapter refers to an adapter with two male ends. This is often referred to as a "barrel" adapter. A female-to-female adapter has two female ends; it is often referred to as a "bullet" adapter. An adapter with one male end and one female end is often referred to as a "connector saver". This is because this type of adapter is often screwed onto an expensive piece of test equipment or component that requires a lot of connect/disconnect cycles. If an incident occurs where one of the connectors is damaged, it is far cheaper to throw away and replace the connector saver than to repair expensive equipment that it is protecting. Below is a picture of an SMA connector saver, barrel and bullet adapter. A V-to-2.92mm adapter already costs 250 euros. A 1mm-to-V adapter costs 1000 euros in 2013.

Some simple handling procedures can prevent damaging expensive high-speed connectors [1].

- Do not use pliers on a "stuck" connector ever. There are wrenches for every size adapter, even SMA bullets. If you cannot fit a wrench to your stuck connector, see below.
- Learn how to clean connectors with alcohol and cotton swabs. Cleaning the threads is good practice, but stay away from cleaning the center conductor of an air dielectric connectors such as 3.5mm, 2.9mm and 2.4mm.
- Learn how to gage connectors to determine if they are out of specification. One bad connector can damage many others.
- Do not use higher frequency connector than you need. Save the 2.4mm and 1.85mm and 1mm parts.

Figure D.9: RF adapters [1].

- Never use any part of a calibration kit as an adapter. Ever.
- Use a torque wrench. For most connectors with 5/16 inch hex nuts, use 6-8 inch-pounds.
- Remember to turn the wrench in the right direction.
- Remember that the hardware you hold in your hands could very well be worth more than your automobile. So be gentle with it. Pretend it is made of eggshells and filled with explosives for instance.
- When you are tightening or loosening a connector, try not to spin the mating surfaces against each other. You should only be turning the threaded sleeve. Turning the mating surfaces means you are wearing out the connector for no reason.

Tips about connector care are summarized in Figure D.10. Usually, after delivery, connectors come with some plastic caps on each end. Those plastic caps are called dust caps for a reason, they keep the connectors clean. Keep them as long as you keep the adapters, and the adapters will last longer.

The website [1] also describes how to deal with stuck connectors and how to thouroughly clean them. Before performing any measurement, it is important to check the type of input and output connectors of each machine. This also influences the type of high-speed cables to be used in the experiment. For instance, cables Testline 18 Tyco and Advantest(Junflon A01002) have K-connectors and can operate up to 18GHz. But cables from Totoku-TCF have a V-connector at each end and can operate up to 40 and even up to 67GHz.

References

[1] microwaves101, *http://www.microwaves101.com*.

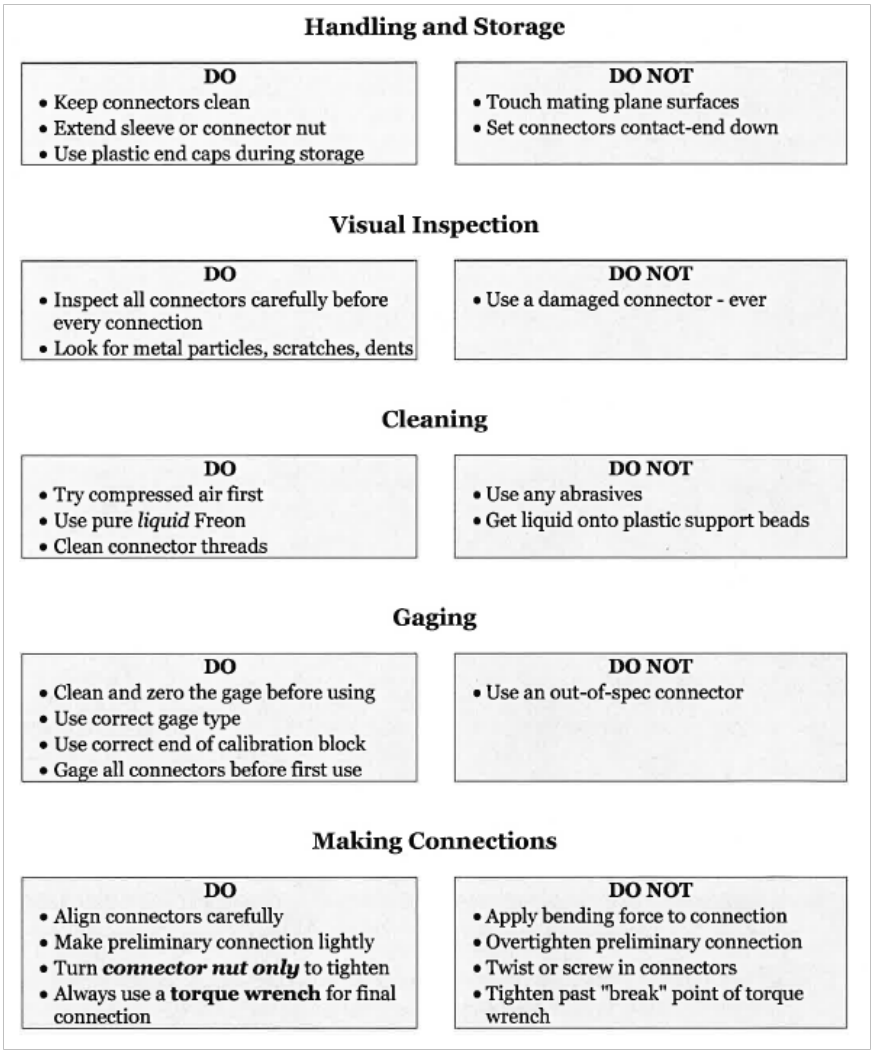

Figure D.10: Principles of microwave connector care [2].

[2] SHF Communication Technologies AG, *www.shf.de*.